
Analysis of the effect of intermittent wind on wind turbines by means of CFD

Sebastian Ehrich

Von der Fakultät für Mathematik und Naturwissenschaften
der Carl von Ossietzky Universität Oldenburg
zur Erlangung des Grades und Titels eines

DOKTORS DER NATURWISSENSCHAFTEN

DR.RER.NAT.

angenommene Dissertation

von Herrn Sebastian Ehrich
geboren am 06.12.1984 in Potsdam



Gutachter: Prof. Dr. Joachim Peinke
Zweitgutachter: Prof. Dr. Laura Lukassen
Tag der Disputation: 18.07.2022

Abstract

The goal of this thesis is to quantify the impact of higher order increment statistics on fatigue loads of wind turbines. Those non-Gaussian statistics are measured in atmospheric turbulence and are closely related to intermittent flow behavior. However, they are not considered in the current industry standard, where increments are always Gaussian distributed.

As the main tool for the generation of wind fields with the corresponding statistics, an improved stochastic turbulent wind model based on Continuous Time Random Walks (CTRWs) is used as an input for Computational Fluid Dynamics simulations. This inflow model is able to generate wind fields with Gaussian one point statistics and Gaussian as well as non-Gaussian increment statistics with a typical scale dependent increment kurtosis, as seen in atmospheric turbulence.

Before the actual wind energy related simulations are performed, several modifications to the CTRW model are presented to allow a definition of the wind fields with few model parameters. These also have a physical meaning and therefore the comparability with real wind fields is simplified. Moreover, different correction methods are presented which ensure a good comparability of simulations among each other with respect to their increment statistics. In this context it is shown how the spectra of two simulations can be adopted to each other with almost arbitrary high precision, while the first four moments of the one-point statistics approach the moments of a Gaussian statistics. Consequently, the differences of those properties for the comparison of load simulations becomes negligible.

To get an idea of the propagation of the generated wind fields in the CFD domain, the flow along an open channel is investigated first, where two different inflow methods are compared with respect to the evolution of the turbulence and the conservation of its input characteristics. Subsequently, the effect of non-Gaussian increment statistics on fatigue loads concerning lift and drag forces on an airfoil are analysed. As an important application, rotor simulations under turbulent inflow conditions are performed, where the main focus lies on torque and thrust, but also tangential and axial forces. Beforehand a comparison of three qualitatively distinct rotor models takes place to keep the quality at a high level with as few computational effort as possible. It is shown that an increased kurtosis of the increment distribution in the wind leads to higher fatigue loads for the airfoil as well as the whole rotor. Furthermore, a relation between correlations within the inflow plane and fatigue loads could be found.

Zusammenfassung

Das Ziel der vorgelegten Arbeit besteht darin, den Einfluss von Inkrement-Statistiken höherer Ordnung auf Ermüdungslasten an Windenergieanlagen zu quantifizieren. Diese nicht-Gaußförmigen Statistiken werden in atmosphärischer Turbulenz nachgewiesen und stehen in engem Zusammenhang mit intermittentem Strömungsverhalten. Allerdings werden diese nicht im derzeitigen Industriestandard berücksichtigt, in welchem Inkremente immer als Gauß-förmig verteilt angenommen werden.

Als Hauptinstrument zur Generierung von Windfeldern mit entsprechender Statistik wird ein verbessertes stochastisches turbulentes Windmodell auf Grundlage von kontinuierlichen Zeitprozessen, sog. Continuous Time Random Walks (CTRWs), als Eingabe für computerbasierten Strömungssimulationen (Computational Fluid Dynamics, CFD) genutzt. Mit diesem Einström-Modell können Windfelder mit Gauß-förmiger Ein-Punkt-Statistik und sowohl Gauß- als auch nicht Gauß-förmiger Inkrementstatistik mit typischem Skalierungsverhalten der Inkrementkurtosis erzeugt werden, wie man sie in atmosphärischer Turbulenz vorfindet.

Bevor die eigentlichen windenergiebezogenen Simulationen durchgeführt werden, werden einige Änderungen am CTRW-Modell vorgestellt, die es erlauben, die Windfelder anhand weniger Modellparameter zu definieren. Diese haben zudem eine physikalische Bedeutung und erleichtern dadurch eine Vergleichbarkeit mit realen Windfeldern. Des Weiteren werden verschiedene Korrekturmethode vorgestellt, die eine gute Vergleichbarkeit von Simulationen untereinander hinsichtlich ihrer Inkrementstatistik gewährleisten. Dazu wird gezeigt, wie die Spektren zweier Simulationen fast beliebig genau aneinander angepasst werden können und gleichzeitig die ersten vier Momente der Ein-Punkt-Statistik denen einer Gauß-Statistik angenähert werden. Folglich werden die Unterschiede dieser Eigenschaften bei vergleichenden Lastsimulationen vernachlässigbar.

Um ein Bild für die Ausbreitung der generierten Windfelder in der CFD-Umgebung zu bekommen, wird zunächst die Strömung in einem offenen Kanal untersucht, wobei an dieser Stelle zwei verschiedene Einströmmethoden hinsichtlich der Turbulenzentwicklung und der Erhaltung der Eingangscharakteristiken verglichen werden. Daraufhin wird der Effekt der nicht Gauß-förmigen Inkrementstatistik auf Ermüdungslasten bezüglich Auftriebs- und Widerstandskräfte an einem Rotorblattsegment analysiert. Als wichtigen Anwendungsfall finden zudem Rotorsimulationen mit turbulenter Einströmung statt, bei denen hauptsächlich das Drehmoment und der Schub, aber auch tangential und axiale Kräfte im Fokus stehen. Hier findet im Vorfeld ein Vergleich dreier qualitativ unterschiedlicher Rotormodellierungen statt, um die Qualität der Ergebnisse hoch und zugleich den rechentechnischen Aufwand möglichst klein zu halten. Es kann gezeigt werden, dass eine erhöhte Kurtosis der Inkrementverteilung des Windfeldes sowohl beim Rotorblattsegment als auch am gesamten Rotor zu größeren Ermüdungslasten führen. Zudem kann eine Beziehung zwischen den Korrelationen innerhalb der Einströmebene und den Ermüdungslasten festgestellt werden.

Contents

Abstract / Zusammenfassung	1
1 Introduction	11
1.1 Motivation and State of Research	11
1.2 Scope and Structure	12
2 Theoretical Foundations	15
2.1 Basic Description of Turbulent Flows	15
2.2 Structure Functions and Intermittency	18
2.3 Basics of Computational Fluid Dynamics	21
2.4 State of the Art Turbulence Models	22
2.5 CTRW Processes in Wind Energy	25
2.5.1 A Brief Introduction to CTRW Processes	25
2.5.2 The Wind Model by Kleinhans	26
2.6 Fatigue Load Estimation	30
3 Improvements on the Kleinhans Model and Study of its Properties	33
3.1 Further Developments on the Model	33
3.1.1 Generalisation of the Velocity Component Equations	33
3.1.2 Improvements on Spatial Correlations	34
3.1.3 Constraints on the Power Spectral Density and Autocorrelation Function	36
3.1.4 An Alternative Time Transformation	41
3.2 Turbulent Characteristics	42
3.2.1 Cross Statistics for a velocity time series	42
3.2.2 Cross Statistics for the in-plane correlated field	43
3.2.3 Turbulent Kinetic Energy and Dissipation	46
3.2.4 Time and Length Scales	47
3.2.5 Ensemble Correlation of the CTRW Process with Lévy Distributed Time .	49
3.2.6 Ensemble Kurtosis of Increment Statistics	51
3.3 Increment Kurtosis Dependence on Model Parameters	54
3.3.1 The Intermittency Parameter	54
3.3.2 The Intrinsic Time Step	56
3.3.3 The Integral Time Scale	60
3.4 Post-Corrections of Generated Wind Fields	62
3.4.1 Estimation Errors for the Power Spectral Density and Autocorrelation Function	62

3.4.2	Correction of the Power Spectral Density	65
3.4.3	Correction of the One Point Statistics	67
3.4.4	Correction of Divergence	68
4	Characterisation of CTRW Fields in an Open Channel	75
4.1	Simulation setup	75
4.2	Turbulence injection methods	76
4.2.1	Direct injection at inlet boundary	77
4.2.2	Injection via actuator	79
4.3	The Evolution Towards Isotropy	83
4.4	Effect of Non-Turbulent Boundary	85
5	Simulation of Airfoils	93
5.0.1	Simulation with Partially Correlated Inflow	97
5.0.2	Simulation with Fully Correlated Inflow	104
5.0.3	Discussion	109
6	Turbulence and Intermittency Study on Wind Turbines	111
6.1	What is the Effect of Turbulence on Wind Turbines? A Comparison of Three Standard Methods	111
6.1.1	Approach	111
6.1.2	Results	115
6.1.3	Discussion	124
6.2	Simulation of a wind turbine with Gaussian and intermittent wind fields	125
6.2.1	Empty Domain Simulation with Partially Correlated Fields	126
6.2.2	Rotor Simulation with Partially Correlated Fields	130
6.2.3	Empty Domain Simulation with Fully Correlated Fields	138
6.2.4	Rotor Simulation with Fully Correlated Fields	141
6.2.5	Discussion	150
7	Conclusions and Outlook	153
	List of publications	165
	Acknowledgements	167
	Curriculum vitae	169
	Erklärung	171

Nomenclature

Abbreviations

AOA	Angle of attack
BEM	Blade Element Momentum (Theory)
CFD	Computational Fluid Dynamics
CFL	Courant-Friedrichs-Lewy-number
Coh	Coherence
CTRW	Continuous Time Random Walk
DFT	Discrete Fourier transform
DNS	Direct Numerical Simulation
EFL	Equivalent fatigue load
LES	Large Eddy Simulation
MSD	Mean square displacement
PDF	Probability density function
PSD	Power spectral density
RANS	Reynolds-averaged Navier-Stokes
SD	Standard deviation
TI	Turbulence intensity
var(x)	Variance of x

Greek Symbols

α	Lévy exponent
β	Skewness parameter in Lévy distribution, Stretching factor for inertial subrange of modified CTRW spectrum
δ	Delta distribution, Tail parameter
δ_{ij}	Kronecker delta
η	First invariant of anisotropy tensor
γ	Damping constant of velocity process of CTRW model for all grid points
γ_d	Auxiliary damping constant
Γ_i	Gaussian distributed random variable of velocity process of CTRW model at point i
Γ_r	Gaussian distributed random variable of reference velocity process of CTRW model
γ_r	Damping constant of reference velocity process of CTRW model
κ	Wave number, Danish standard scaling for variance in CTRW model
λ	Laplace space variable
λ_t	Longitudinal Taylor length scale

μ	Intermittency coefficient, Tempering exponent, Mean value
ν	Kinematic viscosity
ω	Circular frequency
ω_c	Characteristic circular frequency for the inertial subrange in the CTRW model
$\bar{\tau}$	Integral time scale
Φ	Function to characterize Lévy distribution in Laplace space
ϕ	Distribution of jump length of CTRWs
Ψ	Gravitational potential
ρ	Autocorrelation function, Density
ρ_{uv}	Correlation function between u and v
σ	Standard deviation
τ	Time gap of increments, Waiting time of CTRWs
$\tau_{\alpha,C}$	Random number with fully skewed alpha-stable Lévy distribution
Θ	Heaviside function
ε	Rate of dissipation
ξ	Second invariant of anisotropy tensor
ξ_i	Wind profile factor at point i of CTRW model
ζ_n	Structure function scaling exponent

Roman Symbols

Δu_r	Velocity increment $u(x+r)-u(x)$
\hat{x}	Fourier transform of x
A	Drift matrix
B	Diffusion matrix
b	Anisotropy tensor
R	Covariance matrix
S	Spectrum matrix
H	Coupling matrix in CTRW process
a	Constant for definition of CTRW model power spectral density and auto-correlation function for a -5/3 spectrum
b	Logarithmic derivative function
C	Cutoff of Lévy distribution
c	Constant for definition of CTRW model parameters for a -5/3 spectrum, Constant used for exponential tempered Lévy distributions
C_0	Lower limit of cross correlation of CTRW process
c_d	Drag force coefficient
c_l	Lift force coefficient
D_i	Diffusion constant of velocity process of CTRW model at point i
D_r	Diffusion constant of reference process of CTRW model
E	Power spectral density
E_α	Mittag-Leffler function
E_{11}	One-dimensional power spectral density
f	Frequency
$f_{\alpha,\beta}$	Alpha-stable Lévy distribution

f_s	Sampling frequency
h	Transformation function to Laplacian space
K	Kurtosis
k	Turbulent kinetic energy
L	Longitudinal integral length scale
l_c	Correlation length, coupling strength in Kleinhans model
m	Wöhler exponent
P	Pressure
p	Modified pressure, probability density
r, r_{ij}	Spatial distance between two points (i and j)
R	Covariance function
S	Skewness
s	CTRW model intrinsic time
S_n	n-th structure function
s_{ij}	Fluctuating rate of strain
T	Reference number of ranges for fatigue load calculation
t	Time
u'	Velocity fluctuation
U	Mean velocity
u	Velocity
u_0	Mean value of reference process of CTRW model
u_r	Reference velocity of CTRW model
W	Wiener process
w	Distribution of waiting times of CTRWs
x, y, z	Spatial coordinates
y^+	Dimensionless wall distance
z_0	Roughness length
z_r	Reference height
C	Correlation matrix
Re	Reynolds number, Real part of a complex number
$\text{sgn}(x)$	Sign of x

Other Symbols

$\langle \cdot \rangle, \langle \cdot \rangle_t$	Ensemble average, time average
\mathcal{F}	Fourier transform
\mathcal{L}	Laplace transform
∇	Nabla operator
∂_x	Partial derivative with respect to x
\star	Convolution operator

Chapter 1

Introduction

1.1 Motivation and State of Research

Nowadays, wind is an important energy source which will be even more relevant in future times in consideration of climate change and the commitment to reduce greenhouse gas emissions to a very low level. Studies of the wind and its interactions with modern wind turbines are an absolute requirement to increase the power output, reduce the loads and finally also the cost of energy. Those are not least the most important points to make wind energy more competitive to other energy sources like fossil ones.

The IEC norm [1] provides some tools and industrial standards on the characterization of turbulent wind and the most important load cases. Despite of a very well-founded spectral description of atmospheric turbulence by the Mann [2, 3] and the Kaimal [4] model, other higher order statistical properties, related to intermittency and wind gusts, are not accounted for. The difficult implementation of the intermittency concept into existing wind models, as well as the belief that those properties are of minor importance for the design of wind turbines, led to a poor database in this field.

Most recent work on this topic in the scope of wind energy originates from the work of Böttcher et al. [5, 6, 7] who was able to reproduce the scaling behavior of velocity increments of atmospheric turbulence in the wind tunnel and describe the intermittency partially by the Castaing model [8]. In a later publication Milan et al. [9] could show that the scaling behavior of wind velocity increments and power increments of wind turbines is very similar, which led to the conclusion that this scaling is directly transferred from the wind to the power output. Furthermore Hähne et al. [10] could show that intermittency propagates in the power grid and affects the frequency increment distribution distant to the feed-in region.

In the context of loads on wind turbines, several investigations have been made by usage of the Continuous Time Random Walk (CTRW) model [11] which allows the numeric generation of intermittent wind fields by stochastic processes. This model has already been used in combination with Blade Element Momentum (BEM) tools in some works dealing with load calculations on wind turbines [12, 13]. But final conclusions about the effect of intermittency was not found because of the difficulty to make intermittent and non-intermittent wind fields comparable, i.e. the intermittency aspect could not be isolated. However in the work of Schwarz et al. [14, 15] a good comparison by usage of

the CTRW model and the certified and in industry widely used load simulation tool FAST (v8.15) [16, 17] could be made. In this work a comparison of the load dynamics of a large MW turbine for input wind fields with almost identical one- and two-point statistics but different increment probability densities has been conducted. Moreover, it was shown that for extremely coherent wind fields a fatigue load increase of 5 to 10 % can be achieved for several load sensors if the wind velocity increments are heavy-tailed distributed. The improvement of the CTRW model and its usage for wind turbine simulations is an essential part of this thesis and will be presented in more detail in the later sections.

Quite contrary are the results presented by Berg et al. [18] who combined Computational Fluid Dynamics (CFD) fields with BEM turbine simulations. The authors performed an LES simulation of an atmospheric boundary layer which naturally shows intermittency. Those fields are then extracted in the middle of the domain and introduced to a BEM simulation of a wind turbine. Non-intermittent fields, which were used for comparison, have been constructed by a phase randomization after a proper orthogonal decomposition. This work gave a hint that intermittency might increase the loads on the tower, but those effects could be insignificant if a safety factor is taken into account.

One of the main goals of this thesis is to give an additional contribution to this strongly and contradictory discussed topic and to introduce new methods for the sake of comparability of simulations with intermittent and non-intermittent wind inflow.

1.2 Scope and Structure

This thesis contains several improvements to the intermittency generation procedure with the CTRW model, where the model parameters are simplified and made physically more tangible. A first characterization of the resulting flow fields with respect to its turbulent properties and the intermittency in terms of the increment kurtosis is made, and several correction algorithms are presented to ensure a good comparability of Gaussian and non-Gaussian CTRW fields. Several airfoil and rotor simulations by means of CFD are performed for both types of fields, where the flow fields as well as forces and equivalent fatigue loads are discussed in more detail.

The following chapters are structured as follows:

- Chapter 2: An introduction to the theoretical description of turbulence with all relevant turbulence properties, which are used in this work, is given. Furthermore state of the art inflow models are presented and the concept of CTRW, the main simulation tool, namely CFD, and Equivalent fatigue loads are introduced.
- Chapter 3: The original CTRW model is explained in detail with the new improvements. Turbulent characteristics of the new model are derived and several parameter studies are presented. Lastly, different correction algorithms are explained which are essential for making Gaussian and non-Gaussian CTRW fields comparable.

-
- Chapter 4: CFD simulations of CTRW fields in an open channel are shown. For this purpose two different injection methods, namely the direct injection at the inlet boundary and the actuator method, are presented and discussed. For the first method the evolution of isotropy and the effect on the turbulence for different inlet sizes are studied.
 - Chapter 5: Airfoil simulations for partially and fully in-plane correlated CTRW fields are performed and intermittent and Gaussian cases are compared with respect to forces and loads.
 - Chapter 6: The effect of turbulence on wind turbine rotor loads is compared for three different simulation methods (BEM, CFD with actuator lines, CFD with fully resolved blades) with similar inflows. For the actuator line based case sectional as well as integral forces and fatigue loads are analysed for Gaussian and intermittent inflows.
 - Chapter 7: Conclusions are made and an outlook to potential future research is given.

Chapter 2

Theoretical Foundations

In this chapter the theoretical foundations for the following studies are presented in order to achieve some background knowledge and to understand the used methods of this thesis. First some general turbulence properties are introduced and the term "intermittency" is explained in the context of turbulence. After that a short section about the main method for the performed rotor and airfoil simulations, namely CFD, can be found. Furthermore some information on the state of the art turbulence models is given before the unmodified CTRW model is addressed.

2.1 Basic Description of Turbulent Flows

A fluid dynamical systems consists of many molecules which are in motion and interacting with each other all the time. The degree of freedom for such a complex system therefore is generally very high and not predictable on small scales. However it is strongly believed that on a macroscopic scale the Navier Stokes equations completely characterize such a system which are derived from mass, momentum, and energy conservation principles. Because air in the atmosphere can be approximated as an isothermal and incompressible fluid, the Navier Stokes equations simplify to the momentum equation

$$(\partial_t + \vec{u} \cdot \nabla) \vec{u} = -\frac{1}{\rho} \nabla p + \nu \nabla^2 \vec{u} \quad (2.1)$$

and the solenoidal condition

$$\nabla \cdot \vec{u} = 0 \quad (2.2)$$

where \vec{u} is the velocity vector, ρ the density, ν the kinematic viscosity, and $p = P + \rho\Psi$ the modified pressure with the pressure P and the gravitational potential Ψ . The used operators are the time derivative $\partial_t = \frac{\partial}{\partial t}$ and the nabla operator ∇ .

Despite of its seemingly simplicity, no smooth and globally defined solutions of this equation system have been found yet. The complexity and the importance of this problem is the reason why it became one of the Millenium Prize Problems [19].

In addition to that, under certain circumstances, the observed fluid can become turbulent. One of the characteristics of turbulence is its chaotic behavior, i.e. tiny perturbations in the initial or boundary conditions of the studied system lead to large perturbations in a relatively small time. This extreme sensitivity also means that if the same experiment is repeated several times, the flow patterns can deviate a lot, because the initial conditions are never the same.

A good way to encounter turbulence is to treat the velocity field $\vec{u}(t, \vec{x})$ as random with a specific probability density function (PDF) and make statistical predictions for the flow. In one dimension, with the given PDF $p(x, t)$ the most important statistical properties are the ensemble averaged mean

$$\langle u(x, t) \rangle = \int u(x, t) p(x, t) dx, \quad (2.3)$$

and the variance

$$\text{var}(u(x, t)) = \langle u'(x, t)^2 \rangle \quad (2.4)$$

where the fluctuations are defined as

$$u'(x, t) = u(x, t) - \langle u(x, t) \rangle. \quad (2.5)$$

The often used standard deviation is defined as its square root

$$\sigma(u(x, t)) = \sqrt{\text{var}(u(x, t))}. \quad (2.6)$$

Higher order one-point moments are also of interest, which are in particular the skewness

$$S(u(x, t)) = \langle u'(x, t)^3 \rangle / \sigma(u(x, t))^3 \quad (2.7)$$

and kurtosis

$$K(u(x, t)) = \langle u'(x, t)^4 \rangle / \sigma(u(x, t))^4 \quad (2.8)$$

which are for Gaussian distributed variables always $S = 0$ and $K = 3$.

Due to the fact that ensemble averages can only be done in rare cases with many realizations, they have to be substituted by temporal averages

$$\langle u(x, t) \rangle_t = \frac{1}{N} \sum_{i=1}^N u(x, t_i) \quad (2.9)$$

over N discrete time points. If this substitution can be made the system is called *ergodic*. For wind energy models, turbulence is often assumed to be stationary and homogenous which also means that the system is ergodic. Even, as shown in this thesis, ergodicity does not always hold, the time evolution of flow fields is still of main interest because ensemble averages are not very convenient due to limited computational power. Furthermore it is assumed that the same conclusions can be made, independent on the averaging procedure.

Of higher interest is also the two-point description of flows where two spatially or temporally separated points are used for the turbulence characterization. One important property which can be derived is the covariance function

$$R(u(s), v(t)) = \langle u'(s)v'(t) \rangle \quad (2.10)$$

for $t > s$, which describes the tendency in the linear relationship of the fluctuations u' and v' at the times s and t . It is common to normalize the covariance to

$$\rho_{uv}(s, t) = \frac{\langle u'(s)v'(t) \rangle}{\sigma(u)\sigma(v)} \quad (2.11)$$

which is the correlation function.

Even though turbulence is a three-dimensional phenomenon, very important information can be gained by assuming stationarity and focusing on longitudinal aspects of the flow field. As an example a statement about the size of large flow structures can be made by integrating the longitudinal autocorrelation function

$$\rho(\tau) = \frac{\langle u'(s)u'(s+\tau) \rangle}{\sigma(u)^2} \quad (2.12)$$

to

$$\bar{\tau} = \int_0^{\infty} \rho(\tau) d\tau \quad (2.13)$$

which is called the integral time scale. Another very informative function can be gained by Fourier transforming the autocorrelation function to the power spectral density (PSD)

$$E(\omega) = \int \rho(\tau)e^{-i\omega\tau} d\tau \quad (2.14)$$

which may have a very specific shape for most turbulent flows as shown in Figure 2.1 for several measurements for its spatial longitudinal one-dimensional counterpart in wavenumber space [20]

$$E_{11}(\kappa_1) = \int \rho(r_1)e^{-i\kappa_1 r_1} dr_1. \quad (2.15)$$

Such spectra contain up to three different regions, which can be found in any turbulent flow:

- A large anisotropic scale range, which is mainly affected by the boundary of the flow,
- a universal region, the *inertial subrange*, where the PSD drops with $E_{11} \propto \kappa_1^{-5/3}$ or in frequency space $E \propto \omega^{-5/3}$, as long as the Reynolds number $Re = UL/\nu$ is sufficiently high, with the characteristic velocity and length scales of the system U and L , and
- a dissipation range on very small scales, which is dominated by viscous, dissipative effects.

The large flow structures become isotropic in the inertial subrange due to a chaotic scale reduction process, where directional information is lost, before dissipation takes part on smallest scales. The existence of the inertial subrange was stated by Kolmogorov in his fundamental work in 1941 [21] by a dimensional analysis under assumption of isotropy for the small scale motions (*first similarity hypothesis*) and its uniquely determination by the dissipation ε (*second similarity hypothesis*). Due to the universality and importance of this *-5/3 law*, one of the main goals of a turbulence model should be to assemble a spectrum with such an inertial subrange which will be done for the CTRW model in .

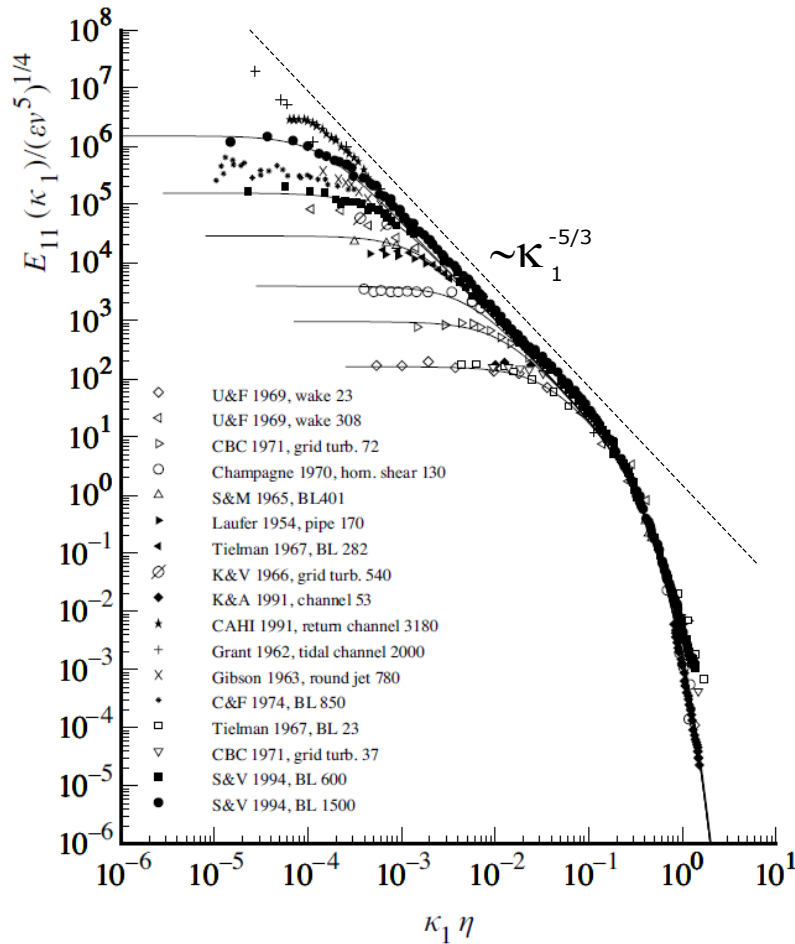


Figure 2.1: Measurements of longitudinal one-dimensional velocity spectra, taken from Pope [20] and modified.

2.2 Structure Functions and Intermittency

More insight into the inertial subrange can be gained by introducing longitudinal velocity increments

$$\Delta u_r(x) = u(x+r) - u(x) \quad (2.16)$$

where especially the statistical moments, the longitudinal structure functions

$$S_n(r) = \langle (\Delta u_r)^n \rangle, \quad (2.17)$$

are of major interest. Kolmogorov conjectured by means of the second similarity hypothesis that those structure functions have to have the self-similar form

$$S_n(r) = C_n (\varepsilon r)^{\zeta_n}, \quad (2.18)$$

where C_n are constants, the scaling exponent is $\zeta_n = n/3$, and

$$\varepsilon = 2\nu \langle s_{ij} s_{ij} \rangle \quad (2.19)$$

is the dissipation rate under consideration of the Einstein notation with the fluctuating rate of strain

$$s_{ij} = \frac{1}{2} \left(\frac{\partial u_i}{\partial x_j} + \frac{\partial u_j}{\partial x_i} \right). \quad (2.20)$$

For $n = 3$ the constant $C_3 = -4/3$ can be calculated by use of an re-expressed Kármán-Howarth equation [22, 20], known as the Kolmogorov equation [21], which describes the evolution for the second and third order structure functions in isotropic turbulence. The resulting un-normalized increment skewness

$$S_3(r) = -\frac{4}{5} \varepsilon r, \quad (2.21)$$

is also known as the *Kolmogorov 4/5 law* and shows that the skewness is generally negative. However the predictions for higher order structure functions like the increment kurtosis

$$K(r) = \frac{S_4(r)}{S_2(r)^2} = \frac{C_4}{C_2^2}, \quad (2.22)$$

proved to be inaccurate, as measured in experiments by Anselmet et al. [23]. Therefore also the assumption of self-similarity must be wrong, which was corrected by Kolmogorov in his *refined similarity hypothesis* [24] where the dissipation rate is not assumed to be constant, but random, log-normally distributed and scale dependent. The conclusion of his study is that self-similarity breaks and the scaling exponent changes to

$$\zeta_n = \frac{n}{3} - \frac{\mu}{18} n(n-3) \quad (2.23)$$

with the *intermittency coefficient* μ which is measured for homogenous isotropic turbulence as $\mu = 0.25 \pm 0.05$ [25]. The Kolmogorov 4/5 law is still valid for the refined hypothesis, however higher order functions change significantly. Moreover due to the change of the second structure function S_2 also the power spectral density exponent in the inertial subrange changes to $E \propto \omega^{-5/3-1/36}$ for $\mu = 0.25$. However, the very small adjustment can be neglected and within this thesis the -5/3 law is used for simplicity reasons.

The scale dependent distributions of increments normalized by the standard deviation for a free jet are shown in Figure 2.2 where the increased increment kurtosis for small distances

r is obvious. Not only in laboratory experiments but also in atmospheric flows intermittency is present as shown in the work of Morales et al. [26]. In this work a dataset taken from the FINO offshore platform has been analysed for its temporal increment statistics. The achieved increment distributions for different time scales are shown in Figure 2.3. It has to be emphasized that an increased increment kurtosis is strongly related to extreme events, e.g. a wind speed increase of up to 15 standard deviations can be noticed in Figure 2.3 which is much higher than for the Gaussian case.

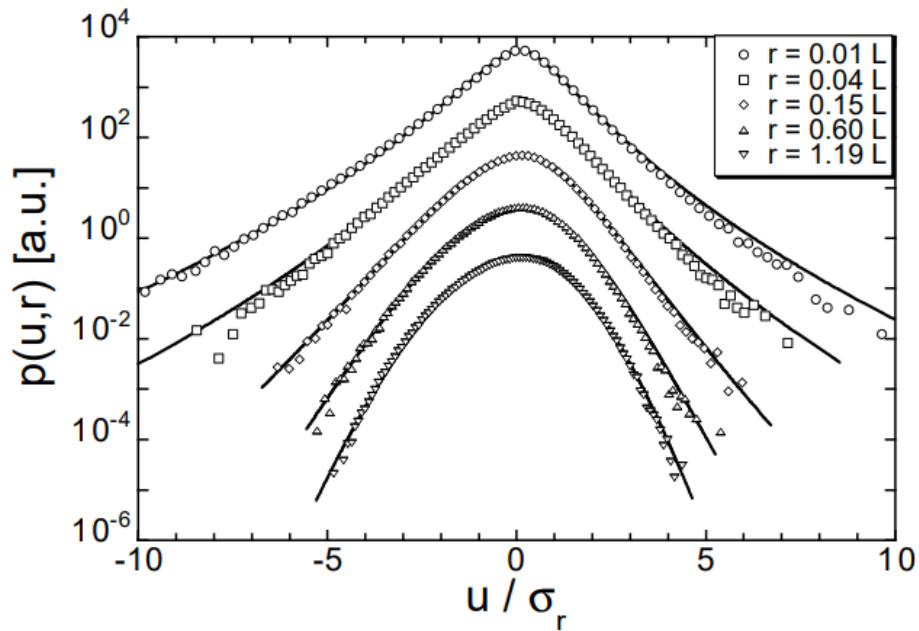


Figure 2.2: Measurements of longitudinal normalized increment distributions for a free jet, taken from Renner [27]. The distributions for different scales are shifted for better visualization.

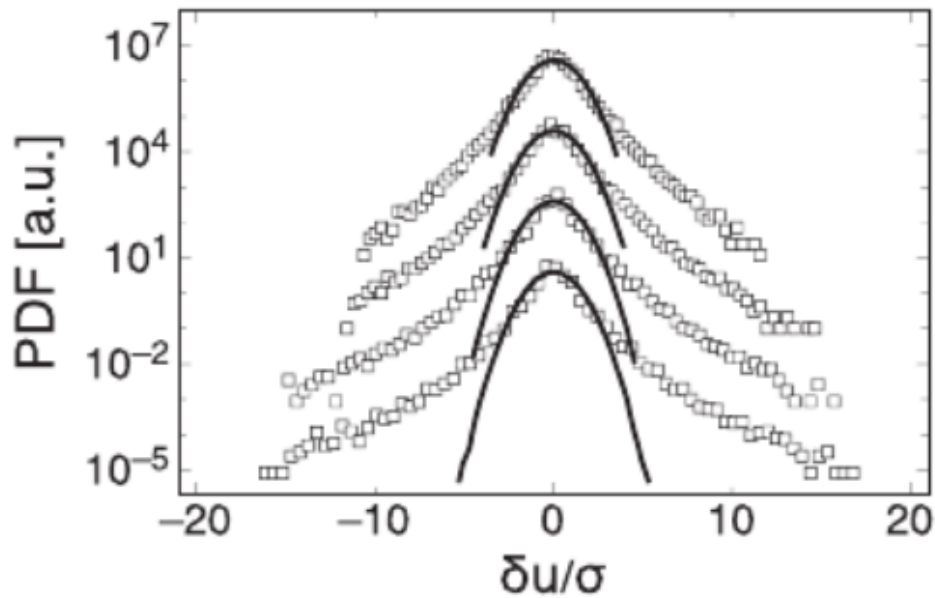


Figure 2.3: Measurements of normalized temporal increment distributions for atmospheric wind measured at the offshore platform FINO with time gaps $\tau = 2, 4, 10,$ and 60 s, taken from Morales et al. [26]. The distributions for different scales are shifted for better visualization.

2.3 Basics of Computational Fluid Dynamics

In general turbulent flows are not homogenous and isotropic and very complex behavior might occur due to non-trivial boundary and initial conditions. For many flows analytic solutions of the Navier-Stokes Equations (2.1) and (2.2) are not derivable with the known mathematical methods, especially because the non-local and nonlinear pressure-gradient term and the convective term are very difficult to handle. Therefore numerical approaches have to be used with help of high-performing computers or computer clusters. As a first step the spatial domain has to be discretized in small cells, where the velocity and pressure are calculated by usage of discretized Navier-Stokes equations. In principle three different simulation methods are available: *Direct Numerical Simulation* (DNS), *Reynolds-averaged Navier-Stokes* (RANS) and *Large-Eddy Simulation* (LES). In the computational very costly DNS the turbulence is fully resolved down to the smallest dissipative scale, the so called *Kolmogorov scale*. RANS is used to solve for the average velocity field by means of averaged Navier-Stokes equations and algebraic equations for the *Reynolds stress* $\langle u'_i u'_j \rangle$. The discretization does not have to be very fine and therefore RANS is also doable with low computational power. However this method is not appropriate if turbulence should be studied because of the missing information of velocity fluctuations. As a middle way, LES can be used, where turbulence is resolved down to the inertial subrange by filtering. Smaller scales are not resolved and have to be modeled. If the reader is interested, further information on these methods can be found in [20]. In this thesis only LES has been used for all simulations and more information on the sub-scale models are given in the appropriate context.

2.4 State of the Art Turbulence Models

The nonlinearity of the Navier-Stokes equation system results in turbulent structures which are at the same time random and coherent. Simulating those motions accurately with resolving CFD methods like DNS or LES leads to several challenges which are to be solved. Important for the physical evolution of the turbulence are numerical correctness but also inflow boundary conditions which represent the spatial and temporal properties in a proper way. Otherwise the turbulent fields can decay instantaneously [28] and prescribed turbulence intensities are not advected through the domain. The evolution of turbulent vortices in the flow are strongly dependent on their initial state. Therefore it is obvious that much effort has to be put into the development of an inlet boundary condition which is able to generate realistic turbulent structures which also persist over large distances downstream. Creating such a boundary condition is in general not an easy task because several statistical properties of turbulence like temporal and spatial correlations, length scales, spectra or even higher order characteristics have to be considered. In the following a very short overview of different methods is given which are used for turbulence generation in the field of wind energy. The wind fields can be used as an inflow for Computational Fluid Dynamics with the purpose to simulate airfoils, rotor blades or even turbines. For all presented models the mathematical background is roughly given and it is discussed which advantages and drawbacks they have. For a more complete overview the reader is encouraged to read the chapter on Turbulent Inflow Models in [29].

In general two different groups of methods of generating turbulent velocity data exist. In the first group, the recycling methods, the equations of fluid motion are solved in an auxiliary CFD simulation where the inflow data is extracted from the interior of the domain. Some basic work has been done in the work of Lund et al. [30] and Spalart et al. [31]. Even though recycling methods are not very popular for simulating wind turbines they are used very often for the generation and study of atmospheric boundary layers [32, 33] and for the study of the wake of wind turbines [34].

The methods of the second group generate artificial inflow data by using mathematical models and are therefore an approximation to the recycling methods and not a solution to the Navier-Stokes equations. These methods normally have some shortcomings in the physicality and correctness compared to the first group but the field generation is less costly, and the characteristics of the created velocity fields are known much better. Linked to these points is the high flexibility of those models which is needed for setups where several simulations with different inflow conditions have to be performed, without the costs of undergoing additional auxiliary simulations. Another main advantage is the potential focus on specific characteristics of turbulence rather than on the whole picture. In conjunction with BEM, synthetic models have the big advantage that the user does not have to worry about complex CFD simulations and the turbulence can directly be introduced to the simulation object without changing its characteristics too much.

One approved approach is the digital filtering method, developed by Klein et al. [35]. This method can be used to generate artificial velocity data with prescribed first and second order one point statistics as well as the autocorrelation function for each inflow cell of a uniform grid. Introducing cross correlations can distort the shape of the autocorrelation function, but this is assumed to be a small change. The method of digital filtering found its

way into a wide range of applications also in the area of wind energy where e.g. Breuer et al. [36] studied the flow past airfoils and the transition to turbulence in the airfoil boundary layer. For this approach they introduced the turbulence by source terms in cells close to the airfoil to overcome the issue of too fast decaying turbulence. Another work of Szasz et al. [37] studied with this inflow model the influence on the wake of a turbine.

A more flexible method than the digital filtering is introduced by Kornev [38] which is based on randomly distributed turbulent spots with specific velocity distributions. Those are superposed to achieve prescribed turbulent characteristics in three dimensions. In this way accurate spatial and temporal autocorrelation functions as well as cross correlations can be defined which even can have analytical forms if homogeneity is assumed. Other advantages compared to the digital filtering is that a non-uniform grid can be used and the involved length scales can be dependent on location and time which allows to simulate boundary layers for CFD or BEM. Kornev reports that for high separation of turbulent spots it is also possible to introduce intermittency to the system. But further publications with more insight are missing. The method of random spots as well as digital filtering have in common that both can not ensure divergence free velocity fields and a correction algorithm, e.g. PISO [39, 40], has to be used. As a CFD example Sale et al. [41] simulated a two bladed wind turbine by means of the actuator line method and an inflow turbulence based on the method of random spots for comparison of the wake structure with particle image velocimetry. Other applications of Kornev's method for environmental flows are shown in the work of Bazdidi-Tehrani et al. [42] and Kubilay et al. [43].

Even though the aforementioned generation algorithms are usable for wind energy applications, other methods based on the spectral description of atmospheric turbulence are preferably used. Veers [44, 45] presented an algorithm, the so called *Sandia method*, where single point spectral densities, e.g. Kaimal [4] or the von Kármán [46] spectra, combined with an isotropic coherence function are converted to real-valued cross spectral densities. With the help of a Cholesky decomposition and random vectors, correlated wind fields are then gained as an input for all inlet cells. The Sandia method is mainly used for the structural analysis of horizontal axis turbines in BEM, but it is in general also valid for CFD simulations. However the involved Cholesky decomposition is very time-consuming for inflows with many grid points and is therefore not recommended for highly resolved flows.

The most sophisticated and widely used model is the *Mann Model* [2, 3] which is a spectral turbulence model developed for the horizontally homogeneous neutral atmospheric boundary layer. This model based on the *Rapid Distortion Theory* and consideration of eddy lifetimes is able to reproduce velocity component spectra as well as coherences and cross spectra of all velocity components at two separated points by adjusting three parameters in total. An anisotropic model with the von Kármán model as a limit case is achieved where the anisotropy can be controlled with a single parameter. As simplifications the Navier-Stokes equations are linearized, the viscosity is neglected, the velocity profile is assumed to be linear, and the gravitation as well as the rotation of earth are neglected. Thus the spectral tensor is only able to model eddies close to the ground where the shear does not change too much. Nevertheless the performance concerning second-order two point statistics is very good. This model has very broad applications in wind energy by means of CFD and BEM. From wake studies of an actuator line [47], actuator disk [48, 49], and full rotor [50], and wind turbine performance [51] to fatigue analysis [13, 52], where the fatigue loads

were compared with the Kaimal, von Kármán and CTRW model. The Mann model already has been implemented in the blade element momentum code HAWC2 [53] and is together with the Kaimal model part of the IEC 61400-1 [1] where they are proposed for fatigue simulations.

2.5 CTRW Processes in Wind Energy

2.5.1 A Brief Introduction to CTRW Processes

Even though several wind models have been developed in the past, intermittency and higher order statistics related to wind velocity increments, i.e. the structure functions, have not been considered in the IEC standard. In particular, in those models the increments are Gaussian distributed which means that e.g. for the normalized fourth order structure functions $K(\tau) = S_4(\tau)/S_2(\tau)^2 = 3$ holds, which is not correct as explained in section 2.2. Taking into account the whole scaling behavior in a correct way is a rather complex task and very difficult to project onto a wind model. Despite of this fact, a big step forward has been done with a wind model based on *Continuous Time Random Walks* (CTRWs) where the increment kurtosis $K(\tau)$ can be modeled dependent on the scale, shown in Figure 2.4. Within the rest of this thesis, intermittency and the scaling of K are often used synonymously for simplicity.

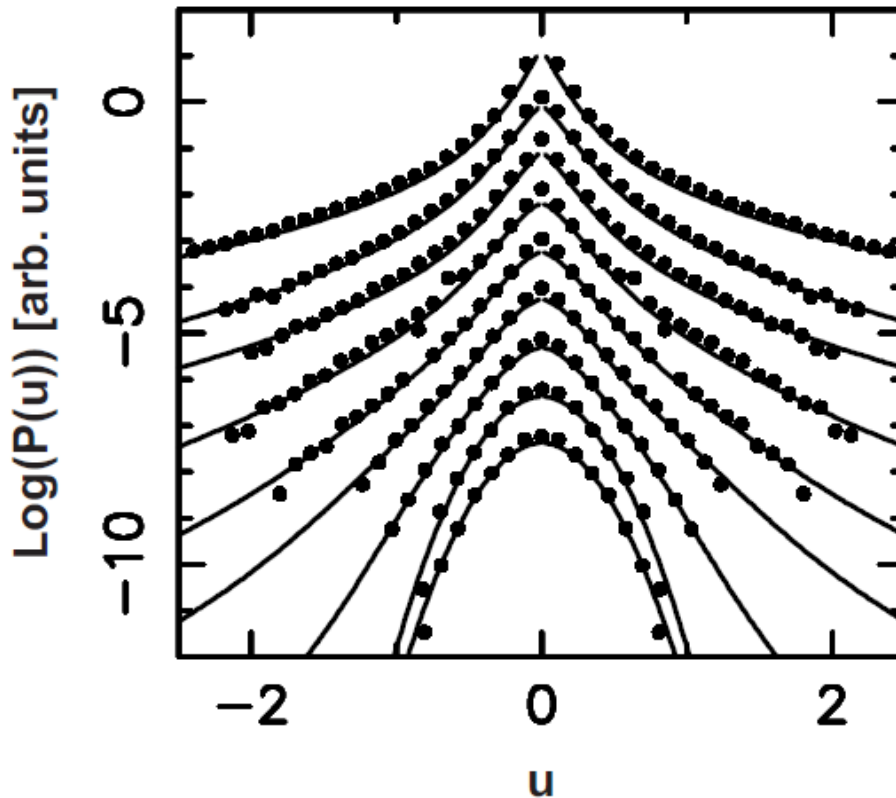


Figure 2.4: Distributions of wind velocity increments of advected particles for different time increments between 0.15 ms (top) to 40 ms (bottom). Measurements are taken from Mordant et al. [54] and the fits were modeled with several CTRW processes with different parameter sets by Friedrich et al. [55]. The distributions for different scales are shifted for better visualization.

CTRWs, first introduced in the work of Montroll and Weiss [56] originally had the goal to describe physical phenomena, like target searching and trapping, and are a generalisation of the well known random walk model, known from Brownian Motion. In contrast to ordi-

nary random walks, where point particles jump at fixed time gaps by a specific jump length, CTRWs allow the particles to rest for some random time before the next jump takes place. The jump lengths as well as the time are sampled from a given distribution $\psi(x, t)$ which can be factorized into $\psi(x, t) = w(t)\phi(x)$ if the jump length and time step are assumed to be independent. This approach can be used to consider trapping-untrapping events for particle trajectories in turbulence which lead to a mean square displacement for Lagrangian particles $MSD(t) = \langle (X(t) - x_0)^2 \rangle \propto t^\alpha$ with $0 < \alpha < 1$. However this anomalous diffusion is strongly connected to non-stationary dynamics, i.e. autocorrelation functions and spectra become time dependent. In addition to that the average waiting time $\langle \tau \rangle = \int_0^\infty \tau w(\tau) d\tau$ diverges which usually makes the generation of pure CTRW time series difficult, because the waiting time can be longer than the observation time. Furthermore the frequency of time steps scales as $\propto t^{\alpha-1}$ which means that the dynamics slow down over time. This effect is known as ageing and is studied in more detail in [57]. Related to ageing and non stationarity is the *weak ergodicity breaking*, which implies the ensemble averages over independent realisations and time averages of trajectories are not equal anymore, because the waiting times become infinitely long in the limit $t \rightarrow \infty$.

Other equivalent models which are usually used in place of CTRWs are fractional Brownian motions [58] or Langevin equations with power-law kernel [59], but they are not in the scope of this thesis.

2.5.2 The Wind Model by Kleinhans

For the generation of three dimensional, intermittent, and time dependent wind fields on a two dimensional grid perpendicular to the main stream direction, a model based on CTRWs has been developed by Kleinhans [60]. This wind field generator makes it possible to change the kurtosis of the increment PDF at the smallest scale arbitrarily in the super Gaussian region. The increment PDF's show a typical multifractal scaling with a more Gaussian like behavior at larger scales. However the exact scaling behavior of the kurtosis from small to larger scales is prescribed by the model equations and can not be influenced directly by the user. Additionally to the ability of tuning the strength of intermittency, temporal and spatial correlation strengths can be set by choosing appropriate model parameters. In general those correlation functions are monotonously decreasing with temporal and spatial distance.

The simulation of each velocity component at each grid point is splitted up into three parts:

- A reference velocity is calculated which can be interpreted as a varying average over time
- The velocity at each grid point is calculated introducing also spatial correlations
- A time transformation is done for introducing intermittency into the field

In the following subsections the different parts of this model are explained in more detail.

The reference velocity

All wind fields generated by this model are based on an underlying stochastic process which corresponds to a slowly varying average of the wind velocity, the so called reference velocity

u_r . This reference velocity is grid independent and a stochastic differential equation in the model intrinsic time s of the form

$$\frac{du_r(s)}{ds} = -\gamma_r(u_r(s) - u_0) + \sqrt{D_r}\Gamma_r(s). \quad (2.24)$$

This is a one dimensional Ornstein-Uhlenbeck process with γ_r being a damping constant which drives the system back to the long time mean velocity u_0 , which would be exponentially approached with $e^{-\gamma s}$ if there would be no stochastic term in this equation. But because the second term on the right hand side is a stochastic term the overall process for the reference velocity is also stochastic. The diffusion constant is D_r and Γ_r is delta correlated Gaussian noise with zero mean and variance equal to two.

The velocity at each grid point

Based on the reference velocity u_r it is now possible to simulate velocity components $u_i^{(k)}$ at all grid points $i = 1, 2, \dots, N$ and directions $k = x, y, z$ by another Ornstein-Uhlenbeck process

$$\frac{du_i^{(k)}(s)}{ds} = -\gamma \left(u_i^{(k)}(s) - \xi_i^{(k)} u_r(s) \right) + \sqrt{D_i^{(k)}} \sum_j^N H_{ij} \Gamma_j^{(k)}(s) \quad (2.25)$$

which is very similar to the equation of the reference velocity, but with a different damping constant, mean value, and diffusion term. The mean value of this process is equal to the reference velocity, but multiplied by a factor $\xi_i^{(k)}$ corresponding to the wind profile. This factor depends only on the height of the grid point and the profile specific constants like the roughness length. $\xi_i^{(k)}$ has to be chosen relative to the reference height, which is the height, where the mean velocity u_0 of the reference process u_r is set. If a logarithmic profile is used and the flow is assumed to propagate in x -direction, then the profile is

$$\xi_i^{(x)} = \frac{\log(z_i/z_0)}{\log(z_r/z_0)} \quad (2.26a)$$

$$\xi_i^{(y,z)} = 0. \quad (2.26b)$$

with reference height z_r and roughness length z_0 . In this case no velocity profile is assumed for directions y and z .

Γ_j is again Gaussian noise similar to Γ_r for the reference velocity. Additionally it is independent and therefore uncorrelated for all directions and grid points. The sum over all grid points in the last term of Equation (2.25) leads to spatial correlations of the diffusion terms of all grid points. This correlation of the noise terms and the coupling of all velocities at the different grid points with the reference velocity are responsible for cross correlations of velocities at different grid points.

Kleinhans proposed a coupling matrix \mathbf{H} with entries

$$H_{ij} = \begin{cases} i \geq j: & \exp\left(-\frac{r_{ij}}{l_c}\right) / \sqrt{\sum_{k=1}^i \exp\left(-2\frac{r_{ik}}{l_c}\right)} \\ i < j: & 0 \end{cases} \quad (2.27)$$

with a constant l_c defining the coupling strength and r_{ij} the distance between points i and j . The prefactor D_i in Equation (2.25) has to be

$$D_i^{(k)} = \gamma \sigma^2 \left(\kappa^{(k)}\right)^2 - \left(\xi_i^{(k)}\right)^2 D_r \frac{\gamma^2}{\gamma_r (\gamma + \gamma_r)} \quad (2.28)$$

to achieve height independent variances $\sigma^2 \left(\kappa^{(k)}\right)^2$ in the wind field. According to the Danish standards[1] the variance of the three velocity components are different, in particular $\kappa^{(x)} = 1, \kappa^{(y)} = 0.8$ and $\kappa^{(z)} = 0.5$. With the coupling mentioned above, Kleinhans intended to introduce exponentially decaying spatial correlation, but as will be shown in section 3.1.2 a correction of this model is needed.

The time transformation

Equations (2.24) and (2.25) define a system of two coupled Ornstein-Uhlenbeck processes with statistical properties which can be easily derived. But the most important and at the same time complicated part of the CTRW model is the time transformation

$$\frac{dt(s)}{ds} = \tau_{\alpha,C}(s). \quad (2.29)$$

which can change those statistical properties drastically. But this subordination is essential for intermittency.

Shown here is a stochastic process of the physical time t , which is the time of the model output, dependent on the model intrinsic time s , which is also used in Equations (2.24) and (2.25). The type of the random variable on the right hand side is important for the time evolution of the overall process and the type of intermittency one would achieve out of the model. In this case $\tau_{\alpha,C}$ is chosen to be a realization of the process with a fully skewed alpha-stable Lévy distribution [61, 62], which is defined as an alpha-stable Lévy distribution

$$f_{\alpha,\beta} = \frac{1}{\pi} \operatorname{Re} \left\{ \int_0^\infty d\kappa \exp \left[-i\kappa x - |\kappa|^\alpha \exp \left(-i \operatorname{atan} \left(\beta \tan \left(\frac{\pi\alpha}{2} \right) \right) \right) \right] \right\} \quad (2.30)$$

with $\beta = 1$, and a cutoff C , which was defined by Kleinhans and is introduced below. Originally this distribution was taken because it is the most general stable distribution only defined for positive values which goes hand in hand with the monotony of time. The Lévy exponent α and the cutoff C both prescribe the shape of the Lévy distribution which will be shown in the following.

The effect of α , generally chosen as $0 < \alpha < 1$, on the time distribution is depicted in Figure 2.5, and its effect on the increment distribution in Figure 2.6a. One can summarize: The smaller α is, the higher the intermittency. $\alpha = 1$ means $\tau_{\alpha,C}$ is delta distributed around

the value 1, which corresponds to a constant step size for t and with it to a normal discrete random walk for the whole CTRW process, resulting in Gaussian increment statistics. $\alpha = 0$ leads to a delta distribution around 0. Of course picking such a distribution is not allowed, because the time step Δt is also 0, meaning there are two times s_n and s_{n+1} projected onto the same time t .

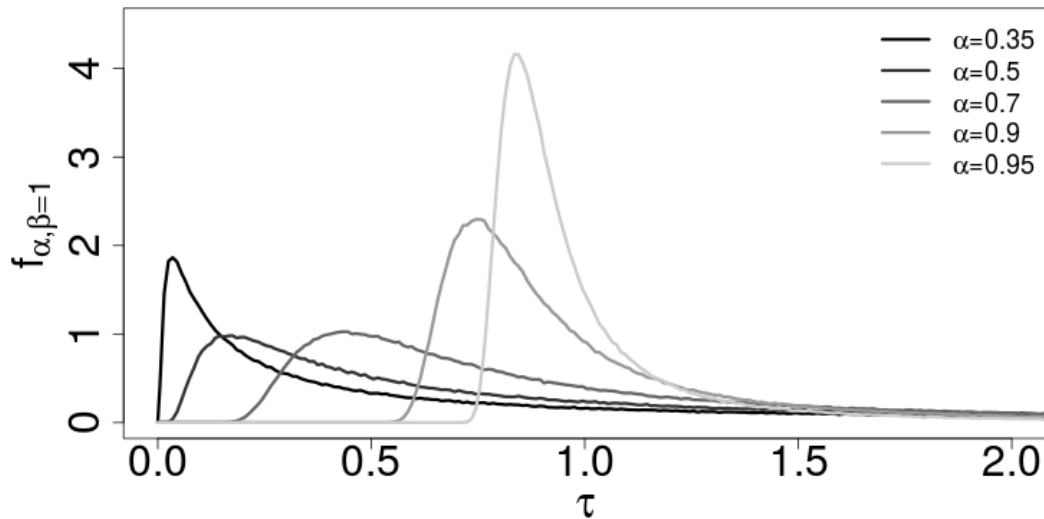


Figure 2.5: Lévy distribution for different values of the exponent α .

One of the big issues with the fully skewed Lévy distribution are the divergent first and second moment, meaning infinite mean and variance. On the one hand the divergence is part of the stable distribution, which makes also the model mathematically describable, but on the other hand a divergent mean and standard deviation also means that a time step Δt of the process can theoretically be infinitely large. Therefore it is possible that the velocity does not change at all for the whole simulated time series. To forbid such behaviour a cutoff value C was introduced for the Lévy distribution. It only allows random variables $\tau_{\alpha, C} < C$, meaning that the mean and variance of the distribution are limited. The cutoff also has an effect on the kurtosis of the increment distribution as shown in Figure 2.6b. The bigger the cutoff, the more heavy-tailed the increment distribution and the more pronounced the inner peak, because longer waiting times are allowed.

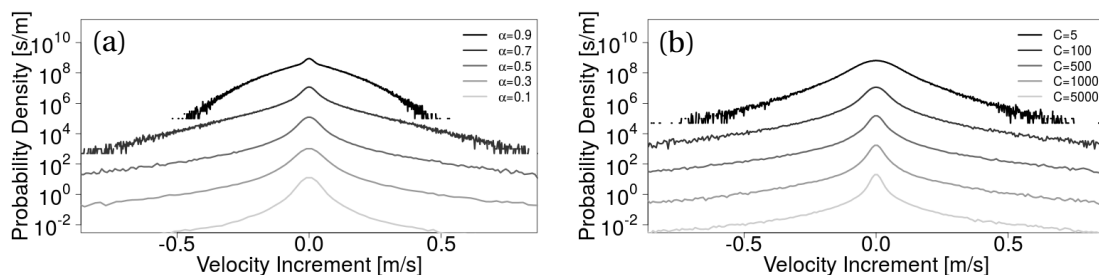


Figure 2.6: Change of increments for $\tau = 0.01$ s with (a) the Lévy exponent α and (b) the cutoff C .

As a second measure, a time interpolation in the s - t -diagram is introduced as shown in Figure 2.7 where the original as well as the interpolated process are shown. This makes sure that different time steps in the t domain show different velocities. In addition, waiting times are fully avoided.

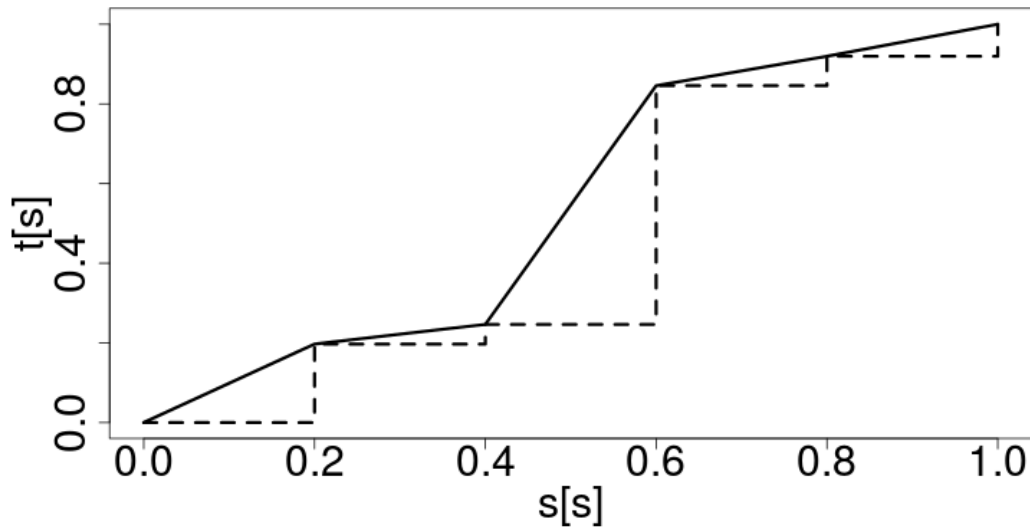


Figure 2.7: Sketch of the process $t(s)$ in its original form (dashed) and interpolated (solid).

However this cutoff makes a proper mathematical description of the evolution of all related quantities very difficult. Actually at the time of this thesis there are no analytical formulations known for power spectral densities (PSD), and time averaged correlation functions or even higher order time averaged quantities of CTRW's. The evolution of ensemble averaged quantities of CTRW's can be calculated as long as the process is kept simple and a cutoff of the Lévy distribution is not included. Later on in section 3.1.4 it will be shown that another type of modification to the Lévy distribution, the tempering, can be applied, whose effect can at least be partially described in terms of ensemble averaged quantities. All in all it has to be emphasized that the intermittency gained by this model is only present in the temporal dimension. Spatial intermittency at the generation grid at one instance of time is not supported.

2.6 Fatigue Load Estimation

One of the most important quantities relevant for wind turbine designs are the fatigue loads on different parts of the turbine estimated by damage equivalent loads. They are also known as Equivalent Fatigue Loads (EFL), which will play a role in the load analysis for the simulation methods investigated in this thesis. In contrast to ultimate loads, which are the maximum loads a component can withstand, fatigue loads are relatively small. They lead to structural failures due to the accumulation of loads over time and the corresponding progression of micro-fractures in the material. This is why fatigue loads are time series dependent while

for ultimate loads only single events are important. This time series dependency also qualifies fatigue loads to be a relevant quantity in the scope of intermittent inflow, because the related higher order statistics are considered.

EFL can be defined as

$$\text{EFL} = \left(\frac{\sum n_i r_i^m}{T} \right)^{\frac{1}{m}}, \quad (2.31)$$

where r_i are the specific load ranges, n_i the corresponding amount of load ranges, T the reference number of ranges (here the dimensionless time in seconds) and m the Wöhler exponent. The Wöhler exponent, also known as *SN slope coefficient*, is an important material constant for fatigue load estimations and characterizes the material fatigue performance under cyclic stresses. Usually it takes the values $m = 4$ for a tower sensor, $m = 8$ for drive train loads and $m = 12$ for the blade root bending moment out of plane and the tower base bending moment fore-aft. Because the main focus of this thesis lies on the drive train loads, in particular thrust and torque, $m = 8$ is chosen for all EFL calculations. In essence, the EFL can be understood as a minimum-maximum load difference of a hypothetical load cycle with a period of 1 s which would cause the same damage over the time T as the originally measured load time series. More information on the estimation of the EFL and the underlying rainflow count algorithm can be found in the work of Madsen [63] and Rychlik [64].

Chapter 3

Improvements on the Kleinhans Model and Study of its Properties

This chapter deals with improvements on the Kleinhans model and the resulting mathematical properties are derived. These improvements are a spectral simplification by parameter reduction, a better spatial and temporal autocorrelation, a better understood time transformation, and several post corrections on the field which allow divergence freeness, more accurate power spectra, and improved Gaussianity of the one point statistics of velocity. In the last section some parameter studies are shown to get an insight into the non-trivial behavior of the CTRW model.

3.1 Further Developments on the Model

In this section several modifications to the model are introduced which simplify model equations or improve the comparability with real wind fields, in particular the wind velocity components and the spatial structures are adjusted. Additionally the parameter space is reduced and the simulation is stabilized in the sense that an unphysical choice of parameters becomes impossible. Those simplifications allow to derive properties like the integral length and time scales in a simple manner. For comparison reasons post-corrections for the PSD and the one point PDF are shown. Additionally an algorithm to create divergence free fields and its effect on spectra and increment distributions is discussed.

3.1.1 Generalisation of the Velocity Component Equations

The model by Kleinhans treats the main stream velocity component and components perpendicular to it in a different way. While for the main component the reference velocity plays a major role, it is neglected for the other components. This leads in general to very different dynamics, including autocorrelations, spectra and time scales. However there is no reason shown for the specific treatment of perpendicular velocity components within the CTRW model. To generalise and simplify the whole process, a modification to the equation system is made in the way that all three velocity components follow the same equation system as for the main stream component, but the mean values $u_0^{(k)}$ for each component are allowed to differ, i.e. the main stream direction does not have to coincide with the direction of one of

the velocity components. This also has the advantage that surrogates to measurement data can be created with a diagonal inflow direction, which itself can be used for CFD or BEM simulations. The reference velocity, mean velocity and noise term are split up into three components

$$\vec{u}_r(s) = \begin{pmatrix} u_r^{(x)}(s) \\ u_r^{(y)}(s) \\ u_r^{(z)}(s) \end{pmatrix}, \quad \vec{u}_0 = \begin{pmatrix} u_0^{(x)} \\ u_0^{(y)} \\ u_0^{(z)} \end{pmatrix}, \quad \text{and} \quad \vec{\Gamma}_r(s) = \begin{pmatrix} \Gamma_r^{(x)}(s) \\ \Gamma_r^{(y)}(s) \\ \Gamma_r^{(z)}(s) \end{pmatrix} \quad (3.1)$$

changing the Equations (2.24) and (2.25) to

$$\frac{d\vec{u}_r(s)}{ds} = -\gamma_r(\vec{u}_r(s) - \vec{u}_0) + \sqrt{D_r}\vec{\Gamma}_r(s). \quad (3.2)$$

and

$$\frac{du_i^{(k)}(s)}{ds} = -\gamma \left(u_i^{(k)}(s) - \xi_i u_r^{(k)}(s) \right) + \sqrt{D_i^{(k)}} \sum_j^N H_{ij} \Gamma_j^{(k)}(s) \quad (3.3)$$

where in the last equation as well as in the definition of $D_i^{(k)}$ (see Equation (2.28)) the velocity profile term is equal for all components, i.e. $\xi_i = \xi_i^{(k)} \forall i, k$. For uniform inflow, the choice $\xi_i = 1 \forall i$ has to be made, which can be chosen if shear effects should be neglected.

If a simulation with different dynamics for all velocity components has to be performed, e.g. if the length scales should differ, the model can be generalized even more by choosing different diffusion and damping constants $D_r^{(k)}$ and $\gamma_r^{(k)}$ in the reference velocity equation or a different coupling matrix $H_{ij}^{(k)}$. In principle it is also possible to introduce Reynold's stresses and two point cross correlations to the velocity by defining H_{ij} as a $3N \times 3N$ matrix, increasing the dimension of all vectors to $3N$, and removing the superscript k . However, the limiting factor here is the memory consumption involved in the Cholesky decomposition, which is explained in more detail in the next section.

In addition to the previously mentioned changes to the model, the constants $\kappa^{(k)}$ of Equation (2.28) are all set to 1, i.e. the field becomes isotropic, for simplicity reasons and because they are not relevant at all for the studies done in this thesis. The main purpose of those parameters, namely scaling the standard deviation for each velocity component, can also be served by directly introducing different values for σ for each velocity component.

3.1.2 Improvements on Spatial Correlations

One important role in Kleinhans' model plays the spatial correlation of the noise terms introduced by the coupling matrix \mathbf{H} in Equation (2.27). In general, if all components of a noise vector $\vec{\Gamma} = (\Gamma_1, \Gamma_2, \dots, \Gamma_N)^T$ are uncorrelated with zero mean and unit variance, i.e. $\langle \vec{\Gamma} \vec{\Gamma}^T \rangle = \mathbb{1}$, they can be correlated by multiplication with the matrix \mathbf{H} . This can be seen by evaluating

$$\langle (\mathbf{H}\vec{\Gamma}) (\mathbf{H}\vec{\Gamma})^T \rangle = \langle \mathbf{H}\vec{\Gamma}\vec{\Gamma}^T\mathbf{H}^T \rangle = \mathbf{H} \langle \vec{\Gamma}\vec{\Gamma}^T \rangle \mathbf{H}^T = \mathbf{H}\mathbf{H}^T = \mathbf{C}. \quad (3.4)$$

\mathbf{C} is the desired correlation matrix and has infinitely many solutions for the decomposition in \mathbf{H} and \mathbf{H}^T . However, a unique way can be found in the Cholesky decomposition where \mathbf{H}

is a lower triangular matrix. Kleinhans intended to involve an exponential decaying spatial correlation function in his model of the form

$$C_{ij} = \exp\left(-\frac{r_{ij}}{l_c}\right) \quad (3.5)$$

which should be independent of the ordering of points in the grid. Nevertheless, if the correlation matrix is calculated by means of Equation (2.27) and (3.4), it can be seen that

$$C_{ij} = \frac{\sum_{k=1}^{\min(i,j)} \exp\left(-\frac{r_{ik}}{l_c}\right) \exp\left(-\frac{r_{jk}}{l_c}\right)}{\sqrt{\sum_{l=1}^i \sum_{m=1}^j \exp\left(-\frac{r_{il}}{l_c}\right) \exp\left(-\frac{r_{jm}}{l_c}\right)}} \quad (3.6)$$

holds. This correlation matrix is in general not independent of the ordering of grid points, as can easily be verified if one swaps the labels i and j of two points, which does not result in the same correlation coefficient due to the changed summands in the numerator. Two different ways of ordering points with the same coordinates are shown in Figure 3.1a and 3.1b, where the normalized velocity $\frac{u^{(x)} - \min(u^{(x)})}{\max(u^{(x)}) - \min(u^{(x)})}$ is color plotted for different coordinates y and z . In the first picture an ordering of labels in horizontal direction and in the second picture in vertical direction is preferred.

In the remaining part of this thesis, a corrected version of the coupling matrix \mathbf{H} is used, namely the Cholesky decomposed lower triangular matrix of the correlaton matrix (3.5), which has to be found numerically. As illustrated in Figure 3.1c, those wind fields are statistically isotropic and the ordering of points does not affect the outcome of the simulation.

However, the number of arithmetic operations for the Cholesky decomposition cubically depends on the number of grid points, which can be very memory and time consuming for highly resolved inflow fields. Therefore the maximum resolution of inflow turbulence is limited, which is especially important for CFD simulations which usually require highly resolved fields.

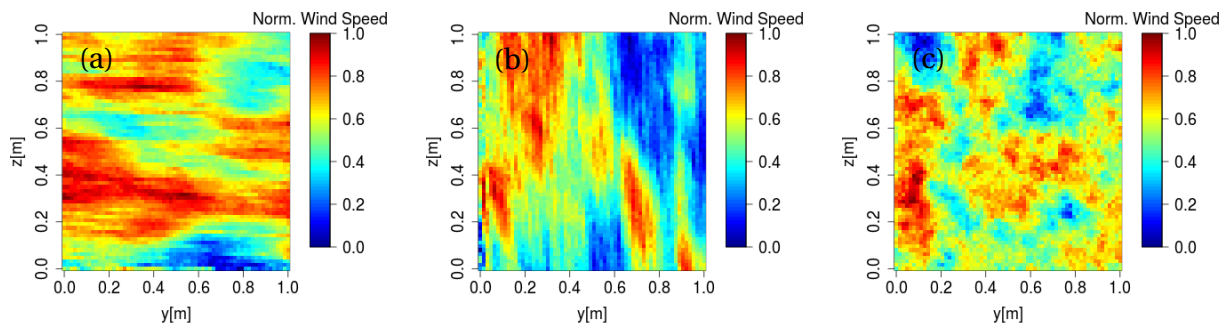


Figure 3.1: Preferred (a) horizontally and (b) vertically ordering of grid points according to Kleinhans' model. (c) Corrected model by using the Cholesky decomposition.

3.1.3 Constraints on the Power Spectral Density and Autocorrelation Function

One of the main questions which could be raised is: What is a proper and simple way to define the constants γ_r, γ and D_r in Equations (3.2) and (3.3) to achieve wind fields which fulfill certain characteristics the user is interested in, i.e. which contain an inertial range in the power spectrum, a certain temporal and spatial correlation length or isotropic structures in the main stream direction. The choice of those parameters is also not arbitrary, because the interplay of them has a high impact on the stability of the field generation process. If the focus lies on Equation (2.28), it is clear that e.g. for very high values of D_r or small standard deviations σ the constant D_i becomes negative, leading to complex numbers in Equation (3.3). This is of course unphysical and a solution for this problem has to be found to overcome this problem.

Winter [65] constrained the choice of parameters γ, γ_r and D_r to

$$\gamma = 0.05 \text{ m}^{-1} \cdot \sigma > 0.11 \text{ s}^{-1} \quad (3.7a)$$

$$\gamma_r = 0.0005 \text{ m}^{-1} \cdot u_0 > 0.11 \text{ s}^{-1} \quad (3.7b)$$

$$D_r = 0.00005 \text{ s}^{-1}. \quad (3.7c)$$

Particularly it is proposed to make γ and γ_r linearly dependent on the standard deviation and the mean velocity and additionally add lower limits. Nevertheless, it is still possible to obtain a negative diffusion constant D_i , because the constants mentioned here are independent of each other. Additionally, the PSD and the autocorrelation function of all velocity components $u_i^{(k)}$ are influenced by those choices in a non-trivial way and it becomes very difficult to compare simulation results with different parameter sets.

Those are the reasons for the development of a more robust parameter set, where a spectrum with an inertial subrange is achieved, i.e. where the Kolmogorov -5/3 law is fulfilled. As a side effect, the problem of choosing the parameters γ, γ_r and D_r is shifted to the selection of only one parameter with a more physical meaning. By this constraint it is assured that D_i is always positive, and in this context failures in the wind field generation become impossible. Next, the major steps to achieve the aforementioned results are explained.

Kleinhans [60] has shown that the PSD of the velocity components at each grid point is given by

$$\begin{aligned} \frac{1}{2}E(\omega) = & \left(\langle u_i^2 \rangle + \langle u_i \rangle u_0 \xi_i \frac{\gamma_r}{\gamma - \gamma_r} - \langle u_r u_i \rangle \xi_i \frac{\gamma}{\gamma - \gamma_r} \right) \frac{\gamma}{\gamma^2 + \omega^2} \\ & + \left(\langle u_r u_i \rangle \xi_i \frac{\gamma}{\gamma - \gamma_r} - \langle u_i \rangle u_0 \xi_i \frac{\gamma}{\gamma - \gamma_r} \right) \frac{\gamma_r}{\gamma_r^2 + \omega^2} \end{aligned} \quad (3.8)$$

where the moments of the process

$$\langle u_i \rangle = \xi_i u_0 \quad (3.9a)$$

$$\langle u_i^2 \rangle = \frac{D_i}{\gamma} + \xi_i^2 \left(u_0^2 + \frac{D_r}{\gamma_r} \frac{\gamma}{\gamma + \gamma_r} \right) \quad (3.9b)$$

$$\langle u_r u_i \rangle = \xi_i u_0^2 + \xi_i \frac{D_r}{\gamma_r} \frac{\gamma}{\gamma + \gamma_r} \quad (3.9c)$$

can be substituted. As a consequence the PSD simplifies to

$$\frac{1}{2}E(\omega) = \frac{D_i}{\gamma^2 + \omega^2} + \xi_i^2 \gamma^2 D_r \left(\frac{1}{(\gamma^2 + \omega^2)(\gamma_r^2 + \omega^2)} \right). \quad (3.10)$$

This is the general equation for the PSD where the diffusion constant D_i is gained from Equation (2.28).

As already mentioned, the important constraint on the PSD is made by considering that an inertial subrange exists in atmospheric turbulence, where the derivative in the double logarithmic plot, the so called logarithmic derivative function

$$b(\omega) = \frac{\omega \frac{d}{d\omega} E(\omega)}{E(\omega)} \quad (3.11)$$

has a value of $-5/3$ (Kolmogorov $-5/3$ law). With the definition of a new damping factor

$$\gamma_d^2 = \gamma_r^2 + \gamma^2 \xi_i^2 \frac{D_r}{D_i} \quad (3.12)$$

and inserting the PSD (3.10) into Equation (3.11), the logarithmic derivative becomes after some manipulations

$$b(\omega) = 2 \left[\frac{\gamma^2}{\gamma^2 + \omega^2} + \frac{\gamma_r^2}{\gamma_r^2 + \omega^2} - \frac{\gamma_d^2}{\gamma_d^2 + \omega^2} - 1 \right]. \quad (3.13)$$

In the following, the goal is to find the conditions under which this logarithmic derivative function gains a saddle point at a characteristic circular frequency ω_c , where the center of the inertial subrange should be located. A straightforward way is to look at the first and second derivative which have to vanish for a saddle point, i.e.

$$b'(\omega_c) = -4\omega_c \left[\frac{\gamma^2}{(\gamma^2 + \omega_c^2)^2} + \frac{\gamma_r^2}{(\gamma_r^2 + \omega_c^2)^2} - \frac{\gamma_d^2}{(\gamma_d^2 + \omega_c^2)^2} \right] = 0 \quad (3.14)$$

$$b''(\omega_c) = -4 \left[\frac{\gamma^2}{(\gamma^2 + \omega_c^2)^2} + \frac{\gamma_r^2}{(\gamma_r^2 + \omega_c^2)^2} - \frac{\gamma_d^2}{(\gamma_d^2 + \omega_c^2)^2} \right] + 16\omega_c^2 \left[\frac{\gamma^2}{(\gamma^2 + \omega_c^2)^3} + \frac{\gamma_r^2}{(\gamma_r^2 + \omega_c^2)^3} - \frac{\gamma_d^2}{(\gamma_d^2 + \omega_c^2)^3} \right] = 0. \quad (3.15)$$

The combination of both derivatives leads after some simple manipulations to an equation for the location of the saddle point

$$\omega_c^2 = \frac{c\gamma^2 - \gamma_r^2}{1 - c} \quad (3.16)$$

with the definition of the constant

$$c = \sqrt[3]{-\frac{\gamma_r^2}{\gamma^2} \left(\frac{\gamma_d^2 - \gamma_r^2}{\gamma_d^2 - \gamma^2} \right)}. \quad (3.17)$$

Under the condition that $b(\omega_c) = -5/3$, it can be shown that

$$c = \frac{29 - 2 \cdot \sqrt{154}}{15} \approx 0.2787102. \quad (3.18)$$

If ω_c is now added back to the first (3.14) and second derivative (3.15) of $b(\omega)$, the relations

$$\gamma = \gamma^* \cdot \omega_c \quad (3.19a)$$

$$\gamma_r = \gamma_r^* \cdot \omega_c \quad (3.19b)$$

$$D_r = D_r^* \cdot \omega_c \cdot \sigma^2 \quad (3.19c)$$

$$D_i = D^* \cdot \omega_c \cdot \sigma^2 \cdot \xi_i^2. \quad (3.19d)$$

with the numerical constants

$$\gamma^* = \sqrt{\frac{c^2 - 4c + 3}{2c^2 + 2c}} \approx 1.6595 \quad (3.20a)$$

$$\gamma_r^* = \gamma^* \sqrt{\frac{3c^2 - c}{c - 3}} \approx 0.2150 \quad (3.20b)$$

$$D_r^* = \gamma_r^* \frac{c^3(1 - r^2)}{c^3 + r^3} \approx 0.1921 \quad (3.20c)$$

$$D^* = \gamma^* \frac{c^3 r + r^3}{c^3 + r^3} \approx 0.3468. \quad (3.20d)$$

can be obtained.

By inserting those properties into the PSD Equation (3.10) and neglecting the indices i , the simple form

$$E(\omega) = \frac{2\sigma^2}{\pi} \left(a \frac{\gamma}{\gamma^2 + \omega^2} + (1 - a) \frac{\gamma_r}{\gamma_r^2 + \omega^2} \right) \quad (3.21)$$

can be achieved, where a new constant

$$a = \frac{r^3}{c^3 + r^3} \approx 0.0913 \quad (3.22)$$

with the ratio $r = \gamma_r^*/\gamma^*$ is introduced.

The spectrum (3.21) has now a very simple form if it is compared with the general form derived by Kleinhans in Equation (3.8). It is shown in Figure 3.2, and the compensated spectrum $E(\omega)\omega^{5/3}$ together with the logarithmic derivative in Figure 3.3, where the inertial sub-range is clearly visible in both plots.

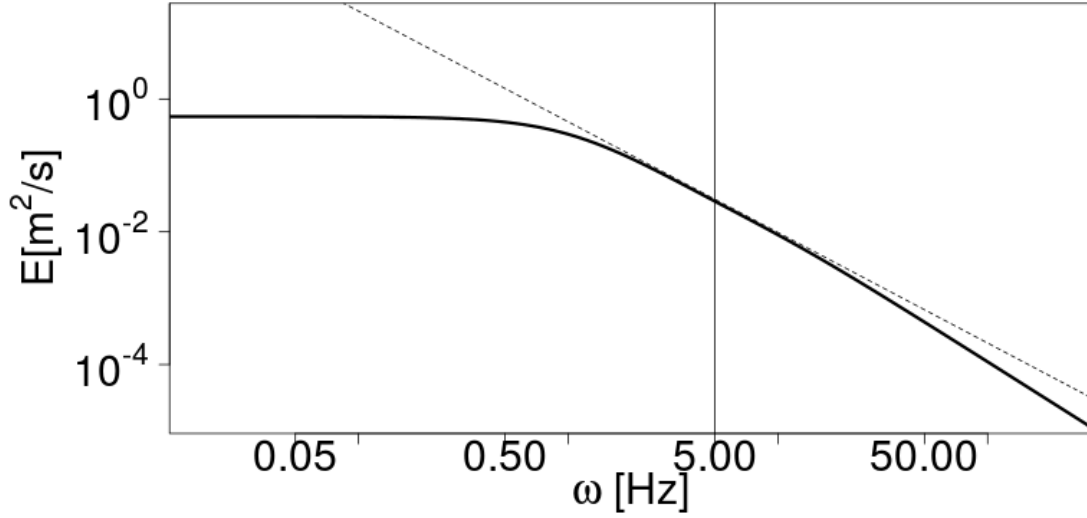


Figure 3.2: PSD from Equation (3.21) for $\omega_c = 5$ Hz. The vertical line marks ω_c and the dashed line a slope of $-5/3$.

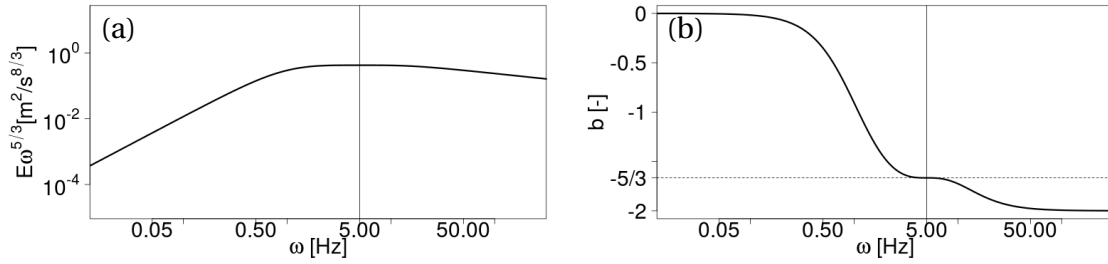


Figure 3.3: (a) PSD from Equation (3.21) and (b) logarithmic derivative for $\omega_c = 5$ Hz. The vertical line marks ω_c

In essence, in the previous steps a plateau for the logarithmic derivative is obtained, which is consistent with the inertial subrange assumptions of Kolmogorov. In addition to that, all the previously unknown and not intuitive model parameters from the model Equations (3.2), (3.3) and (2.28) are now calculated by setting the characteristic circular frequency of the inertial subrange ω_c , the standard deviation σ and the wind profile ξ_i . In section 3.2.4 it will be shown that ω_c is directly related to the integral length and time scale for isotropic turbulence and therefore is a property with physical relevance.

With the known spectrum, the autocovariance function of velocity can be obtained by Fourier transforming (3.21) into

$$\begin{aligned} R(\tau) &= \int_0^{\infty} E(\omega) \cos(\omega\tau) d\omega \\ &= \sigma^2 (a \cdot e^{-\gamma\tau} + (1-a) \cdot e^{-\gamma_r\tau}). \end{aligned} \quad (3.23)$$

So the autocovariance function of the velocity at each grid point is a weighted sum of exponential functions where the decaying time depends with Equations (3.19a) and (3.19b) on

ω_c . If the plateau exists at a high frequency, the covariance function decays very fast and the signal decorrelates in a short time. Vice versa, the signal contains a long memory when ω_c is chosen to be small. In this case the integral time scale and the structure size within the signal are large.

For convenience it is also useful to define the autocorrelation function

$$\rho(\tau) = a \cdot e^{-\gamma\tau} + (1 - a) \cdot e^{-\gamma_r\tau} \quad (3.24)$$

which is the normalized autocovariance function.

One drawback of the process discussed here is that the logarithmic derivative has the $-5/3$ -plateau only at one point. Accordingly, the inertial subrange is infinitesimal, which is not seen in atmospheric turbulence, where it extends over several orders of magnitude [1]. It is believed that there is no stochastic process available which can create a spectrum with this property. In theory, if the here discussed PSD of the velocity should have a broad inertial subrange, it has to be extended by the transformations

$$E(\omega) \rightarrow E^\beta(\omega) \quad (3.25a)$$

$$\omega_c \rightarrow \omega_c^\beta \quad (3.25b)$$

$$\omega \rightarrow \omega^\beta \quad (3.25c)$$

to have a PSD of the form

$$E(\omega) = \left(\frac{\sigma^2}{\pi} \left(a \frac{\gamma}{\gamma^2 + \omega^{2\beta}} + (1 - a) \frac{\gamma_r}{\gamma_r^2 + \omega^{2\beta}} \right) \right)^{\frac{1}{\beta}} \quad (3.26)$$

with the redefined constants

$$\gamma = \gamma^* \cdot \omega_c^\beta \quad (3.26a)$$

$$\gamma_r = \gamma_r^* \cdot \omega_c^\beta. \quad (3.26b)$$

The stretching factor β can be an arbitrary positive number and represents the size of the plateau. With decreasing β the shape of the spectrum changes and the size of the plateau increases as shown in 3.4, where the same parameters are used as in Figure 3.3, but for $\beta = 0.4$. Furthermore the drop of energy is much slower throughout the whole frequency range and starts on very small frequencies.

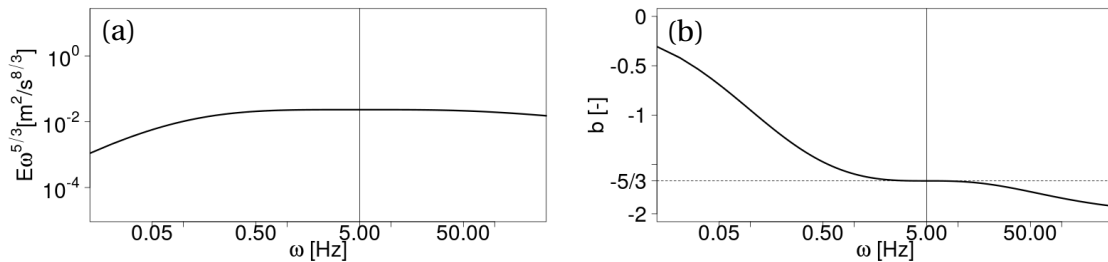


Figure 3.4: (a) Spectrum and (b) logarithmic derivative for $\omega_c = 5$ Hz of Equation (3.26). The vertical line marks ω_c .

3.1.4 An Alternative Time Transformation

In this section an alternative to the time transformation used by Kleinhans is shown. For CTRWs, the characteristic function of the time process $t(s)$ in Laplace space generally is

$$\langle e^{-\lambda t(s)} \rangle = e^{-s\Phi(\lambda)} \quad (3.27)$$

where for the original Lévy process without modifications the involved function is $\Phi(\lambda) = \lambda^\alpha$ [61]. However here the aforementioned problems join, which are the diverging mean and variance of the process and the connected unlimited waiting times which are not allowed if physical time series shall be simulated. Kleinhans introduced a cutoff to the Lévy distribution itself, which can be understood as a maximum waiting time. Then he renormalized numerically the distribution such that the average derivative of $t(s)$ is 1. This is needed to assure a better comparability of simulations with different α or C .

However to the authors knowledge this way of making the Lévy process finite has not been investigated mathematically yet and the renormalization even increases the complexity of the problem.

Another approach is followed e.g. by Cairoli et al. [66, 67] who used the formalism of exponential tempering by setting $\Phi(\lambda) = (\mu + \lambda)^\alpha - \mu^\alpha$ with the tempering exponent μ . This tempering speeds up the decay of the heavy tail of the Lévy distribution compared to the original process, which finally makes the mean and variance converge.

In the following the constraints on the tempering are shown to make fields with different intermittency parameters more comparable like in the work of Kleinhans, but mathematically much more capturable. Furthermore a comparison with the sharp cutoff of the Lévy distribution is made which both can have very similar behavior. It is known that the totally skewed α -stable Lévy motion for $0 < \alpha < 2, \alpha \neq 1$ has a probability density function (PDF) $p(t, s)$ that solves the fractional diffusion equation

$$\partial_s p(t, s) = c \partial_t^\alpha p(t, s) \quad (3.28)$$

where $c > 0$ for $1 < \alpha < 2$, and $c < 0$ for $0 < \alpha < 1$ and all the moments of order $n > \alpha$ diverge. The tempering ansatz modifies the density to the form $e^{-\mu t} p(t, s)$ after which a renormalization takes place to $e^{-sc\mu^\alpha} e^{-\mu t} p(t, s)$. Baeumer et al. [68] have shown that the new mean value for the time is

$$\langle t(s) \rangle = -cs\alpha\mu^{\alpha-1} \quad (3.29)$$

where in the current study only $\alpha < 1$ is used and therefore $c = -1$ has to be chosen. This knowledge allows it to equalize the mean value of the intrinsic time s and physical time t for consistency reasons. This is achieved by setting $\alpha\mu^{\alpha-1} = 1$ or after rearranging

$$\mu = \left(\frac{1}{\alpha} \right)^{\frac{1}{\alpha-1}} \quad (3.30)$$

which shows the direct connection of the Lévy exponent α and the tempering exponent μ .

It was explained in section 2.5.2 how the model of Kleinhans introduced a cutoff and normalized numerically the resulting distribution. There is no mathematical formula given for the resulting distribution, not even in Fourier or Laplace space.

3.2 Turbulent Characteristics

In this part important turbulent properties to characterize the output of the CTRW model will be pointed out. A similar study has not been done yet which makes it mandatory to go into details at this point. The focus lies on correlations, spectral properties, kinetic energy and dissipation, important length and time scales, but also the kurtosis of increments.

3.2.1 Cross Statistics for a velocity time series

In section 3.1.3 the PSD (Equation (3.21)) and the corresponding autocorrelation function (Equation (3.24)) of the process used in this work are shown under the defined constraints. However the cross spectra, cross correlations and coherence were not analysed at all. Because they are essential for a physical description of CTRW turbulence they are part of this section.

The CTRW fields are described by the Equations (3.2) and (3.3). The properties at one specific grid point can be analyzed by neglecting the coupling term \mathbf{H} , which leads to an equation system of the form

$$d\vec{u}(s) = -\mathbf{A}\vec{u}(s)ds + \vec{f}(s)ds + \mathbf{B}d\vec{W}(s) \quad (3.31)$$

with the definitions

$$\vec{u}(s) = \begin{pmatrix} u_r(s) \\ u(s) \end{pmatrix} \quad (3.31a)$$

$$\vec{f}(s) = \begin{pmatrix} \gamma_r u_0 \\ 0 \end{pmatrix} \quad (3.31b)$$

$$\mathbf{A} = \begin{pmatrix} \gamma_r & 0 \\ -\gamma & \gamma \end{pmatrix} \quad (3.31c)$$

$$\mathbf{B} = \sqrt{2} \begin{pmatrix} \sqrt{D_r} & 0 \\ 0 & \sqrt{D} \end{pmatrix} \quad (3.31d)$$

$$d\vec{W}(s) = \vec{\Gamma}(s)ds \quad (3.31e)$$

where \mathbf{A} and \mathbf{B} are the drift and diffusion matrices and $d\vec{W}(t)$ the increments of the Wiener process with the delta correlated noise $\vec{\Gamma}$. This equation system has the general solution

$$\vec{u}(s) = e^{-s\mathbf{A}}\vec{u}(0) + \int_0^s e^{-(s-s')\mathbf{A}}\vec{f}(s')ds' + \int_0^s e^{-(s-s')\mathbf{A}}\mathbf{B}d\vec{W}(s') \quad (3.32)$$

which can be used to calculate the covariance matrix of the stationary state [69]

$$\begin{aligned} \mathbf{R} &= \langle \vec{u}_s(s), \vec{u}_s^T(s) \rangle = \\ &= \frac{\text{Det}(\mathbf{A})\mathbf{B}\mathbf{B}^T + [\mathbf{A} - \text{Tr}(\mathbf{A})\mathbb{1}]\mathbf{B}\mathbf{B}^T[\mathbf{A} - \text{Tr}(\mathbf{A})\mathbb{1}]^T}{2\text{Tr}(\mathbf{A})\text{Det}(\mathbf{A})} \\ &= \sigma^2 \begin{pmatrix} (1-a)(1-r^2) & (1-a)(1-r) \\ (1-a)(1-r) & 1 \end{pmatrix} \end{aligned} \quad (3.33)$$

where $r = \gamma_r/\gamma \approx 0.13$. The variance R_{11} of the reference process is a bit smaller than for the resulting wind time series $R_{22} = \sigma^2$. The off-diagonal components are the co-variances between the wind time series and the reference process.

With the known covariance matrix in the stationary state it is also possible to gain the time covariance matrix for $s_2 > s_1$ in the stationary state

$$\begin{aligned} \boldsymbol{\rho}(\tau) &= \langle \vec{u}_s(s_1), \vec{u}_s^T(s_2) \rangle \\ &= e^{-(s_2-s_1)\mathbf{A}} \mathbf{R} = e^{-\tau\mathbf{A}} \mathbf{R} \\ &= \sigma^2 \begin{pmatrix} (1-a)(1-r^2)e^{-\gamma_r\tau} & (1-a)(1-r)e^{-\gamma_r\tau} \\ (1-a)(-2re^{-\gamma\tau} + (1+r)e^{-\gamma_r\tau}) & ae^{-\gamma\tau} + (1-a)e^{-\gamma_r\tau} \end{pmatrix} \end{aligned} \quad (3.34)$$

where the relation

$$e^{-\tau\mathbf{A}} = \begin{pmatrix} e^{-\gamma_r\tau} & 0 \\ \frac{1}{r-1}(e^{-\gamma\tau} - e^{-\gamma_r\tau}) & e^{-\gamma\tau} \end{pmatrix} \quad (3.35)$$

has been used in the last step. The last element of the covariance matrix is the already derived correlation function in Equation (3.24) which contains the expected variance σ^2 at $\tau = 0$.

For $t < s$ a similar term can be calculated as $\boldsymbol{\rho}(\tau) = \mathbf{R}e^{\tau\mathbf{A}^T$ which is the same as $\boldsymbol{\rho}^T(-\tau)$.

By Fourier transforming the matrix from Equation (3.34) the spectrum matrix in the stationary state can be achieved

$$\begin{aligned} \mathbf{S}(\omega) &= \frac{1}{\pi} \int_{-\infty}^{\infty} e^{-i\omega\tau} \boldsymbol{\rho}(\tau) d\tau \\ &= \frac{1}{\pi} (\mathbf{A} + i\omega\mathbb{1})^{-1} \mathbf{B}\mathbf{B}^T (\mathbf{A}^T - i\omega\mathbb{1})^{-1} \\ &= \frac{2\sigma^2}{\pi} \begin{pmatrix} (1-a)(1-r^2)\frac{\gamma_r}{\gamma_r^2+\omega^2} & \frac{(1-a)(\gamma^2-\gamma_r^2)r}{(\gamma_r^2+\omega^2)(\gamma-i\omega)} \\ \frac{(1-a)(\gamma^2-\gamma_r^2)r}{(\gamma_r^2+\omega^2)(\gamma+i\omega)} & a\frac{\gamma}{(\gamma^2+\omega^2)} + (1-a)\frac{\gamma_r}{(\gamma_r^2+\omega^2)} \end{pmatrix} \end{aligned} \quad (3.36)$$

with the spectrum S_{11} of the reference velocity and the spectrum S_{22} of resulting velocity, which is already known from Equation (3.21). The off-diagonal components $S_{12} = S_{21}^*$ are the complex cross spectra between u and u_r . This matrix can now be used to calculate the coherence between u and u_r as

$$\begin{aligned} \text{Coh}_{u,u_r}(\omega) &= \frac{|S_{1,2}|^2}{\sqrt{S_{1,1}S_{2,2}}} \\ &= \frac{1}{1 + \frac{1}{\gamma^2-\gamma_r^2} \left(1 + \frac{a}{r(1-a)}\right) (\gamma_r^2 + \omega^2)} \end{aligned} \quad (3.37)$$

which gives a good measure of the correlation of the two time series. The coherence is quadratically decaying for $\omega \rightarrow \infty$ which is also the case for the spectrum.

3.2.2 Cross Statistics for the in-plane correlated field

The more general system of Equations (3.2) and (3.3) where the coupling of grid points by the matrix \mathbf{H} is included can be written in a more compact form as

$$d\vec{u}(s) = -\mathbf{A}\vec{u}(s)dt + \vec{f}(s)ds + \mathbf{B}\mathbf{H}d\vec{W}(s) \quad (3.38)$$

with the components

$$d\vec{W}(s) = \vec{\Gamma}(s) ds \quad (3.38a)$$

$$\vec{u}(s) = \begin{pmatrix} u_r(s) \\ u_1(s) \\ u_2(s) \\ u_3(s) \\ \vdots \end{pmatrix} \quad (3.38b)$$

$$\vec{f}(s) = \begin{pmatrix} \gamma_r u_0 \\ 0 \\ 0 \\ 0 \\ \vdots \end{pmatrix} \quad (3.38c)$$

$$\mathbf{A} = \begin{pmatrix} \gamma_r & 0 & 0 & 0 & \dots \\ -\gamma & \gamma & 0 & 0 & \dots \\ -\gamma & 0 & \gamma & 0 & \dots \\ \vdots & & & \ddots & \end{pmatrix} \quad (3.38d)$$

$$\mathbf{B} = \sqrt{2} \begin{pmatrix} \sqrt{D_r} & 0 & 0 & 0 & \dots \\ 0 & \sqrt{D_1} & 0 & 0 & \dots \\ 0 & 0 & \sqrt{D_2} & 0 & \dots \\ 0 & 0 & 0 & \ddots & \end{pmatrix} \quad (3.38e)$$

$$\mathbf{C} = \mathbf{H}\mathbf{H}^T \quad (3.38f)$$

where \mathbf{C} is the spatial correlation matrix. The solution of this stochastic equation is

$$\vec{u}(s) = e^{-s\mathbf{A}}\vec{u}(0) + \int_0^s e^{-(s-s')\mathbf{A}}\vec{f}(s')ds' + \int_0^s e^{-(s-s')\mathbf{A}}\mathbf{B}\mathbf{H}d\vec{W}(s'). \quad (3.39)$$

which can be solved with similar steps as for Equation (3.31). A time covariance matrix can also be derived for this more complex system, which is

$$\boldsymbol{\rho}(\tau) = \sigma^2 \begin{pmatrix} (1-a)(1-r^2)e^{-\gamma_r\tau} & (1-a)(1-r)e^{-\gamma_r\tau} & \dots \\ (1-a)(-2re^{-\gamma\tau} + (1+r)e^{-\gamma_r\tau}) & (C_{ij} - (1-a)(C_{ij}(1-r) + r))e^{-\gamma\tau} + (1-a)e^{-\gamma_r\tau} & \\ \vdots & & \end{pmatrix} \quad (3.40)$$

where $\rho_{i1} = \rho_{21}$ and $\rho_{1j} = \rho_{12}$ for all $i, j > 1$ which means that all time series on the different grid points are correlated with the reference velocity in the same way. All other components with $i, j > 1$ are only differing by C_{ij} which are the entries of the spatial correlation matrix \mathbf{C} .

Here it can easily be seen that at the diagonal elements, where $C_{ij} = 1$, the expected autocovariance function for a time series from Equation (3.34) is achieved and the variance is again σ^2 .

However also an issue of this model can be shown here which concerns the cross covariance of the velocity time series at different grid points, i.e. the off-diagonal elements of the matrix (3.40) for indices $i, j > 1$. The normalized cross covariance, i.e. the cross correlation, is calculated for $\tau = 0$ and $i, j > 1$ as

$$\frac{R_{ij}}{\sigma^2} = C_{ij}(1 - C_0) + C_0 \quad (3.41)$$

where $C_0 = (1 - a)(1 - r) \approx 0.791$ is the minimal cross correlation which can be obtained under the assumption of $C_{ij} \geq 0$. In general this minimum results from the coupling of all grid points via the reference velocity.

If the reference velocity would be neglected, i.e. $\gamma_r = r = 0$ and $a = 1$, the cross correlation would be equal to C_{ij} . This is also what would be expected, because if a correlation matrix is given, the correlation should also be equal to the entries of the matrix.

To support these theoretical results, two spatially correlated grid points with $C_{ij} = 0$ are simulated under consideration of the reference velocity and the cross correlation between both is shown in Figure 3.5 together with the theoretical result from Equation (3.40). It is clearly visible that even if C_{ij} is chosen to be zero, the cross correlation approaches the very high value of C_0 for small time delays. In general it is different to the spatial average at one time instant, where the spatial correlation is exactly C_{ij} and no differences to the expectations are found even if a reference velocity is used.

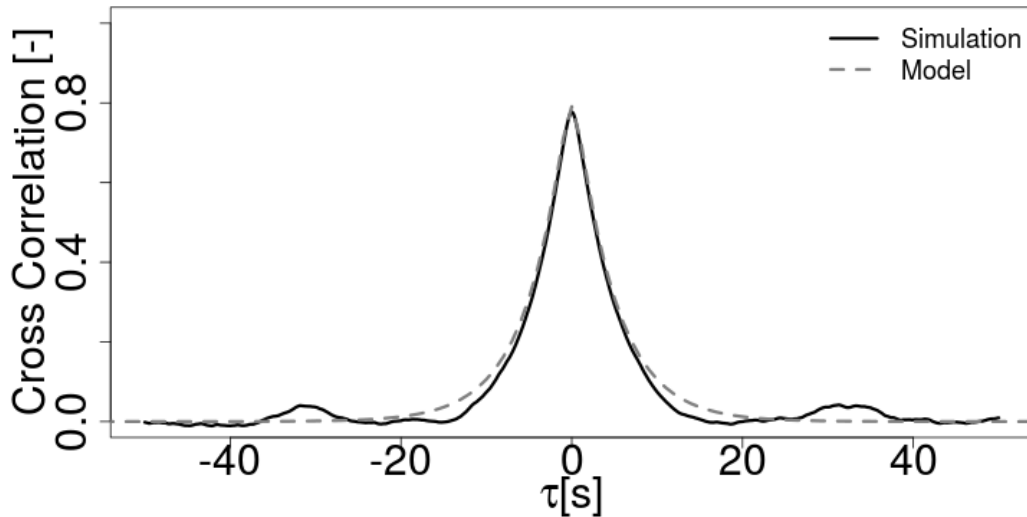


Figure 3.5: Cross correlation of two points i and j with a zero correlation coefficient $C_{ij} = 0$ gained from simulation (solid) and Equation (3.40) (dashed).

The coherence matrix for two grid points is

$$Coh_{u_i, u_j}(\omega) = 1 - (1 - C_{ij}) \frac{(r - ar + 1)(\gamma_r^2 + \omega^2)}{a(\gamma_r^2 + \omega^2) - (a - 1)r(\gamma^2 + \omega^2)} \quad (3.42)$$

where a quadratic decay for the limit $\omega \rightarrow \infty$ is present as also has been seen before for the time series in Equation (3.37). The same issue as for the covariance matrix in Equation (3.41) is apparent. In this case the coherence is not zero for $C_{ij} = 0$ but has a lower limit which depends on ω and the parameter ω_c which is involved in γ and γ_r . But if the reference velocity is neglected, the coherence is constant with $Coh_{u_i, u_j}(\omega) = C_{ij}$ for all frequencies. So in this case the coherence and the correlation are actually the same.

In conclusion the user of this model has to decide which properties are more important for the final use case. The model without reference velocity has proper cross correlations where the correlation coefficient may vary between 0 and 1. This is very important for use cases where small structures are of interest and where the correct exponentially decaying spatial correlation is important. However the inertial subrange described by Kolmogorov is not achieved at all and the spatial coherence is constant over all frequencies, where an exponential decay would be expected, like e.g. in the IEC for the Kaimal model [1]. If wind fields should be simulated where in general the correlation is very large over large distances and if the inertial subrange in the time evolution plays a major role, the reference velocity should be taken into account. However, the hard lower limit of $C_0 \approx 0.791$ has to be considered for the cross correlation.

3.2.3 Turbulent Kinetic Energy and Dissipation

With the known spectral density of $u_i(s)$, see Equation (3.21), integral properties like the turbulent kinetic energy or the dissipation can be estimated, which are of fundamental importance for turbulence. For the non-solenoidal CTRW fields no energy spectrum function, which demands solenoidal fields, can be calculated and it should be enough to calculate properties like the turbulent kinetic energy or dissipation with one dimensional energy spectra. With the relation $\omega = \kappa \langle u \rangle$ the turbulent kinetic energy at each grid point is

$$k = \frac{3 \langle u \rangle}{2\pi} \int_0^\infty E(\omega = \kappa' \langle u \rangle) d\kappa' = \frac{3\sigma^2}{2} \quad (3.43)$$

which is also expected for isotropic turbulence. The energy content on high frequencies is also interesting, because those are the frequencies which are usually affected by filters and aliasing. Thus a big insight into the resulting fields can be gained by knowing the amount of turbulent kinetic energy on this frequency range. For $\kappa' > \kappa$ and with the rule

$$\int \frac{x^2}{c^2 + x^2} dx = x - c \tan^{-1} \frac{x}{c} \quad (3.44)$$

this is easily calculated as

$$\begin{aligned} k_{(\kappa, \infty)} &= \frac{3 \langle u \rangle}{2\pi} \int_\kappa^\infty E(\omega = \kappa' \langle u \rangle) d\kappa' \\ &= \frac{3\sigma^2}{2} \left(1 - a \tan^{-1} \left(\frac{\kappa \langle u \rangle}{\gamma} \right) - (1 - a) \tan^{-1} \left(\frac{\kappa \langle u \rangle}{\gamma_r} \right) \right) \end{aligned} \quad (3.45)$$

and vice versa the energy on small wave numbers $\kappa' < \kappa$ has to be

$$\begin{aligned} k_{(0,\kappa)} &= \frac{3\langle u \rangle}{2\pi} \int_0^\kappa E(\omega = \kappa' \langle u \rangle) d\kappa' \\ &= k_{(0,\infty)} - k_{(\kappa,\infty)} \\ &= \frac{3\sigma^2}{\pi} \left(a \tan^{-1} \left(\frac{\kappa \langle u \rangle}{\gamma} \right) + (1-a) \tan^{-1} \left(\frac{\kappa \langle u \rangle}{\gamma_r} \right) \right) \end{aligned} \quad (3.46)$$

where the graph for $\sigma = \langle u \rangle = 0$ is shown in Figure 3.6a with its limit $\lim_{\kappa \rightarrow \infty} k_{(0,\kappa)} = 3/2\sigma^2$. In the same way the dissipation rate can be calculated as

$$\varepsilon = 3\nu \frac{\langle u \rangle}{\pi} \int_0^\infty E(\omega = \langle u \rangle \kappa') \kappa'^2 d\kappa' \quad (3.47)$$

where analogue to the calculation of the turbulent kinetic energy in Equation (3.46) the dissipation content in the range $0 < \kappa' < \kappa$ can be obtained as

$$\begin{aligned} \varepsilon_{(0,\kappa)} &= 3\nu \frac{\langle u \rangle}{\pi} \int_0^\kappa E(\omega = \langle u \rangle \kappa') \kappa'^2 d\kappa' \\ &= 6 \frac{\sigma^2 \nu}{\langle u \rangle \pi} \left[a\gamma \left[\kappa - \frac{\gamma}{\langle u \rangle} \tan^{-1} \frac{\kappa \langle u \rangle}{\gamma} \right] + (1-a)\gamma_r \left[\kappa - \frac{\gamma_r}{\langle u \rangle} \tan^{-1} \frac{\kappa \langle u \rangle}{\gamma_r} \right] \right] \end{aligned} \quad (3.48)$$

which is shown for convenience in Figure 3.6b.

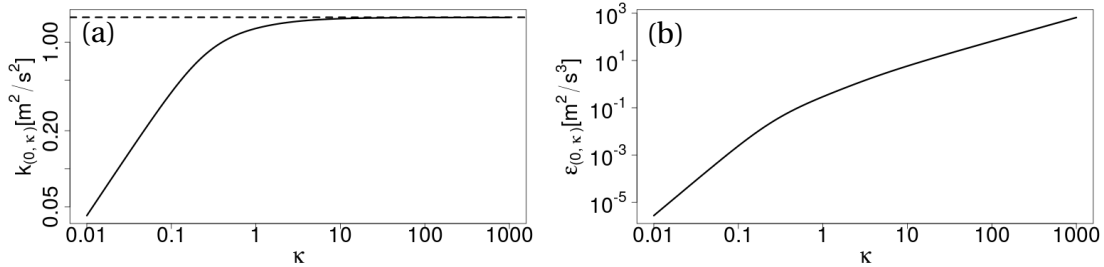


Figure 3.6: Wave number dependence of (a) $k_{(0,\kappa)}$ with the limit $3/2\sigma^2$ (dashed line) and (b) $\varepsilon_{(0,\kappa)}$.

Important here is the limit $\lim_{\kappa \rightarrow \infty} \varepsilon_{(0,\kappa)}$ which is finite for real turbulence and which is needed for a proper characterization of the fields. However it can be shown in Equation (3.48) that this limit tends to infinity. At this point it has to be added that there is no classical stochastic process possible which has a finite dissipation because real turbulence shows on small scales a smooth behaviour which is in general missing for stochastic processes. Real velocity fields are infinitely differentiable from which follows that those fields have to drop faster than any power of κ [20]. On the other hand stochastic processes generally show only a power law decay.

3.2.4 Time and Length Scales

In addition to the turbulent kinetic energy and dissipation one is usually interested in the length scales of the flow field. The three most important here are the longitudinal integral

length scale L , which is strongly connected to the integral time scale $\bar{\tau}$, the longitudinal Taylor microscale λ_t and the Kolmogorov scale η .

With the relation between spectra and covariance functions

$$E(\omega) = \frac{2}{\pi} \int_0^{\infty} R(\tau) \cos(\omega\tau) d\tau \quad (3.49)$$

and the variance of the longitudinal velocity component $\langle u_1^2 \rangle = \sigma^2$, the integral time scale

$$\bar{\tau} = \frac{\int_0^{\infty} R(t) dt}{\langle u_1^2 \rangle} \quad (3.50)$$

can be obtained from the one dimensional spectra at $\omega = 0$ by

$$\begin{aligned} \bar{\tau} &= \frac{\pi E(0)}{2 \langle u_1^2 \rangle} \\ &= \left(\frac{a}{\gamma} + \frac{1-a}{\gamma_r} \right) \\ &= \frac{1}{\omega_c} \left(\frac{a}{\gamma^*} + \frac{1-a}{\gamma_r^*} \right) = \frac{L}{\langle U_1 \rangle} \end{aligned} \quad (3.51)$$

where in the last step the relation between integral time and length scale L is introduced under consideration of Taylor's frozen turbulence hypothesis $\partial u_1 / \partial t = \langle U_1 \rangle \partial u_1 / \partial x$ with the mean velocity in main stream direction $\langle U_1 \rangle$ [70]. Here the important observation can be made that the integral scales are dependent on the characteristic circular frequency at the $-5/3$ slope ω_c . For isotropic structures the integral length scale should be equal to the correlation length l_c resulting from the correlation matrix (3.5) as is shown by $L = \int_0^{\infty} C(r) dr = \int_0^{\infty} \exp^{-\frac{r}{l_c}} dr = l_c$. This should be considered for the field creation if isotropic structures lie in the foreground.

If all the constants in Equation (3.51) are inserted a relation between ω_c and the correlation length l_c can be gained. For the full process including the reference velocity it is

$$\omega_c = \frac{\langle U_1 \rangle}{l_c} \left(\frac{a}{\gamma^*} + \frac{1-a}{\gamma_r^*} \right) \approx 4.2820 \frac{\langle U_1 \rangle}{l_c} \quad (3.52)$$

and if the reference velocity is missing (meaning $a = 1$), the relation becomes

$$\omega_c = \frac{\langle U_1 \rangle}{l_c} \frac{1}{\gamma^*} \approx 0.6026 \frac{\langle U_1 \rangle}{l_c}. \quad (3.53)$$

The second often used length scale, the longitudinal Taylor lengthscale, can be calculated with help of the second derivative of the autocorrelation function $\rho(\tau)$ and $r = \tau \langle u \rangle$ as [20]

$$\begin{aligned} \lambda_t &= \left[-\frac{1}{2} \rho'' \left(\tau = \frac{r}{\langle U_1 \rangle} \right) \Big|_{r=0} \right]^{-1/2} \\ &= \left[-\frac{1}{2} \left(a \left[\exp \left\{ -\frac{\gamma^* \omega_c r}{\langle U_1 \rangle} \right\} \right]'' \Big|_{r=0} + (1-a) \left[\exp \left\{ -\frac{\gamma_r^* \omega_c r}{\langle U_1 \rangle} \right\} \right]'' \Big|_{r=0} \right) \right]^{-1/2} \\ &= \left[-\frac{\omega_c^2}{2 \langle U_1 \rangle^2} \left(a \gamma^{*2} + (1-a) \gamma_r^{*2} \right) \right]^{-1/2}. \end{aligned} \quad (3.54)$$

This term is always complex valued, which might also be expected because the first derivative at the origin is also not continuous. The conclusion drawn is that the Taylor lengthscale is not defined for stochastic processes of this kind.

If the discrete ansatz for the estimation of the Taylor lengthscale from Aronson and Löfdahl [71] is used, i.e.

$$\lambda_t(s)^2 = \frac{2\langle u_1^2 \rangle}{\left\langle \left(\frac{\partial u_1}{\partial s} \right)^2 \right\rangle} \quad (3.55)$$

the Taylor length scale goes to zero if the velocity derivative is approximated by velocity increments as follows from

$$\begin{aligned} \lambda_t^2 &= \frac{2\langle u_1^2 \rangle}{\left\langle \left(\frac{\partial u_1}{\partial s} \right)^2 \right\rangle} = \lim_{\tau \rightarrow 0} \frac{2\langle u_1^2 \rangle}{\left\langle \left(\frac{u_1(s+\tau) - u_1(s)}{\tau} \right)^2 \right\rangle} = \lim_{\tau \rightarrow 0} \frac{2\langle u_1^2 \rangle \tau^2}{\langle (u_1(s+\tau) - u_1(s))^2 \rangle} \\ &= \lim_{\tau \rightarrow 0} \frac{2\langle u_1^2 \rangle \tau^2}{2\langle u_1^2 \rangle (1 - e^{-\gamma|\tau|})} = \lim_{\tau \rightarrow 0} \frac{\tau^2}{1 - e^{-\gamma|\tau|}} = 0 \end{aligned} \quad (3.56)$$

where for simplicity an exponentially decaying auto correlation function $\langle u_1(s+\tau)u_1(s) \rangle = e^{-\gamma|\tau|}$ like in Equation (3.24) has been used. So in this case the Taylor length scale is zero which again supports the argument that stochastic process like the CTRW process cannot have a Taylor length. In addition to that it is also not possible to define a Kolmogorov length scale $\eta = (v^3/\varepsilon)^{1/4}$ due to the fact that the dissipation tends to infinity for high frequencies, i.e. small scales. However it should be kept in mind that in the context of CFD a discretized time and space domain is required which cut the energy spectrum at high frequencies. Therefore a finite dissipation, as seen in real turbulence, is gained which also alters the process.

3.2.5 Ensemble Correlation of the CTRW Process with Lévy Distributed Time

In the following the ensemble averaged autocorrelation function for the specific CTRW process in this work with a random time evolution is derived based on the work of Baule et al. [72].

As described in more detail in section 3.2.2 the stationary correlation matrix of the CTRW process with a fixed time step is

$$\begin{aligned} \langle \vec{u}_s(s_1), \vec{u}_s^T(s_2) \rangle &= \\ \sigma^2 &\begin{pmatrix} (1-a)(1-r^2)e^{-\gamma r \tau} & (1-a)(1-r)e^{-\gamma r \tau} & \dots \\ (1-a)(-2re^{-\gamma r \tau} + (1+r)e^{-\gamma r \tau}) & (C_{ij} - (1-a)(C_{ij}(1-r) + r))e^{-\gamma r \tau} + (1-a)e^{-\gamma r \tau} & \\ \vdots & & \end{pmatrix}. \end{aligned} \quad (3.57)$$

which can be transformed into the physical time domain, i.e. with time variables t_1 and t_2 , by performing a transformation to the Laplace space

$$\langle \vec{u}(\lambda_1), \vec{u}^T(\lambda_2) \rangle = \int_0^\infty \int_0^\infty ds_1 ds_2 \langle \vec{u}_s(s_1), \vec{u}_s^T(s_2) \rangle h(s_1, \lambda_1; s_2, \lambda_2) \quad (3.58)$$

by use of the function

$$\begin{aligned} h = & \frac{1}{\lambda_1 \lambda_2} \left[\delta(s_2 - s_1) (\lambda_1^\alpha + \lambda_2^\alpha - (\lambda_1 + \lambda_2)^\alpha) e^{-s_1(\lambda_1 + \lambda_2)^\alpha} + \right. \\ & + \Theta(s_2 - s_1) (\lambda_2^\alpha [(\lambda_1 + \lambda_2)^\alpha - \lambda_2^\alpha]) e^{-(\lambda_1 + \lambda_2)^\alpha s_1 - \lambda_2^\alpha (s_2 - s_1)} + \\ & \left. + \Theta(s_1 - s_2) (\lambda_1^\alpha [(\lambda_1 + \lambda_2)^\alpha - \lambda_1^\alpha]) e^{-(\lambda_1 + \lambda_2)^\alpha s_2 - \lambda_1^\alpha (s_1 - s_2)} \right]. \end{aligned} \quad (3.59)$$

where λ_1 and λ_2 are Laplace variables, δ the Dirac delta distribution, Θ the Heaviside function, α the Lévy exponent and s_1 and s_2 time points in the subordinated Equations (3.2) and (3.3).

Calculating the integral results in the correlation functions in Laplace space for the different matrix components

$$\frac{\langle \vec{u}(\lambda_1), \vec{u}^T(\lambda_2) \rangle_{11}}{\sigma^2} = (1 - a)(1 - r^2)R(\lambda_1, \lambda_2; \gamma_r) \quad (3.60a)$$

$$\frac{\langle \vec{u}(\lambda_1), \vec{u}^T(\lambda_2) \rangle_{12}}{\sigma^2} = (1 - a)(1 - r)R(\lambda_1, \lambda_2; \gamma_r) \quad (3.60b)$$

$$\frac{\langle \vec{u}(\lambda_1), \vec{u}^T(\lambda_2) \rangle_{21}}{\sigma^2} = (1 - a)(-2rR(\lambda_1, \lambda_2; \gamma) + (1 + r)R(\lambda_1, \lambda_2; \gamma_r)) \quad (3.60c)$$

$$\frac{\langle \vec{u}(\lambda_1), \vec{u}^T(\lambda_2) \rangle_{22}}{\sigma^2} = [(C_{ij} - (1 - a)(C_{ij}(1 - r) + r))R(\lambda_1, \lambda_2; \gamma) + (1 - a)R(\lambda_1, \lambda_2; \gamma_r)] \quad (3.60d)$$

where the new function

$$R(\lambda_1, \lambda_2; \gamma) = \left(\frac{\lambda_1^{\alpha-1}}{\lambda_2(\gamma + \lambda_1^\alpha)} + \frac{\lambda_2^{\alpha-1}}{\lambda_1(\gamma + \lambda_2^\alpha)} - \frac{1}{\lambda_1 \lambda_2} \right) + \frac{\gamma}{(\lambda_1 + \lambda_2)^\alpha} \left(\frac{\lambda_1^{\alpha-1}}{\lambda_2(\gamma + \lambda_1^\alpha)} + \frac{\lambda_2^{\alpha-1}}{\lambda_1(\gamma + \lambda_2^\alpha)} \right) \quad (3.61)$$

is introduced. Under the assumption that the initial value is set to the thermal equilibrium of the mean square displacement and $t_2 > t_1$, the inverse Laplace transform of $R(\lambda_1, \lambda_2; \gamma)$ can be calculated as

$$\begin{aligned} \mathcal{L}^{-1} \{R(\lambda_1, \lambda_2; \gamma)\} &= R(t_1, t_2; \gamma) \\ &= \gamma \left(\frac{\partial}{\partial t_2} + \frac{\partial}{\partial t_1} \right)^{-\alpha} [E_\alpha(-\gamma t_2^\alpha) + E_\alpha(-\gamma t_1^\alpha)] + [E_\alpha(-\gamma t_2^\alpha) + E_\alpha(-\gamma t_1^\alpha) - 1] \end{aligned} \quad (3.62)$$

with the Mittag-Leffler function E_α and the two dimensional fractional differentiation operator $(\partial/\partial t_1 + \partial/\partial t_2)^\alpha$. More information on this operator can be found in the work of Baule

et al. [72]. In the last step the two dimensional fractional differentiation operator can be resolved and R can be written as

$$R(t_1, t_2; \gamma) = \frac{\gamma t_1^\alpha}{\Gamma(\alpha + 1)} \sum_{n=0}^{\infty} \frac{(-\gamma t_2^\alpha)^n}{\Gamma(\alpha n + 1)} {}_2F_1\left(\alpha, -\alpha n, \alpha + 1; \frac{t_1}{t_2}\right) + E_\alpha(-\gamma t_2^\alpha) \quad (3.63)$$

with the Gamma function Γ and the Hypergeometric function ${}_2F_1$. With this function and the correlations from Equations (3.60d) the final form of the correlations

$$\frac{\langle \vec{u}(t_1), \vec{u}^T(t_2) \rangle_{11}}{\sigma^2} = (1 - a)(1 - r^2)R(t_1, t_2; \gamma_r) \quad (3.64a)$$

$$\frac{\langle \vec{u}(t_1), \vec{u}^T(t_2) \rangle_{12}}{\sigma^2} = (1 - a)(1 - r)R(t_1, t_2; \gamma_r) \quad (3.64b)$$

$$\frac{\langle \vec{u}(t_1), \vec{u}^T(t_2) \rangle_{21}}{\sigma^2} = (1 - a)(-2rR(t_1, t_2; \gamma) + (1 + r)R(t_1, t_2; \gamma_r)) \quad (3.64c)$$

$$\frac{\langle \vec{u}(t_1), \vec{u}^T(t_2) \rangle_{22}}{\sigma^2} = [(C_{ij} - (1 - a)(C_{ij}(1 - r) + r))R(t_1, t_2; \gamma) + (1 - a)R(t_1, t_2; \gamma_r)] \quad (3.64d)$$

can be achieved. It has to be emphasized that this correlation function is not stationary and it highly depends on t_1 and t_2 and not the time difference $t_2 - t_1$. In addition to that it is only valid for ensemble averages and can not be compared with time averages because no stationary state is present where time averages are justified. However if α is not too small ensemble and time averages may be close to each other at small times t_1 .

The correlation function with an underlying tempered Lévy distribution can also be calculated where the work of Cairoli et al. [66, 67] can be used as a reference.

3.2.6 Ensemble Kurtosis of Increment Statistics

In addition to the ensemble correlations it is also possible to calculate other two time ensemble averages in the physical time t with a stationary subordinated process if the corresponding two time ensemble average in the model intrinsic time s is known. In the following the focus is laid on the ensemble averaged increment kurtosis in physical time, which is gained by the same formalism as for the correlation function, namely the characterization in Laplace space by Equation (3.58) and inverse transform to physical time variables. However a closed form in the physical time could not be derived but a numerical solution, which is compared to simulation results and time averages, will be shown.

With the increments $\Delta u_\tau(t) = u(t + \tau) - u(t)$ the increment kurtosis is generally defined as

$$K(\Delta u_\tau(t_1), \Delta u_\tau(t_2)) = \frac{\langle (\Delta u_\tau(t_2) - \Delta u_\tau(t_1))^4 \rangle}{\langle (\Delta u_\tau(t_2) - \Delta u_\tau(t_1))^2 \rangle^2} = \frac{\langle f(\Delta u_\tau(t_1), \Delta u_\tau(t_2)) \rangle}{\langle g(\Delta u_\tau(t_1), \Delta u_\tau(t_2)) \rangle^2} \quad (3.65)$$

where the ensemble averaging for the functions

$$f(\Delta u_\tau(t_1), \Delta u_\tau(t_2)) = (\Delta u_\tau(t_2) - \Delta u_\tau(t_1))^4 \quad (3.66a)$$

$$g(\Delta u_\tau(t_1), \Delta u_\tau(t_2)) = (\Delta u_\tau(t_2) - \Delta u_\tau(t_1))^2 \quad (3.66b)$$

has to be done.

To achieve the kurtosis in Laplace space the two time ensemble averages are used as the starting point. For the function f it has to hold

$$\langle \tilde{f}(\Delta \tilde{u}_\tau(\lambda_1), \Delta \tilde{u}_\tau(\lambda_2)) \rangle = \int_0^\infty \int_0^\infty ds_1 ds_2 \langle f(\Delta u_\tau(s_1), \Delta u_\tau(s_2)) \rangle \tilde{h}(s_1, \lambda_1; s_2, \lambda_2) \quad (3.67)$$

with the two time density in Laplace space

$$\begin{aligned} \tilde{h}(s_1, \lambda_1; s_2, \lambda_2) = & \frac{1}{\lambda_1 \lambda_2} \left[\delta(s_2 - s_1) (\Phi(\lambda_1) + \Phi(\lambda_2) - \Phi(\lambda_1 + \lambda_2)) e^{-s_1 \Phi(\lambda_1 + \lambda_2)} + \right. \\ & + \Theta(s_2 - s_1) (\Phi(\lambda_2) [\Phi(\lambda_1 + \lambda_2) - \Phi(\lambda_2)]) e^{-\Phi(\lambda_1 + \lambda_2) s_1 - \Phi(\lambda_2)(s_2 - s_1)} + \\ & \left. + \Theta(s_1 - s_2) (\Phi(\lambda_1) [\Phi(\lambda_1 + \lambda_2) - \Phi(\lambda_1)]) e^{-\Phi(\lambda_1 + \lambda_2) s_2 - \Phi(\lambda_1)(s_1 - s_2)} \right] \quad (3.68) \end{aligned}$$

where $\Phi(\lambda) = \lambda^\alpha$ for a Lévy distributed time without modifications and $\Phi(\lambda) = (\lambda + \mu)^\alpha - \mu^\alpha$ if a tempered Lévy distribution is assumed. For simplicity reasons in the next step the fact is used that in the model intrinsic time s the kurtosis has to be 3 according to a Gaussian distribution of increments, i.e.

$$\langle f(\Delta u_\tau(s_1), \Delta u_\tau(s_2)) \rangle = 3 \langle g(\Delta u_\tau(s_1), \Delta u_\tau(s_2)) \rangle^2 \quad (3.69)$$

which can be substituted in Equation (3.67). Further rearranging and using the definition of the increments shows that

$$\langle \tilde{f}(\Delta \tilde{u}_\tau(\lambda_1), \Delta \tilde{u}_\tau(\lambda_2)) \rangle = 12 \int_0^\infty \int_0^\infty ds_1 ds_2 (\sigma^4 - 2\sigma^2 R(s_1, s_2) + R(s_1, s_2)^2) \tilde{h}(s_1, \lambda_1; s_2, \lambda_2) \quad (3.70)$$

has to be solved where the autocovariance function is given as $R(s_1, s_2) = \sigma^2 (a \cdot e^{-\gamma|s_2 - s_1|} + (1 - a) \cdot e^{-\gamma r|s_2 - s_1|})$ with the standard deviation σ . Solving the integral with respect to the first term of h yields

$$\begin{aligned} \langle \tilde{f}_1(\Delta \tilde{u}_\tau(\lambda_1), \Delta \tilde{u}_\tau(\lambda_2)) \rangle &= 12 [\sigma^4 - 2\sigma^2 R(0) + R^2(0)] \left[-\frac{1}{\lambda_1 \lambda_2} + \frac{\Phi(\lambda_1) + \Phi(\lambda_2)}{\lambda_1 \lambda_2 \Phi(\lambda_1 + \lambda_2)} \right] \\ &= 12 [-\sigma^4 + \sigma^4 (a + (1 - a))^2] \left[-\frac{1}{\lambda_1 \lambda_2} + \frac{\Phi(\lambda_1) + \Phi(\lambda_2)}{\lambda_1 \lambda_2 \Phi(\lambda_1 + \lambda_2)} \right] \\ &= 0 \quad (3.71a) \end{aligned}$$

such that this term can be neglected. The second term which includes the Heaviside function resolves in

$$\langle \tilde{f}_2(\Delta \tilde{u}_\tau(\lambda_1), \Delta \tilde{u}_\tau(\lambda_2)) \rangle = 12 \frac{\Phi(\lambda_2) [\Phi(\lambda_1 + \lambda_2) - \Phi(\lambda_2)]}{\lambda_1 \lambda_2 \Phi(\lambda_1 + \lambda_2)} \left[\frac{\sigma^4}{\Phi(\lambda_2)} - 2\sigma^2 \tilde{R}_1(\Phi(\lambda_2)) + \tilde{R}_2(\Phi(\lambda_2)) \right] \quad (3.71b)$$

with the Laplace transforms of the autocovariance and the squared autocovariance

$$\tilde{R}_1(\Phi) = \mathcal{L}\{R\}(\Phi) = \sigma^2 \left(a \frac{1}{\Phi + \gamma} + (1 - a) \frac{1}{\Phi + \gamma_r} \right) \quad (3.72a)$$

$$\tilde{R}_2(\Phi) = \mathcal{L}\{R^2\}(\Phi) = \sigma^4 \left(a^2 \frac{1}{\Phi + 2\gamma} + (1 - a)^2 \frac{1}{\Phi + 2\gamma_r} + 2a(1 - a) \frac{1}{\Phi + \gamma + \gamma_r} \right). \quad (3.72b)$$

The third term $\langle \tilde{f}_3(\Delta \tilde{u}_\tau(\lambda_1), \Delta \tilde{u}_\tau(\lambda_2)) \rangle$ with swapped s_1 and s_2 is also zero because $s_2 > s_1$ and $t_2 > t_1$ and consequently $\Theta(s_2 - s_1) = 0$.

For g similar steps can be performed, where the results for the three terms are

$$\langle \tilde{g}_1(\Delta \tilde{u}_\tau(\lambda_1), \Delta \tilde{u}_\tau(\lambda_2)) \rangle = 0 \quad (3.73a)$$

$$\langle \tilde{g}_2(\Delta \tilde{u}_\tau(\lambda_1), \Delta \tilde{u}_\tau(\lambda_2)) \rangle = 2 \frac{\Phi(\lambda_2) [\Phi(\lambda_1 + \lambda_2) - \Phi(\lambda_2)]}{\lambda_1 \lambda_2 \Phi(\lambda_1 + \lambda_2)} \left[\frac{\sigma^2}{\Phi(\lambda_2)} - \tilde{R}(\Phi(\lambda_2)) \right] \quad (3.73b)$$

$$\langle \tilde{g}_3(\Delta \tilde{u}_\tau(\lambda_1), \Delta \tilde{u}_\tau(\lambda_2)) \rangle = 0. \quad (3.73c)$$

After inserting the function Φ for the unmodified Lévy distribution and the tempered distribution, the functions $\langle \tilde{f} \rangle$ and $\langle \tilde{g} \rangle$ can be numerically inverse Laplace transformed and the kurtosis $K(\Delta u_\tau(t_1), \Delta u_\tau(t_2))$ is achieved from Equation (3.65). The results are depicted in Figure 3.7 together with ensemble averaged simulation results for $t_1 = 1$ s and $t_2 = t_1 + \tau$. For this purpose the kurtosis of 10000 simulations with a time step of $\Delta t = 0.01$ s has been ensemble averaged. The results fit very well to the theoretical values which support the developed theory in this section. Nevertheless if the more relevant time averaged simulation results over 10^6 time steps are compared to the theory, big differences occur for both time distributions, as can be seen in Figure 3.8. In general the increment kurtosis of the time averaged simulations is always larger than the increment kurtosis of the ensemble averaged simulations. This highlights the non-stationary character of the increment kurtosis of the CTRW fields and the impossibility of the theoretical description of its time average by ensemble averages.

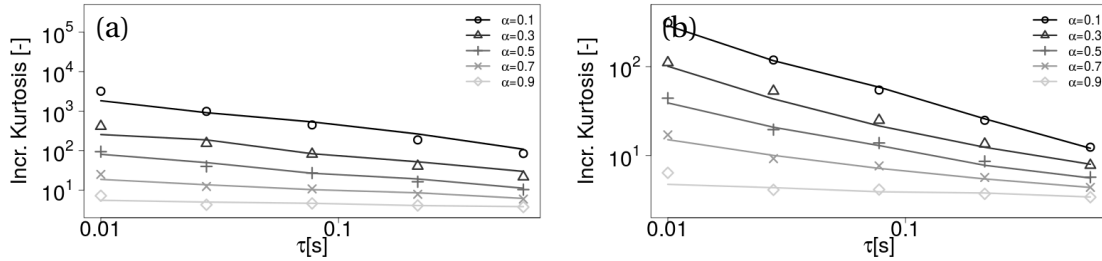


Figure 3.7: Increment kurtosis gained by Equation (3.65) with the numerically inversed functions $\langle \tilde{f} \rangle$ and $\langle \tilde{g} \rangle$ (symbols), and simulated ensemble averages (lines) for (a) an unmodified Lévy distribution and (b) a tempered Lévy distribution.

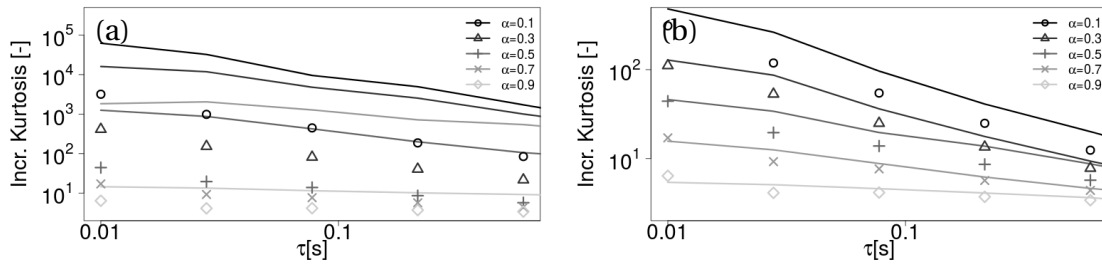


Figure 3.8: Increment kurtosis gained by Equation (3.65) with the numerically inversed functions $\langle \tilde{f} \rangle$ and $\langle \tilde{g} \rangle$ (symbols), and simulated time averages (lines) over 10^6 time steps for (a) an unmodified Lévy distribution and (b) a tempered Lévy distribution.

3.3 Increment Kurtosis Dependence on Model Parameters

As described in section 2.5.2, the CTRW model consists of several parameters which affect the increment kurtosis, which has to be scale dependent according to Kolmogorov's refined similarity hypothesis [24]. This scale dependence as well as their relation to the spectra should be studied in more detail in the following. In particular the intermittency parameter α , the intrinsic time step Δs and the integral time scale $\bar{\tau}$ are chosen for this study. Dependent on the underlying type of time transformation the effect of these parameters is different. In particular a Lévy distribution with a sharp cutoff $C = 10000$ and a tempered Lévy distribution with the tempering parameter $\mu = \alpha^{-1/(\alpha-1)}$, where a fixed mean time evolution is ensured for all α , are taken. In addition the effect of time interpolation in the s - t diagram is studied, which can be seen as a workaround to prohibit unphysical constant wind speeds over long time periods, which otherwise are naturally included in CTRW generated fields. To achieve a more robust result, ten independent realizations with a fixed time step $\Delta t = 0.01$ s and a total time of $t = 600$ s are generated and averaged for each parameter set.

3.3.1 The Intermittency Parameter

The most important parameter which influences the increment kurtosis is the Lévy exponent α which generally has to be smaller than one to obtain a behavior different from Gaussian. However it is not clear how the increment kurtosis changes with decreasing α , especially because the Lévy distribution is not kept in its theoretical form. Tempering and cutting lead to different observations. For both simulations the intrinsic time step is chosen as $\Delta s = 0.01$ s, the characteristic frequency as $\omega_c = 1$ Hz and the intermittency parameter as $\alpha \in \{0.1, 0.3, 0.5, 0.7, 0.9\}$.

As seen in Figure 3.9a, a sharp cutoff results in an increased increment kurtosis while reducing α from 1 to 0.5, but only on small scales. At large scales the choice of higher α seems to be relevant for a higher increment kurtosis. Reducing the intermittency parameter to values $\alpha < 0.5$ gives rise to an opposing trend where a kurtosis reduction becomes apparent on all scales. The reason for this behavior lies also in the cutoff itself but the main contribution comes from the connected renormalization of the Lévy distribution to ensure a mean step size $\langle \Delta t \rangle = \Delta s$. The interpolation is not important at all for the parameters shown here, as can be seen in comparison with Figure 3.9b.

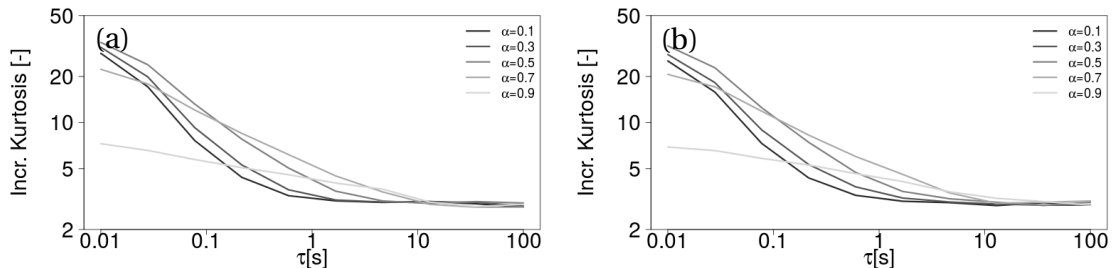


Figure 3.9: Kurtosis for $\Delta s = 0.01$ s and $\omega_c = 1$ Hz for a sharp cutoff (a) without and (b) with time interpolation.

If the tempered Lévy distribution is considered, smaller values for α always correspond

to an increased increment kurtosis as seen in Figure 3.10a. Therefore this distribution is much more reliable than a sharp cutoff if it is desired to change the degree of intermittency in a specific direction. In terms of the achievable kurtosis range, this distribution should also be favored. For the parameters chosen here the increment kurtosis reaches a ten times bigger value than for the distribution with a cutoff. Again the time interpolation is not relevant at all.

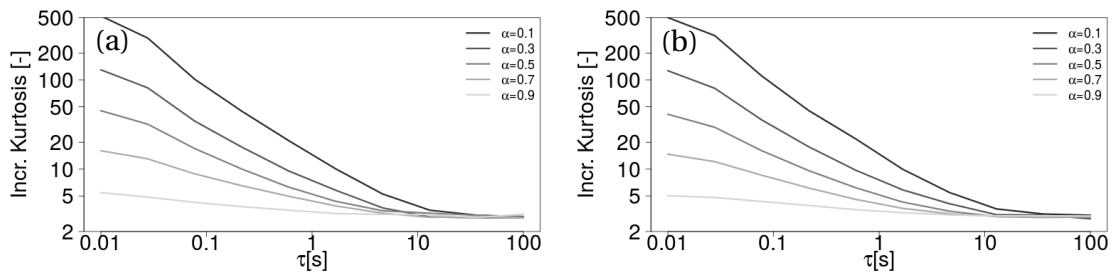


Figure 3.10: Kurtosis for $\Delta s = 0.01$ s and $\omega_c = 1$ Hz for a tempered distribution (a) without and (b) with time interpolation.

Even though the increment kurtosis can theoretically be increased to arbitrary high values on small scales by changing α , a fast (power-law-like) drop appears with increasing τ for both distributions and the Gaussian value of 3 is reached for relatively small time gaps. This is the reason why a high kurtosis on scales larger than 10 s is very difficult to achieve without very unphysical extreme values in the small range of τ . An additional drawback of small α is that the wind fields show very slow dynamics on big time scales, as seen in Figure 3.11 for the tempered distribution without time interpolation, where also the time evolution with the intrinsic time step is shown. The long waiting times in the time evolution are a big problem if one is interested in converged statistics of the time series in a relatively short time interval, e.g. 10 minutes. So high intermittency and converged statistics exclude each other for the CTRW model, but post-corrections can be used to achieve time series with improved characteristics. Those post-corrections are discussed in more detail in section 3.4.

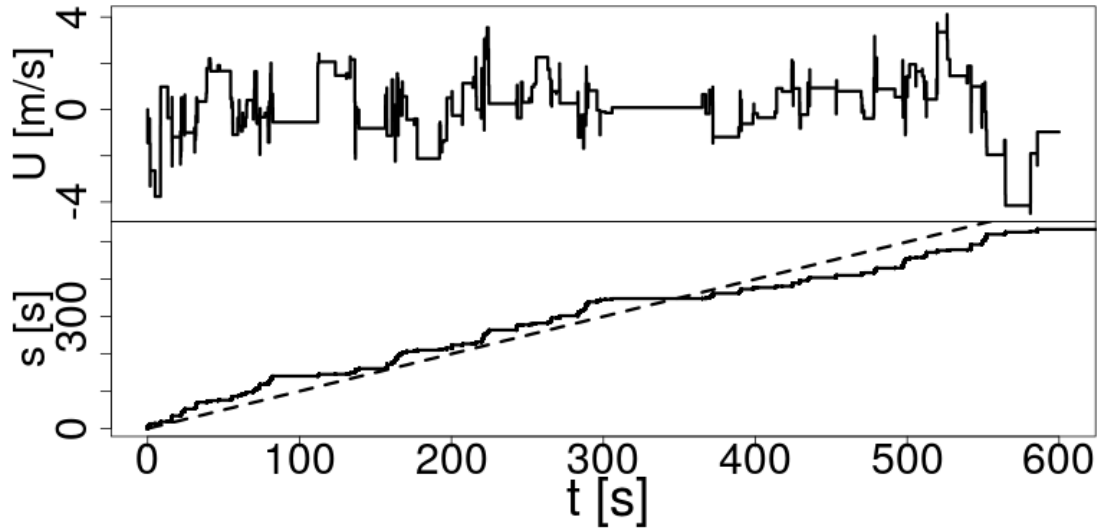


Figure 3.11: Exemplary time series of the wind speed and the time evolution $s(t)$ for $\Delta s = 0.01$ s, $\omega_c = 1$ Hz and $\alpha = 0.1$ with an underlying tempered Lévy distribution.

3.3.2 The Intrinsic Time Step

The Lévy exponent α is a very obvious parameter to change the increment statistics. But other parameters are not so obvious on first glance. One of those parameters is the intrinsic time step Δs which is used to simulate the wind field before the time transformation takes place. Usually a very small value for this time step has to be chosen to prevent numerical errors and to achieve a wind field with well defined characteristics. Nevertheless in the past authors took values of 1 s, 72 s [65] or even up to 100 s [11]. The reason behind this was that for such large time steps the autocorrelation function fitted best to wind data [65] or that presumably the degree of intermittency reached a specific target value which could not be achieved otherwise. However as shown in section 3.1.3 the autocorrelation function as well as the spectral density can be controlled best by ω_c . The intermittency on the other side can be manipulated best by choice of a tempered Lévy distribution with the corresponding α .

Because confusion on how to choose Δs may come up, the dependency will be studied in the following for $\alpha = 0.5$, $\omega_c = 1$ Hz and $\Delta s \in \{0.001, 0.013, 0.173, 2.279, 30\}$ s. Again the different time distributions, namely with a sharp cutoff and a tempering are investigated. In addition the effect of time interpolation is also considered.

As can be seen for both time distributions in Figures 3.12a and 3.13a, large intrinsic time steps always cause a large increment kurtosis if no time interpolation is performed. For the case with a sharp cutoff the sensitivity of the increment kurtosis on the intrinsic time step is very high even for the smallest time steps used for this study. This is a sign for an improper stochastic process in the sense that it does not provide a stable distribution. The tempered distribution is much more robust and the kurtosis converges for small time steps to a level, which is much higher than for the first distribution.

Interestingly the time interpolation procedure, which is used between time steps, changes the results for both time distributions into different directions. On the one side for a sharp cutoff no big change can be observed in Figure 3.12b except for the two largest

time steps, which originate from convergence issues. On the other side the tempered distribution shows up a pretty high reduction of increment kurtosis for all time step sizes but the effect of the interpolation on the smallest time step is almost not present. In addition to that a convergence to the graph of the smallest time step appears with decreasing step size, as before the interpolation procedure. Most importantly the graphs with varying Δs follow now a trend which is vice versa to the one before the interpolation. Large time steps result in a small increment kurtosis and at the same time small time steps let the kurtosis converge. This is the expected behavior of a correct stochastic model. Small time steps, which are important for numerical stability, should not lead to the inconsistent outcome that intermittency is destroyed. Rather, the overall accuracy of the generated time series has to increase and intermittency, as a core element of the model, has to be present.

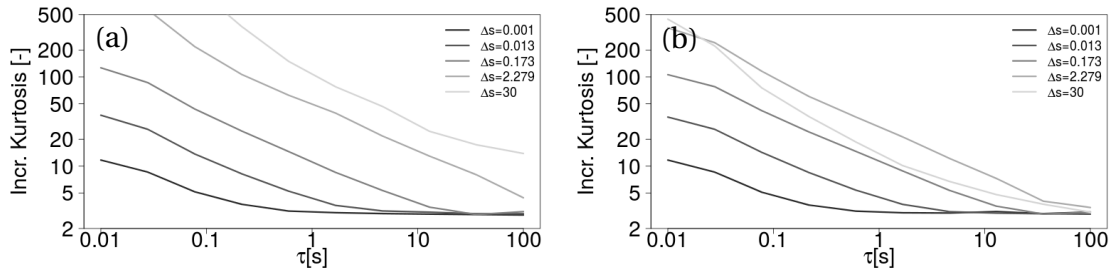


Figure 3.12: Kurtosis for $\alpha = 0.5$ and $\omega_c = 1$ Hz for a sharp cutoff (a) without and (b) with time interpolation.

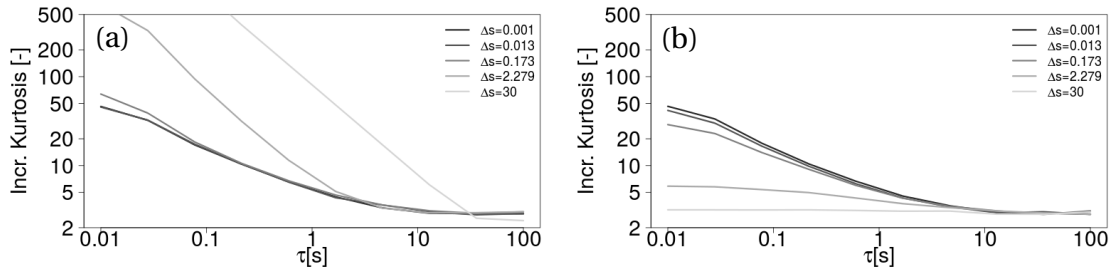


Figure 3.13: Kurtosis for $\alpha = 0.5$ and $\omega_c = 1$ Hz for a tempered distribution (a) without and (b) with time interpolation.

Why large Δs are responsible for a large increment kurtosis becomes obvious if the time series and the time evolution are investigated in more detail. Figures 3.14 and 3.15 show for the sharp cutoff what happens with the wind speed if the intrinsic time step is increased. While Figure 3.14a shows small intervals with waiting times, the duration of those waiting times increases a lot for the large time step in Figure 3.15a. As can be seen, the long waiting times, where $t(s)$ does not change, are directly transferred to the wind speed time series. Depicted in Figures 3.14b and 3.15b are the time series with where a time interpolation has been done. The waiting times are prevented, but the dynamics are slowed down in the regions, where the slope in the $t(s)$ diagram is very flat. So a time series mixed of slow and fast patterns is generated.

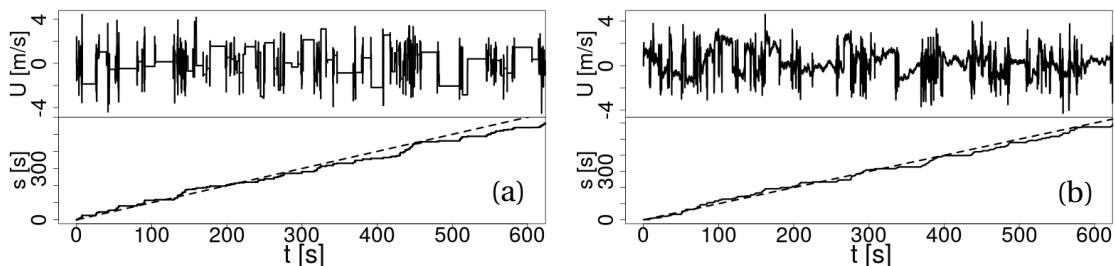


Figure 3.14: Time series of the wind speed and evolution of $s(t)$ for $\alpha = 0.5$, $\omega_c = 1$ Hz and $\Delta s = 0.173$ s for a sharp cutoff (a) without and (b) with time interpolation.

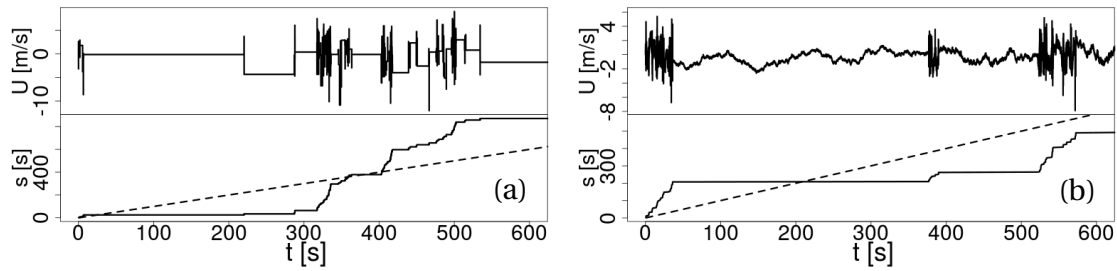


Figure 3.15: Time series of the wind speed and evolution of $s(t)$ for $\alpha = 0.5$, $\omega_c = 1$ Hz and $\Delta s = 2.28$ s for a sharp cutoff (a) without and (b) with time interpolation.

Changing the time step results in similar patterns for the case where a tempered distribution is chosen, shown in Figures 3.16, and 3.17. The time series look much more smooth compared to the case where a sharp cutoff is taken, even if no time interpolation is used. Furthermore with the time interpolation the distinction between highly and slowly fluctuating parts in the time series becomes much more difficult. Interestingly one could argue that time steps with a resulting high increment kurtosis goes hand in hand with long waiting times. But if a direct comparison of $\Delta s = 0.173$ s of the sharp cutoff case with the tempered case is done without taking the interpolation into account, the first one consists of longer waiting time events but it shows similar intermittency. In other words, the intermittency mainly results from the shape of the time distribution and not the weighting of long waiting time events.

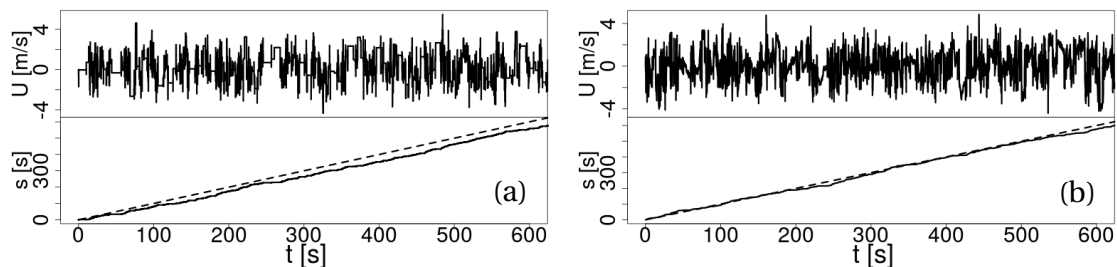


Figure 3.16: Time series of the wind speed and evolution of $s(t)$ for $\alpha = 0.5$, $\omega_c = 1$ Hz and $\Delta s = 0.173$ s for a tempered distribution (a) without and (b) with time interpolation.

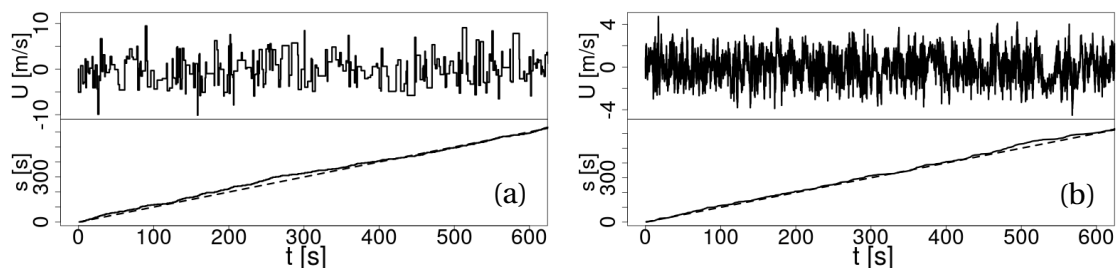


Figure 3.17: Time series of the wind speed and evolution of $s(t)$ for $\alpha = 0.5$, $\omega_c = 1$ Hz and $\Delta s = 2.28$ s for a tempered distribution (a) without and (b) with time interpolation.

3.3.3 The Integral Time Scale

The last parameter which is focused on is the integral time scale $\bar{\tau}$ which can be controlled by the characteristic frequency ω_c by means of Equation (3.51). In addition to the increment kurtosis also the power spectra are taken into account, where a comparison with the theoretical results for $\alpha = 1$ is performed, which corresponds to the Gaussian case. Here an intrinsic time step $\Delta s = 0.01$ s and the Lévy exponent $\alpha = 0.5$ is chosen. The time scale takes the values $\bar{\tau} \in \{0.043, 0.43, 4.3, 43, 430\}$ s.

Figures 3.18 and 3.19 show for the both time distributions considered here that the integral time scale also plays a role for the increment kurtosis. In general larger time scales increase the increment kurtosis independent on which time distribution has been taken. For both cases a factor of 2 is reached between the increment kurtosis of the largest and the smallest time scale. The interpolation only has a very small damping effect and can be neglected.

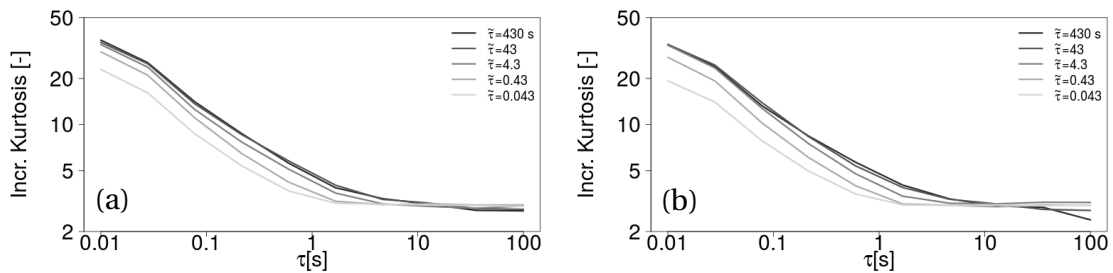


Figure 3.18: Kurtosis for $\alpha = 0.5$ and $\Delta s = 0.01$ s for a sharp cutoff (a) without and (b) with time interpolation.

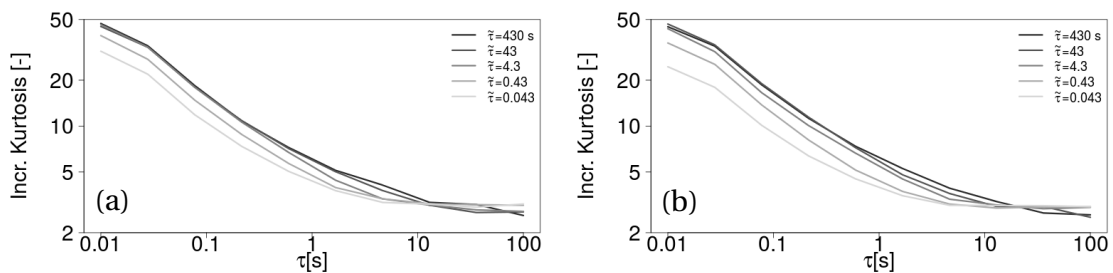


Figure 3.19: Kurtosis for $\alpha = 0.5$ and $\Delta s = 0.01$ s for a tempered distribution (a) without and (b) with time interpolation.

Figures 3.20 and 3.21 show how the power spectra behave for the different time scales and how they fit to the theoretical Gaussian result for $\alpha = 1$ taken from Equation (3.21). The spectrum with an underlying Lévy distribution with a sharp cutoff shows very good agreement on all time scales except the smallest one. The tempered distributed time distribution leads to similar results but the second smallest time scale also does not fit perfectly. The reason here is that the increment kurtosis is even higher than for the other case. All in all a positive correlation between the increment kurtosis and the deviation of the spectra from the Gaussian case is found for each time scale.

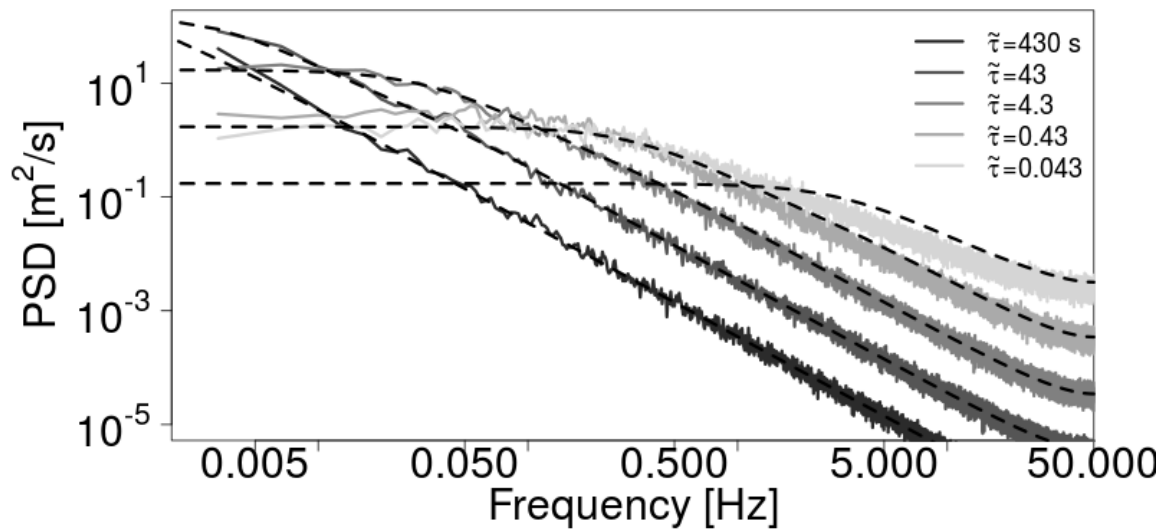


Figure 3.20: Power spectra for $\alpha = 0.5$ and $\Delta s = 0.01$ s for a Lévy distribution with a sharp cutoff. The dashed lines correspond to the theoretical result from Equation (3.21).

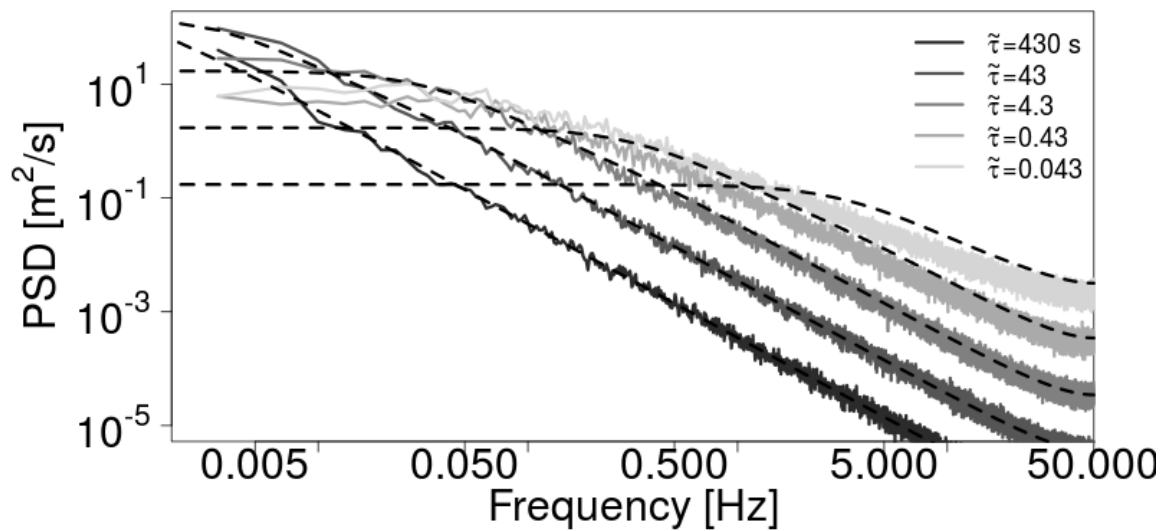


Figure 3.21: Power spectra for $\alpha = 0.5$ and $\Delta s = 0.01$ s for a tempered Lévy distribution. The dashed lines correspond to the theoretical result from Equation (3.21).

3.4 Post-Corrections of Generated Wind Fields

Because one of the main studies done in this thesis is the comparison of the effects of intermittent and non-intermittent wind fields on wind turbines, it is essential to make those two different types of fields statistically comparable. The term "comparable" means here that the one point distributions are Gaussian with the same mean and variance, kurtosis of three and zero skewness. Additionally the two time and two point correlations and the corresponding spectra should be as equal as possible.

While adjusting the mean and standard deviation is trivial, corrections of the other properties are generally accompanied by some difficulties which are to be solved. One issue is that wind fields can be very different due to instabilities of the Gaussian shape of the one point distribution for intermittent fields. This results from the long waiting times shown in Figure 3.11 which makes the distribution converge slower. Additionally numerical artifacts like spectral leakage and aliasing can occur which distort the shape of the PSD and the total energy content. The main parts done are a correction of the PSD for all velocity time series at each grid point and an even more important correction of the one point PDF. Finally if one is interested in solenoidal wind fields, a correction method for the divergence of the whole wind field is shown.

3.4.1 Estimation Errors for the Power Spectral Density and Autocorrelation Function

Even if the input parameters and their influence on the properties of the wind field are theoretically well known it may happen that the outcome of the model is still very different from what is expected. This is due to numerical issues resulting from too coarse simulation grids, temporal resolution or too few grid points. The difficulties in the simulation of proper wind fields and the expected errors are presented in this part. Different numerical artifacts are illustrated, which change the theoretical PSD from section 3.1.3 and the corresponding correlation functions. In more detail a priori estimations of spectral densities will be shown which consider the effects of aliasing and spectral leakage. The errors shown here are also very interesting for simulations which naturally have a very coarse mesh, like Blade Element Momentum (BEM) simulations, where in addition the grid typically has only very few points (up to 30 points in each direction, say). For those meshes spectral leakage but also aliasing have big effects on the simulation results which should be known beforehand.

In general aliasing is a numerical effect which occurs if discretizations with low sampling frequencies in time or space are performed. In particular the highest frequency where the system contains energy has to be lower than half the sampling frequency (Nyquist frequency), otherwise a mirror image of the missing high frequency part of the spectrum is added to the low frequency part and pronounced low frequency effects are seen in the spectrum and time series, which were originally not existent. This can also lead to patterns which would not be seen for higher sampling frequencies and can therefore lead to wrong interpretations. The aliasing effect is shown in Figure 3.22 for an arbitrary spectrum. The highest frequency f_{\max} of the spectrum is in this case bigger than half the sampling frequency f_s . Because the spectrum is periodic with f_s and symmetric it is unavoidable that the original spectrum and its alias overlap and sum up at the high frequency region $f_s - f_{\max} < f < f_s$.

The resulting spectrum is exactly the same with the difference that clearly an increased tail from $f_s - f_{\max}$ onwards is visible.

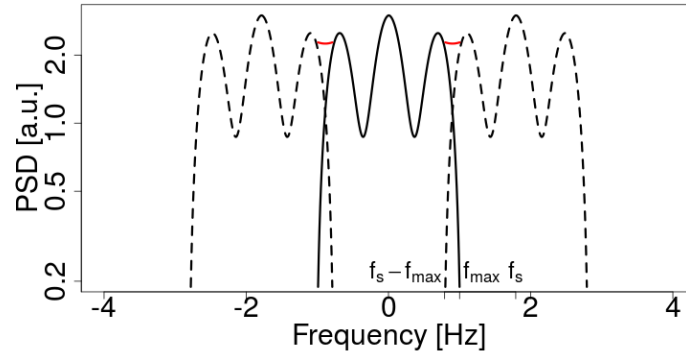


Figure 3.22: Spectrum with energy content up to the maximal frequency f_{\max} (solid) and its aliases (dashed) with the sampling frequency f_s . Overlapping occurs for $f_s - f_{\max} < f < f_s$ where the increased energy content is marked in red.

The second most important effect is the effect of spectral leakage which does not appear due to the sampling frequency but to the windowing which is used to sample the time series. Spectral leakage also has an effect on the energy spectra in the sense that energy from frequencies, which are not captured by the discretization, is distributed to neighbouring frequencies to keep the total energy content constant. Windowing can be understood as a convolution of the time series $x(t)$ with a window function $w(t)$ which is in Fourier space a product of the energy spectrum of the time series with the Fourier transformed window function, i.e.

$$x(t) \star w(t) = \hat{x}(f) \cdot \hat{w}(f) \quad (3.74)$$

where \star is the convolution operator. In Figure 3.23 an example of spectral leakage is shown for two cosine shaped time series with different frequencies which are sampled with the same sampling rate and window length. In the top picture the window length coincides with a multiple of the period of the cosine function, i.e. the time series can be repeated periodically without jumps, from which follows that the discrete Fourier transform fully captures the correct frequency of the time series. In the second case (bottom) the window length does not coincide with a multiple of the cosine function and a periodic continuation of the time series leads to a jump at the border of the sampling window. The simple representation by only one peak in the discrete Fourier spectrum is not possible anymore but the original peak is distributed to neighbouring frequencies.

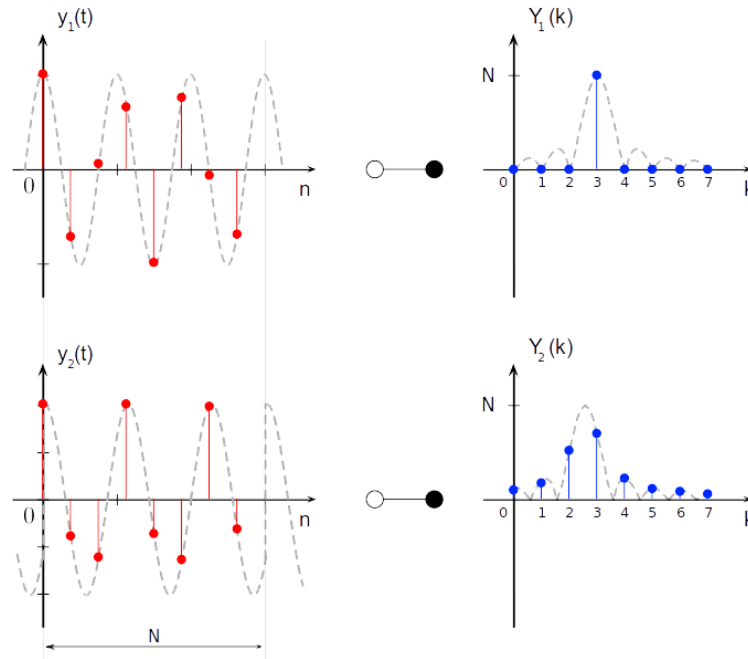


Figure 3.23: Time series and DFT spectrum for two cosine functions with different frequencies but same window lengths and sampling frequencies, the first correctly fits the chosen window size while spectral leakage occurs for the second. Picture from Puente et al. [73].

For CTRW fields aliasing and spectral leakage effects are important and a small study on simulation results and their predictability is performed where the autocovariance function and PSD are investigated. For this sake a time series of length $N = 10^6$ is generated and a rectangular window with 200 points is used as a windowing function, i.e. the statistics for a time series with 200 data points are gained.

Figure 3.24 shows the effect on the PSD and the autocovariance function of simulations and theoretical predictions for $N \rightarrow \infty$ as well as for $N = 200$. Several theoretical models are analysed for $N = 200$: The first one does not take into account any numerical effects (Model), the second one considers aliasing (Model+A), and the third case aliasing and spectral leakage (Model+A+L). For the simulations as well as the theoretical model the aliasing error at high frequencies in the spectrum in Figure 3.24a is obvious. The effect of spectral leakage is also visible, which lifts the PSD function to higher energies, because the energy from the missing low frequencies is blurred out to high frequencies. The resulting autocovariance functions in Figure 3.24b are also quite different for all approaches. In particular, the difference to the theoretical autocorrelation function for $N \rightarrow \infty$ is very big and the standard deviation at $\tau = 0$ is below 40% if numerical errors are considered.

Finally it can be said that an excellent prediction of the PSD and the covariance function can be made if aliasing and spectral leakage are taken into account. It is possible to quantify the resulting numerical errors without even simulating the time series. Thus deviating correlation lengths, structure sizes and energy content are not surprising anymore. Especially for BEM simulations, where a very coarse grid with few points is taken, differences between expected and simulated spatial correlations can be explained.

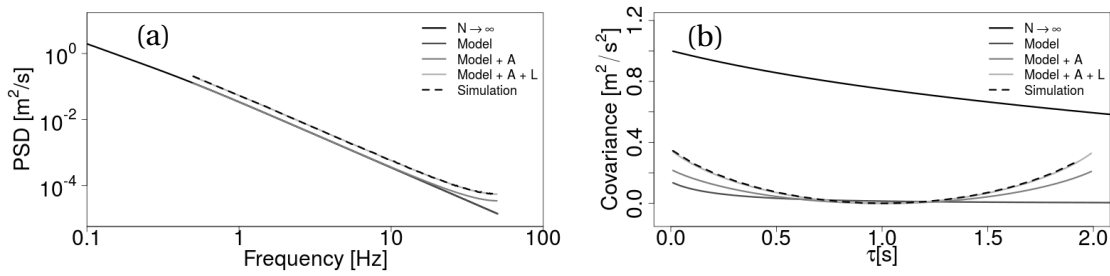


Figure 3.24: (a) PSD and (b) autocovariance function for $N \rightarrow \infty$ and $N = 200$ simulated points. The theoretical spectra for $N = 200$ are shown without aliasing (Model), with aliasing (Model+A), and with aliasing and spectral leakage (Model+A+L).

3.4.2 Correction of the Power Spectral Density

Because the PSD plays a major role for the wind characterization and in load dynamics it has to be made sure that the effect resulting from the spectrum can be neglected if a comparison of intermittent and non-intermittent fields takes place. In the following the procedure to correct frequency spectra of intermittent and non-intermittent wind fields to a prescribed spectrum is shown with the goal to isolate the intermittency, i.e. the increment kurtosis, as much as possible. It has to be decided what should be the reference spectrum, where the fields are to be projected on. It could be the intermittent, the non-intermittent or the analytic spectrum (3.21) for the non-intermittent case. For this work the latter one has been taken because it has well defined characteristics like the variance and integral scales which also makes parameter studies much more reliable.

The spectral correction is based on the definition of the PSD

$$E(\omega) = |\hat{x}(\omega)|^2 = |\mathcal{F}\{x(t)\}|^2 \quad (3.75)$$

where $\hat{x} = \mathcal{F}\{x\}$ is the Fourier transformed counterpart of the series x . Equation (3.75) can be used for a relation between the originally simulated field x_s and the field with the analytic spectrum x_a

$$|x_a(t)| = \mathcal{F}^{-1} \left\{ \sqrt{\frac{E_a(\omega)}{E_s(\omega)}} |\mathcal{F}\{x_s(t)\}| \right\} \quad (3.76)$$

where the phase of the Fourier transform is not present and therefore could be arbitrary. However, to keep the new field as similar as possible to the original one the phase of the original field is adopted such that the final relation is

$$x_a(t) = \mathcal{F}^{-1} \left\{ \sqrt{\frac{E_a(\omega)}{E_s(\omega)}} \mathcal{F}\{x_s(t)\} \right\}. \quad (3.77)$$

The effect of this spectral correction on the time series and PSD's for Gaussian and intermittent cases with a tempered Lévy distribution and $\omega_c = 1$ Hz, $\Delta s = 0.01$ s, and 60000 sample points are shown in Figures 3.25 and 3.26. It becomes obvious that the spectral correction

has a big influence not only on the spectrum of the intermittent case but also on the intermittent time series itself. The original waiting times vanish due to the break-up of the amplitude-phase relation. However the increment kurtosis does not become zero as illustrated in Figure 3.27, where for different Lévy exponents α the effect on the increment kurtosis is shown. The spectral correction in the way done here seemingly has a damping effect on all scales which should be taken into account if the correction is necessary.

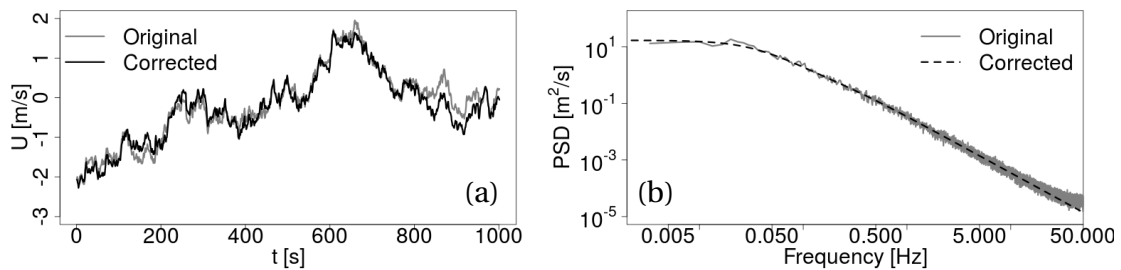


Figure 3.25: (a) Timeseries and (b) PSD for a Gaussian time series before and after the spectral correction.

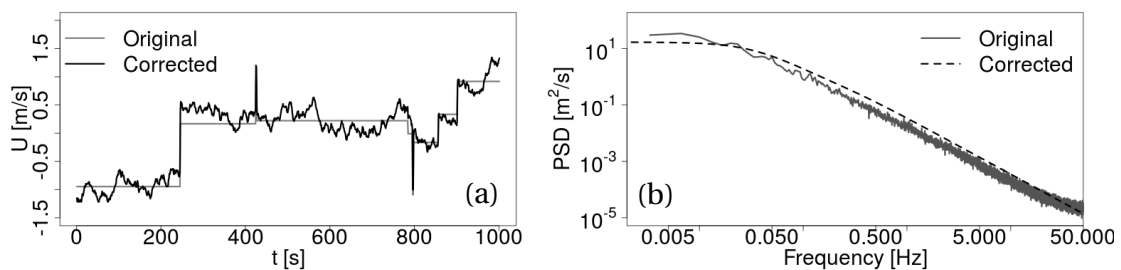


Figure 3.26: (a) Timeseries and (b) PSD for an intermittent time series before and after the spectral correction.

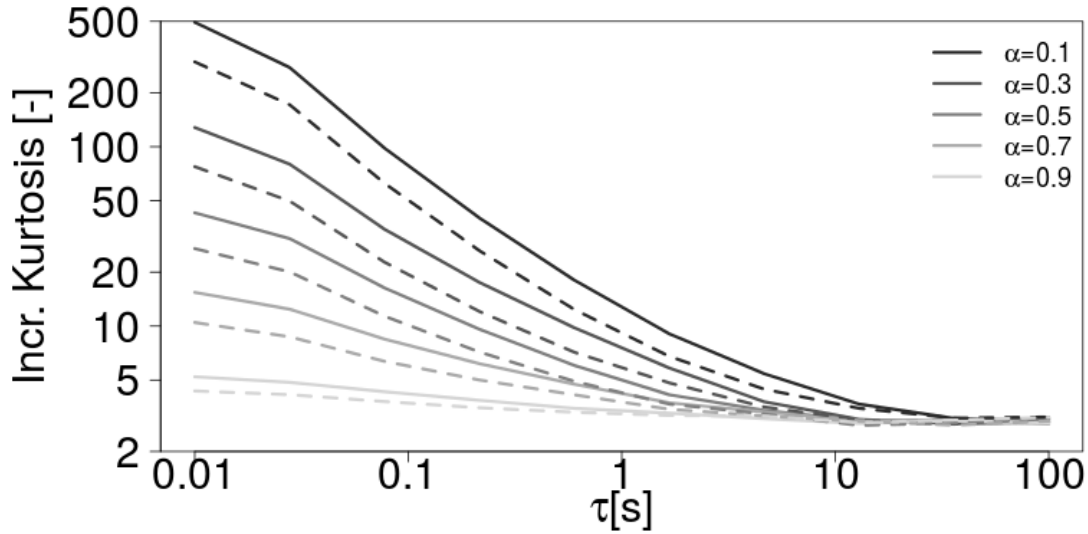


Figure 3.27: Kurtosis of a time series with an uncorrected (solid) and corrected (dashed) spectrum for $\omega_c = 1$ Hz, $\Delta s = 0.01$ s, a tempered time distribution and different values of α .

3.4.3 Correction of the One Point Statistics

According to the IEC norm [1] the velocity fluctuations are assumed to be Gaussian. To achieve Gaussian one point statistics independent of binning is a much harder task than correcting the power spectra. If the intermittency is not too strong the following approach developed by Goerg [74, 75] can be used to Gaussianize data with the condition that the original data is heavy-tailed and the distribution is smooth. However, it has to be emphasized that this correction becomes harder and harder with higher intermittency degree, because the smoothness decreases by introducing longer waiting times due to convergence issues. An R-package for this approach with different useful functionalities is also provided on CRAN [76].

As a special case of his work Goerg could show that an inverse transform exists for a random variable

$$Y = \left\{ U \exp\left(\frac{\delta}{2} U^2\right) \right\} \sigma_X + \mu_X, \quad \delta \in \mathbb{R}, \quad (3.78)$$

where δ is the tail parameter and $U = (X - \mu_X) / \sigma_X$ is a Gaussian distributed random variable with standard deviation σ_X and mean μ_X . In this case Y is a heavy-tailed Tukey's h (Lambert $W \times$ Gaussian) distributed variable [77] which reduces to the Gaussian for $\delta \rightarrow 0$. The general inverse transform has the form

$$W_\tau(Y) = W_\delta\left(\frac{Y - \mu_X}{\sigma_X}\right) \sigma_X + \mu_X = U \sigma_X + \mu_X = X \quad (3.79)$$

with

$$W_\delta(z) = \text{sgn}(z) \left(\frac{W(\delta z^2)}{\delta} \right)^{\frac{1}{2}} \quad (3.80)$$

where τ is the parameter set $(\mu_X, \sigma_X, \delta)$ and $W(z)$ is the Lambert W function which is the inverse of $z = x \exp(x)$ and satisfies $z = W(z) \exp(W(z))$. Because of bijectivity for any data $Y \in \mathbb{R}$ it is always possible to obtain the corresponding X for a given parameter set τ . Goerg presented a similar approach if a skewed heavy-tailed random variable is considered for Y which comes in handy if not only the kurtosis but also the skewness has to be corrected.

The effect of this transformation on the one-time density function is shown in Figure 3.28.

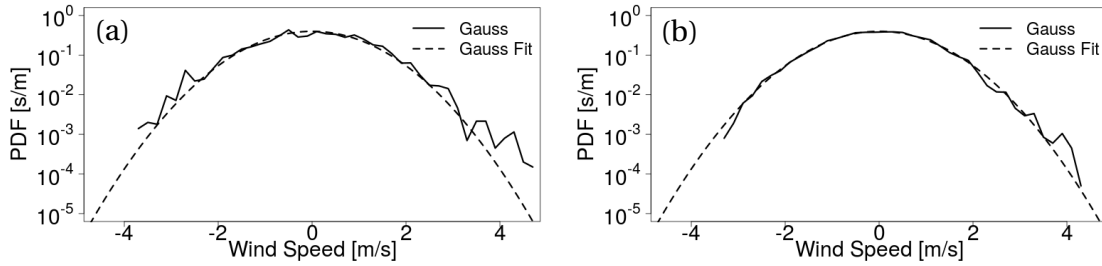


Figure 3.28: (a) Original and (b) Gaussianized density function of a CTRW time series.

Because Gaussianization changes the spectral properties of the process a spectral correction from section 3.4.2 has to follow which again introduces small deviations in the shape of the one point distribution. Therefore an algorithm has been implemented where both correction types are used in an alternating way up to the point where the desired skewness, kurtosis and spectrum are reached. In the studies, where the Lambert W approach has been used, the final kurtosis was in the range 3 ± 0.0001 and the skewness in the range 0 ± 0.0001 . However for very unsmooth distributions this algorithm is able to set the kurtosis and skewness to the desired value but the shape of the distribution might differ a lot from Gaussian.

3.4.4 Correction of Divergence

One of the most important conditions a wind field has to satisfy is the continuity equation

$$\frac{d\rho}{dt} = -\rho \nabla \cdot \vec{u}. \quad (3.81)$$

Under the assumption that the flow is incompressible, which is the case for atmospheric flows, the density ρ is constant and the continuity equation simplifies to

$$0 = \nabla \cdot \vec{u}. \quad (3.82)$$

As a natural property wind fields arising from stochastic differential equations do not exhibit incompressibility, in contrast to spectral models like the Mann model [3]. For models like the CTRW model divergence in the flow field might lead to high non-physicality and numeric instabilities induced by strong pressure fluctuations. This serious issue makes it useful to think about a divergence correction with the drawback kept in mind that some properties from the original field change.

To capture mathematically the change of divergence of vector fields the concept of

Fourier space can be used. The advantage of this approach is the simplification of differentials to products which allows to directly convert the expression of the divergence to

$$\mathcal{F} \{ \nabla \cdot \vec{u} \} (\vec{\kappa}) = i \kappa_i \hat{u}_i(\vec{\kappa}). \quad (3.83)$$

where the Einstein notation has been used. For a divergence free field this has to be zero. If the Fourier transformed velocity field $\hat{\vec{u}}$ is decomposed in components parallel and normal to $\vec{\kappa}$, i.e. $\hat{\vec{u}} = \hat{\vec{u}}^\perp + \hat{\vec{u}}^\parallel$, it becomes clear that only the parallel component $\hat{u}_i^\parallel = \kappa_i \kappa_j |\vec{\kappa}|^{-2} \hat{u}_j$ plays a role for the divergence in Equation (3.83). If it is not zero a correction of the velocity field

$$\hat{u}_i^\perp = \hat{u}_i - \frac{\kappa_i \kappa_j}{|\vec{\kappa}|^2} \hat{u}_j \quad (3.84)$$

or in vector notation

$$\hat{\vec{u}}^\perp = \hat{\vec{u}} - \frac{\vec{\kappa} \cdot \hat{\vec{u}}}{|\vec{\kappa}|^2} \vec{\kappa}. \quad (3.85)$$

has to be performed to obtain only the solenoidal normal component.

However, Equation (3.85) is only the theoretical result for continuous fields. For discretized fields as used in CFD an analogous formula for the discrete Fourier transform (DFT) has to be found. It is important what kind of discretization is used because the definition of "divergence" also depends on it. In the following for the discrete divergence operator ∇_d the central difference approach

$$\nabla_d \vec{u}(\vec{x}) = \frac{u_i(x_i + \Delta_i) - u_i(x_i - \Delta_i)}{2x_i} \quad (3.86)$$

is assumed with the spacing Δ_i in the direction of the i -component. For this case the DFT is [78]

$$\text{DFT} \{ \nabla_d \vec{u} \} (\kappa) = \vec{w}(\vec{\kappa}) \cdot \text{DFT} \{ \vec{u} \} (\vec{\kappa}) \quad (3.87)$$

where \vec{w} is the vector

$$\vec{w}(\vec{\kappa}) = \frac{i}{2} \begin{pmatrix} \frac{1}{\Delta_1} \sin \frac{\kappa_1}{N_1} \\ \frac{1}{\Delta_2} \sin \frac{\kappa_2}{N_2} \\ \frac{1}{\Delta_3} \sin \frac{\kappa_3}{N_3} \end{pmatrix}. \quad (3.88)$$

Analogous to the continuous version (3.83) the discrete Equation (3.87) has to be zero to satisfy divergence freeness for \vec{u} . This can be achieved by the transformation

$$\text{DFT} \{ \vec{u} \}^\perp (\vec{\kappa}) = \text{DFT} \{ \vec{u} \} - \frac{\vec{w}(\vec{\kappa}) \cdot \text{DFT} \{ \vec{u} \} (\vec{\kappa})}{|\vec{w}(\vec{\kappa})|^2} \vec{w}^*(\vec{\kappa}) \quad (3.89)$$

which is done in the same way as in Equation (3.85), but with the replacements $\mathcal{F} \rightarrow \text{DFT}$ and $\vec{\kappa} \rightarrow \{ \vec{w}(\vec{\kappa}), \vec{w}^*(\vec{\kappa}) \}$. Note that this equation is a corrected version of [78] where the complex conjugation of \vec{w} is missing. Even if this is the procedure relevant for the correction

of numerically generated wind fields, further analysis is preferred to be done in the more general continuous space to be more consistent and independent of the used discretization scheme.

For simplicity in the following it is assumed that the velocity components of the uncorrected fields follow the same generating procedure, i.e. the same model parameters will be used. Furthermore they are independent of each other which also implies independence of the Fourier transforms \hat{u}_i , i.e. they are also uncorrelated $\hat{R}_{ij} = \langle \hat{u}_i \hat{u}_j^* \rangle = \hat{u}'^2 \delta_{ij}$. The covariance of the corrected field in Fourier space is (without Einstein summation)

$$\begin{aligned} \hat{R}_{ij}^\perp(\vec{\kappa}) &= \langle \hat{u}_i^\perp{}^* \hat{u}_j^\perp \rangle \\ &= \left\langle \left(\hat{u}_i^* - \frac{\kappa_i \kappa_k}{\kappa^2} \hat{u}_k^* \right) \left(\hat{u}_j - \frac{\kappa_j \kappa_l}{\kappa^2} \hat{u}_l \right) \right\rangle \\ &= \hat{u}'^2 \left(\delta_{ij} - \frac{\kappa_i \kappa_j}{\kappa^2} \right) \end{aligned} \quad (3.90)$$

which follows from Equation (3.84) by multiplication with its complex conjugate.

Now it is possible to make a statement about the kinetic energy of the each Fourier mode which has to be

$$\begin{aligned} \hat{E}^\perp(\vec{\kappa}) &= \frac{1}{2} \sum_{i=1}^3 \hat{R}_{ii}^\perp(\vec{\kappa}) = \frac{1}{2} \sum_{i=1}^3 \hat{u}'(\vec{\kappa})^2 \left(1 - \frac{\kappa_i^2}{\kappa^2} \right) = \hat{u}'(\vec{\kappa})^2 \\ &= \frac{2}{3} \hat{E}(\vec{\kappa}), \end{aligned} \quad (3.91)$$

i.e. the loss due to this correction corresponds to one third of the original kinetic energy $\hat{E}^\perp(\vec{\kappa}) = 3/2 \hat{u}'(\vec{\kappa})^2$. A consequence is that also one third of the original turbulent kinetic energy $k^\perp = \sum_{\vec{\kappa}} \hat{E}^\perp(\vec{\kappa}) = 2/3 k$ is lost.

This observation is very general and more steps for the mathematical analysis of the corrected fields derived from the CTRW model can not be done due to the difficulty of finding the Fourier coefficients $\hat{R}_{ij}(\vec{\kappa}) = \mathcal{F}_{\vec{\kappa}} \{ R_{ij}(\vec{x}) \}$. If the Fourier coefficients could be found it would be easy to find \hat{R}_{ij}^\perp from Equation (3.90), and the corrected correlation by building up the Fourier series $R_{ij}^\perp = \sum_{\vec{\kappa}} \hat{R}_{ij}^\perp(\vec{\kappa}) \exp(i\vec{\kappa} \cdot \vec{r})$. With knowledge of the velocity spectrum tensor $\Phi_{ij}^\perp(\vec{\kappa}) = \sum_{\vec{\kappa}'} \delta(\vec{\kappa} - \vec{\kappa}') \hat{R}_{ij}^\perp(\vec{\kappa}')$, the one dimensional spectra $E_{ii}^\perp(\kappa_1) = 2 \iint_{-\infty}^{\infty} \Phi_{ii}^\perp(\vec{\kappa}) d\kappa_2 d\kappa_3$ could also be determined. However at this point it has to be sufficient to gain more information numerically.

For this study a 30000 m \times 64 m \times 64 m non-intermittent CTRW field with a resolution of one grid point per meter, standard deviation of 0.2 m/s, and the model parameters $\omega_c = 0.4282$ Hz and $r = 10$ m is created. Those model parameters are used to make sure that the longitudinal and transversal integral length scales are equal. The conversion to three dimensional space has been done by means of Taylor's frozen turbulence hypothesis.

To get an idea of the correction effect on a three dimensional flow Figure 3.29 illustrates the structure change of fields for the v -component, i.e. perpendicular to the mainstream direction x , before and after the correction in a 64 m \times 64 m \times 64 m section of the whole domain. A change of structures can be seen but the size is seemingly unchanged. For the mainstream component u , shown in Figure 3.30, the structures change more drastically. In particular the

variance goes down by a large amount which has already been predicted by the aforementioned Equation (3.91) which is related to the loss of energy.

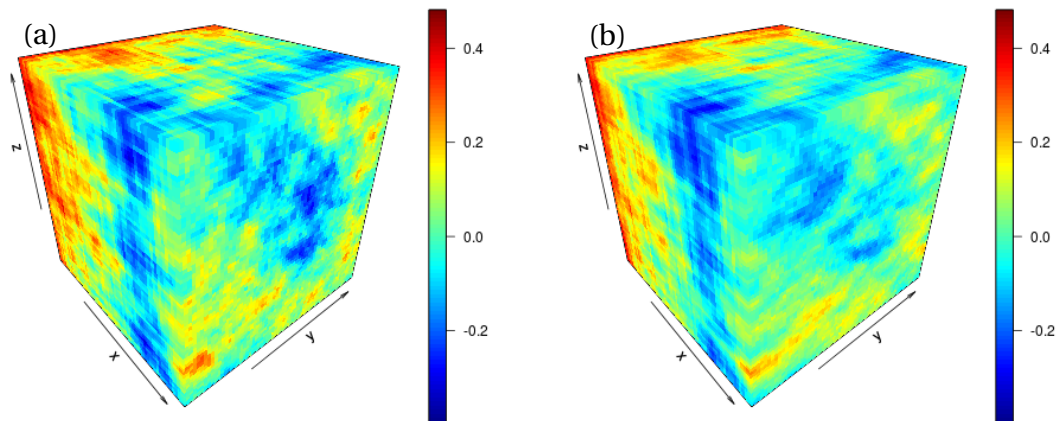


Figure 3.29: v-component of wind velocity vector (a) before and (b) after the divergence correction.

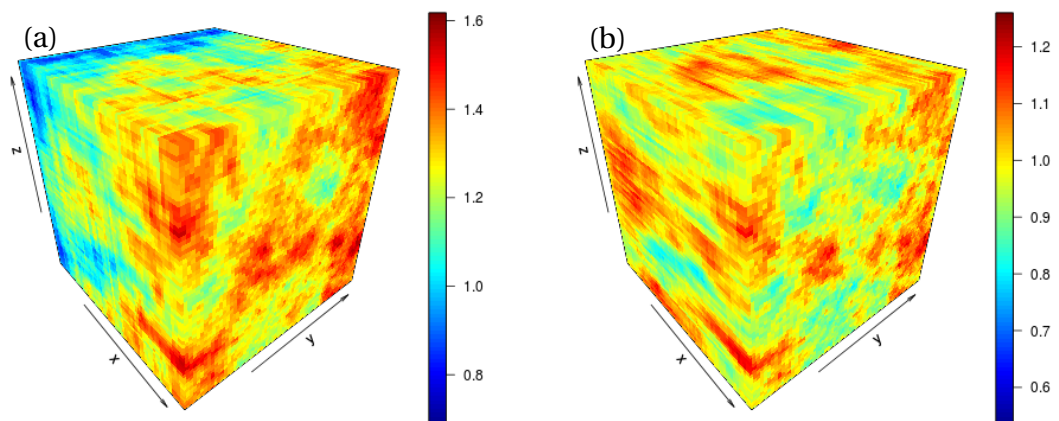


Figure 3.30: u-component of wind velocity vector (a) before and (b) after the divergence correction.

To check the domain size dependence of the theoretical result $k/k^\perp = 3/2$ the ratio k/k^\perp has been plotted for different box sizes in mainstream direction in Figure 3.31a. It is obvious that this relation holds in the mean for all box sizes. More interesting is to quantify the different contributions of velocity components to the turbulent kinetic energy with

changing box sizes. If the domain in main stream direction contains more cells than perpendicular to it, additional wavenumbers for κ_1 have to be considered in $\sum_{\vec{\kappa}} \hat{R}_{11}^{\perp}(\vec{\kappa})$ which also decreases the variance for this component. This effect becomes visible in Figure 3.31b where the ratio of variances before and after the correction $\sigma_i^{\perp 2} / \sigma_i^2$ for each component $i \in \{u, v, w\}$ is illustrated.

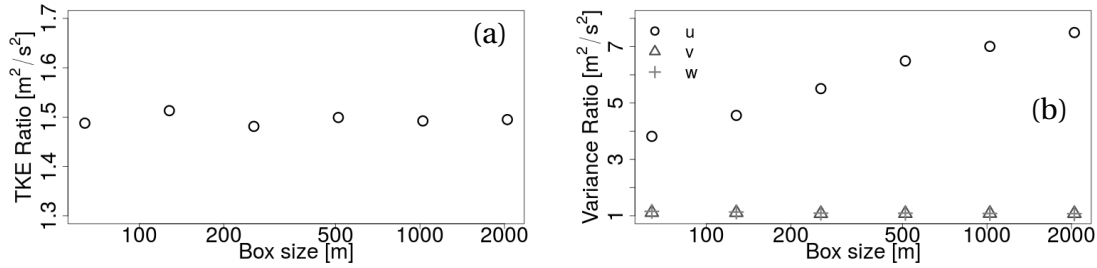


Figure 3.31: Ratio of (a) turbulent kinetic energy, and (b) variances of each velocity component changing with box size in mainstream direction.

As expected from the different treatment of mainstream and perpendicular velocity components by the correction algorithm, also the one dimensional energy spectra of the corrected fields differ a lot from each other. The comparison of original and corrected spectra for v - and u components in Figure 3.32 highlights the special role of the mainstream velocity component. A loss of energy on all but the smallest scales is visible, whereas the perpendicular v -component is almost not affected at all. Figure 3.33 shows the one-dimensional spectra for an intermittent field with the same parameters and $\alpha = 0.8$, where the correction effect is very similar. This different reaction of velocity components to the correction presented here can be seen as the main drawback of this method. In addition to that the change of energy spectra for the main stream component does not allow to create velocity fields where the energy spectrum is given by the model equations or by the spectral adjustments in the method (3.75).

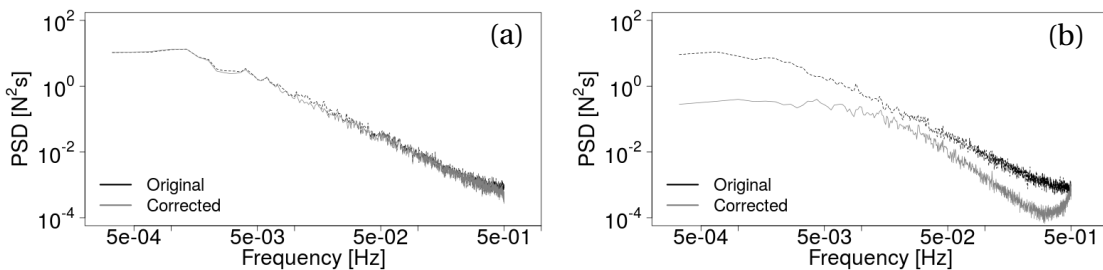


Figure 3.32: Original and divergence corrected one dimensional spectra for the (a) v -component, and (b) u -component of non-intermittent wind fields.

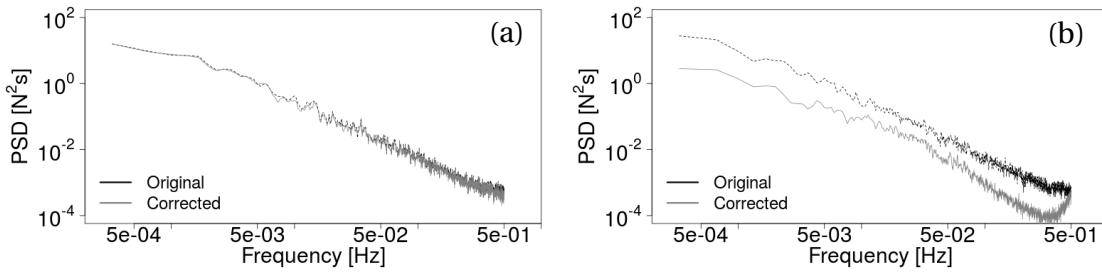


Figure 3.33: Original and divergence corrected one dimensional spectra for the (a) v -component, and (b) u -component of intermittent wind fields.

It is natural that a change of velocity fields not only has an effect on the spectrum and the variance but also entails a variation of intermittency. To gain insight into the effect on intermittency, the increment pdf of u and the corresponding kurtosis are plotted in Figure 3.34. The correction algorithm leads to a loss of intermittency in terms of increment kurtosis over all scales. This might be obvious as intermittency is understood as a complex collaboration of phase and amplitude in Fourier space which is partially destroyed by the divergence correction.

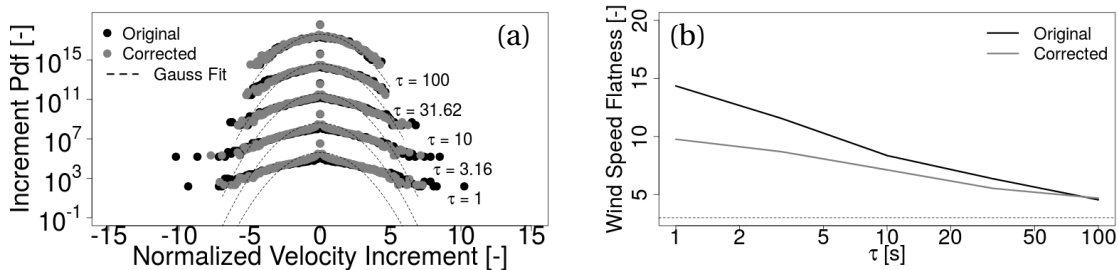


Figure 3.34: (a) Increment PDF and (b) kurtosis evolution with increasing τ before and after the divergence correction.

In conclusion, despite of the physics won by the divergence correction algorithm, some drawbacks have to be highlighted. The algorithm presented here needs a lot of computational effort in terms of memory and simulation time if fields for a time interval of ten minutes with a rather good resolution should be generated. Another important drawback is the already mentioned change of spectra for the mainstream component and the included, potentially very big, loss of energy. The last negative aspect is the loss of intermittency which might be unavoidable for correction algorithms in general and therefore can be condoned. Because of the first two issues this pre-simulation correction was not used for BEM or CFD simulations for this thesis but it is still mentioned for the case that solenoidal CTRW fields become necessary and other correction algorithms are not accessible or useful. For CFD simulations another divergence correction algorithm can be used based on pressure corrections which is introduced by Kondo et al. [79], but the resulting field also shows a strong drop in energy for the main stream component similar to the correction method presented here. As the tool of choice for all CFD simulations done in this thesis the PISO algorithm [39, 40] is applied which makes use of several pressure and velocity corrections. The outcome of the PISO algorithm is not predictable but the impact on the CTRW fields is small as will be seen.

Chapter 4

Characterisation of CTRW Fields in an Open Channel

After the CTRW fields have been characterized, fields for different use cases can be generated by choosing an appropriate parameter set. The next step is to combine the generated CTRW fields with CFD, where the main focus in this chapter lies on the evolution of the fields in a simple domain without any objects. Two different turbulence injection methods are compared with respect to stability of the introduced CTRW fields and their evolution in general. In the first approach the generated two dimensional time dependent velocity field slices from the CTRW model are directly introduced at the inlet of the domain while in the second one the fluctuating part is superimposed to a constant flow in the inner part of the domain by an actuator.

4.1 Simulation setup

Because intermittency is one of the most important characteristics of the CTRW fields, a clean study has to be performed where a superposition with other effects is kept as low as possible. Therefore shear within the CTRW field is not taken into account as well as shear introducing walls in the simulation domain, which would add turbulent kinetic energy as well as intermittency into the domain. This is clearly not wanted for a first simple study if one is interested in the free evolution of specific CTRW fields. For this reason a cuboid shaped open channel with dimensions $12\pi \text{ m} \times 2\pi \text{ m} \times 2\pi \text{ m}$ and $384 \times 64 \times 64$ cells has been chosen as the simulation domain, as seen in Figure 4.1. With this setup each cell has a dimension of approximately $\Delta x = \Delta y = \Delta z = 0.1 \text{ m}$ in each direction. An infinite height and width of the domain is simulated by using periodic boundary conditions at the corresponding boundaries. At the inlet the velocity field is given and the pressure underlies a zero-gradient condition, while as an outlet condition a constant pressure and zero-gradient velocity condition is taken. No CFD specific additional turbulence models are used because no significant effect could be observed for the performed simulations and no wall modeling is needed.

Two different kinds of CTRW fields are generated, one with Gaussian and one with heavy-tailed increment statistics. For both fields the general parameters are set to $\bar{u} = 1 \text{ m/s}$, $\sigma = 0.2 \text{ m/s}$, $r = 0.5 \text{ m}$, $\Delta t = 0.01 \text{ s}$, $t = 3000 \text{ s}$ and $\omega_c = 1.16 \text{ Hz}$ while for the intermittent case

additionally $\alpha = 0.3$ has been chosen. In Figure 4.2 the increment skewness, and increment kurtosis are shown for different time scales of the inflow. According to Taylor's frozen turbulence hypothesis, the flow passes one cell in $\Delta x / \bar{u} = 10\Delta t = 0.1$ s, which translates to the smallest spatial scale where intermittency potentially can be observed.

To avoid a contradiction between non-periodic CTRW fields and periodic boundary conditions, the covariance matrix used for the CTRW field generation is also made periodic.

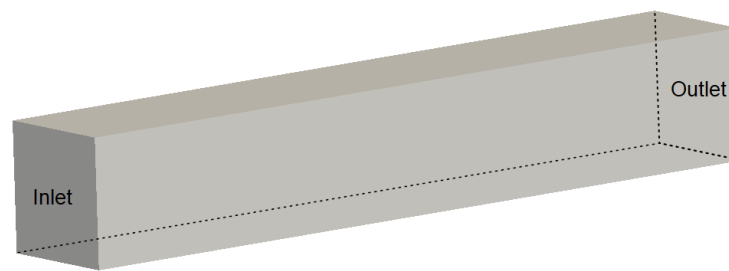


Figure 4.1: Simulation domain of the open channel with inlet and outlet. All other boundaries are periodic.

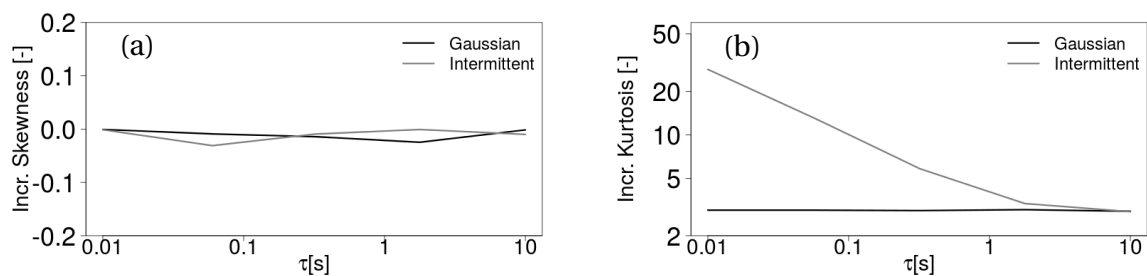


Figure 4.2: (a) Increment skewness and (b) increment kurtosis of the CTRW fields used for the channel simulation.

4.2 Turbulence injection methods

After the CTRW fields are created there exist several ways to inject those fields into the CFD domain. Two approaches are investigated in more detail, namely the inlet and the actuator method which both have their advantages and disadvantages.

4.2.1 Direct injection at inlet boundary

The most simple way which comes into mind is to impose the field directly at the inlet boundary of the domain via setting the velocity field at each boundary face. For this purpose the "timeVaryingMappedFixedValue" boundary condition is used which is provided by OpenFOAM. The pressure is automatically adjusted due to the zero-gradient boundary condition. Depending on the target resolution and the inlet boundary size, an appropriate number of cells is needed, which have to be simulated with the CTRW generator. Due to the quadratic growth of entries in the correlation matrix with the number of boundary faces and the cubic dependence of the number of arithmetic operations for the Cholesky decomposition, special care has to be put on a reasonable number of cells needed for the inflow field without unnecessary high computational effort. Figure 4.3 shows the velocity field gained by using the injection method presented here. A decay of turbulence starting at the inlet becomes obvious and the fluctuations become very small close to the outlet of the domain. In comparison with the region close to the inlet small structures are not that dominant anymore but the mean wind speed is still conserved.

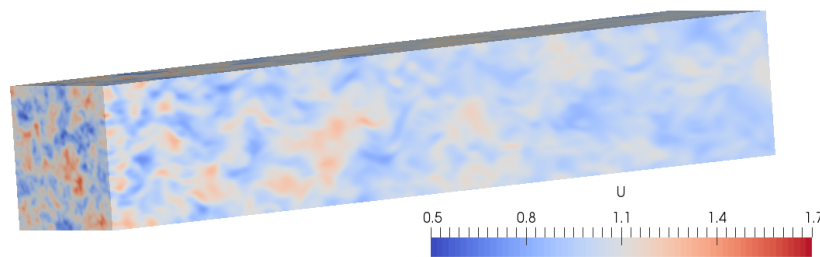


Figure 4.3: Velocity field in the open channel gained by injecting the CTRW field at the inlet of the domain.

Several properties are investigated across the channel for Gaussian as well as intermittent CTRW fields. First the mean and the standard deviation (SD) are looked at in Figures 4.4a and 4.4b. The mean behaves constant throughout the whole channel which is also expected because of the incompressibility of the flow and the absence of walls and other objects within the domain which would lead to shear effects. In contrast to that the standard deviation shows a different behavior. It is introduced at the inlet of the domain and decays due to the conversion of turbulent kinetic to thermal energy by dissipation according to the power law $A(x - x_0)^{-n}$ with $n = 0.55$ and $n = 0.69$, for the Gaussian and intermittent simulation case respectively. Those exponents fit well to the experimental values between 0.57 and 0.73 for decaying grid turbulence reported in the literature [20, 80].

As a measure of temporal similarity of the field in the domain and the original field generated by the CTRW model, the cross correlation of both fields is analysed. In particular the maximum value of the cross correlation is of main interest here, which characterizes the similarity with the original field at the time, where the field actually reaches the measurement point. In Figure 4.4c the evolution of the maximal cross correlation is depicted together with a power law fit similar to the standard deviation fit. The intermittent and Gaussian fields show up a similar cross correlation decay along the channel which occurs due to the decay of turbulence and general structure changes in the flow. The decaying exponents are much

higher than for the standard deviation with $n = 1.81$ and $n = 1.43$ for Gaussian and intermittent fields.

The spectra for the Gaussian fields at different distances up to 30 m from the inlet are presented in Figure 4.4d together with the model spectrum of the original CTRW field before injection and the Kolmogorov -5/3 law. First a general decay across the channel on all scales can be observed. For small distances from the inlet the turbulent kinetic energy in large flow structures is maintained while a decay becomes visible for higher frequencies, i.e. smaller structures. That means that the loss of variance from Figure 4.4b for small distances mainly happens due to dissipation on small scales. On those scales local isotropy is reached which is indicated by the -5/3-law, i.e. the inertial subrange. For larger distances also the large scales start to decay and the inertial subrange extends. This means that the flow becomes even more isotropic, which is expected in natural decay processes. The spectra for the intermittent wind field show a similar behavior and are therefore not presented here.

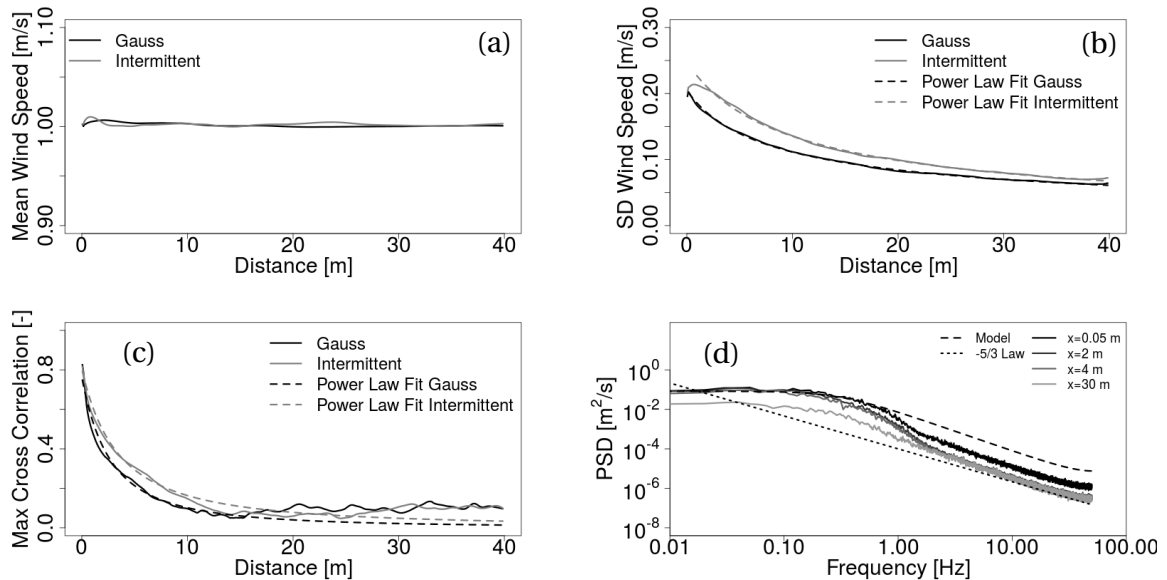


Figure 4.4: Evolution of (a) mean, (b) standard deviation, (c) maximal cross correlation with the original CTRW field, and (d) spectra for the flow field downstream of the inlet.

Even though small differences in the evolution of the previously mentioned properties are apparent, it is justified to assume that intermittency as an outcome of the CTRW model has no significant impact, as long as the original Gaussian and intermittent field are comparable in terms of one time statistics and two time correlations which are directly transferred into the domain. The deviations occurring here are due to differences in the realizations of the field, but those are expected to vanish if a significant amount of simulation cases are ensemble averaged. However due to the high computational effort of each simulation such an averaging is not an option in this work. To the authors best knowledge no similar studies have been performed in such a setup and theoretical laws of decay are not known, especially because the decay depends mainly on the imposed turbulence, which is not divergence free by default, and therefore does not necessarily underly the rules for decaying divergence free and isotropic turbulence.

Focus on the increment statistics is put in Figures 4.5a and 4.5b, which show how the increment skewness and increment kurtosis evolve at the centerline of the channel for both field types. As desired, the inlet increment skewness and kurtosis of the Gaussian fields are unchanged throughout the whole domain and no intermittency builds up. The intermittent inflow fields are a bit more unstable in terms of skewness and kurtosis but more or less those characteristics are transferred throughout the domain. In contrast to the increment skewness the increment kurtosis shows up a significant initial jump, which might occur due to the not fully evolved flow field and some instabilities close to the boundary. Despite of this anomaly no drastic change can be observed for the distances studied here.

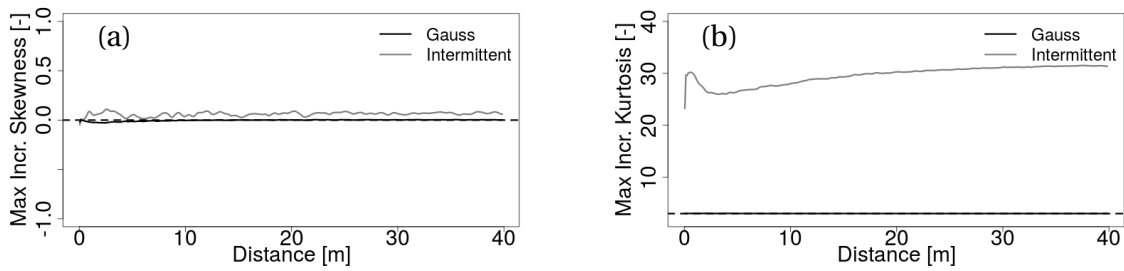


Figure 4.5: Evolution of the maximum of (a) increment skewness, and (b) increment kurtosis in the range of τ between 0.01 s and 10 s for the flow field downstream of the actuator.

Even though the increment properties are well transported through the domain, injecting velocity fields at the inlet of the domain has a big drawback, namely the high resolution which has to be kept from the inlet until the object of interest within the domain. This can result in a fairly high computational effort in some simulation cases. However if the grid around the simulation object is resolved on a very high degree, the additional cells due to this injection method might be negligible.

4.2.2 Injection via actuator

An alternative to the inlet method is an approach based on forces acting on the flow on a slice perpendicular to the main stream direction. This slice is generally positioned behind the inlet and induces a change in velocity u' for each cell separately by means of pressure jumps Δp . The concept of the actuator method is well described in the work of Gilling et al. [81] and illustrated in Figure 4.6. To achieve the desired velocity change the Bernoulli equation is used to calculate the necessary pressure jump. The equations for the pressure jump and the corresponding three dimensional forces

$$\begin{aligned}\Delta p &= \frac{1}{2}\rho \left((U_\infty + u')^2 - U_\infty^2 \right) \\ &= \rho \left(U_\infty + \frac{1}{2}u' \right) u'\end{aligned}\quad (4.1)$$

$$\vec{F} = \rho A_c \left(U_{\infty,\perp} + \frac{1}{2}u'_\perp \right) \vec{u}' \quad (4.2)$$

$$(4.3)$$

hold, where the density ρ , the mean velocity U_∞ , the velocity components perpendicular to the mean flow $U_{\infty,\perp}$ and u'_\perp , and the area of the actuator crossed by the corresponding cell A_c have been used.

Because turbulence does not have to be resolved from the inlet until close to the simulation object of interest, a fine mesh in between can be avoided by this method. However it should be taken care of the distance between simulation object and actuator, which should not be too small in order to avoid disturbances. The actuator method finds use in simulations where otherwise large meshes are needed and where turbulent structures are mainly important close to the object like airfoils and other objects with a dense mesh in front of the simulation object.

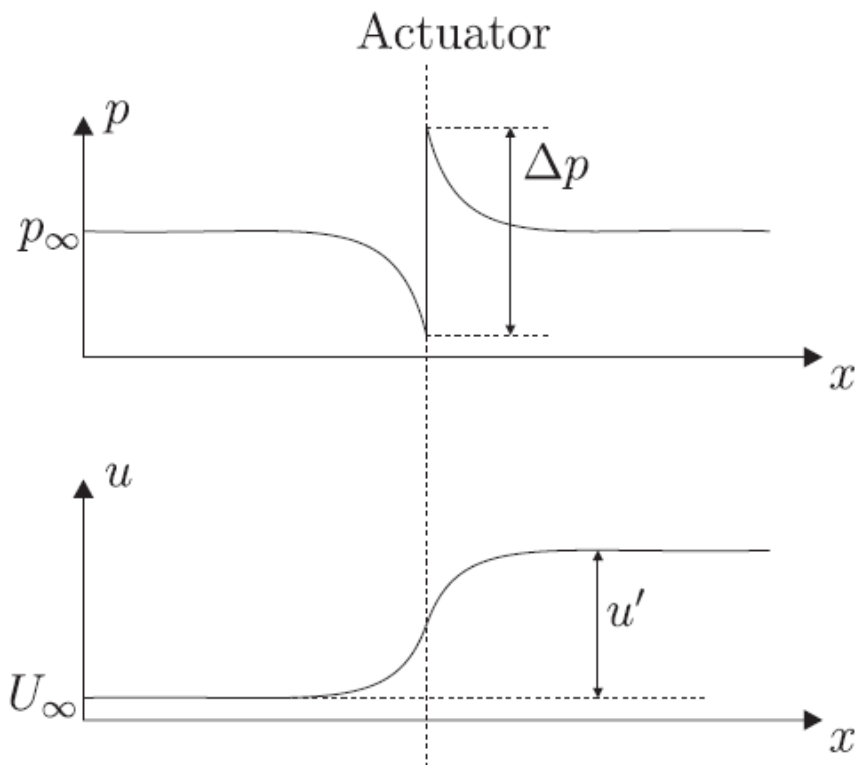


Figure 4.6: Working principle of an actuator (Picture from Gilling et al.[81]).

Figure 4.7 shows the velocity field in the channel domain, where a constant velocity, usually the target mean velocity, is injected at the inlet and the fluctuations from the CTRW generator are superimposed 4 m downstream of the inlet by an actuator. It can be observed that the structures are a bit larger compared to injecting the CTRW fields at the inlet, shown in Figure 4.3, even though the original CTRW fields are the same.

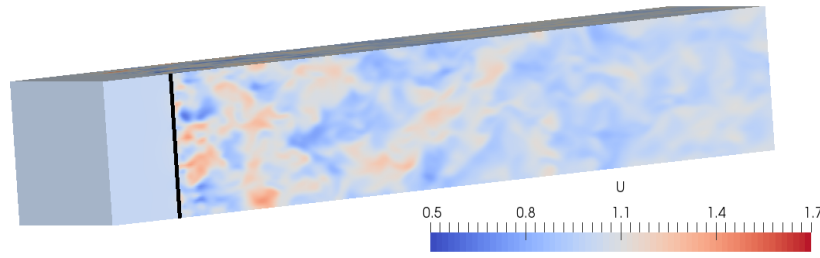


Figure 4.7: Velocity field in the open channel gained by superimposing the CTRW field onto the mean field by an actuator (black line) in the middle of the domain.

Again, the wind field is studied in Figure 4.8 with respect to its basic properties, namely mean, standard deviation, maximal cross correlations with the original CTRW field and power spectra.

The mean value again starts almost at the same value for intermittent and Gaussian fields at the actuator position as it also was the case for the inlet injection method. Again it does not change much throughout the domain and the differences can be explained by variations in the realizations used here.

The standard deviation and the maximal cross correlation in Figures 4.8b and 4.8c show a monotonous decay which can be explained in a similar way as for the properties observed by injecting the fields at the inlet boundary. But in contrast to that a ramp up before the decay can be noticed where the actual turbulence is created by the local forces at the actuator position. Because the forces introduced here lead to a smooth transition between stationary and fluctuating flow fields no sudden jump can occur. As for the turbulence injection at the inlet boundary the standard deviation can be fitted by a power law curve, but with slightly higher decay exponents $n = 0.77$ and 0.73 for the Gaussian and intermittent cases. The maximal cross correlation can be fitted by decay exponents $n = 1.81$ and $n = 1.83$. In comparison with the first injection method, the actuator leads to a significant slightly lesser standard deviation as well as cross correlation close to the actuator. However far behind the actuator those differences almost compensate and only a small difference can be noticed. It should also be noticed that an increased standard deviation and cross correlation can be observed upstream of the actuator. While the standard deviation is relatively small, the cross correlation is pretty high with a value of 0.25 at the inlet position which shows that the actuator has a high influence on the flow in front of it.

The spectra show a different behavior than for the injection at the inlet boundary. Closely behind the actuator, in the ramp up region, the whole spectrum lies below the original one. At around 4.4 m behind the inlet, i.e. 0.4 m behind the actuator, the spectrum reaches its maximum, i.e. the energy is also maximal. Further downstream it decays again, but the large scales are not affected by this decay. However compared to the inlet injection method, this decay is very fast and the small scale fluctuations are almost not present anymore at large distances. This also explains the bigger structures observed in Figure 4.7 and the slightly lesser standard deviation than for the inlet injection method. In addition to it, low energy sinc-like mesh effects become visible at high frequencies, because the energy in the turbulence is too small to hide them. An important observation can be made if the comparison with the Kolmogorov $-5/3$ -law is made. In essence, the inertial subrange is not present at all, but a region with a much steeper slope, especially for large distances from the

actuator. In other words homogenous isotropic turbulence is not achieved throughout the whole channel, which also disqualifies this method, at least for this setup, if one is interested in the evolution of such well known flow fields.

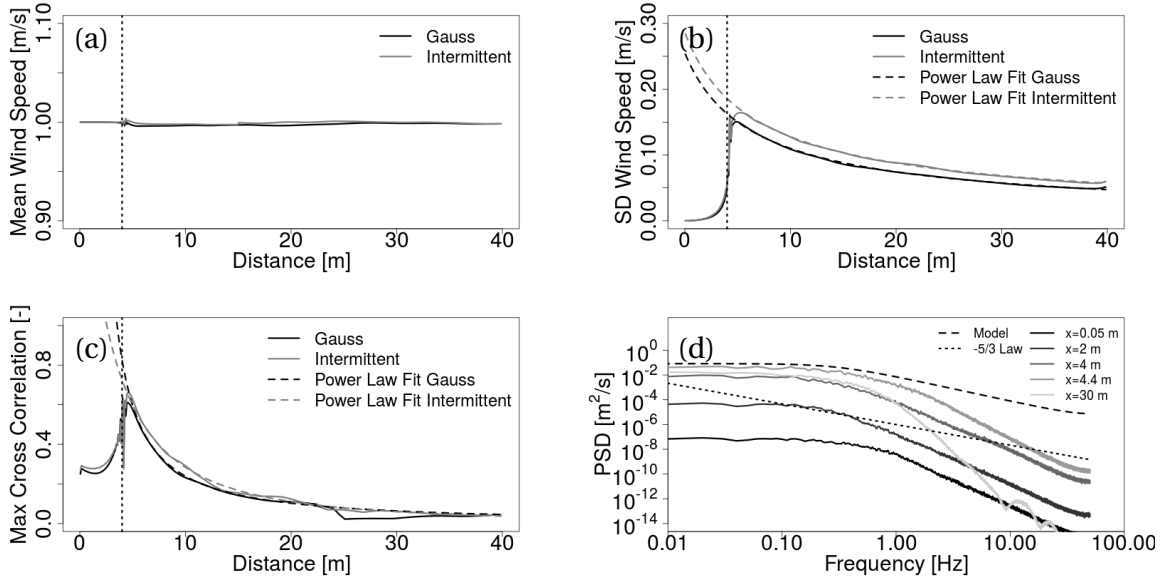


Figure 4.8: Evolution of (a) mean, (b) standard deviation, (c) maximal cross correlation with the original CTRW field, and (d) spectra for the flow field downstream of the inlet. The vertical dashed lines mark the position of the actuator.

The increment skewness and kurtosis behave quite different to the previous injection method. The increment skewness is far away from being constant and reaches pretty large negative values of -0.7 behind the actuator. This skewness change can be observed not only for the intermittent case but also for the Gaussian case, which both should have a zero skewness according to the CTRW model. This increase of skewness is a good indicator for a change of the type of turbulence, i.e. the CTRW fluctuations might change to a new type of turbulence with different properties. A negative skewness is also predicted for homogenous locally isotropic fields according to Kolmogorov's theory, but because no inertial subrange is achieved in the spectra, this conclusion has to be dropped.

The increment kurtosis for Gaussian and intermittent fields both increase behind the actuator and satisfy to a relatively small level around 3.9 and 4.3. The strong intermittency of the original field is visible only in a very small spatial range behind the actuator where a peak occurs at 4.4 m. A very steep decay follows. It can be concluded that it becomes impossible to keep the high increment kurtosis of the original CTRW field in the domain without an alteration of the actuator method presented here. Interestingly the introduced increment kurtosis can also be observed upstream of the actuator which may come hand in hand with the increased cross correlation in Figure 4.8c. This indicates that the fluctuations upstream of the actuator are very similar to the original CTRW fields.

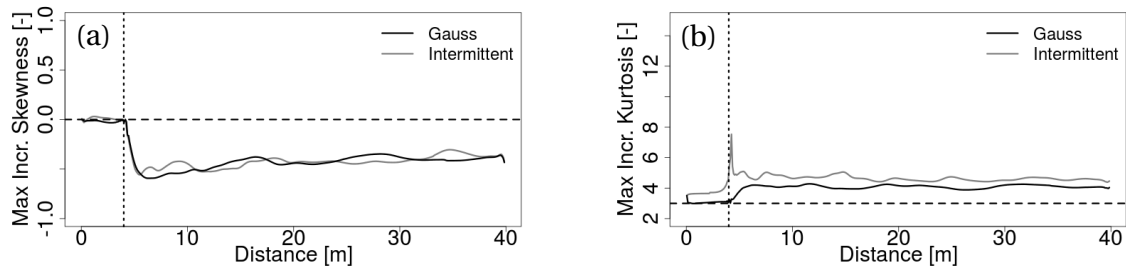


Figure 4.9: Evolution of the maximum of (a) increment skewness, and (b) increment kurtosis in the range of τ between 0.01 s and 10 s for the flow field downstream of the actuator. The vertical dashed lines mark the position of the actuator.

4.3 The Evolution Towards Isotropy

Another interesting property can be studied by investigating the evolution of the wind field along the channel without energy production, i.e. without shear. Particularly in this section the isotropy is in the focus. The isotropic state, i.e. $\langle u_x^2 \rangle = \langle u_y^2 \rangle = \langle u_z^2 \rangle$, is the result of all natural decaying processes as Kolmogorov already predicted. The most straight forward way to describe the isotropy evolution is found by investigating the space dependence of the normalized anisotropy tensor $b_{ij} = \langle u_i u_j \rangle / \langle u_k u_k \rangle - \delta_{ij}/3$, where the Einstein notation has been used. But a much more enlightening, coordinate independent, representation can be found by using the two invariants of b_{ij} , namely η and ξ which are defined as

$$\eta^2 = b_{ii}^2 = \frac{1}{3} (\lambda_1^2 + \lambda_1 \lambda_2 + \lambda_2^2) \quad (4.4)$$

$$\xi^3 = b_{ii}^3 = -\frac{1}{2} \lambda_1 \lambda_2 (\lambda_1 + \lambda_2) \quad (4.5)$$

and which build up the so called Lumley triangle, as shown in Figure 4.10. In this context λ_i are the eigenvalues of \mathbf{b} .

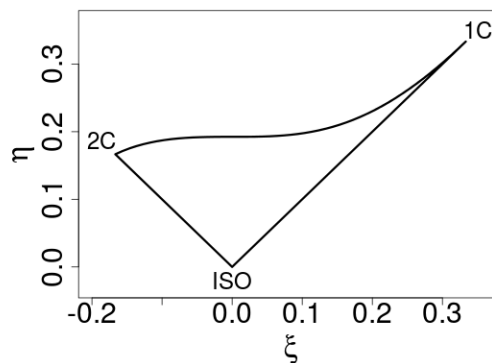


Figure 4.10: Lumley triangle.

This triangle illustrates the different states a system can have, i.e. where the eigenvalues of the Reynolds stresses are non-negative and real. The corners of the triangle are

defined by $\xi = -\frac{1}{6}$ and $\eta = \frac{1}{6}$ for two-component axisymmetric turbulence (one zero eigenvalue of the Reynolds stress tensor), $\xi = \frac{1}{3}$ and $\eta = \frac{1}{3}$ for one-component turbulence (two zero eigenvalues of the Reynolds stress tensor) and the isotropic state at the origin $\eta = \xi = 0$. At some point every decaying process without shear will converge to the isotropic state. The straight borders of the triangle, where $\eta = \xi$ or $\eta = -\xi$ holds, correspond to axisymmetric flows with one large or one small eigenvalue.

In general there are infinite possibilities to reach isotropy and there are also many different models. Those models are based on the evolution equation for the anisotropy tensor

$$\frac{k}{\varepsilon} \frac{db_{ij}}{dt} = \left(1 + \frac{1}{2}f_1\right) b_{ij} + \frac{1}{2}f_2 \left(b_{ij}^2 - \frac{1}{3}b_{kk}^2 \delta_{ij}\right) \quad (4.6)$$

where the functions $f_1(\xi, \eta, \text{Re})$ and $f_2(\xi, \eta, \text{Re})$ are model specific. For the Rotta model with a linear evolution to the origin of the $\xi - \eta$ diagram the functions are constant, namely $f_1 = -2C_R$ with $C_R > 1$ and $f_2 = 0$. However this linear behavior is unphysical and a much better description is given by the model of Sarkar and Speziale [82] who used $f_1 = -3.4$ and $f_2 = 4.2$. Even if existing models seemingly give mathematically correct results for the evolution of isotropy, real world experiments and DNS simulations can differ a lot from those models because important characteristics, e.g. spectra, which are not described by the Reynolds stresses are omitted in Equation 4.6. Additionally experiments which give insight of the inner part of the Lumley triangle are not known which makes it difficult to find parameters which describe well the decaying process.

In the scope of this work a Gaussian CTRW flow in a high resolution channel with a size of $12\pi \text{ m} \times 2\pi \text{ m} \times 2\pi \text{ m}$ and a resolution of $800 \times 128 \times 128$ cells has been studied along the centerline, where no shear has been taken into account. Figure 4.11 shows the zoomed in right part of the Lumley triangle and three different trajectories: the simulation, the model of Sarkar and Speziale, and a fit to the simulation data by means of Equation 4.6. To ensure comparability, the initial conditions of the models are adjusted to the initial conditions of the simulation. The red arrow points into the direction of the evolution of the graph as the flow moves across the channel. At first glance, the differences of the simulation and the model of Sarkar and Speziale are quite big, but the curves are bended into the same direction and the axisymmetric state $\eta = \xi$ is preferred by both flows. The big differences can be explained by the aforementioned spectral (and higher order) freedom which leads to non-unique trajectories in this plot. However the simulated flow can still be described by the model Equation 4.6, where the model parameters have been chosen as $f_1 = -4$ and $f_2 = 30$. Low Reynolds number DNS simulations by Kim et al [83] show a similar behaviour as in the simulation performed here, but small deviations occur due to a fully developed channel flow in the first case and the difference in the data extraction method, where the data is achieved not along the centerline of the channel but from different points across the channel with varying y^+ . It should be emphasized that the most axisymmetric state in the fully developed channel flow is obtained at the centerline of the channel, which is seemingly close to the results at the end of the channel of the CTRW simulation.

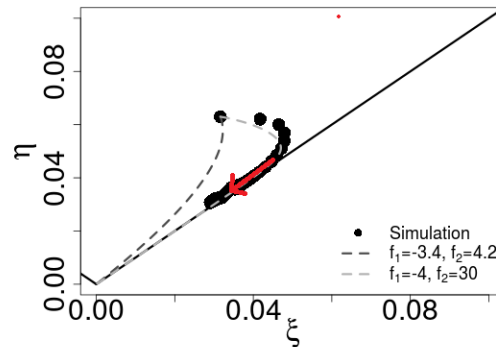


Figure 4.11: Evolution of the simulated channel flow in the Lumley triangle, the model by Sarkar and Speziale ($f_1 = -3.4, f_2 = 4.2$) and a best fit to the simulation data ($f_1 = -4, f_2 = 30$). The red arrow points into the direction of the evolution of the graph as the flow moves across the channel.

4.4 Effect of Non-Turbulent Boundary

CFD simulations with turbulent inflow are in general very expensive. The first reason for the high expense is the demand on a high resolution of the CFD domain between the position of turbulence generation and the actual simulation object. This is due to the needed ability to sustain the small scales of turbulence up to the important objects. Second, the inflow generation procedure can be very time and resource consuming, especially if the inflow patch is very big, in terms of the number of cells, and the needed time interval very long. Field generations by spectral models are based on computational expensive inverse Fourier transforms which can be made much more effective by a reduction of the space dimensions or the number of time instants needed. For the CTRW field the number of time instants is not a big problem because there is just a linear relation between time steps and the number of computational operations. The main computational effort is put into the correlation structure which is realized by the Cholesky decomposition. This decomposition demands for a number of operations proportional to n^3 , where n is the number of grid points on the inflow patch. If a quadratic inflow patch is assumed and the size or the resolution is doubled in each direction this ends in a multiplication with a factor of $4^3 = 64$. This is the reason why the size of the inflow patch could be reduced for a much faster computation. Although seemingly a smaller inlet patch gives a big advantage in terms of computational resources needed, the field characteristics will evolve differently to a fully turbulent inlet patch. The smaller the inlet patch, the bigger the differences.

In the following different properties of the flow are analysed along the centerline of the channel for three inflow patches with different sizes where Gaussian and intermittent turbulence is injected. Those inflow patches are circularly shaped and located in the center of the inlet, which is exemplary shown in Figure 4.12.



Figure 4.12: Shape of the domain with the turbulent inlet patch in red.

The large inflow patch (I1) has a radius of 3 m, so it almost extends to the boundaries of the channel, and the other patches are smaller with a radius of 2 m (I2), 1 m (I3) and 0.5 m (I4). Figure 4.13 illustrates these flows at a slice through the center of the domain from the side. It is characterized by a mean velocity of $\bar{u} = 1$ m/s, a standard deviation of $\sigma = 0.2$ m/s, a well described PSD with $\omega_c = 1$ s⁻¹, a correlation length of $r = 0.5$ m and a Gaussian or intermittent increment distribution, where for the intermittent case $\alpha = 0.6$ and $C = 35$ s. For both inflow field types the increment distribution and the increment kurtosis (before injection into the domain) are plotted in Figure 4.14 where both fields are clearly distinguishable.

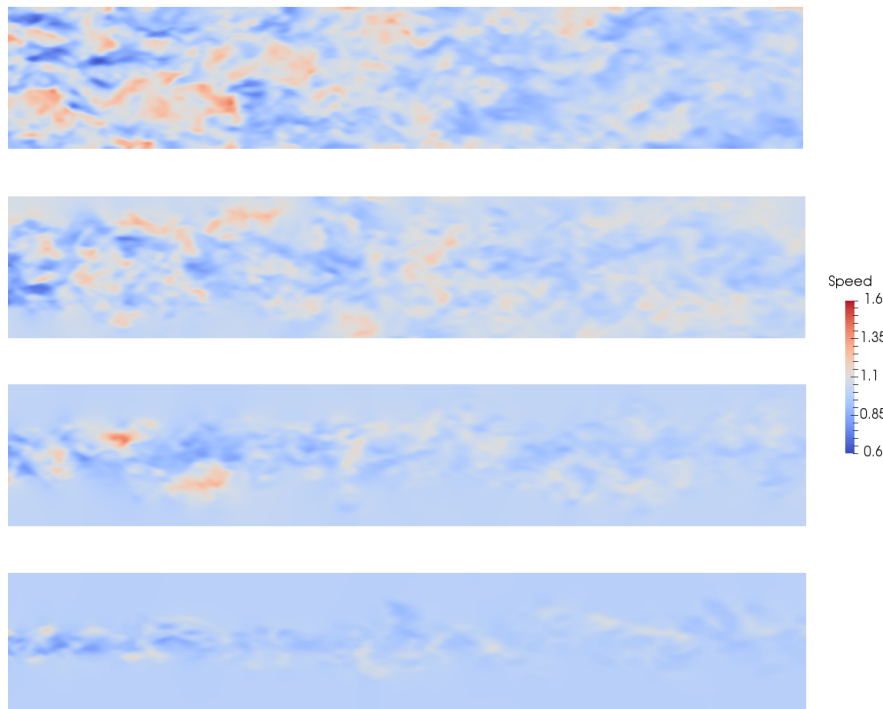


Figure 4.13: Snapshots of simulations with turbulent inlet areas with radius 0.5, 1, 2, and 3 m (from top to bottom).

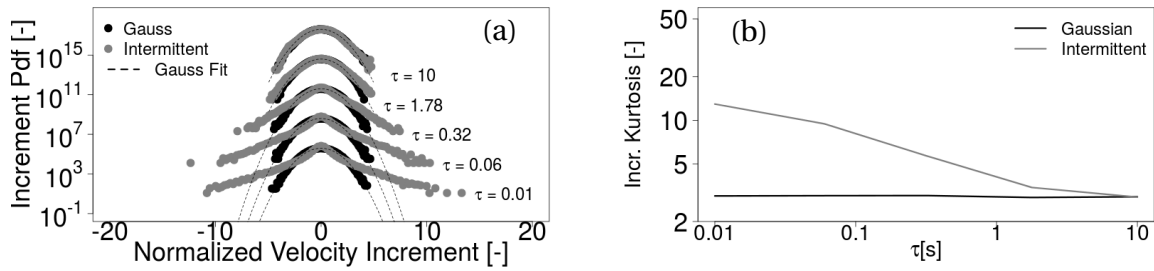


Figure 4.14: (a) Distribution of normalized velocity increments for different time delays, and (b) increment kurtosis dependent on the time delay τ before injection into the domain.

The part of the inflow boundary which is not turbulent contributes a uniform inflow with a constant velocity of 1 m/s such that no mean shear can lead to an energy production. As a consequence a decay of turbulence is expected. The properties looked at are in particular the mean velocity, standard deviation, PSD, the kurtosis and skewness of the increment distribution, as well as the maximal cross correlation with the inflow.

First the one time characteristics are studied in Figure 4.15, i.e. mean and standard deviation. Due to no significant differences for the Gaussian and intermittent cases, only the Gaussian case is shown here.

At first glance, it can be seen that the mean velocity in Figure 4.15a is not constant through the whole domain, but it changes more and more with decreasing turbulent inlet size. The most interesting case is the case with the smallest inlet size, because the change in the mean velocity is strongest in this case. In the first 3 meters the velocity is constantly dropping before it increases again. This behavior can be explained by taking into account the mixing with the surrounding constant flow.

In contrast to the mean, the standard deviation of all cases is monotonously dropping with increasing distance from the inlet, which is depicted in Figure 4.15b. This is clear because no turbulent energy is injected by shear or other effects and the flow loses turbulent kinetic energy due to dissipation. In addition to that differences between the different inlet sizes can be observed. The smallest inlet also leads to the fastest energy dissipation because the surrounding not turbulent flow is mixed with the turbulent flow and the resulting flow at the centerline has to be less turbulent than without this mixing. Vice versa the surrounding flow undergoes a transition from non-turbulent to turbulent behavior. However because only measurements at the centerline are done, this effect is not studied in more detail.

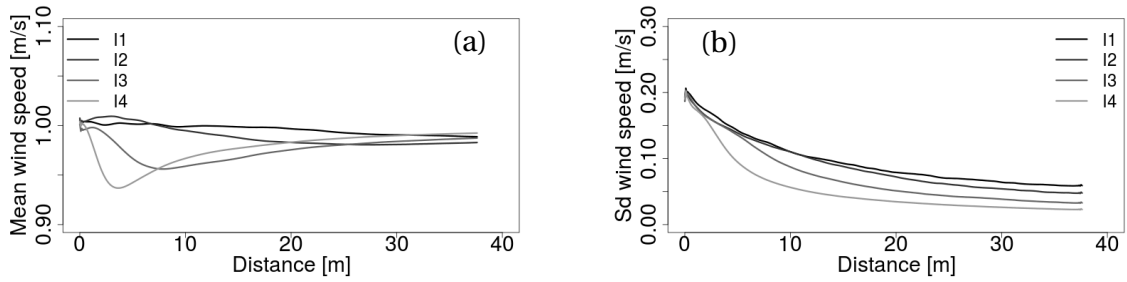


Figure 4.15: Evolution of (a) mean, and (b) standard deviation for all four turbulent inlet sizes.

Another perspective can be gained by performing the Fourier transform on the original time series. The achieved compensated PSD's $E(\omega)\omega^{5/3}$ for all four inlet types are shown in Figure 4.16 at different positions of the centerline. Because there is no significant difference for Gaussian and intermittent inflow, only the spectra for the Gaussian case are shown.

In the region close to the inlet the energy content for all patch sizes is equivalent, because the injected fields are the same and mixing with the steady flow does not play a role yet. But further downstream, a $5/3$ region appears and the total energy content decreases with smaller inlet patches as already seen for the Reynolds stresses. This energy loss happens on all scales but it is biggest on the smallest scales, i.e. high frequencies. An additional effect is seen if the inertial subrange, i.e. the flat part of the spectra, is looked at at the different positions. This subrange becomes larger and larger for all inlet sizes while the flow propagates downstream. Furthermore the energy content in this subrange is also stable as soon it is reached.

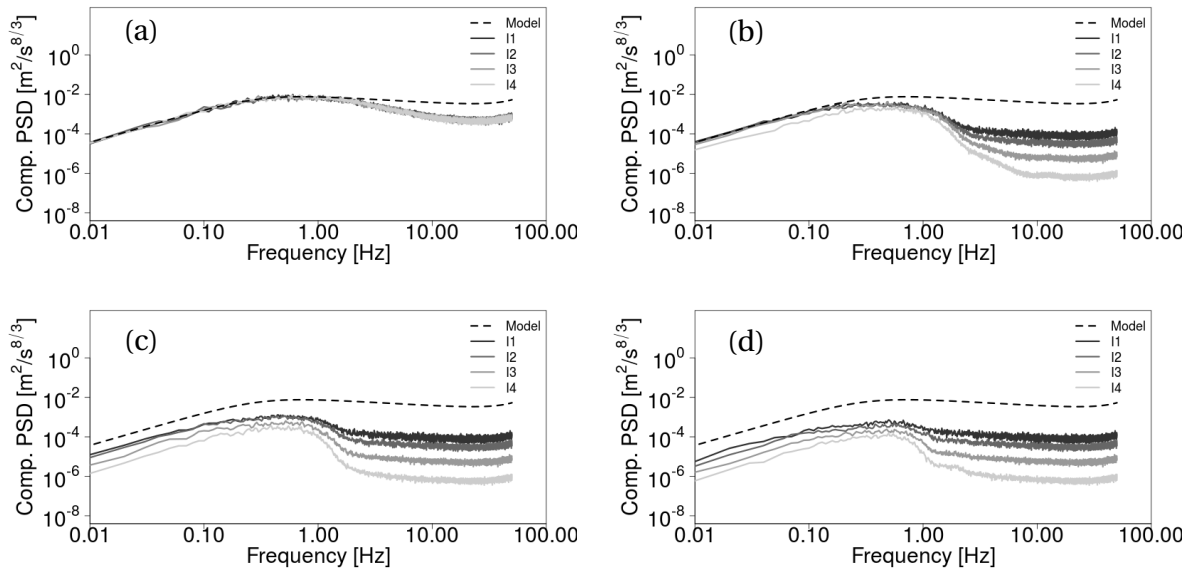


Figure 4.16: PSD of velocity for all four turbulent inlet sizes at (a) first cell, (b) 5 m, (c) 20 m, and (d) 40 m downstream of the inlet.

Next, the evolution of the third and fourth moments of increment distributions is discussed. The increment kurtosis at several positions behind the inlet on different time scales

τ are illustrated in Figures 4.17 and 4.18 for Gaussian and non-Gaussian inflows. The original field with a Gaussian increment distribution has a zero skewness and a kurtosis of three which is also seen close to the inlet. For increasing distances a bump appears which reaches its maximum magnitude between 50ms and 100ms for the distances analysed here. Especially the smallest inlet dominates here and shows up highest increment kurtosis throughout the whole time scale range even though close to the inlet all inlet show the same Gaussian behavior. Even at the end of the channel no relaxation to the Gaussian state can be seen for any of the inlets but the case with the largest inlet is very close to it. So here is clearly visible that the flow builds up intermittent structures and it's own turbulence just by propagating through the channel. The structures become most dominant for the cases where a strong mixing with the surrounding flow is present, i.e. for the small turbulent inlets.

For the non-Gaussian inflow simulations the small turbulent inlet simulation shows a slower decay and even an increase in the increment kurtosis of larger time scales close to the inlet. However with increasing distance from the inlet the larger inlet cases contain the highest increment kurtosis and it reaches the outlet without big differences to the inflow.

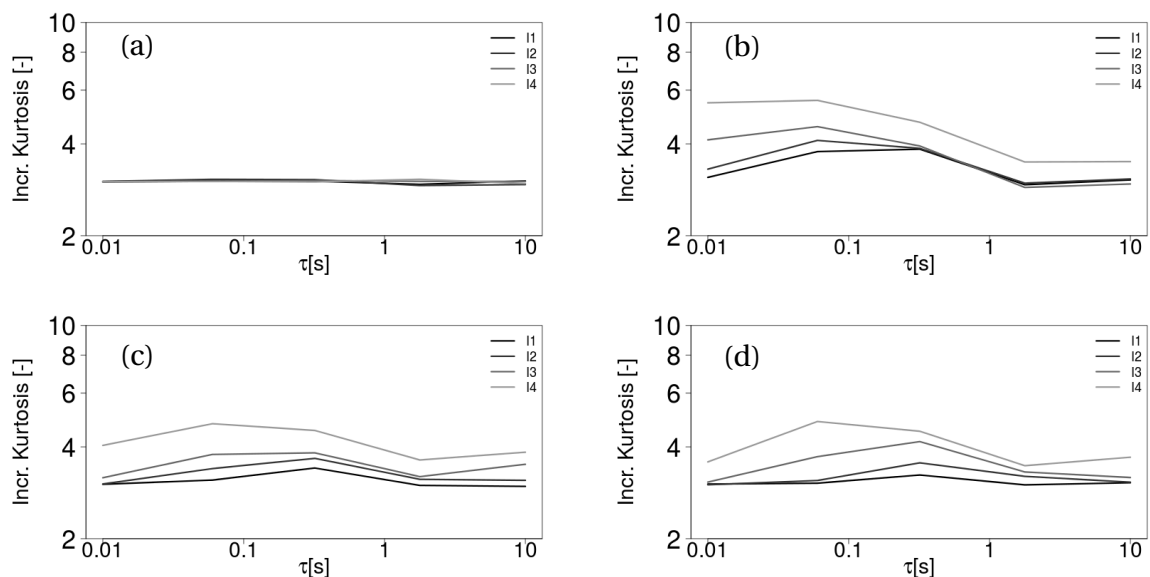


Figure 4.17: Increment kurtosis of velocity for all four turbulent inlet sizes with Gaussian inflow at (a) first cell, (b) 5 m, (c) 20 m, and (d) 40 m downstream of the inlet.

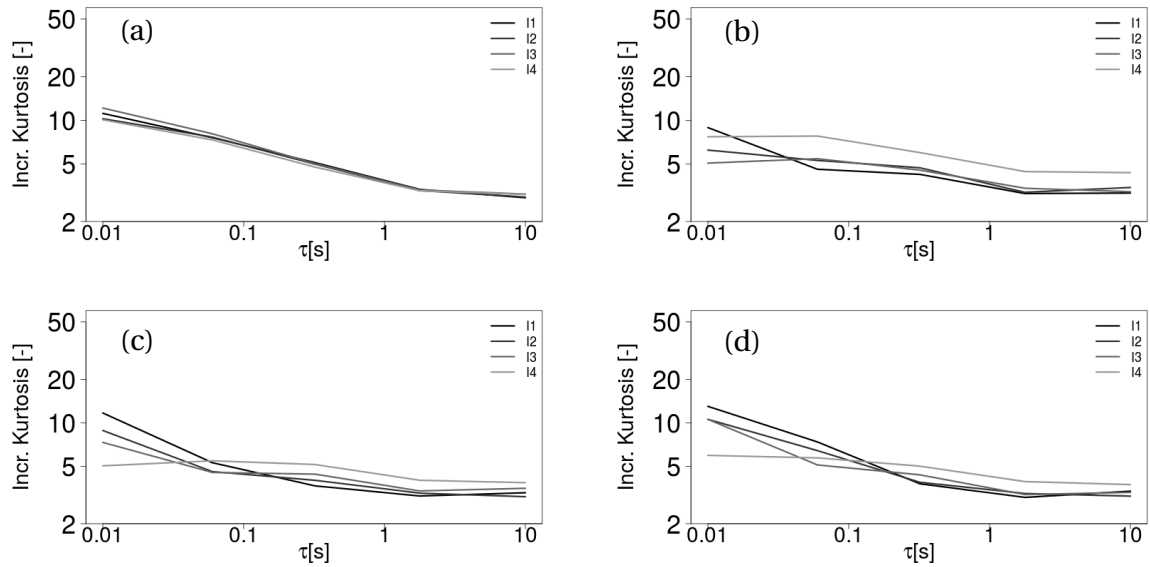


Figure 4.18: Increment kurtosis of velocity for all four turbulent inlet sizes with non-Gaussian inflow at (a) first cell, (b) 5 m, (c) 20 m, and (d) 40 m downstream of the inlet.

If now the maxima for the increment kurtosis are tracked over the distance from the inlet in Figure 4.19, the increment kurtosis within the domain is obviously much higher for the intermittent case than for the Gaussian one, especially for larger inlet sizes. Here it has to be paid attention to the different ordinate axis ranges of the plots. The Gaussian inflow in Figure 4.19a builds up increment kurtosis depending on the inlet size. Due to the mixing with the environmental flow the smallest inlet size builds up highest increment kurtosis and all turbulences decay again with increasing distances from the inlet. Close to the outlet of the domain the original increment kurtosis is regained for all cases except for the smallest turbulent inlet size, which probably needs a longer channel to relax completely.

For the intermittent inflow in Figure 4.19b the initial high increment kurtosis is even more increased in the first meter of the domain, followed by a fast drop before it slowly increases again up to the range of the original value. The only exception occurs for the smallest inlet size where the kurtosis satisfies after a small maximum is reached between 5 and 10 m downstream of the inlet. So for that case additional turbulence builds up before it decays again. Interestingly, the shapes for the increment kurtosis with Gaussian and intermittent inflow are very similar for the smallest inlet which emphasizes that another type of turbulence dominates here, which originates from the fluctuating jet.

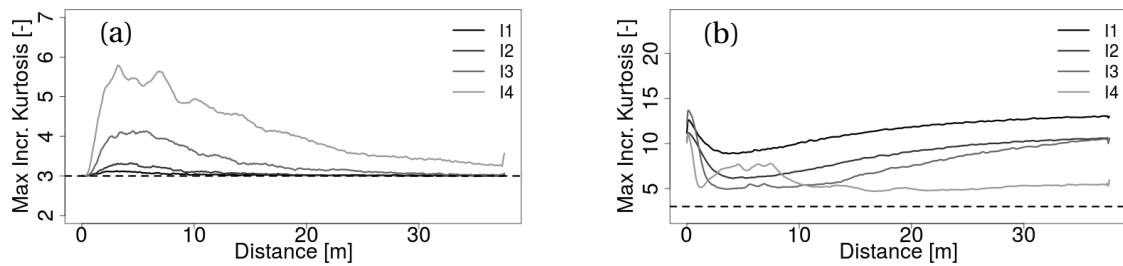


Figure 4.19: Maximal increment kurtosis for (a) Gaussian and (b) intermittent inflow.

The maximal magnitude of the increment skewness in Figure 4.20 is very similar for Gaussian and intermittent inflows. No significant differences occur, which is also clear because the CTRW model only changes the increment kurtosis and not the skewness. Independent of the inflow type, the skewness reaches the largest magnitude for the smallest inlet patch. Again the mixing effect with the surrounding flow becomes visible here, which is strongest for smallest turbulent inlets. If a larger turbulent inlet is taken the flow at the centerline can almost keep the zero skewness from the CTRW fields due to the missing mixture with the environmental flow. However sooner or later all cases show a convergence to zero at larger distances from the inlet.

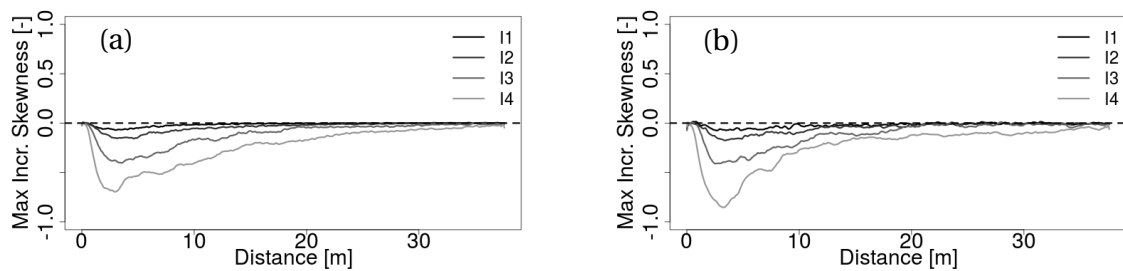


Figure 4.20: Maximal increment skewness for (a) Gaussian and (b) intermittent inflow.

Looking back at the results achieved so far the following can be concluded. If intermittency is understood as an intermediate state between laminar flow and unordered flow patterns, which appears due to mixing, all results gained here are also comprehensible and the occurrence of intermittency in the flow even for non-intermittent inflow is logical. The region with most mixing also contains highest intermittency, and for the channel flow studied here mixing at the centerline occurs very early for the small turbulent inlet.

To achieve an overview of how well the inlet turbulence is conserved while propagating through the domain, the maximal cross correlation with the inlet turbulence is studied in Figure 4.21. First a clear drop with the distance from the inlet is obvious, which occurs due to the change of turbulent structures while they are moving. The mixing with the surrounding non-turbulent flow also plays a role here. Surprisingly, the smallest turbulent inflow patch shows largest cross correlation throughout the domain although the variance drops fastest. That means that the overall structures in the turbulence change very slowly while the fluctuation amplitude decreases fast.

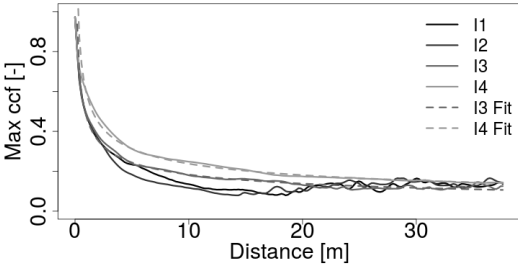


Figure 4.21: Maximal cross correlation of velocity field with the inflow at different distances from the inlet.

Chapter 5

Simulation of Airfoils

After a very first insight is gained into the flow dynamics of CTRW fields in an open channel, a more wind energy related approach is followed by a simulation of a rotor blade airfoil in order to catch important aspects of the interaction of the airfoil and Gaussian as well as intermittent flow fields. CFD has been used as a tool for these studies because it allows to simulate the whole turbulent wind field from the region where the flow field is injected up to the airfoil, but also the wake of the airfoil is resolved. A simulation of the DU 91-W2-250 airfoil is performed, because of its well studied characteristics across several publications from basic studies [84, 85, 86], up to studies, where vortex generators or leading edge slats have been attached [87, 88], or dynamic stall is considered [89].

The main focus of this work lies on the evaluation of the load dynamics under turbulent Gaussian and intermittent inflow conditions, where the comparability of both types of fields has to be assured, i.e. mean value, standard deviation and spectral statistics should be as similar as possible. In general this is not an easy task, because several obstacles have to be overcome. One of these is that the boundary layer of the airfoil has to be fully resolved up to the viscous sublayer, where viscous stresses are dominating. In other words, the first cell at the airfoil has to have a height of the dimensionless wall distance $y^+ = 1$, in order to obtain decent simulation results without the need of wall models [20]. Due to this very fine mesh close to the airfoil the inflow field should also be highly resolved if the effect of small turbulence structures should be taken into account. Furthermore the overall number of cells in the domain is usually strongly connected to the resolution close to the airfoil, because cell sizes of neighbouring cells should not differ by more than a factor of 1.4, i.e. the total number of cells becomes very big. In addition to it, the time step Δt has to be very small with a small cell size in order to achieve stable and accurate results. The time step is limited by the Courant-Friedrichs-Lewy-number

$$\text{CFL} = \Delta t \sum_{i=1}^3 \frac{u_i}{\Delta x_i} \quad (5.1)$$

with the cell size Δx_i and the velocity component u_i in the direction $i \in \{x, y, z\}$. This characteristic number, which is often used for stability analysis, should be less than $\text{CFL}_{\max} = 1$ for explicit solvers. Typically for turbulent simulation cases other definitions based on the turbulent kinetic energy, like $\text{CFL} = \sqrt{k}\Delta t/\Delta x < \text{CFL}_{\max} = 1/20$ for DNS in a cubic domain, are

used in practice [20]. This condition predefines the upper limit of the turbulence intensity for any kind of CFD simulations and should thereby not be neglected.

Due to the high resolution of the performed airfoil simulations, the involved small time step of down to 10^{-4} s and the related high computational effort, the total simulated time is restricted to 60 s. This leads to the problem of convergence of wind fields, i.e. a minimal simulation time is needed to achieve the target statistics, which are set by the model parameters. This issue raises in difficulty if the goal is the convergence of intermittent wind fields, due to the fact that introducing waiting times distorts the statistics by a considerable degree on smaller time scales. This distortion can only be resolved by much longer time series or by reducing the intermittency. Because longer time series are no option on account of limited computational power, the degree of intermittency has to be reduced by adjusting the model parameters α or C . Therefore very big differences for the increment statistics between Gaussian and intermittent wind fields are not expected. Furthermore an additional intermittency loss results from the decay of wind fields in front of the airfoil.

With the previously mentioned aspects in mind two different parameter sets have been used for the airfoil simulations. Both sets have in common the mean velocity $u = 15 \text{ ms}^{-1}$, standard deviation $\sigma = 1.5 \text{ ms}^{-1}$, correlation length $r = 0.5 \text{ m}$, time step $\Delta t = 0.01 \text{ s}$, simulation time $t = 60 \text{ s}$, and the frequency for the -5/3-law $\omega_c = 18.0618 \text{ Hz}$. Additionally, no shear is assumed and the energy spectrum has been corrected for both to the model spectrum to be identical for intermittent and Gaussian fields. While one field is Gaussian the other is intermittent with the intermittency parameters $\alpha = 0.6$.

The time series, one point statistics, and the common spectrum of both fields are shown in Figures 5.1, 5.2a, and 5.2b. While the one or two time statistics are not distinguishable just by pure examination of the time series in Figure 5.1, the differences become more pronounced in the pdf, shown in Figure 5.2a. Compared to the intermittent case the Gaussian wind field exhibits a smoother distribution of wind velocities with low variety even for the tails. The origin of these differences lies in the aforementioned short simulation time and the convergence problems of the wind field statistics for intermittent fields. For the corrected identical spectrum of both fields in Figure 5.2b holds the -5/3 slope at $f_c = 2\pi\omega_c \approx 2.86 \text{ Hz}$.

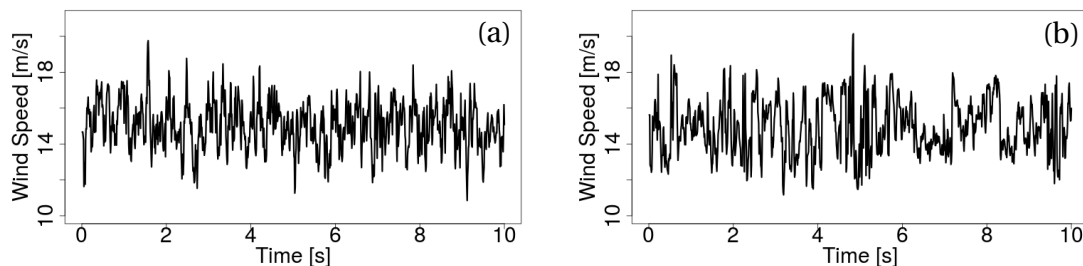


Figure 5.1: Time series of (a) Gaussian and (b) intermittent inflow used for airfoil simulations.

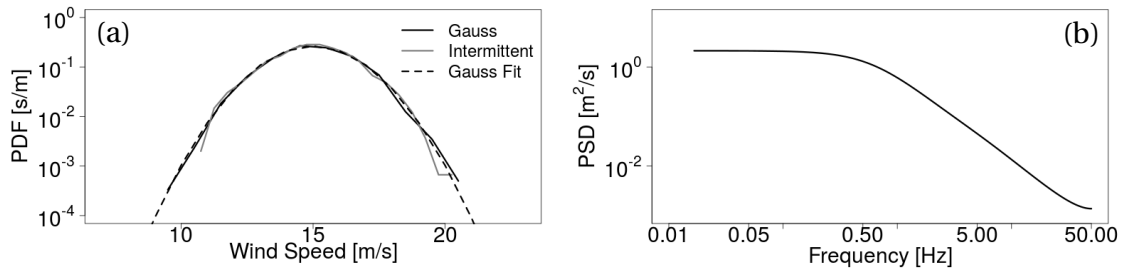


Figure 5.2: (a) PDF and (b) common spectrum of Gaussian and intermittent inflow.

Further differences of both fields become visible if the increment statistics are investigated by plotting the increment pdf and the increment kurtosis over a range of time increments τ . Figure 5.3a illustrates the heavy tailed increment distribution for small timescales τ up to the range of almost a second. The fast drop of intermittency with increasing scales becomes clear in Figure 5.3b where increments of Gaussian and intermittent fields are only slightly different for $\tau > 1$ s. Here one can also guess that changing the intermittency parameter α increases in particular the increment kurtosis on small scales but the effect on larger scales is very small. It becomes practically impossible to achieve wind fields with high increment kurtosis on a broad range of scales with the background of obtaining converged statistics. The intermittency study done in section 3.3.1 also supports this statement. However the increment kurtosis has realistic values for atmospheric turbulence [90] where values up to 12 are measured.

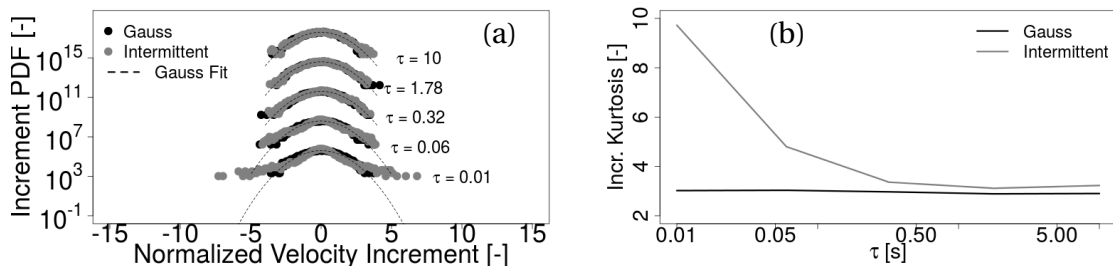


Figure 5.3: (a) Increment PDF's and (b) increment kurtosis of Gaussian and intermittent inflow for different time increments τ .

After generating the wind fields, CFD can be used to investigate the effect of intermittency on forces acting on the DU profile. Herefore a quadratic mesh with 3.086 million cells and $80 \text{ m} \times 80 \text{ m}$ is used where the airfoil with chord length 1 m is located in its center. Figure 5.4a shows the whole mesh used for the simulation. where on the left border a steady inflow is introduced to the domain. For the outflow on the right side a zero gradient condition is used for the velocity. All other sides underly a no-slip condition, i.e. no shear is taken into account and the walls are impermeable. In the center, where the airfoil is located, the mesh is highly resolved, while it is very coarse far away from the center in the corners of the domain, which are not important for forces on the airfoil.

Figure 5.4b illustrates the zoomed in center of the domain where different meshes are visible. The inner circular mesh contains the airfoil and can be rotated to simulate different

AOA's. The outer mesh around the circular part is fixed and is connected to the circular mesh via an Arbitrary Mesh Interface (AMI). 1.5 chord lengths in front of the airfoil an actuator, shown in red, is used to superimpose fluctuations from the CTRW model onto the steady inflow. The alternative, where fluctuations are directly fed into the domain by a turbulent inflow patch, has been rejected due to the need of very fine grid cells up to the airfoil to keep the turbulence with its characteristics alive. Furthermore, additional computational time would have been taken into account where the turbulence has to overcome the distance between the inlet and the airfoil. Simulations with such an increase in computational effort are not feasible and therefore the actuator method is preferred.

The fine grid close to the the airfoil, shown in Figure 5.4c is resolved down to $y^+ \approx 0.4$ such that no wall function is needed to simulate the flow close to the airfoil boundary.

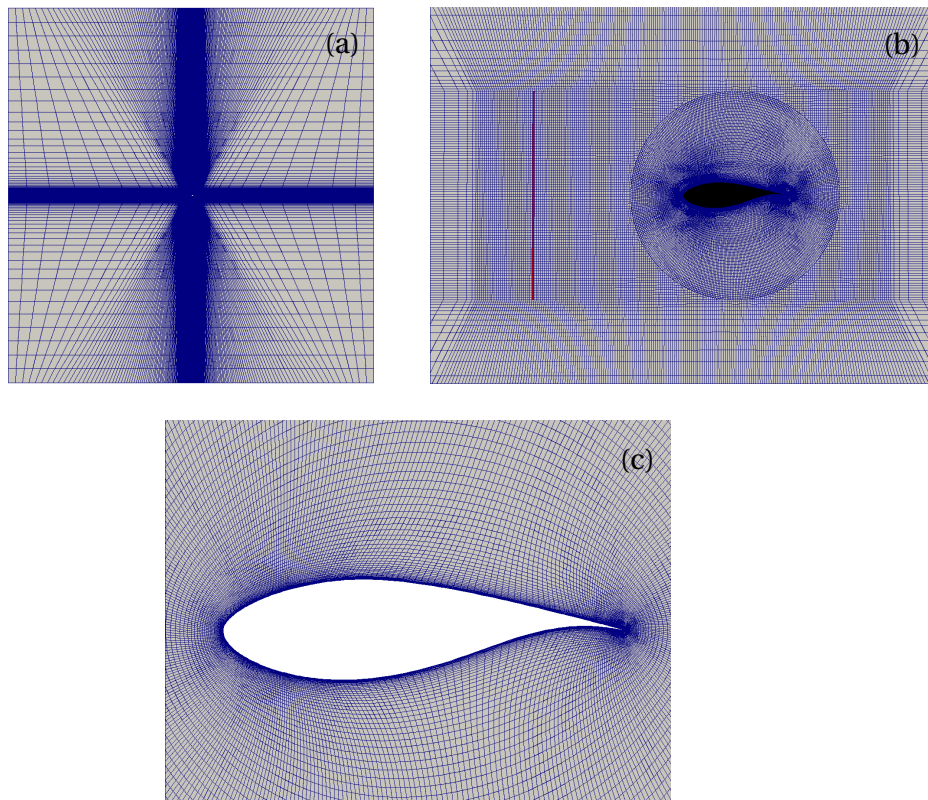


Figure 5.4: Mesh used for CFD simulations of the 91-W2-250 Airfoil (a) in the farfield, (b) at the center with actuator in red, and (c) close to the arfoil.

For all simulations the Improved Delayed Detached Eddy Simulation (IDDES) method provided by OpenFOAM and based on the DDES method from Spalart et al. [91] is used together with the PIMPLE algorithm to be able to resolve the small turbulent structures in an accurate way. Furthermore AOA's from 0° to 18° have been simulated in steps of 2° such that for Gaussian and intermittent wind fields 40 simulations have been performed in total with the wind fields described before. Additionally the same simulations have been repeated with fully correlated wind fields where $r \rightarrow \infty$ because those fields show much more stability in terms of conservation of input properties as seen in the next sections.

5.0.1 Simulation with Partially Correlated Inflow

For comparison reasons the airfoil has been simulated under constant inflow conditions without injection of turbulence. For different AOA's it can be seen in Figure 5.5 that a speed up of velocity appears on the pressure side of the airfoil while the suction side can be related to a speed down, at least close to the leading edge. With increasing AOA the separation point moves more and more into the direction of the leading edge and the wake effects become more clear.

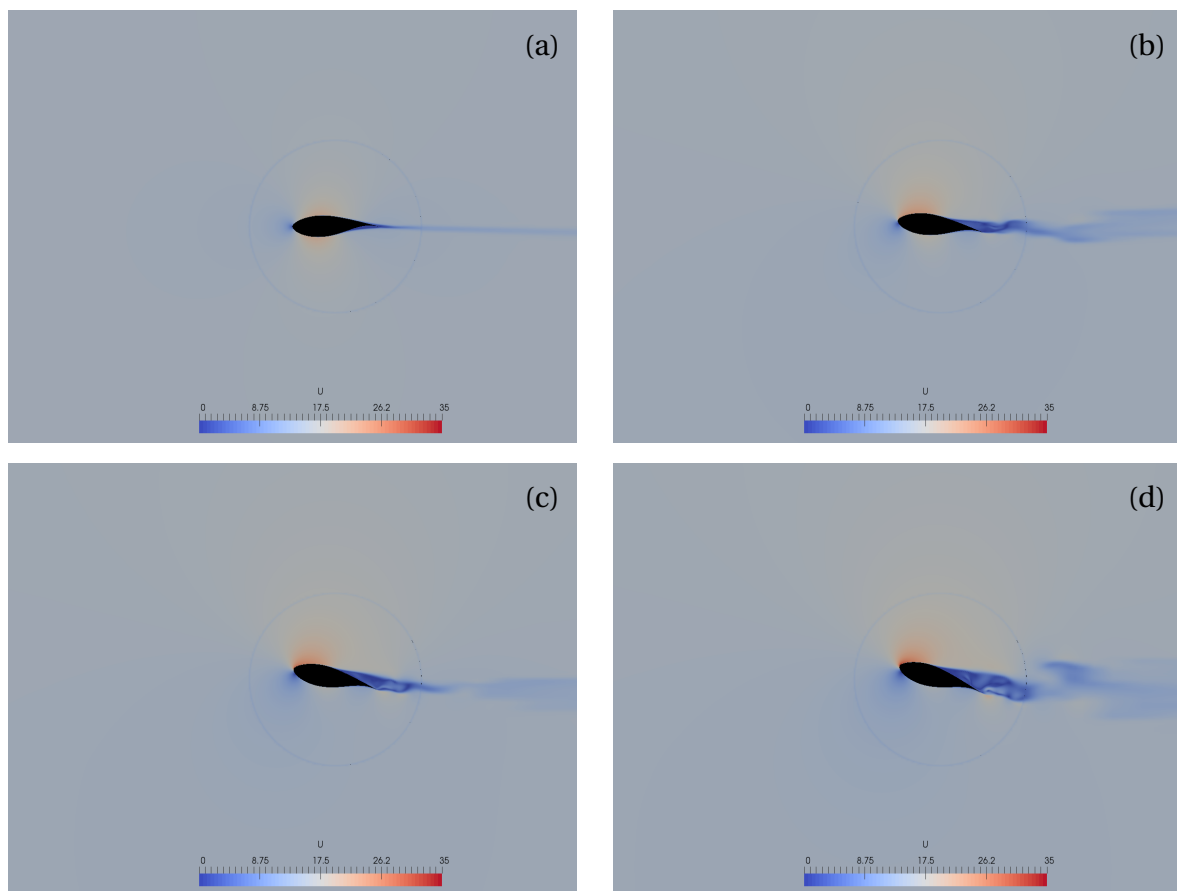


Figure 5.5: Snapshot of wind field in x direction for airfoil simulations with constant inflow for AOA's of (a) 0°, (b) 8°, (c) 12°, and (d) 18°.

Next the airfoil has been simulated with Gaussian and intermittent wind fields defined by the aforementioned parameters where the correlation length is $r = 0.5$ m. Figures 5.6 and 5.7 are taken at the same time instance and give an insight of the wind structures and the flow behavior around the airfoil for different AOA's. What becomes obvious here is that the flow field in front of the airfoil is not influenced much by its orientation but the wake is still strongly visible. Regions of speeding up and slowing down can also be perceived close to the leading edge. A small area upstream of the actuator shows strong feedback effects with the input field and differs a lot from the actual fields which are generated. The reason here is the big difference between the constant field in front of the actuator and the injected strong turbulence which makes an abrupt change of flow unavoidable. The PIMPLE algo-

rhythm makes this transition spatially as compact as possible under consideration of fulfilling the Navier Stokes equations. Therefore in front of the actuator neither the large structures from the downstream region nor an instant change of velocities is expected. Structural differences between Gaussian and intermittent wind fields are also not visible due to similar one point statistics and equal spectra.

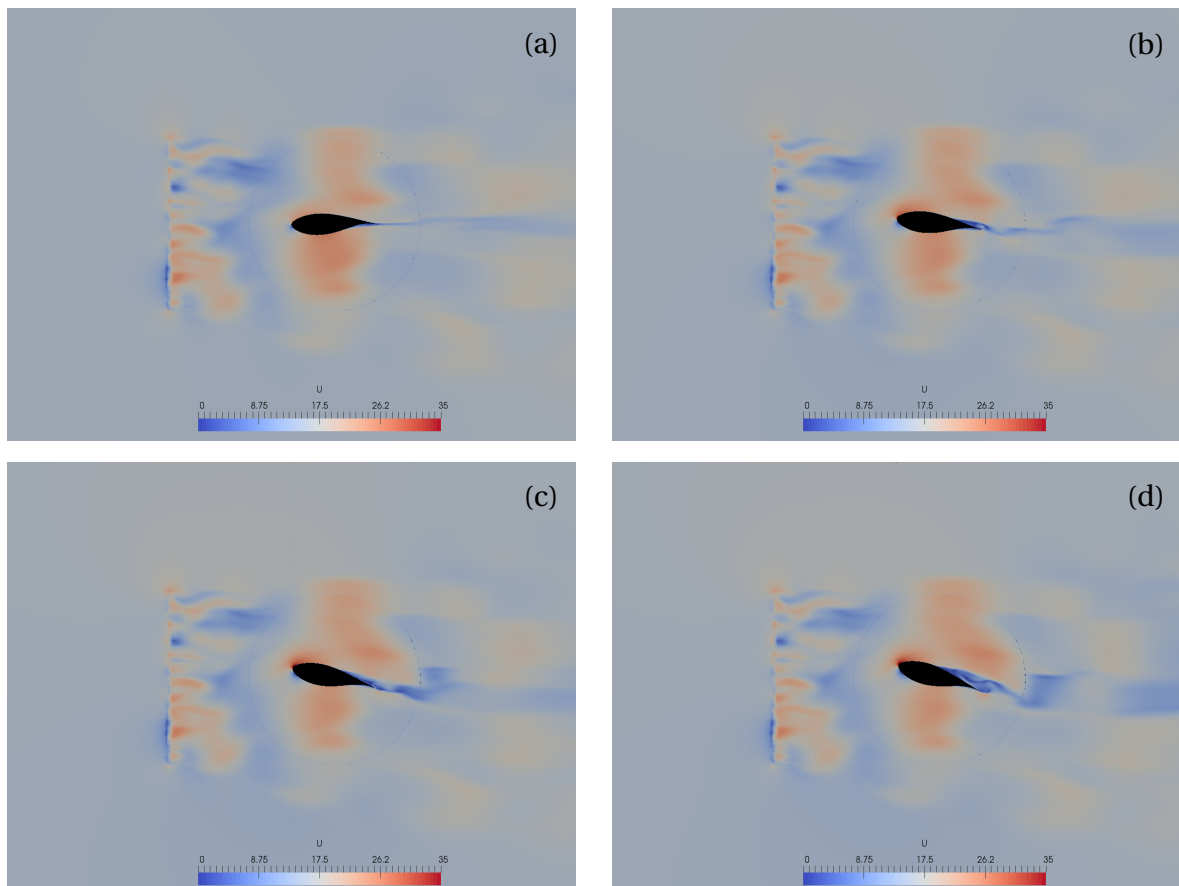


Figure 5.6: Snapshot of wind field in x direction for airfoil simulations with partially correlated Gaussian inflow and $r = 0.5$ m for AOA's of (a) 0°, (b) 8°, (c) 12°, and (d) 18°.

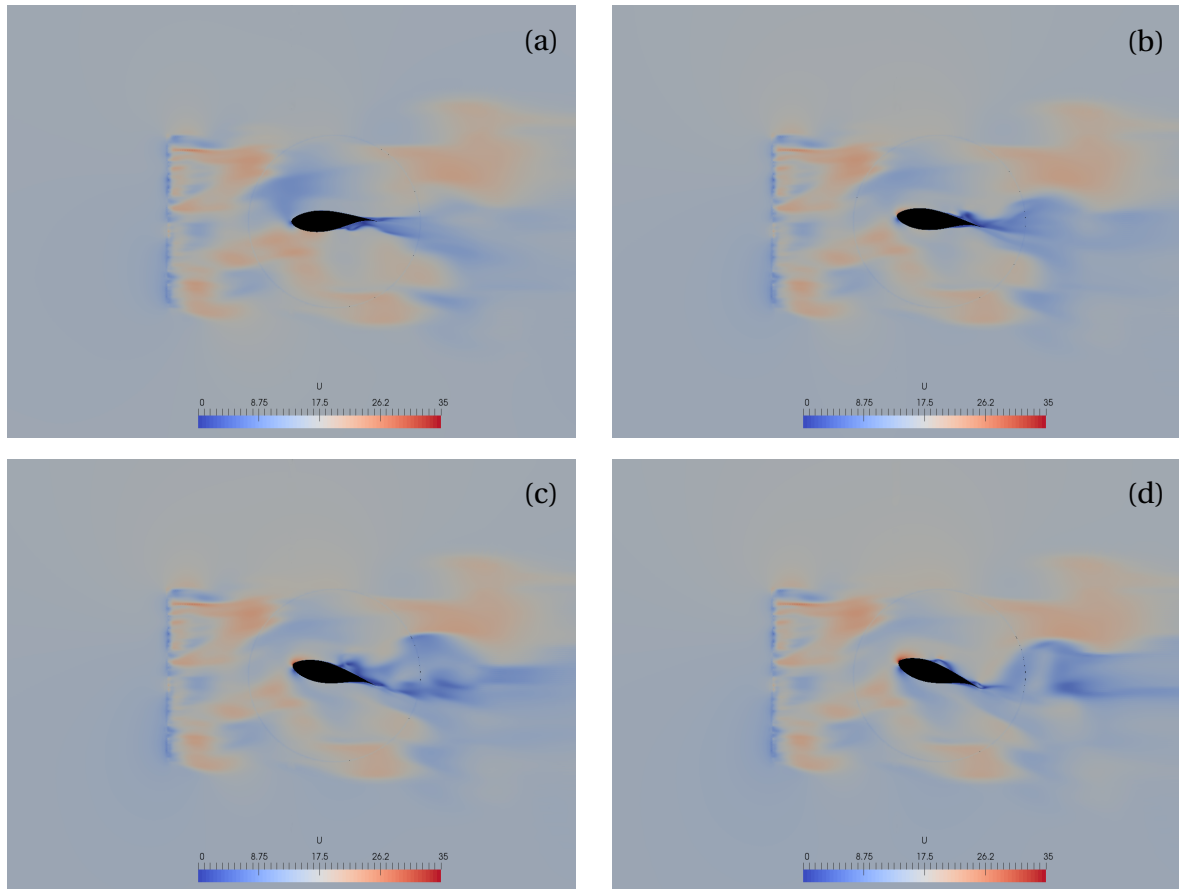


Figure 5.7: Snapshot of wind field in x direction for airfoil simulations with intermittent inflow and $r = 0.5$ m for AOA's of (a) 0° , (b) 8° , (c) 12° , and (d) 18° .

With all three different types of inflows done the evolution of wind properties can be studied and compared as it is done in Figure 5.8. Four different properties are compared at different positions in front of the leading edge up to the point where the turbulence is injected, namely the mean wind speed, the standard deviation, the wind speed increment kurtosis and the maximum of cross correlations with the original CTRW field.

The mean wind speed shown in Figure 5.8a is almost identical 2.5 m in front of the airfoil but evolves in separate ways for the turbulent fields and the case where no turbulence has been injected. However close to the airfoil the values differ by less than 2%. The different evolutions are not explainable in detail but a reason might be that the turbulence is dominating the flow up to the point where the geometry of the airfoil decelerates the flow field by a considerable amount, i.e. around 0.3 m in front of the leading edge. It seems that the mean value is more stable in a turbulent flow than in a flow without turbulence. Interestingly the effect of the injected forces at the actuator can also be perceived in the mean velocity before the actuator is actually reached.

The standard deviation in Figure 5.8b is zero everywhere for the non turbulent case because the flow is not changing at all after a steady state is reached. For the turbulent cases it starts with a much smaller value than defined by the model parameter $\sigma = 1.5$ m/s. As already seen in the channel simulation in section 4.2.2 the flow becomes turbulent with an

increase of the standard deviation in front of the actuator. At the injection plane the standard deviation is higher than for the original field and increases even more to almost 3 m/s while approaching the airfoil. Finally a decaying process occurs and the standard deviation drops to approximately 2 m/s at the leading edge. This is still higher than defined in the model.

The evolution of wind increment kurtosis is shown in Figure 5.8c. Here the maximum and minimum kurtosis over the whole range of τ are plotted and the area in between is shaded. While the Gaussian inflow has an almost constant kurtosis around three everywhere, the intermittent flow shows big differences between the injection area and the leading edge. The discrepancies have their origin in the steep drop of intermittency at 1.5 m before the airfoil which is related to the. It can also be noted that the kurtosis and with it intermittency drops over the whole range of distances.

Finally the maximum cross correlation between the turbulent fields in the domain and the original CTRW fields resulting from the model is plotted in Figure 5.8d. As expected from section 4.2.2 the correlation is very small throughout the measured region and the Gaussian and intermittent fields behave similar due to their similar characteristics at the inflow. Close to the actuator the maximal cross correlation is only 30% then it builds up to approximately 45% and eventually it drops to less than 20% close to the leading edge of the airfoil. Interestingly the maximal cross correlation shows a maximum at 1.5 m in front of the airfoil, while the increment kurtosis of the intermittent case is continuously falling. But the steep drop at smaller distances seems to be connected to the drop of the maximal cross correlation.

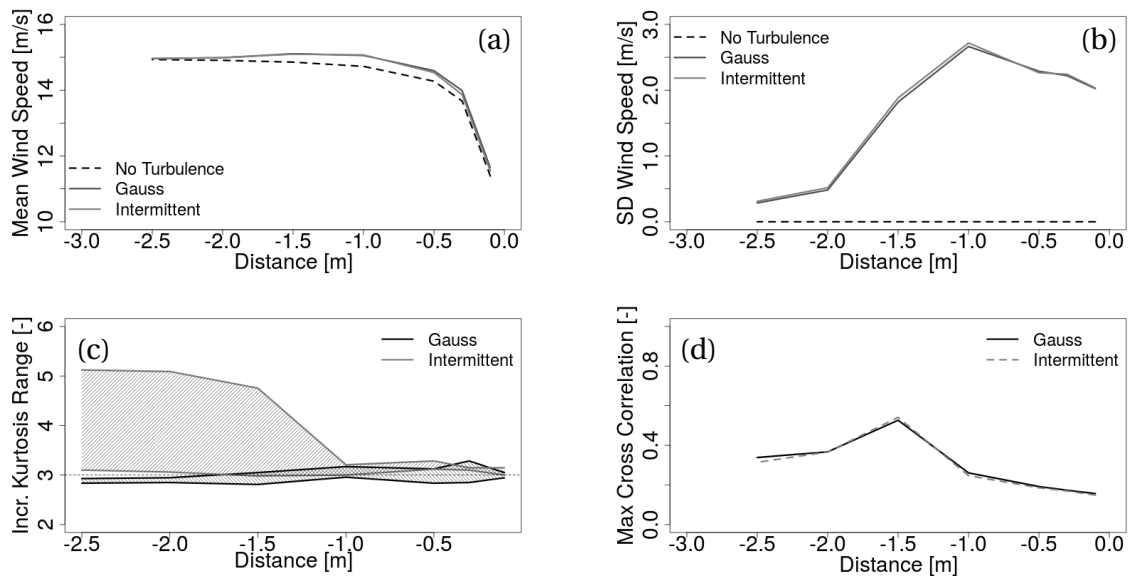


Figure 5.8: Evolution of (a) mean, (b) standard deviation, (c) range of increment kurtosis for τ between 0.01 s and 10 s, and (d) maximal cross correlation with the inflow field for the flow field at the centerline in front of the airfoil.

After the wind flow has been characterized, the forces on the airfoil, i.e. drag and lift, are brought into focus. Because of the linear relation of forces and corresponding non-dimensional lift and drag coefficients c_l and c_d , it is sufficient to look at the coefficients where the advantage is the gained comparability. For an AOA of 4° excerpts of time series

of both coefficients for Gaussian as well as intermittent wind fields are shown in Figure 5.9.

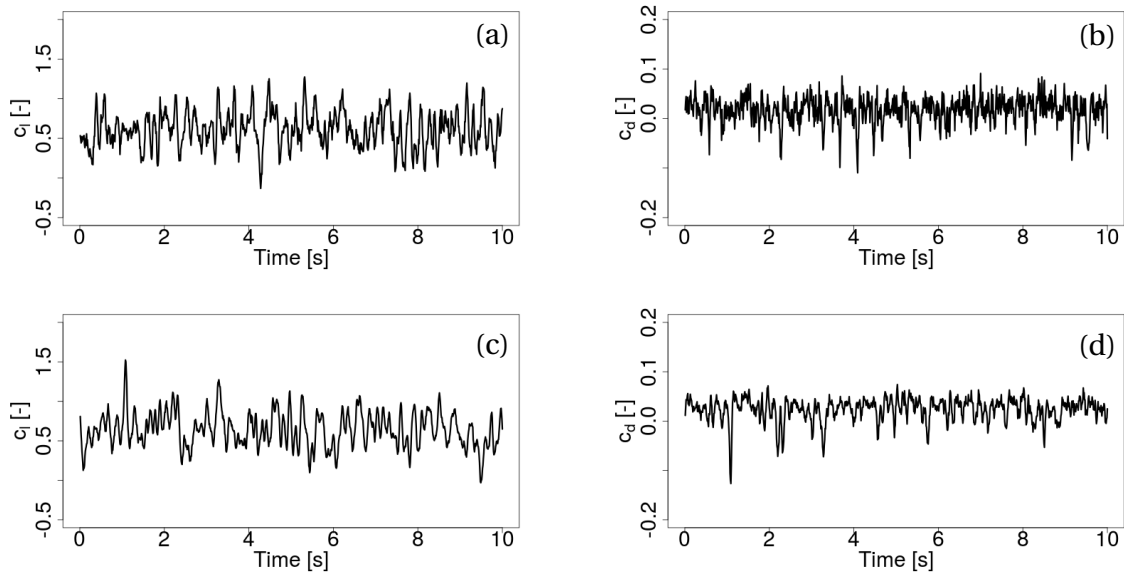


Figure 5.9: Time series of lift and drag force coefficients at 4° AOA for (a,b) Gaussian, and (c,d) intermittent inflow fields.

Their mean values and standard deviations are plotted in Figure 5.10 and 5.11. It can be said that both, the mean and standard deviation, do not show big differences between Gaussian and intermittent inflow cases for almost all AOA's except for 18°. There the deviation is quite big due to general difficulties of simulations for high AOA and the complex flow in the wake of the airfoil. The non-turbulent case shows up an almost zero standard deviation up to 16° and a slight increase for 18°. Contrary to the standard deviation, the mean value follows the same trend as for the turbulent cases for small angles, but from 4° onwards the average force coefficients of the turbulent cases predominate.

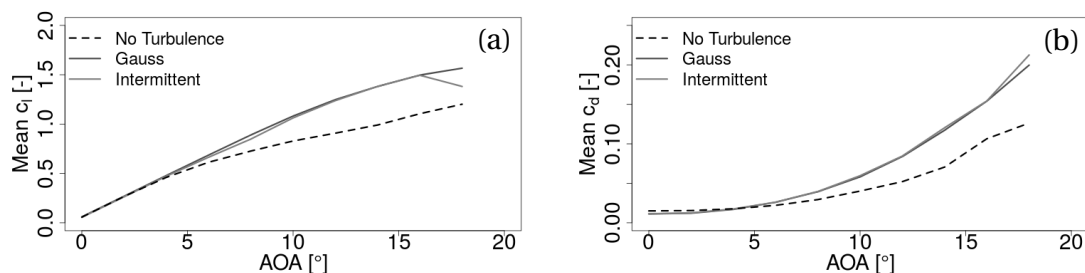


Figure 5.10: (a) Mean lift, and (b) mean drag coefficients for different AOA's for constant, Gaussian and intermittent inflow.

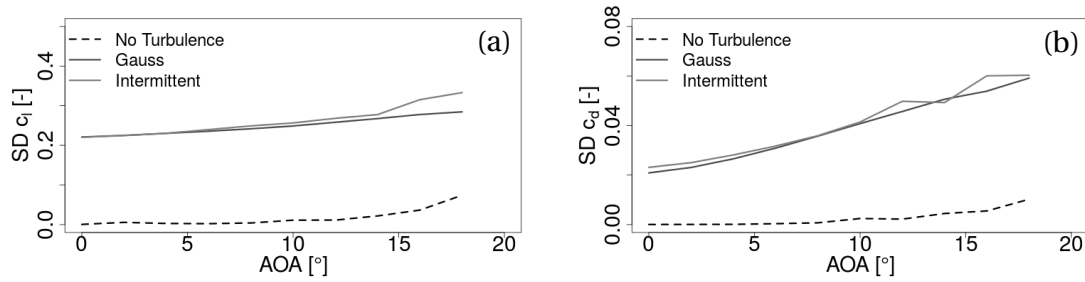


Figure 5.11: (a) Standard deviation of lift, and (b) drag coefficients for different AOA's for constant, Gaussian and intermittent inflow.

Now the kurtosis of lift and drag force increments for Gaussian and intermittent fields is looked at in Figures 5.12 and 5.13. For all angles the kurtosis for intermittent inflow is slightly larger than for Gaussian inflow. A reason for this can be the small difference already seen in Figure 5.8c at the closest point of the leading edge. Interestingly the same inflow leads to deviating results for the angles shown here, even if the deviations are not that big. The drag also shows an increased kurtosis compared to the lift. Additionally, the kurtosis of force increments for the intermittent cases is also higher than the kurtosis of wind increments close to the leading edge. This is an indication that the forces are not only influenced by the wind field very close to the airfoil but also by points further away. Moreover only the wind field at the line directly in front of the leading edge has been analysed and not the ones above or below it, where additional shear could increase the increment kurtosis. The shape of the airfoil might also amplify the kurtosis by a considerable amount.

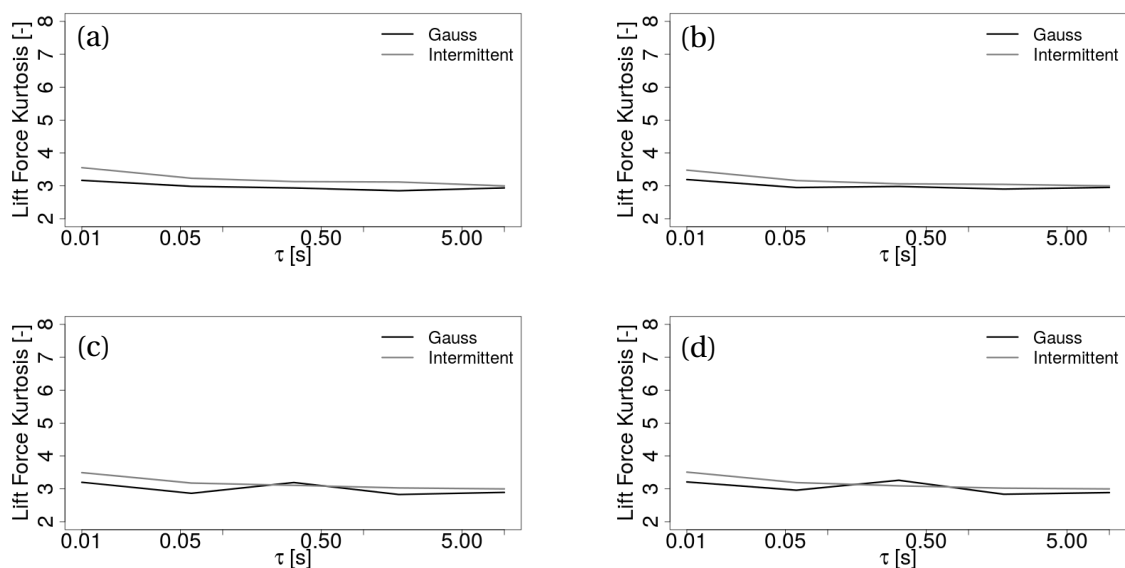


Figure 5.12: Increment kurtosis of the lift forces for Gaussian and intermittent inflows with AOA's of (a) 0°, (b) 8°, (c) 12°, and (d) 18°.

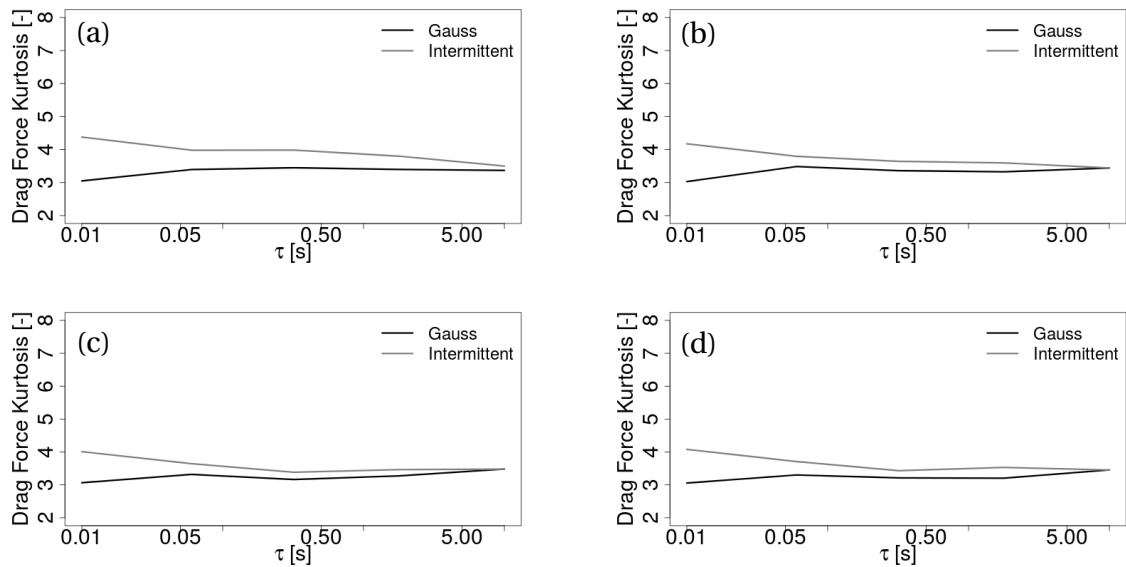


Figure 5.13: Increment kurtosis of the drag forces for Gaussian and intermittent inflows with AOA's of (a) 0° , (b) 8° , (c) 12° , and (d) 18° .

Finally to be able to make a statement about fatigue loads on the rotor blade the EFL have been calculated for all three cases shown here in Figure 5.14. Again the turbulent cases show much higher activity than the simulations with constant inflow, as expected. Furthermore the loads on the airfoil with intermittent inflow is significantly higher for all AOA's for the lift as well as the drag. A minimal EFL difference between Gaussian and intermittent conditions for the lift and the drag is measured at an AOA of 10° where both differ by only 2%. At an AOA of 16° the lift and the drag show the biggest deviation with 7% and 15%. There are two different ways to interpret the relatively big difference in the EFL. One reason could originate from the difference in the standard deviation, because a higher standard deviation leads to bigger load ranges which are counted for the EFL. The second reason for the deviating loads could be the differences in the increment kurtosis between Gaussian and intermittent wind fields. However at this point no clear separation of both effects can be done, especially because the size of intermittent structures is unknown, and more simplifications have to be implied in the studies.

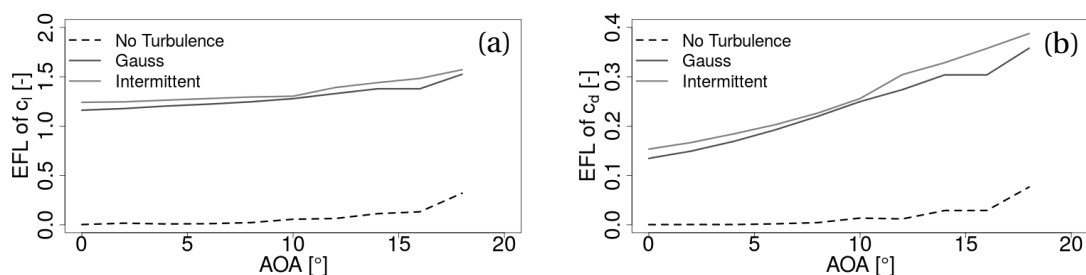


Figure 5.14: EFL of the (a) the lift, and (b) the drag coefficient.

5.0.2 Simulation with Fully Correlated Inflow

Due to the fact that the lift and drag are strongly affected by the inflow and that even small differences in the inflow might be relevant for the results achieved before, more comparable inflow fields shall be used as a basis for the former studies. For this reason wind fields are generated with the same parameter set as in the last section but with the correlation length $r \rightarrow \infty$, i.e. all points in the inflow plane exhibit the same time series. In the following this is referred as a fully correlated wind field. Furthermore the one point statistics of the used time series have been corrected by the Lambert W algorithm presented in section 3.4.3 to be for both fields as Gaussian as possible while the energy spectrum is kept nearly identical.

Figures 5.15 and 5.16 give an insight of the structure of the generated fields at the same instance of time for AOA of 0° , 8° , 12° and 18° . Similar to the fields from the previous section the flow fields shown here are not influenced that much by the airfoil except in the wake.

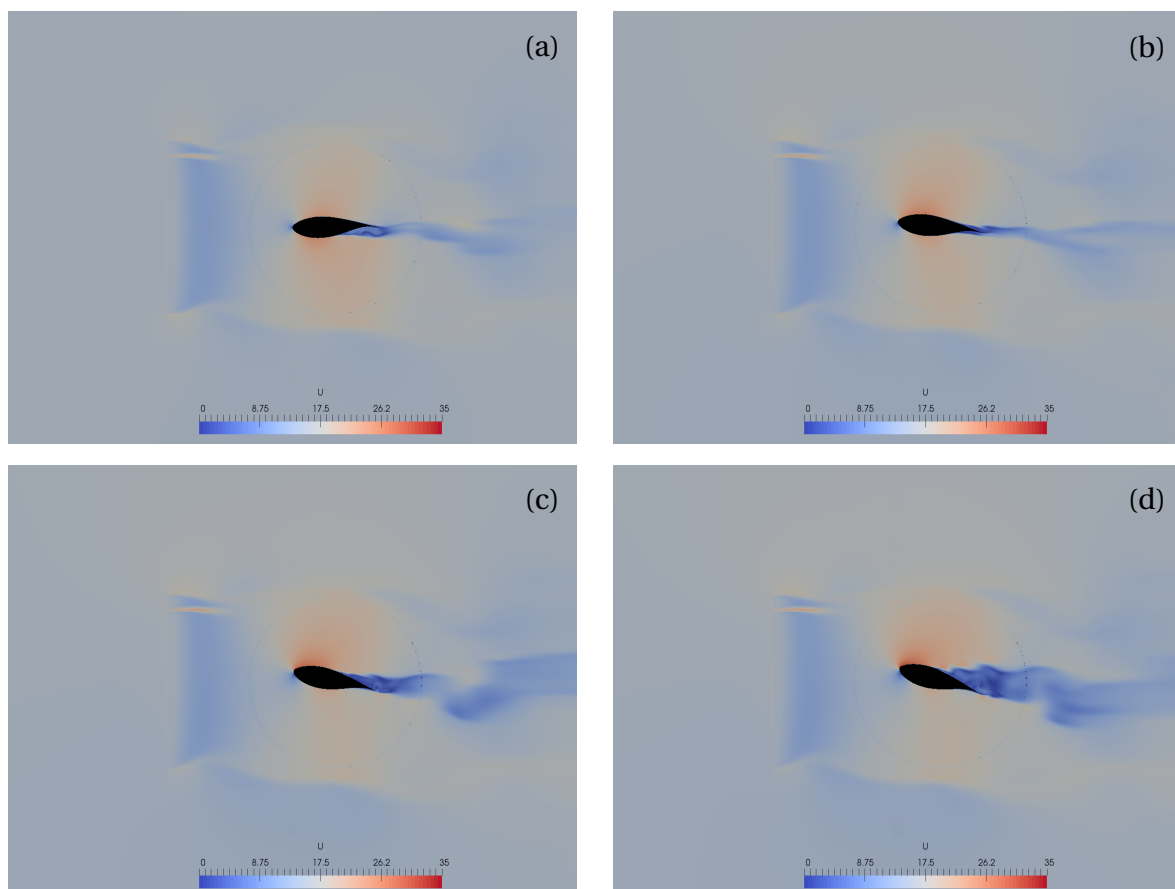


Figure 5.15: Pictures of airfoil simulations with fully correlated Gaussian inflow with AOA's of (a) 0° , (b) 8° , (c) 12° , and (d) 18° .

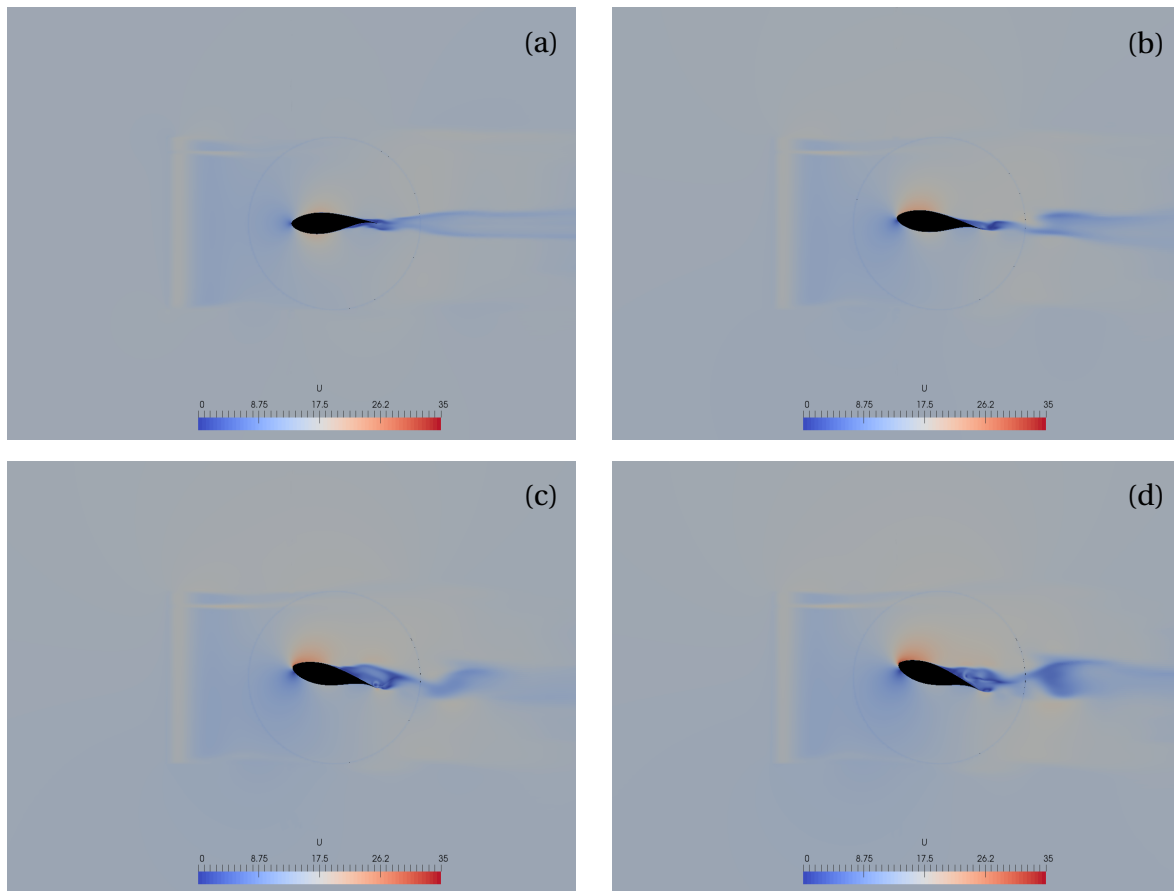


Figure 5.16: Pictures of airfoil simulations with fully correlated intermittent inflow with AOA's of (a) 0° , (b) 8° , (c) 12° , and (d) 18° .

Again different properties of the flow field are looked at in Figure 5.17, namely the mean, standard deviation, velocity increment kurtosis, and maximal cross correlation with the original field, respectively. The simulation where no turbulence has been injected is again used as a reference. The statistically almost identical inflow for the Gaussian and intermittent time series make the quantities evolve in exactly the same manner. The only difference is the increment kurtosis shown in Figure 5.17c which is for the Gaussian case around three and for the intermittent case clearly above three everywhere. The full correlation in the inflow plane is responsible for the comparatively high increment kurtosis even a further distance away from the actuator.

Looking at the standard deviation in Figure 5.17b reveals a totally different trend for its evolution than for the previous simulations with limited correlation length. It does not build up to 3 m/s but only to 0.5 m/s. The big correlations in plane hinder the build up of self evolving turbulence which amplified the turbulence for smaller in-plane correlations.

One of the advantages of the fully correlated fields used here is visible in Figure 5.17d. As already seen for the standard deviation, full correlations imply a stability of the fluctuation characteristics over a large range which is expressed by the large maximal cross correlation with the original field of around 80% everywhere. This is also the reason why fully correlated fields can be seen as a first step if specific characteristics of the original time series should be

studied while a correct physical representation does not lie in the focus.

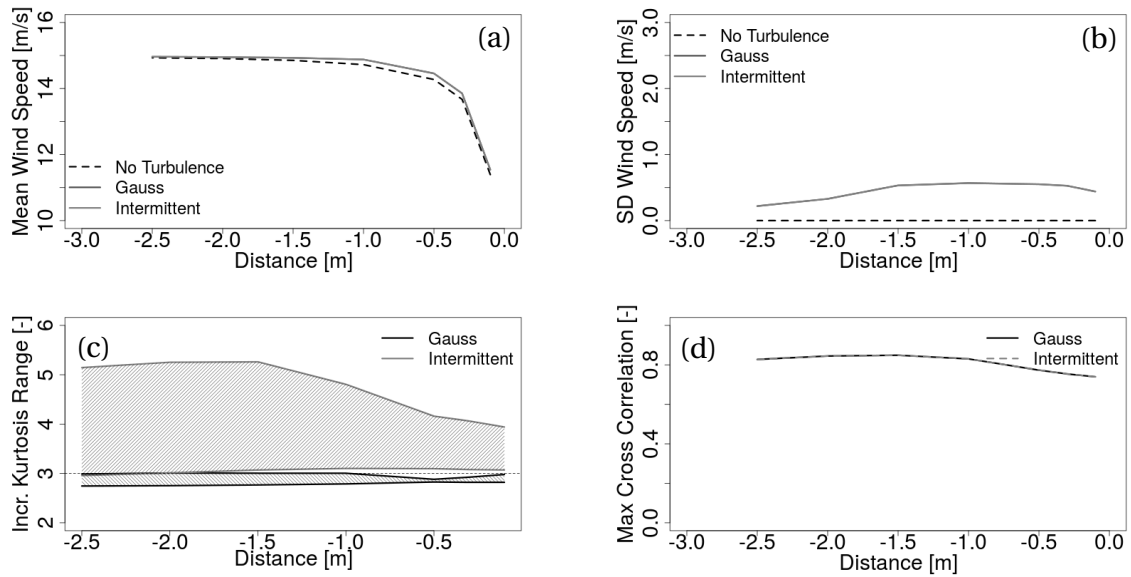


Figure 5.17: Evolution of (a) mean, (b) standard deviation, (c) range of increment kurtosis for τ between 0.01 s and 10 s, and (d) maximal cross correlation with the inflow field for the flow field at the centerline in front of the airfoil.

The lift and drag time series in Figure 5.18 do not show any differences between Gaussian and non-Gaussian fields on first sight. The characteristics are nearly identical because of the similar inflow.

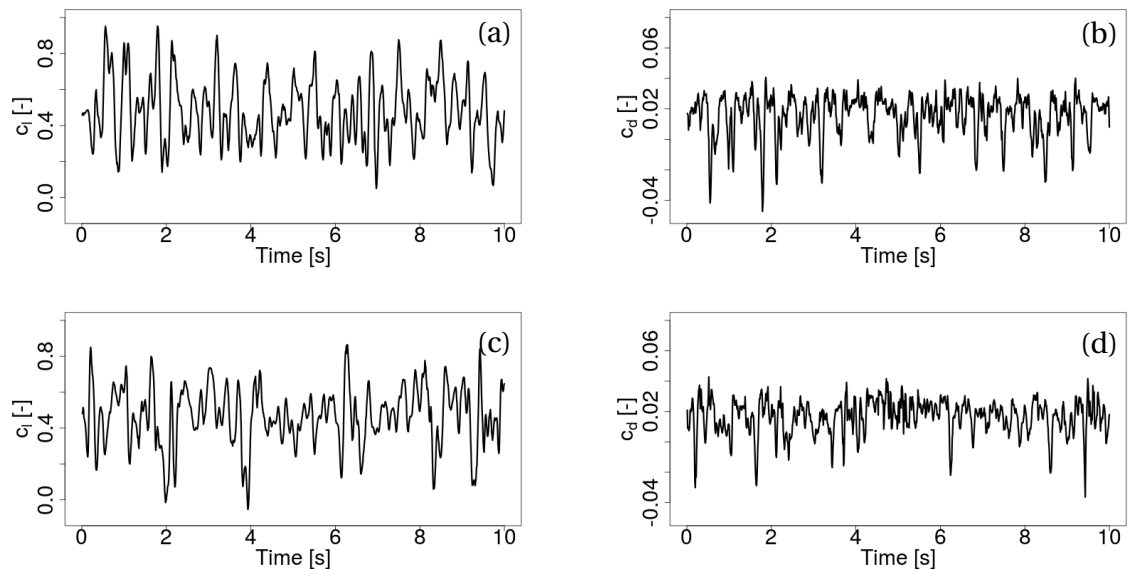


Figure 5.18: Time series of lift and drag force coefficients at 4° AOA's for (a,b) Gaussian, and (c,d) intermittent fully correlated inflow fields.

The mean values of lift and drag for the fully correlated cases in Figure 5.19 are again

higher than for the constant inflow case but not as high as for the previous simulations where the in-plane correlation length was limited. At first glance, this is a result which is not expected because a spatial averaging effect should reduce the impact of turbulence on the mean value if the structures become smaller. However looking at the standard deviation of both, drag and lift, in Figure 5.20 reveals that the standard deviation is in general smaller for the fully correlated cases due to the less fluctuating inflow. This also explains the reduced mean value.

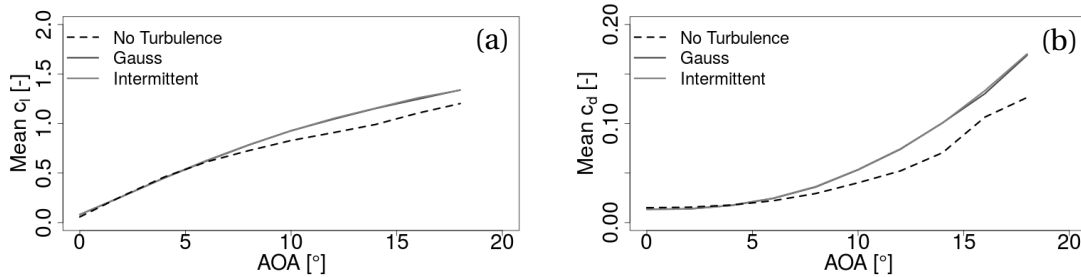


Figure 5.19: (a) Mean lift, and (b) mean drag coefficients for different AOA's for constant, Gaussian and intermittent fully correlated inflow.

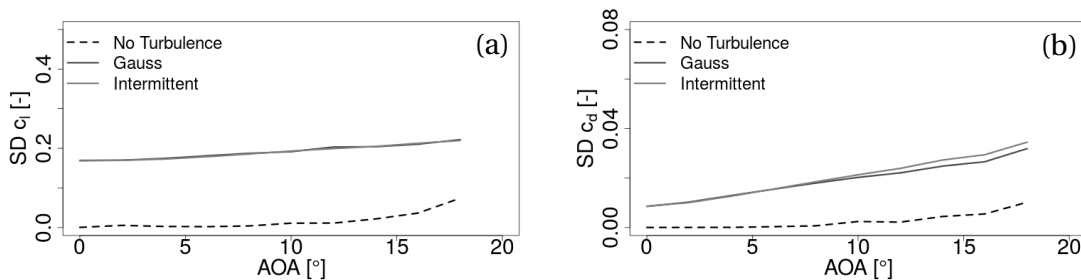


Figure 5.20: (a) Standard deviation of lift, and (b) standard deviation of drag coefficients for different AOA's for constant, Gaussian and intermittent inflow.

After the mean and standard deviation have been studied, the increment kurtosis of lift and drag for the fully correlated field is focused on in Figure 5.21 and 5.22 for the same AOA's as before. One of the first impressions gained is that under intermittent inflow all angles exhibit a higher increment kurtosis for the forces for full correlations than for limited correlations. Especially for small τ they are much higher under intermittent inflow conditions than for the Gaussian case. For both the lift and drag it can be noted that intermittency is much more dominant than for inflow fields with spatially limited correlations over all scales. Surprisingly, for the fully correlated fields it seems that the forces do not show Gaussian behavior for all AOA's under Gaussian inflow conditions. A reason might be the abrupt changes of flow field planes along the airfoil which seem to make the airfoil react in a different way than for flow fields with limited in-plane correlations. Nonlinear stall effects certainly will also have an impact on these results. Interesting is also the increasing increment kurtosis for the drag for small τ which shows up for the Gaussian but also for the intermittent fields, which are not related to each other except by the CTRW model parameters. This was not visible with that strength for the flow fields with limited correlations and augments the assumption that

the full in-plane correlations used here also affect the general trend of the increment kurtosis with changing τ . As already explained for the simulations with wind fields with limited correlations, the kurtosis of force increments is higher than for the wind increments. Surprisingly for angles of 8° and 12° the drag increment kurtosis is even above the maximum of the input flow field increment kurtosis from Figure 5.17c. Again the reason can only be the complex interaction of flow field and airfoil geometry and the missing information of the flow above and below the airfoil.

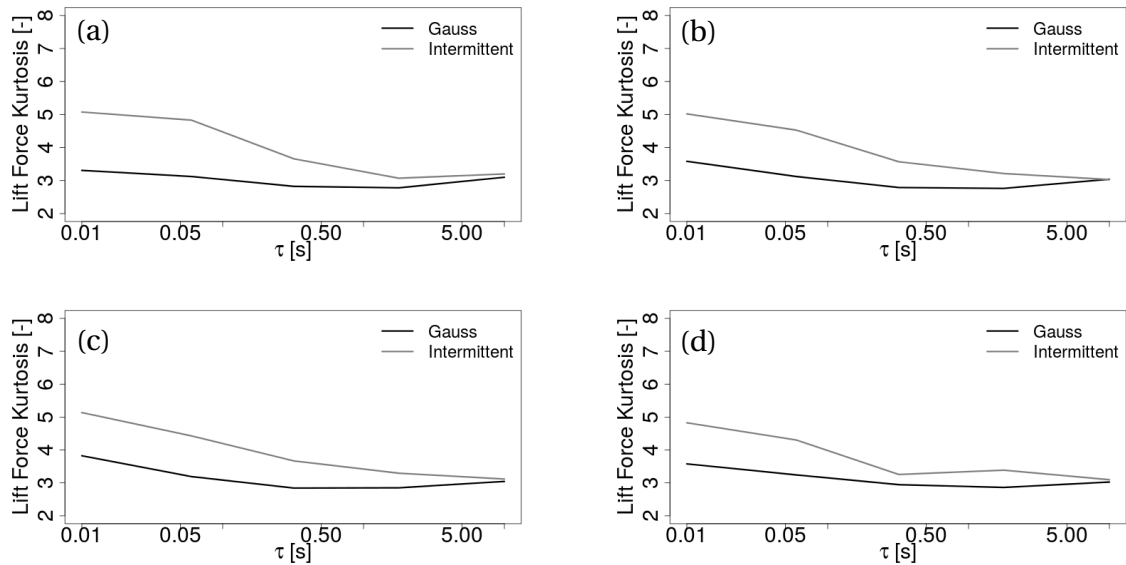


Figure 5.21: Increment kurtosis of the lift forces for Gaussian and intermittent inflows with AOA's of (a) 0° , (b) 8° , (c) 12° , and (d) 18° .

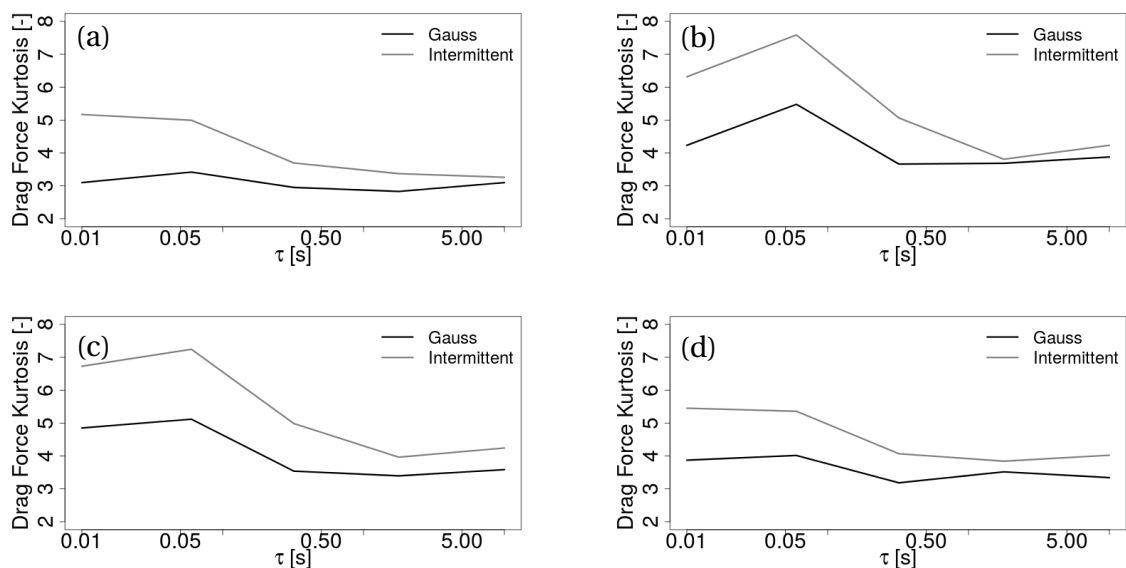


Figure 5.22: Increment kurtosis of the drag forces for Gaussian and intermittent inflows with AOA's of (a) 0° , (b) 8° , (c) 12° , and (d) 18° .

In the last step the fatigue loads are analysed for full correlations in Figure 5.23. Similar to 5.14 the intermittent inflow leads to higher fatigue even for small AOA's where the standard deviation does not deviate between intermittent and non-intermittent cases. For lift and drag the smallest deviation between Gaussian and intermittent inflow appears at an angle of 2° where the curves differ by 5% and 8% respectively. The largest difference is 11% for the lift at an AOA of 10° while it is even 24% for the drag at an angle of 14° . But for larger AOA's the increase in standard deviation has to be taken into account for the drag which also has a big effect on the EFL. Contrary to that, the standard deviation does not have any effect on the EFL difference of the lift.

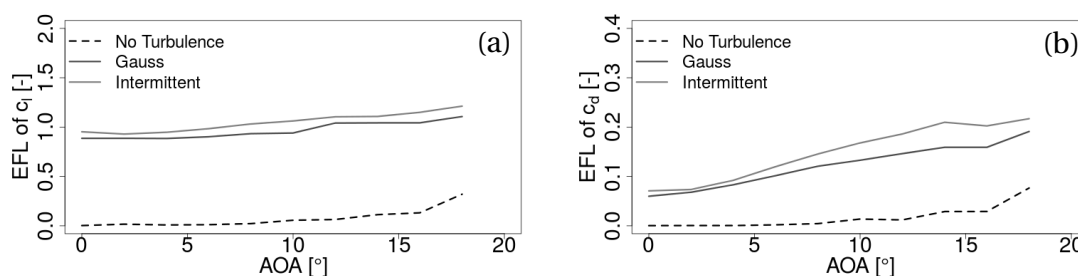


Figure 5.23: EFL of the (a) the lift, and (b) the drag coefficient.

5.0.3 Discussion

Even if differences of other properties, like the standard deviation, are not negligible for the outcome of this study, it can be concluded that there is a good indication that inflow fields with an increased increment kurtosis can be responsible for increased fatigue loads, at least for fully in-plane correlated wind fields. To give a more sophisticated result more simulations with different realizations of inflow fields could be performed. Moreover an averaging over all simulations would allow to quantify the kurtosis effect on EFL and an appropriate error estimation would be possible. Additionally different levels of intermittency could be studied and, if possible, larger and more relevant scales τ should lie in the focus. Herefore it is recommended to modify the CTRW model or use another model to account for such scales while at the same time the one point statistics and spectral properties stay untouched.

Chapter 6

Turbulence and Intermittency Study on Wind Turbines

6.1 What is the Effect of Turbulence on Wind Turbines? A Comparison of Three Standard Methods

In this section the next step into the direction of a more realistic simulation of wind turbines under turbulent inflow is taken. For this purpose instead of an airfoil the full rotor will be simulated with two different CFD models and the results will be compared with a BEM simulation with similar inflow gained from a CFD simulation.

The research conducted in this field is limited with recent studies done by Madsen et al. [92] and in the AVATAR project [93]. In both cases BEM is compared to higher fidelity codes. In the work by Madsen et al. a 2.5MW turbine was simulated with BEM and Blade Resolved (BR) CFD with a turbulent inflow based on the model by Mann [94]. The wind fields for BEM were extracted at the rotor position in the empty CFD domain. Additionally, measurement data of this turbine and BEM results for the same data were compared. In both cases spectra of sectional forces were investigated. In the AVATAR project similar quantities were in the focus of the study, but one Mann box was generated and used for the CFD as well as the BEM simulation. In CFD the natural decaying process of the wind fields leads to a decreased turbulence intensity and different turbulent structures at the turbine compared to BEM. Therefore the simulation results of BEM and CFD are not comparable. Also global quantities like thrust and torque as well as their corresponding fatigue loads were not investigated. Although those works are giving a valuable insight to BEM modeling uncertainties when combined with turbulent inflow, there is still a lack of comparable studies and a best practice guide for the comparison of CFD and BEM simulations is still missing.

6.1.1 Approach

The following results shown here were published in the work of Ehrich et al. [95], where a comparison of three different wind turbine simulation methods is aimed for. Two of them are high fidelity CFD methods while the third one is BEM based. The CFD methods are distinguished by the model used for the rotor blades. In particular the first one uses the

Actuator Line (AL) model [96] and the second one, which will be named Blade Resolved (BR) simulation in the following, contains the full blade geometry. Compared to previous studies, new in this work is the combination of the investigation of frequency resolved integral forces, the analysis of fatigue loads and a bridge between BR and BEM calculations, namely the AL method. The goal of this study is to shed light into the difficulties and expectations of the different methods proposed and information for future comparisons of CFD and BEM based simulations shall be provided. Additionally the information gained in this study should find its way into the next section, where intermittent and Gaussian CTRW fields are used as an inflow for AL based simulations.

The Wind Turbine Model

The numerical studies are performed on the NREL-5MW reference wind turbine with a rotor diameter of 126 m [97]. This three bladed horizontal axis wind turbine with a blade length of 61.5 m was designed by the National Renewable Energy Laboratory. It is close to the current average rotor size of newly installed wind turbines which accounts to 100–120 m. More details on the reference turbine can be found in Table 6.1.

Table 6.1: Overview of NREL-5MW turbine specification.

Parameter	Value
Number of rotor blades	3
Rotor diameter	126 m
Rated aerodynamic power	5.3 MW
Rated wind speed	11.4 m/s
Rated rotational speed	12.1 rpm
Blade cone angle	2.5°
Shaft tilt angle	5.0°
Blade length	61.5 m
Blade mass	17,740 kg

To make the comparison between different codes in a similar manner, the pitch and rotor speed are fixed and the effect of structural deformations, tilt and cone as well as the tower and nacelle are neglected.

The Wind Fields

It is assumed that the specific inflow turbulence model does not change the general trend of the outcome of the study presented here as long as some main properties of the wind fields are fulfilled like spatial and temporal correlations, Gaussianity and stationarity. However, the model used here should also be as simple as possible with a very low memory consumption which is for spectral methods usually very high if the time and space domains are large. Therefore velocity fluctuations are represented by a Gaussian process realized at the inflow

patch of the CFD domain. In particular, as a simplified version of Equation (3.3), coupled stochastic Ornstein-Uhlenbeck processes of the form

$$\frac{du_i^{(k)}(t)}{dt} = -\gamma \left(u_i^{(k)}(t) - \bar{u}^{(k)} \right) + \sqrt{D} \sum_j^N H_{ij} \Gamma_j^{(k)}(t) \quad (6.1)$$

with an exponentially decaying spatial and temporal correlation function with correlation length $l_c = 20$ m for all wind components are used without taking shear and intermittency into account. For the damping factor and the diffusion coefficient $\gamma = 0.56 \text{ s}^{-1}$ and $D = 0.62 \text{ m}^2 \text{ s}^{-3}$ have been chosen such that $\omega_c \approx 0.34$ Hz holds which ensures the length scale l_c in streamwise direction.

Fields with a mean wind speed of $\bar{u}^{(x)} = 11.4 \text{ ms}^{-1}$ corresponding to the rated operating condition of the wind turbine and $\text{TI} = 20\%$ are fed into the CFD domain by using an inflow boundary condition. As opposed to the previous airfoil simulations this boundary condition has been taken because injecting the turbulence by an actuator patch led to a much too high decay of intermittency before the turbine has been reached. This is the reason why using an actuator patch did not allow a proper comparison of the impact of Gaussian and intermittent inflow conditions. The relatively high TI had to be chosen, because of the natural decaying process leading to much smaller turbulence intensities, namely 11%, in the vicinity of the turbine in the absence of shear.

Numerical Methods

In the following the BR, AL and BEM method are described in more detail:

- BR: The blade resolved simulations are performed with the CFD software OpenFOAM V4.1 [98], which is an open-source package with a collection of modifiable libraries written in C++. The simulation domain is discretized using the bladeblockMesher [99] and windTurbine mesher tools [100] with a combination of structured and unstructured grids consisting of a total of 36M cells. To exclude influences of the mesh on the solution, a mesh study has been done in our previous work [101]. The grid of the complete simulation domain and the rotating part are shown in Figure 6.1 and a sectional view on the mesh near the blade in Figure 6.2. The cell length at the inlet, which is three rotor diameters upstream of the rotor, is 1m. This mesh is uniformly extruded up to the near blade mesh where a refinement takes place and the smallest cell length of approximately 0.2 m is reached. In order to limit the cell aspect ratio in radial direction, adaptive wall functions are being applied. The solution for the flow field is achieved by solving the incompressible Delayed Detached Eddy Simulations equations. It is assumed that the flow is fully turbulent, i.e., the laminar-turbulent transition in the boundary layer is not considered, because the inflow itself is turbulent and therefore the laminar boundary layer is not expected to have a strong influence on the blade. The closure problem is treated by use of the turbulence model proposed by Spalart et al. [102] with the proposed standard parameters. In order to solve the pressure-velocity coupling, the PIMPLE algorithm, is used, which is a combination of the loop structures of SIMPLE [103] and PISO [39, 40]. Integration in time is performed using the implicit second order backward scheme together with the second order linear upwind scheme

for discretizing the convection terms. For these simulations 360 cores are used for approximately 20 days resulting in 600 s simulation time with a time step of 0.01 s. This corresponds to 121 revolutions of the rotor.

- **AL:** The rotor is simplified by an AL model [96], where all rotor blades are reduced to rotating lines with a radial distribution of body forces at 60 positions along the lines. A Gaussian filtering kernel with the dimensionless smoothing parameter ε equal to 4 is used to obtain well fitting sectional forces and power output to the BR case. Based on the angle of attack at the given positions on the line, body forces are gained from lookup tables containing polars of two dimensional airfoils. A Prandtl tip [104] and root loss correction, as well as a 3D correction proposed by Du and Selig [105] are applied to the airfoil data. Except for a coarser resolution in the vicinity of the rotor with an average cell length of 1m the domain is exactly the same as for the BR case leading to a domain size of 22M cells. The flow field is simulated by Large Eddy Simulations (LES) with a Smagorinsky subgrid-scale model [106]. These simulations have been conducted on 360 cores for 25 h real time reaching 600 s simulation time with a time step of 0.01 s.
- **BEM:** This method uses wind fields recorded in the CFD domain on an equidistant 31×31 grid with a grid cell size of 4.5 m in both directions. In this case the fields are obtained at the position of the rotor from the same mesh as for the AL method but in an empty CFD domain. This seems to be a reasonable choice, because under this condition the TI at the rotor will be comparable for the CFD and BEM simulations. The BEM based tool FAST v8 [16, 17] in combination with AeroDyn v15 [107] with the Beddoes Leishman type unsteady aerodynamics model [107, 108] and an equilibrium wake model is used in this work. The BEM model relies on the very same airfoil data and correction models as the AL, but with only 17 blade sections. Because of the simplicity of the BEM approach the simulation with the same time stepping and total time as for the higher fidelity approaches only took two minutes on one core.

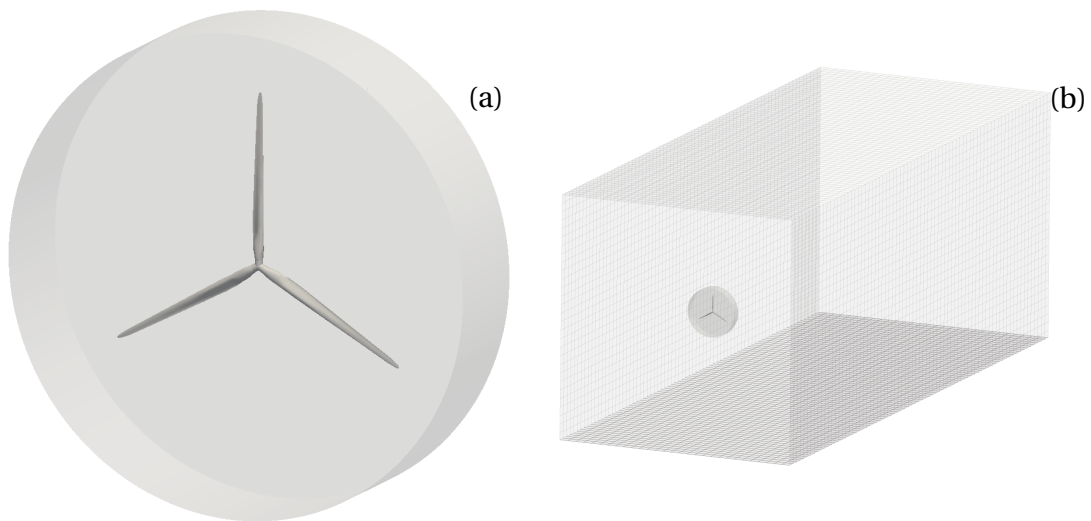


Figure 6.1: Grids of (a) rotating part and (b) full domain of Blade Resolved (BR) simulation.

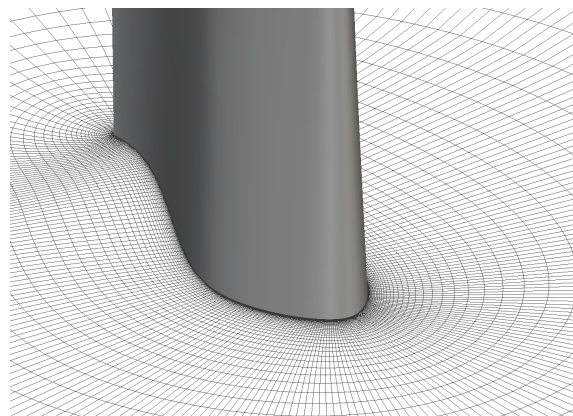


Figure 6.2: View onto the grid at the pressure side of the rotor blade.

6.1.2 Results

In this section the results of this study are presented. The focus lies on the wake structure, average and standard deviation of sectional and integral forces, as well as fatigue loads and PSD's.

Wake Dynamics

Snapshots of the velocity magnitude for the BR and AL cases are shown in Figure 6.3. Despite the differences in the methods both simulations show similar fields in terms of the velocity magnitude upstream of the turbine. This leads to the conclusion that the induction zone of the turbine is also similar for both simulations. For a more detailed view of the similarities and differences of the two compared CFD methods the wake structure is analyzed by the time series of the main stream component at 0.5, 1 and 2 diameters at the centerline

downstream of the nacelle in Figure 6.4. It can be seen that the wind velocity time series is in good agreement in most time intervals. As a quantitative measure of similarity of the wake structure, the coefficients for the correlation between both simulations are calculated by

$$\rho(x) = \frac{\langle (u_{AL}(x, t) - \bar{u}_{AL}(x)) (u_{BR}(x, t) - \bar{u}_{BR}(x)) \rangle_t}{\sigma_{AL}(x) \sigma_{BR}(x)} \quad (6.2)$$

where we used the time averaging operation $\langle \cdot \rangle_t$, the standard deviations σ_{AL} and σ_{BR} and the local mean values \bar{u}_{AL} and \bar{u}_{BR} of the time series of AL and BR simulations. The correlation is 0.54, 0.41 and 0.51 for 0.5, 1 and 2 diameters downstream, respectively. This shows that the wind field dynamics are rather similar and not uncorrelated at different distance from the rotor for both simulation methods. However, the BR simulation is resolving the tip and root vortex in a more physical way which results in smaller structures in the near wake.

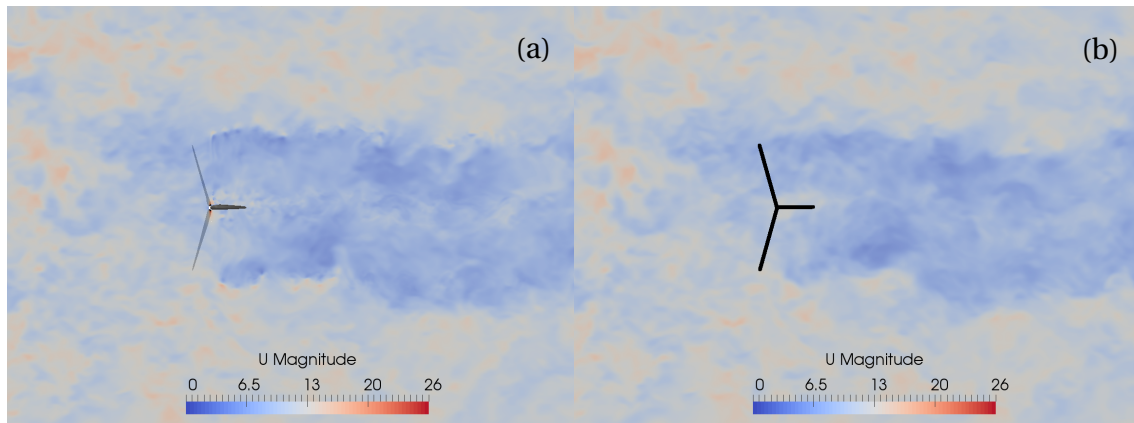


Figure 6.3: Snapshots of the velocity magnitude for (a) BR and (b) Actuator Line (AL) simulations.

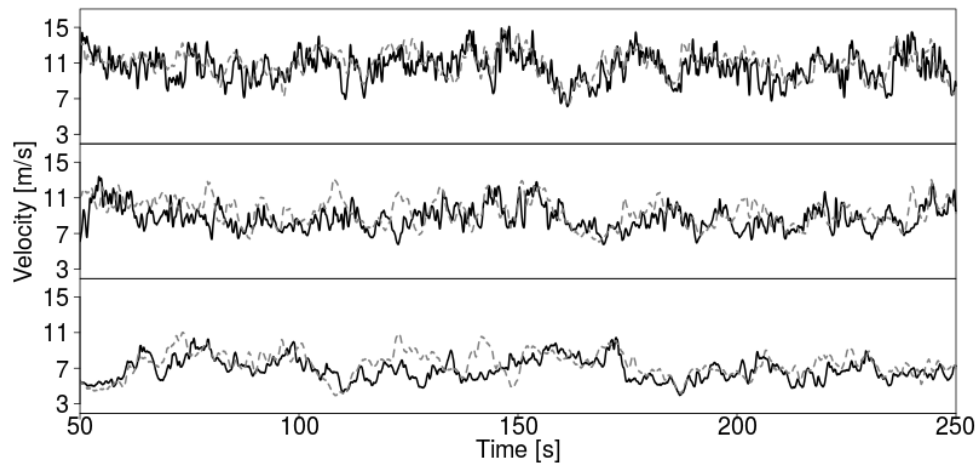


Figure 6.4: Wind velocity time series of BR (black, solid) and AL (grey, dashed) simulation for 0.5, 1 and 2 diameters (from top to bottom) at the centerline downstream of the rotor nacelle.

Sectional Forces

All three simulation methods (BR, AL and BEM) are compared based on averaged sectional quantities, namely axial and tangential forces, the corresponding standard deviations and the EFL. The sectional axial and tangential forces on the blade do not reveal big differences for the average between all cases in the mid-span as shown in Figure 6.5. However at the root (up to 30% of span) and the very tip (from 80% of span onwards) some differences can be observed. BEM and AL rely on similar root and tip correction models and the very same airfoil data which explains their good agreement. In comparison to the more realistic BR case, where 3D effects are modeled physically, the forces at the root and tip section are far off supporting the well known issues with 3D effects for BEM and AL. The more developed vortices in the BR simulation induce much higher loads in the root and tip region than for the other methods.

The standard deviations for the tangential and axial force distributions, shown in more detail in Figure 6.6, are very different for all three methods. With the BR case as the reference the standard deviation of sectional forces tend to be lower at the root of the blade for the BEM and AL methods whereas they are larger in the mid-span. Close to the tip at approximately 95% of the blade the AL method gives much smaller values while BEM is in the range of the BR simulation. The corresponding errors are estimated by following three steps. In the first step the time series for the specific forces at each radial position are separated into five distinct sub time series. In the second step the standard deviation for each sub time series is calculated. Finally the standard deviation of the set of the standard deviations from the second step is computed which provides the error for the whole time series.

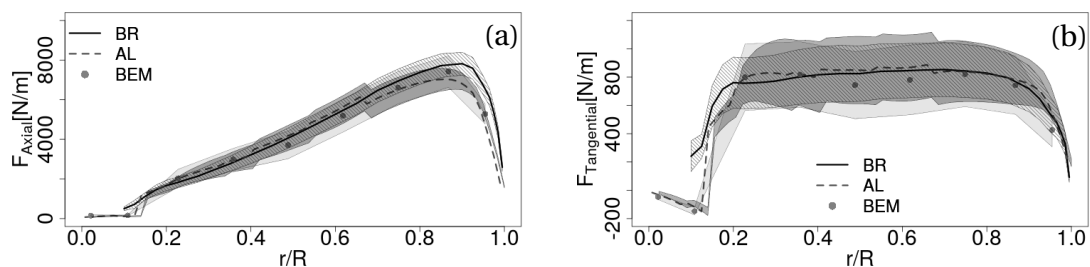


Figure 6.5: Radial distributions of (a) axial and (b) tangential forces per unit span. The shaded areas illustrate one standard deviation of the fluctuations.

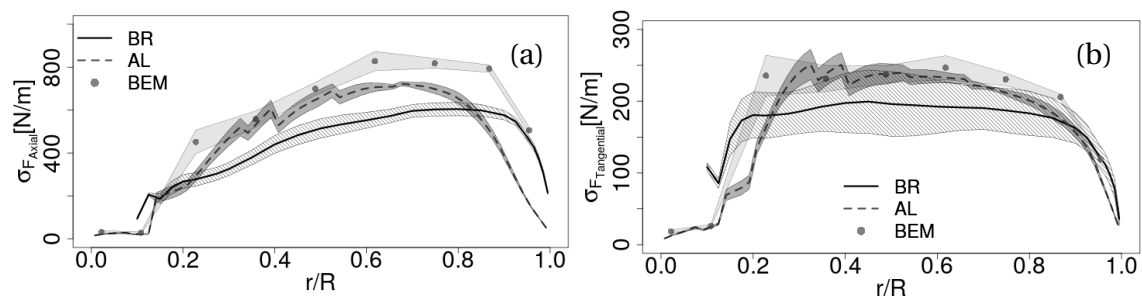


Figure 6.6: Radial distribution of standard deviation of (a) axial and (b) tangential forces per unit span. The shaded areas correspond to errors.

A more detailed insight in the standard deviation is gained by looking at the PSDs of axial and tangential forces at 22%, 50%, 75% and 95% radial position, shown in Figures 6.7 and 6.8.

All blade sections have in common that the spectra of the highly resolved BR case drop fastest between 2 and 10 Hz to a constant noise level. This is due to the expected bigger structures generated by the blade geometry but also due to the DDES model which is treated as RANS in the boundary layer acting as a filter.

For the AL method the energy drop happens at much higher frequencies because of the missing geometry and the LES model, which generally filters at smaller scales. The noisy behavior at high frequencies is part of every simulation of this kind and is due to numerical instabilities resulting from the convolution of the forces given at the airfoil sections with a Gaussian kernel [109].

The BEM spectra show filtering effects at higher frequencies corresponding to a multiplication with a sinc-like-function but with different frequencies for different radial positions. The origin of this effect could not be found and has to be investigated further. Due to the missing geometry and the lack of unsteady wake effects BEM is also expected to make worse predictions than the higher fidelity methods in the high frequency range. Therefore this high frequency part has to be taken with care like for the other two methods with their aforementioned problems of smoothing for the AL and the RANS treatment for the BR case and none of them can be considered trustworthy in this range.

In the low frequency range, for axial as well as tangential forces it can be observed that in comparison to the other two methods BEM has a much higher energy content for the inboard section. This is responsible for the high standard deviation at this section.

At radial position of 50% and 75% of the blades all the spectra are very similar in the low frequency range but it is still obvious that BEM has a higher energy content up to the 1P frequency, especially for the axial forces. Furthermore all three methods are able to capture the 1P frequency which is based on the passing of the blades through long time correlated structures.

At the outboard section at 95% the energy content of the BEM results in low frequencies is in the same range as for the BR case, but the AL method shows significant smaller values and the 1P frequency is not captured anymore, especially for the axial forces, which is due to a smeared out tip vortex.

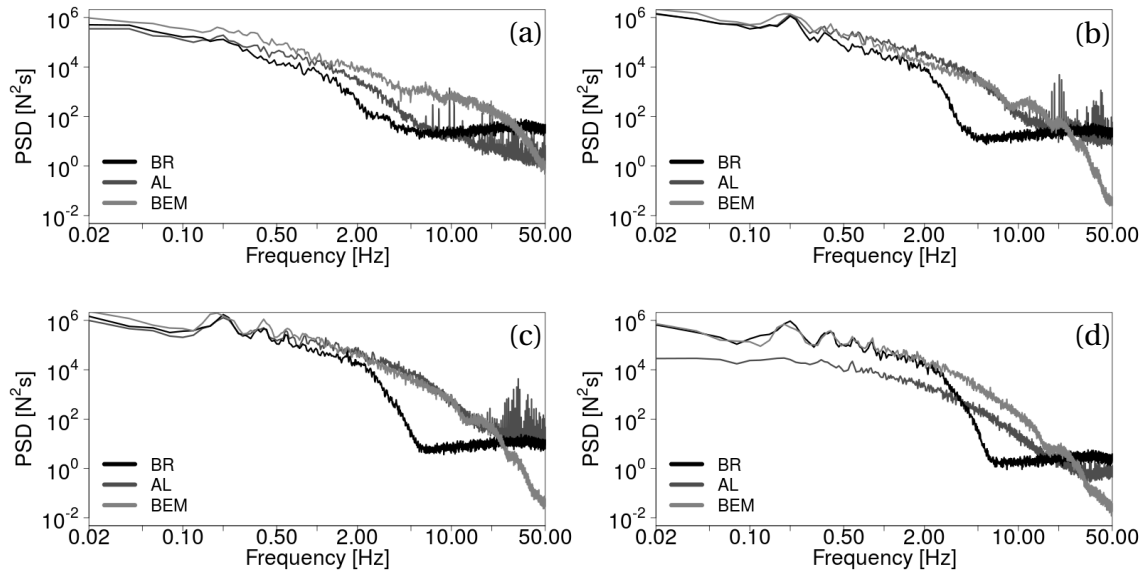


Figure 6.7: PSD of axial forces at (a) 22.5%, (b) 50%, (c) 75% and (d) 95% radial position.

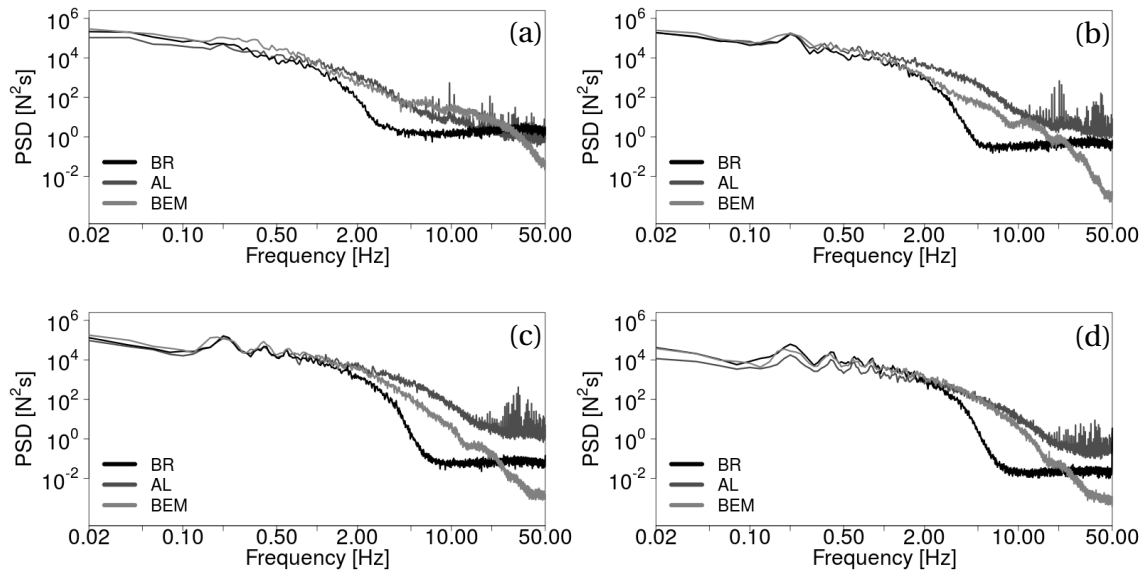


Figure 6.8: PSD of tangential forces at (a) 22.5%, (b) 50%, (c) 75% and (d) 95% radial position.

To illustrate the different flow structure sizes in the different simulation methods, the two point correlation of the sectional forces along the blade are measured. The argument for this approach is that the correlation of sectional forces is similar to the correlation of the wind velocity close to the blade surface, which is strongly connected to the integral scales of wind. In Figure 6.9 the correlation at each radial position with the forces at a reference position, here 22.5% radial location, is shown. This specific position is in principle arbitrary, but if the focus lies on the measurement of big structures, this point should not be too close to the tip or root where smaller flow structures dominate. However, even if the tendency for the correlation functions of the three different models is the same, the larger correlation

values for the BR case along the whole blade indicate that the structure sizes are also bigger than for the AL and BEM cases.

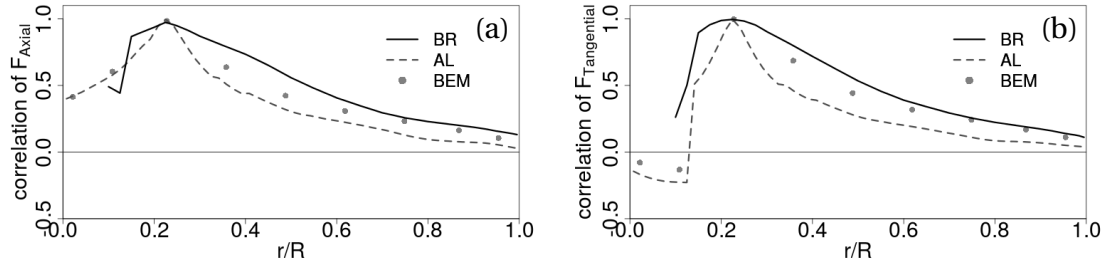


Figure 6.9: Correlation of (a) axial and (b) tangential forces at different radial positions with 22.5% position.

To give a more detailed description of the effect of forces on the rotor blades, fatigue loads at each section have been investigated. As observed in Figure 6.10, the EFL distribution over the whole blade is similar to the distribution of standard deviation in Figure 6.6. The BEM method gives higher EFL for every section for axial forces and almost everywhere higher values for tangential forces. All other points mentioned for sectional standard deviations also hold for sectional EFL. The errors are calculated with the same method as for Figure 6.6.

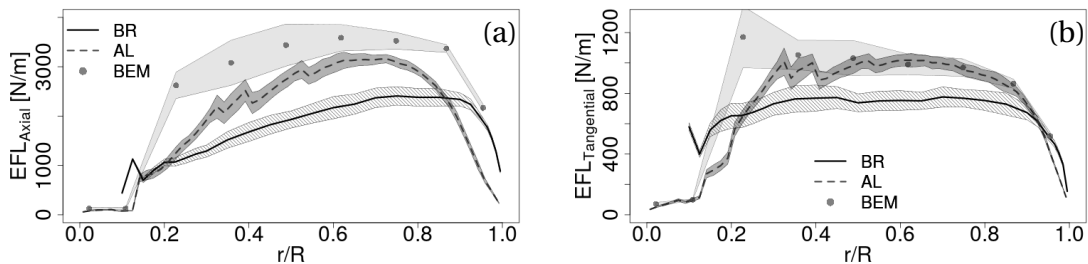


Figure 6.10: Radial distribution of (a) axial and (b) tangential equivalent fatigue loads per unit span. The shaded areas correspond to the errors.

The sectional EFL are linearly dependent on the sectional standard deviation for all simulation methods as seen in Figure 6.11. This raises the point that the dynamics quantified by two different properties of the load time series, namely standard deviation and EFL, are similar for all three methods. With the Wöhler Exponent $m = 8$ and the wind fields used here, this linear relation follows approximately $EFL = 4\sigma$ for axial and tangential forces.

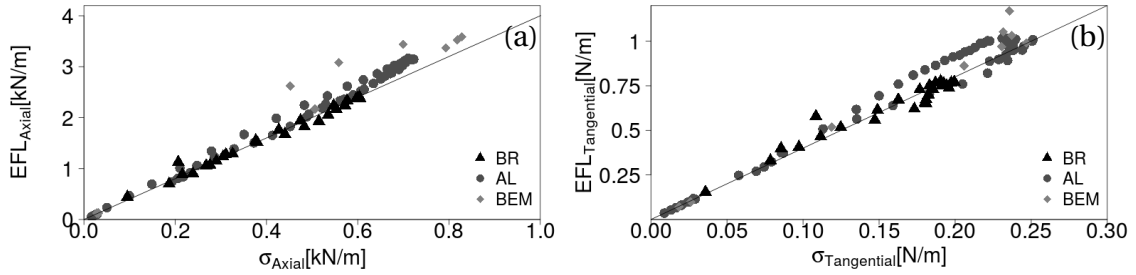


Figure 6.11: EFL dependence on standard deviation for (a) axial and (b) tangential forces for all three methods. The diagonal line is governed by $EFL = 4\sigma$.

Integral Forces

In the following, integral forces resulting from sectional forces from Section 6.1.2 are discussed. Time series of the aerodynamic thrust and torque are shown in Figure 6.12. As can be observed, the thrust as well as the torque evolution is very similar for BR and AL. With the definition of the correlation coefficient

$$\rho = \frac{\langle (F_1(t) - \bar{F}_1)(F_2(t) - \bar{F}_2) \rangle_t}{\sigma_1 \sigma_2} \quad (6.3)$$

where F_1 and F_2 are the considered forces and σ_1 and σ_2 the corresponding standard deviations, the correlation is calculated as 0.90 and 0.93 for thrust and torque respectively, even if the distribution of sectional forces and the wake dynamics are more different (see Figures 6.4–6.6). A comparison between BR and BEM reveals a much smaller correlation with values of 0.08 and 0.09 for thrust and torque. This supports the argument that the wind dynamics are handled in a very different way for BEM and CFD simulations for the current setup.

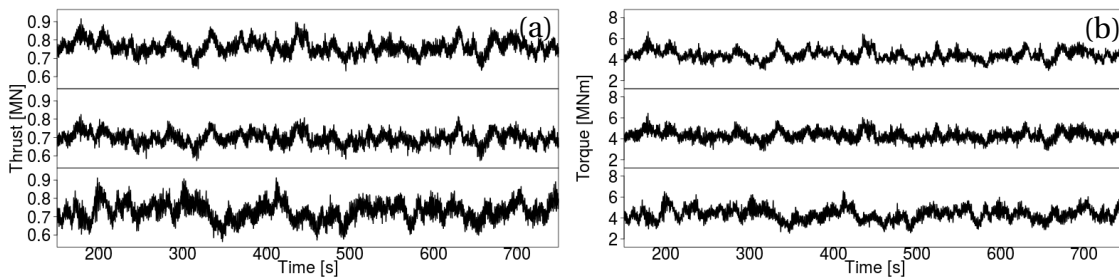


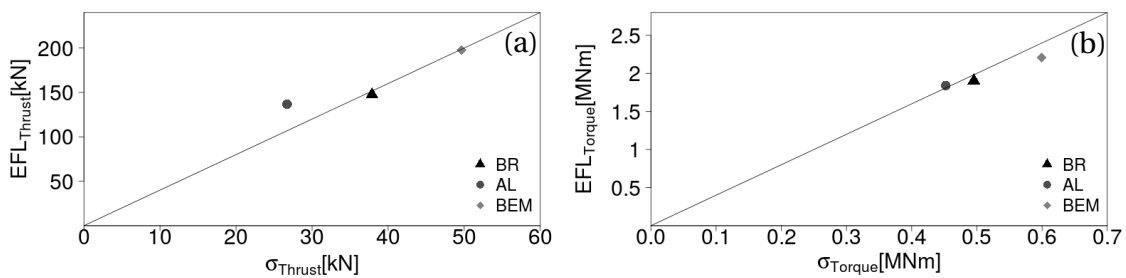
Figure 6.12: Time series for (a) thrust and (b) torque for Blade Resolved (BR), Actuator Line (AL) and Blade Element Momentum (BEM) methods (from top to bottom).

In Table 6.2 the means, standard deviations and EFL of torque and thrust for all three methods are illustrated with their corresponding errors. Those errors are obtained by separating the corresponding time series into five distinct equally sized ensembles and calculating the ensemble standard deviation. For comparison reasons the ratios of the calculated quantities for AL and BR as well as BEM and BR are shown, because the BR case is assumed to be the highest fidelity approach. For aerodynamic thrust and torque AL and BEM show lower values than the BR case with a minimum ratio of 91.7%, which can also be estimated from the sectional forces in Figure 6.5.

Table 6.2: Thrust and torque comparison by mean, standard deviation σ and EFL between BR, AL and BEM.

		BR	AL	BEM	AL/BR [%]	BEM/BR [%]
Thrust [kN]	mean	761 \pm 7.3	698 \pm 4.0	729 \pm 9.6	91.7	95.8
	σ	37.9 \pm 4.3	33.9 \pm 2.6	49.7 \pm 6.5	89.4	131.1
	EFL	147.6 \pm 9.7	136.7 \pm 4.2	190.1 \pm 8.0	92.6	128.8
Torque [MNm]	mean	4.43 \pm 0.10	4.32 \pm 0.08	4.35 \pm 0.13	97.5	98.2
	σ	0.495 \pm 0.044	0.452 \pm 0.038	0.599 \pm 0.061	91.3	121.0
	EFL	1.90 \pm 0.15	1.90 \pm 0.13	2.29 \pm 0.12	99.6	116.0

Analog to the relation between mean sectional forces and mean integral forces, the standard deviations of tangential and axial forces in Figure 6.6 correspond to a standard deviation in the thrust and torque. The standard deviation for the AL case is for both quantities approximately 10% smaller than for the BR simulation, because of the missing variance in the root and tip region. Especially for the torque the tip region plays a significant role. In contrast to that, for the BEM simulation an approximately 20 to 30% increase in the standard deviation is obtained which is also very clear from the much higher sectional standard deviation except at the root. A reason for the high standard deviation could be the equilibrium wake model used here, where the wake dynamics are not captured in a proper way. The relation between EFL and the standard deviation of integral forces is shown in Figure 6.13 where we additionally added the diagonal line governed by $EFL = 4\sigma$ like for sectional forces in Figure 6.11. Sectional as well as integral forces seem to follow the same linear trend.

Figure 6.13: EFL dependence on standard deviation for (a) thrust and (b) torque for all three methods. The diagonal line is governed by $EFL = 4\sigma$.

Further analysis of the EFL by the underlying range histograms in Figure 6.14 shows that for the thrust and torque force all three methods have in general a similar trend. But especially in the moderate ranges for the thrust and for large ranges in both quantities BEM has more counts than AL and BR. Due to their large weight the most important part for the EFL are the high ranges. Those high ranges must not be neglected, even if they have very few counts, because very important quantities like the difference of global maxima and minima contribute to them. Also the similarity of the inflow conditions justifies the comparison of

the loads. The contribution of all ranges to the EFL in Equation (2.31), namely $n \cdot r^m$, is shown in Figure 6.15, where the big contribution of the highest ranges to fatigue loads is very clear.

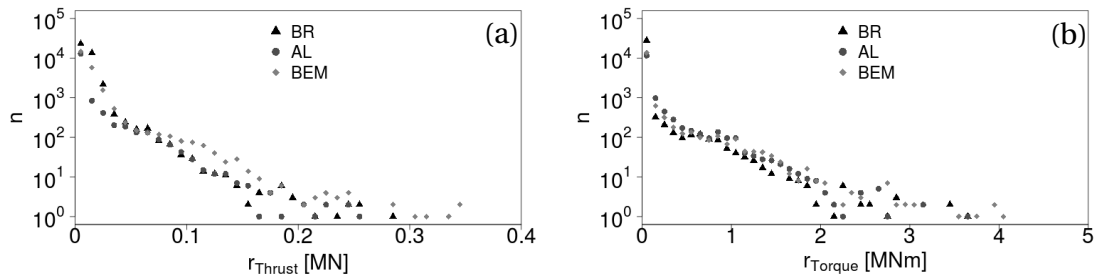


Figure 6.14: Range histograms for (a) thrust and (b) torque.

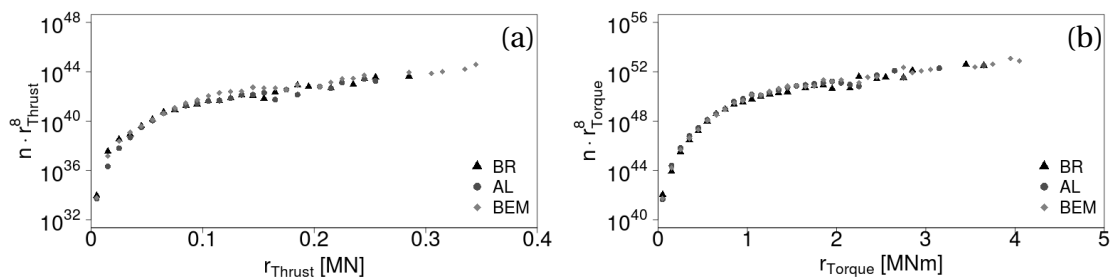


Figure 6.15: Contribution of ranges to EFL for (a) thrust and (b) torque.

For an analysis of the dynamics of torque and thrust, PSDs are investigated and shown in Figure 6.16. All three methods show a very good agreement in the shape of spectra for low frequencies in region I up to 1.5 Hz including the 3P frequency and the first harmonic. For higher frequencies up to approximately 4 Hz, here region II, BEM and AL are very similar but the BR method drops very quickly and saturates in a white noise like behaviour for higher frequencies in region III. The reason for this is the big structures generating blade geometry and the RANS model working in the boundary layer of the blade while the AL does not have a geometry and it uses LES everywhere and therefore does not smooth out the wind field in the vicinity of the blade as has been discussed already for the sectional forces. It again has to be emphasized that the BR case has the highest resolution in the blade region and therefore has the most reliable results. The difference between BEM and AL in the high frequency range in region III could be according to the missing damping, filtering and dynamic wake effects in the BEM case. The AL method uses a Gaussian filter to smooth out the forces along the blade and the wake is much more complex than in the static wake model of BEM. It has to be amplified, that especially for the torque, a transition from BEM to AL can not be made just by filtering the signals, because filtering corresponds to a drop in the PSD, which is not observed in the mid range.

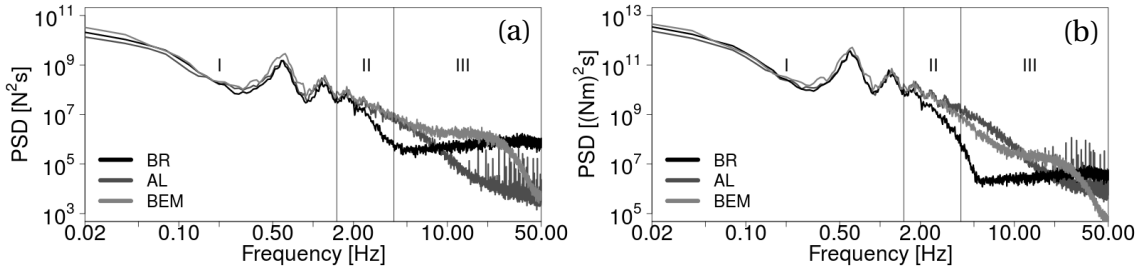


Figure 6.16: PSD of (a) thrust and (b) torque.

For a more detailed analysis, the cumulative frequency dependent variance normalized by the total variance, i.e.,

$$\hat{\sigma}^2(f) = \frac{\int_0^f PSD(f')df'}{\sigma^2} \quad (6.4)$$

has been investigated in Figure 6.17. This is equivalent to the energy content of the spectrum at frequencies smaller than f , normalized by the total energy contained in the spectrum. The energy content for the different regions can be determined as $\hat{\sigma}_{\text{region}}^2 = \hat{\sigma}^2(f_{\text{max}}) - \hat{\sigma}^2(f_{\text{min}})$ with f_{max} the upper frequency limit and f_{min} the lower frequency limit of the region. For all three methods the conclusion can be drawn that by far the most energy is contained in region I, in particular for the thrust: BR 95.4%, AL 93.3% and BEM 94.9%. Region II also contains a small amount of energy with 2.3% for BR, 5.8% for AL and 3.2% for BEM. The torque is distributed similarly with 97.7% for BR, 91.7% for AL and 91.1% for BEM in region I and 2.2%, 7.1% and 3.5% in region II. The variance contained in region III is negligible for both quantities. Based on the high percentage of variance contained in region I it can be concluded that the big difference in the total variance between BEM and the other two methods mainly stems from this frequency range. Therefore the extraction of wind fields at the position of the rotor plane has to be seen as a first step for this comparison and it has to be investigated if it is more appropriate to extract the fields downstream of the rotor position or to artificially damp the wind input in BEM on large scales.

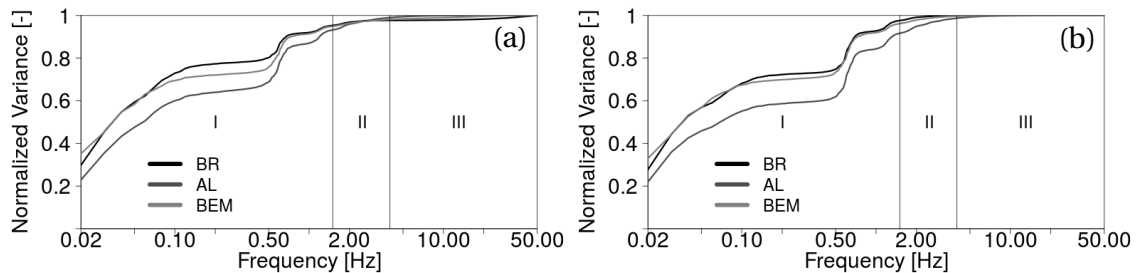


Figure 6.17: Normalized cumulative frequency dependent variance of (a) thrust and (b) torque.

6.1.3 Discussion

From this work it can be concluded that the AL, BR and the BEM method with extracted wind fields at the rotor plane from an empty domain are very similar with respect to averaged tan-

gential and axial forces, except close to the root and the tip. However, a comparison of BEM with the CFD methods with respect to the standard deviations of sectional and integral forces shows clear differences. For the integral quantities thrust and torque, BEM tends to overestimate the standard deviation compared to the other two methods. It is found out that the standard deviation differences between all methods mainly come from the different amplitudes in the first part of the spectrum and not from the filtering effects on larger frequencies. This leads to the conclusion that, if similar results for the standard deviation for BEM and CFD should be achieved, either the wind fields have to be extracted downwind of the rotor position from the empty domain simulation or a correction of wind fields for the BEM case has to be considered. A good starting point could be to substitute the equilibrium wake model by a dynamic wake model which could damp the oscillations and with it the standard deviation. Additionally, extracting the wind fields in an empty domain downwind from the position where the turbine is normally located will be part of the future work. Another contribution to the differences, which also should not be neglected, comes from the fact that the turbulent wind field decays across the CFD domain due to the missing energy injection. In an empty domain, the turbulence intensity is higher upstream and lower downstream of the position, where the turbine would be located. This decay is not considered within the BEM simulation and could be a reason for the differences.

An indication for a linear dependence between standard deviation and EFL could be found for sectional as well as integral forces which seem to follow the same trend. This shows that the dynamics characterized by the EFL and by the standard deviation are similar for all three methods. However, this dependence is assumed to be existent only if the wind fields are comparable with respect to temporal and spatial correlations to assure similar turbulent structures which play a big role for EFL estimations. An advantage of this linear relationship could be that the computational expensive rainflow count algorithm may not be needed if one is interested in a rough estimation of equivalent fatigue loads, because a simple calculation of the standard deviation could give this information as well. It is believed that this relationship will change for more complex atmospheric wind, which is usually not characterized by a unique standard deviation but a distribution of standard deviations (see e.g. the Castaing model [8]).

Even if no experiments for comparison were performed, the BR simulation with its high resolution close to the blades and the full geometry consideration can be expected to be the most physical and therefore it should be seen as a benchmark case. However, a further part of the future work should be a fair comparison with experiments where the focus should be set on the statistical equivalence of the wind fields at least across the full rotor size in the CFD domain, in the BEM simulation and in the experiments.

6.2 Simulation of a wind turbine with Gaussian and intermittent wind fields

In the last section a first step has been done to study the effect of turbulent wind fields on forces and loads of wind turbines. By following a step by step approach the next logical part is to deal with the effect of intermittent turbulence on wind turbines. For this reason similar simulations in the same CFD domain as in the last section have been performed, i.e. the tur-

bulence is injected at the domain boundary by an inflow condition and not by an actuator in the middle of the domain like for the airfoil simulations. Also the rotor is simulated by three rotating actuator lines which are rotating with a constant circular velocity with the same characteristics as explained before. The actuator line approach has been chosen because it does not need a highly resolved grid next to the rotor which allows to inject turbulence at the inlet of the domain. Furthermore the relatively small number of cells is accompanied by a small computation time which outweighs the quality increase for fully resolved blade simulations. This approach is justified by the fact that for the following very coarse studies such high resolutions are not expected to change the general outcome.

As has been done for the airfoil simulations, two different kinds of fields have been generated, namely a non-intermittent and an intermittent one. By using the energy correction introduced in section 3.4.2 the Gaussian and intermittent fields gain the same energy spectrum as defined originally by the CTRW model parameters. Additionally to partially correlated wind fields, where the in-plane correlation length is limited, also fully correlated wind fields with unlimited in-plane correlation have been created. In contrast to the former one, full correlations also allow a Gaussianization of the one point statistics by using the algorithm explained in section 3.4.3. With this algorithm the kurtosis and the skewness are brought to the Gaussian level up to a maximum deviation of 10^{-5} . This allows to make the fields even more comparable and to filter out low order statistical effects which otherwise are expected to dominate the outcome of the load analysis.

A mean wind speed of 11.4 m/s has been set for all fields, but the standard deviation had to be chosen differently for partial and full correlations due to the increased decay of turbulence in the partially correlated case. The goal is always to reach a turbulence intensity of approximately 10% close to the rotor position to be able to neglect variance differences in the wind for the upcoming load analysis. For the field generation the parameters $l_c = 20$ m, $\omega_c \approx 0.34$, $t = 660$ s, $u = 11.4$ m/s, $\sigma = 2.28$ m/s, and $\Delta t = 0.01$ s have been chosen with $\alpha = 1$ for Gaussian and $\alpha = 0.6$ for intermittent wind fields.

In the next sections first partially correlated fields are studied before full in-plane correlations are considered. For both inflow types a simulation in an empty domain has been performed before the rotor in form of the rotating actuator lines is added into the center of the domain. With the simulation of an empty domain the objective to characterize the evolution of the different types of turbulence throughout the domain shall be pursued. An approximation of the expected wind fields in the vicinity of the rotor can therefore be made and comparable fields can be created.

6.2.1 Empty Domain Simulation with Partially Correlated Fields

Partially correlated Gaussian and intermittent inflow fields are injected into the empty domain at the inlet patch 300 m in front of the planned rotor position. A first impression on the flow field can be gained in the snapshots shown in Figure 6.18. If the flow is tracked at the center line from the inlet to the outlet, the velocity field becomes more uniform which is an indicator for decaying variance.

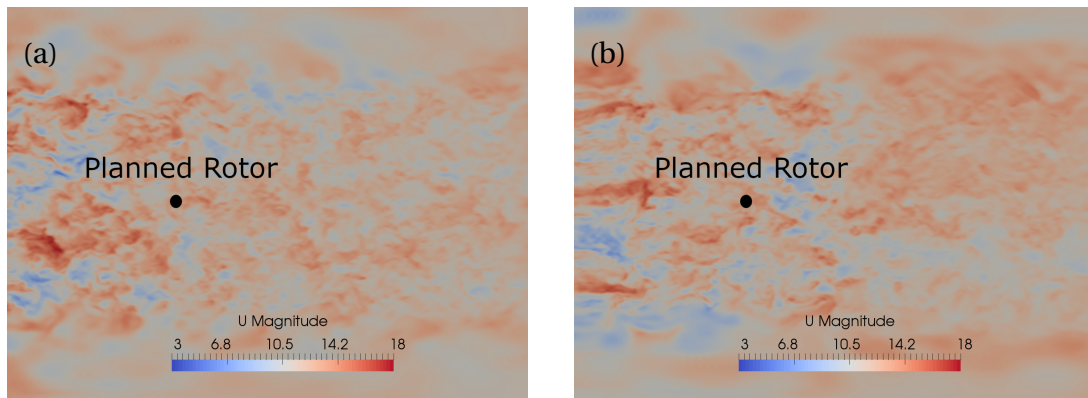


Figure 6.18: Snapshot of the flow field in an empty domain under partially correlated (a) Gaussian and (b) intermittent inflow conditions.

The evolution of mean wind speed and standard deviation at hub height from the beginning up to 300 m downstream of the planned rotor are depicted in Figure 6.19. For the distance calculation the rotor location is used as a reference. At the rotor position itself no measurements have been taken but data has been collected up to 50 m upstream and downstream of the rotor.

Both the intermittent and the Gaussian wind fields show very unsteady mean wind speeds across the whole domain in Figure 6.19a. Up to 150 m upstream of the virtual rotor position both means are approximately equal while they differ by almost only 1% at a downstream distance of 50 m and 2% at a distance of 200 m.

The standard deviation for both fields in Figure 6.19b shows a transient in the first part of the domain and can be considered as equal in the inner region between -150 m and 150 m. Further downstream the curves start to separate again. Overall the standard deviation is decreasing in downstream direction due to the absence of shear and the missing injection of energy. So the standard deviation at the turbine position is smaller than the inlet turbulence by almost a factor of two. The dotted line marks the target value of 1.14 m/s which stands for a turbulence intensity of 10% if a mean value of 11.4 m/s is assumed. It can be noticed that the turbulence intensity is reached exactly at the rotor position which was managed by doing several simulations beforehand and changing the standard deviation of the inflow each time until the target value is hit. If computational resources and time are limited, it has to be kept in mind that different realizations of the inflow naturally evolve in a different way and the aforementioned pre-simulations have to be performed for the sake of comparability. A reduction of the domain resolution or the simulation time can be carried out to fit the requirements in an appropriate way.

Despite of the differences of mean and standard deviation for both types of wind fields, the most important region, i.e. close to the position where the rotor should be added, is comparable and rotor simulations are expected to be almost unaffected by those small differences.

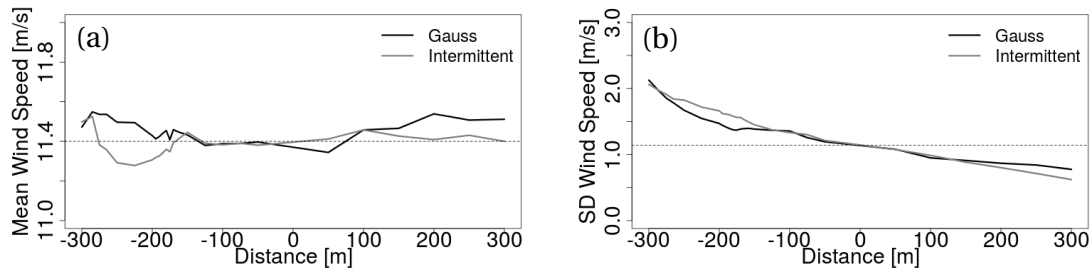


Figure 6.19: Evolution of (a) mean and (b) standard deviation of the Gaussian and intermittent windfields at the centerline of the domain. the dotted horizontal lines mark the mean wind speed of 11.4 m/s and the standard deviation of 1.14 m/s.

The histograms of the wind speed close to the inlet and 50 m in front of the rotor position shown in Figures 6.20a and b make clear that both fields differ quite a bit at the tails of the distribution even after the generated CTRW fields are made comparable with the spectrum correction algorithm mentioned before and the adjusted mean and standard deviation. This deviation can be attributed to the short time series accompanied by the lack of high and low wind speed events which makes those tails not reliable in the statistical sense. Also a small skewness seems to build up in the decaying process. Still the inner part around the mean wind speed equals quite well a Gaussian distribution for both cases. The already mentioned loss of energy of the flow throughout the domain is also visible in terms of the reduced width of the wind speed distribution close to the planned rotor position.

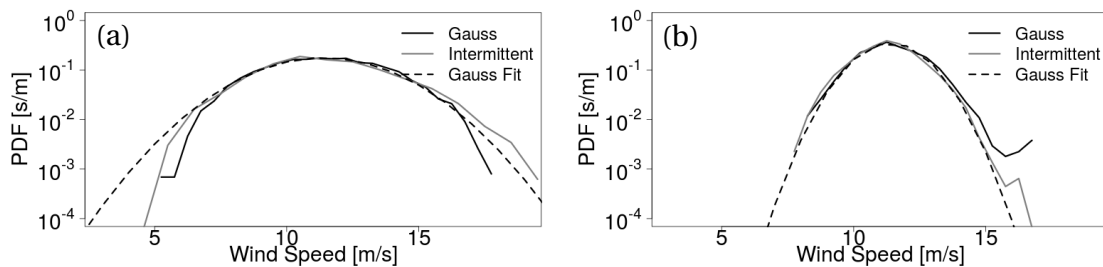


Figure 6.20: Distribution of wind speed in main stream direction for Gaussian and intermittent wind fields (a) close to the inlet and (b) 50 m in front of the planned turbine in an empty domain.

In addition to the one point distributions also normalized increment distributions are plotted in Figure 6.21 for the same positions where two different effects become visible. First, the kurtosis of the heavy-tailed distribution of the intermittent case decreases with going downstream due to the decaying process. Second, the originally Gaussian distributed wind field shows a contrary development by building up intermittency close to the turbine position which can easily be noticed in the heavy-tails and the increased skewness. Here a transition to another, maybe more natural, type of turbulence happens but with a much smaller variance because no additional energy is injected.

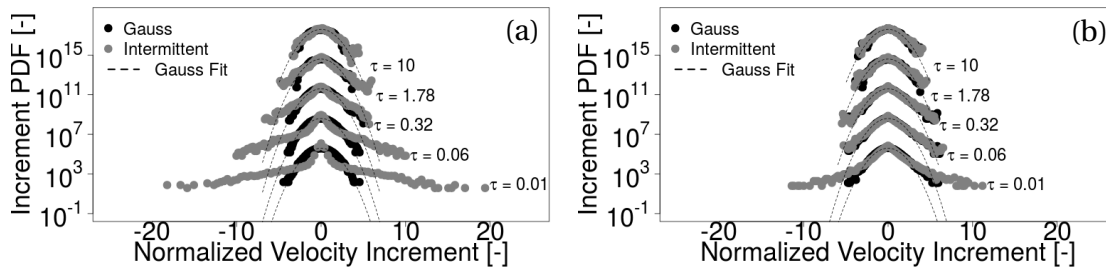


Figure 6.21: Increment distribution in main stream direction for Gaussian and intermittent wind fields (a) close to the inlet and (b) 50 m in front of the planned turbine in an empty domain.

The overall evolution of increment kurtosis is illustrated in Figure 6.22 where the maximal and minimal values are plotted for time gaps between $\tau = 0.01$ s and $\tau = 10$ s, while the area in between is shaded. Clearly the strong decay of the maximum for the intermittent wind field is visible in the first part of the domain until it reaches an equilibrium close to the position where the rotor shall be located in further simulations. The equilibrium value has a realistic value, which was measured to be around 12 at offshore met masts [90]. For measurement points downstream of the planned rotor the increment kurtosis increases again. A reason for this might be the strong coarsening gradient of the mesh behind the turbine position which will have an impact on the flow field and can alter especially higher order statistics, which are more sensitive to the relatively small errors introduced by the grid. The inlet of Figure 6.22 shows the zoomed in evolution of the maximal and minimal increment kurtosis under Gaussian inflow conditions. Here the increase of increment kurtosis can be observed, which was already present in Figure 6.21b.

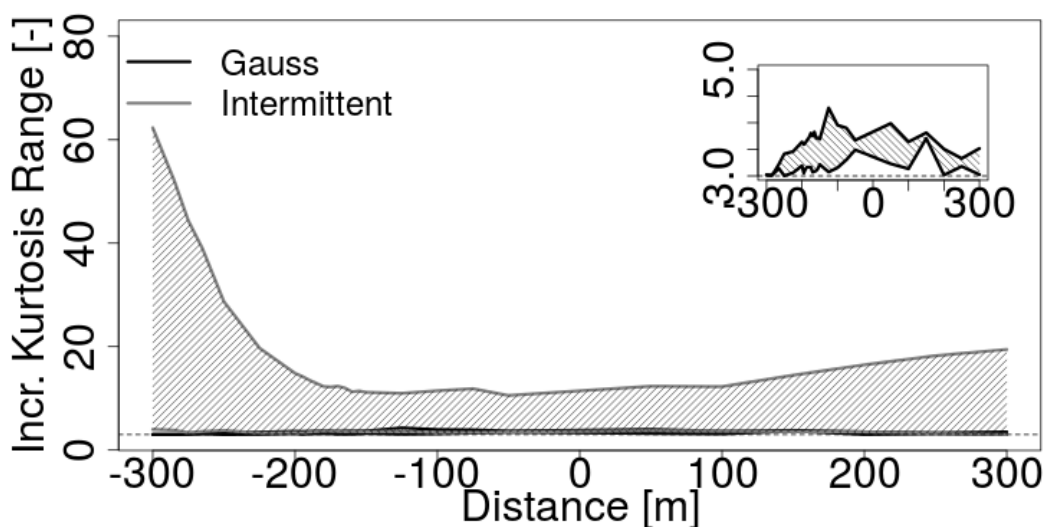


Figure 6.22: Evolution of the range of increment kurtosis of the Gaussian and intermittent windfields for τ between 0.01 s and 10 s at the centerline of the domain. The inlet shows the zoomed in Gaussian case.

6.2.2 Rotor Simulation with Partially Correlated Fields

With the known evolution of the CTRW fields in an empty domain the rotor in form of three rotating actuator lines is added at the previously planned position and similar properties of the flow are investigated before forces and loads on the rotor are studied.

Flow Fields

The corresponding flow fields are depicted in Figure 6.23 at the same instance of time as in Figure 6.18. In front of the rotor the flow field is almost identical to the one in the empty domain but the wake of the rotor leads to very different structures behind the rotor. A wake meandering effect is also visible for both cases. Remarkably is also the jet originating from the center of the rotor due to the missing nacelle in the actuator line model.

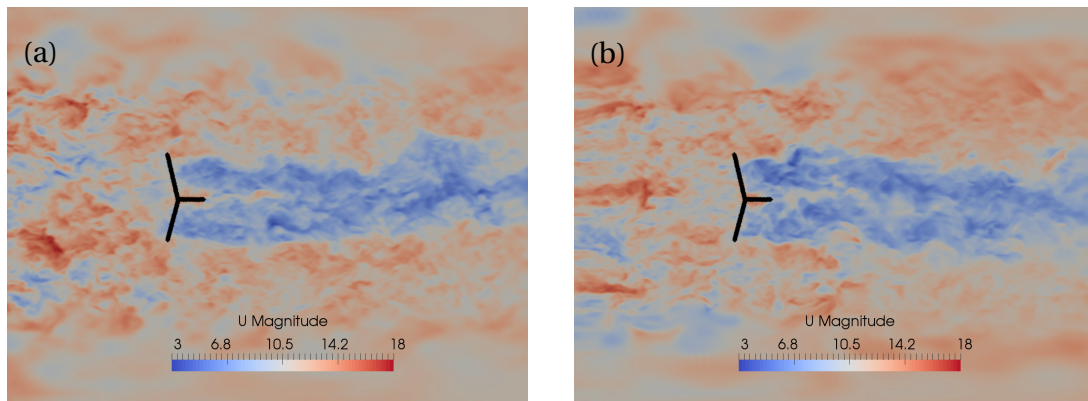


Figure 6.23: Snapshot of the flow field in the domain with a rotor under partially correlated (a) Gaussian and (b) intermittent inflow conditions.

Compared to the simulation without a rotor, the mean wind speed at hub height in Figure 6.24a is not constant anymore but drops due to induction up to the distance of 50 m upstream of the rotor, which is the measurement point closest to the rotor. At the rotor position the flow experiences a speed up due to the jet generated in the middle of the rotor, where no hub is simulated. Downstream of the next measurement point at 50 m behind the rotor the wake of the rotor evolves where the mean wind speed drops by a large amount up to the end of the domain. Almost one third of the mean wind speed from the inflow is lost due to the energy extraction by the rotor and mixing effects. If the differences of Gaussian and intermittent wind fields are focused on no difference between those flows can be perceived close to the rotor. Further away at distances larger than 150 m the Gaussian flow shows up higher mean values than the intermittent one but this may be accounted to the random nature of turbulence and the unconverged statistics.

The standard deviations of both fields in Figure 6.24b drop until the rotor position is reached but then they converge to a more or less constant level which is higher than the value at the rotor position in the empty domain. The reason for this behavior is that the rotor converts the energy contained in the mean flow partially into turbulent kinetic energy in the wake which compensates the decay. While the mean values of the intermittent and Gaussian flows can be seen as equal close to the rotor, the standard deviation deviate by a

small amount. In front of the rotor the intermittent field is slightly more fluctuating than the Gaussian one while it is vice versa directly behind the rotor. Further away, where also the mean flows start to deviate from each other, the intermittent flow shows up a higher standard deviation.

It is reasonable to assume that the differences in the mean and standard deviation are not related to the type of inflow chosen here but more to the realizations taken from the CTRW generator. Other realizations of Gaussian and intermittent inflows are also possible where the behavior is vice versa to the one shown here.

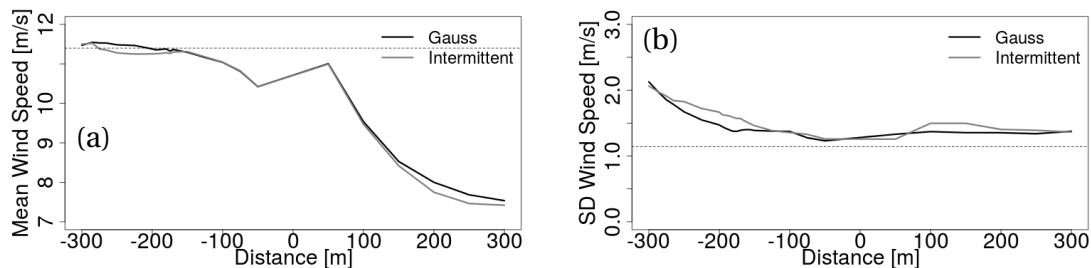


Figure 6.24: Evolution of (a) mean and (b) standard deviation of the Gaussian and intermittent windfields at the centerline of the domain.

If now the wind speed histograms in Figure 6.25 are compared to the histograms in an empty domain (see Figure 6.20) no differences can be observed for the flow fields close to the inlet, because the turbine does not have an impact at this distance. But close to the turbine the shift in the mean as well as the broader distribution can be noticed, which is related to the increased standard deviation. The distributions are still approximately Gaussian in the center but for large wind speeds deviations from the Gaussian distribution are present, similar to the empty domain case, which might be linked to unconverged statistics or an increased skewness of the distribution. Nevertheless a clear answer is not available at this point and further investigations have to be made in future works if one is interested.

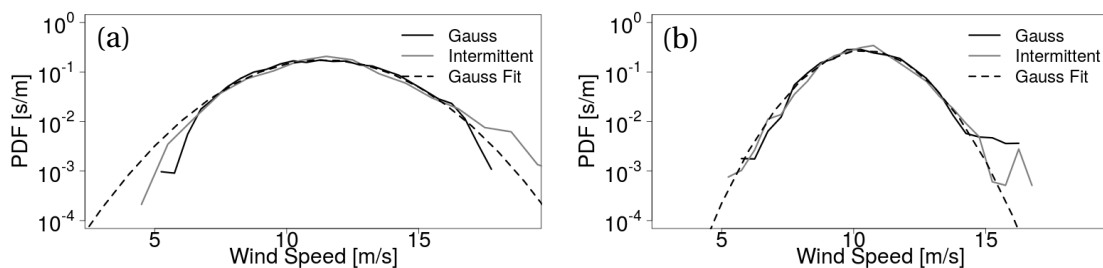


Figure 6.25: Distribution of wind speed in main stream direction for Gaussian and intermittent wind fields (a) close to the inlet and (b) 50 m in front of the planned turbine in an empty domain.

Figure 6.26 shows the compensated power spectra of Gaussian and intermittent wind fields in front of the rotor, which fit quite well to each other. It can be concluded that Gaussian and intermittent wind fields are generally indistinguishable in their spectral properties

and the following load analysis can be performed without taking spectral differences into account. Furthermore the intermittency information can not be achieved out of the power spectrum alone, which is also desired for the sake of comparability.

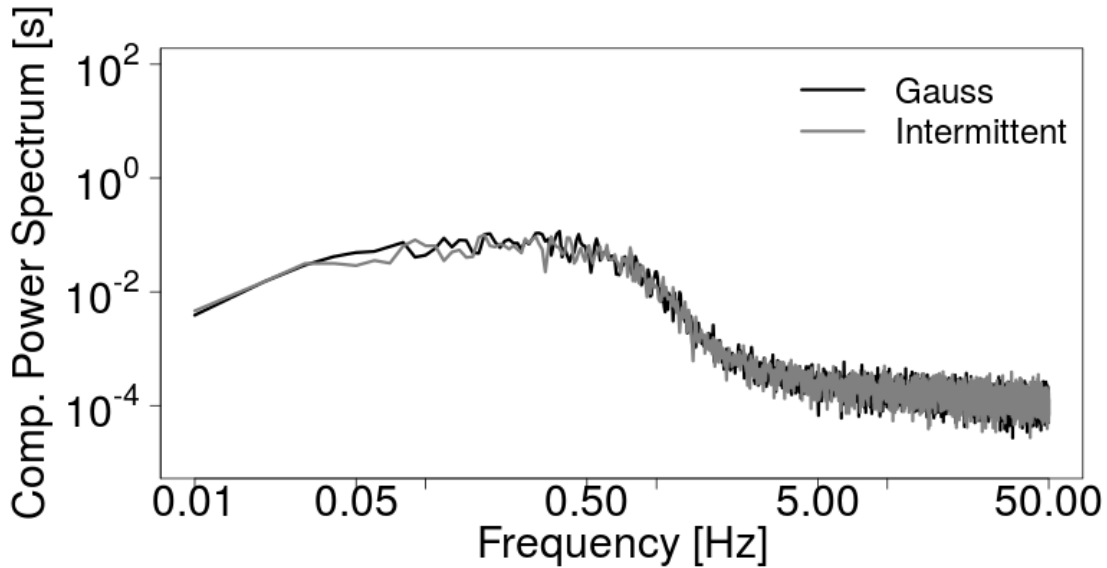


Figure 6.26: Spectra of both wind fields 50 m in front of the rotor.

By looking at the normalized increment distributions in Figure 6.27 it can be highlighted that close to the inlet they are only different to the empty domain simulations if very precise comparisons are performed. In front of the rotor the originally Gaussian wind field developed an increased kurtosis, as already seen in Figure 6.21, but here the skewness is close to zero. This shows that adding the rotor object to the domain can influence the increment characteristics enormously.

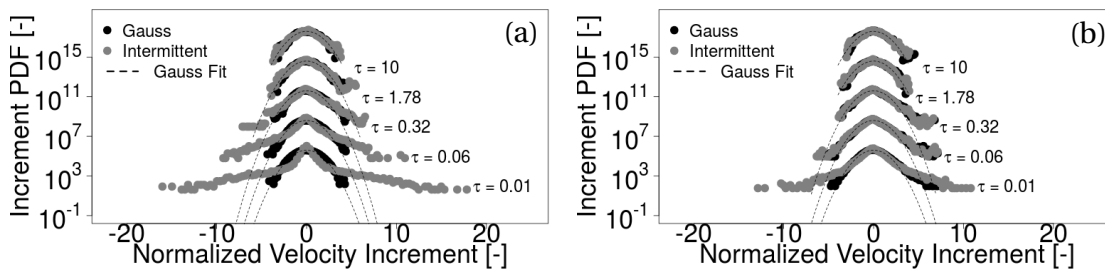


Figure 6.27: Increment distribution in main stream direction for Gaussian and intermittent wind fields (a) close to the inlet and (b) 50 m in front of the planned turbine in an empty domain.

The evolution of the increment kurtosis range throughout the domain is depicted in Figure 6.28. It can be summarized that this plot is very similar to its counterpart in the empty domain in Figure 6.22 except that for the intermittent inflow case the kurtosis in the wake of the rotor is much higher than in the empty domain. The Gaussian inflow case also shows up regions with an increased increment kurtosis in the wake, especially close to the rotor, but

also in front of the rotor. However, the maximum seems to be dominated by chance and the different peaks are not trustworthy. Despite of this fact, here as well as for the empty domain a trend to higher wind speed increment kurtosis with going downstream can be noticed for Gaussian inflow fields.

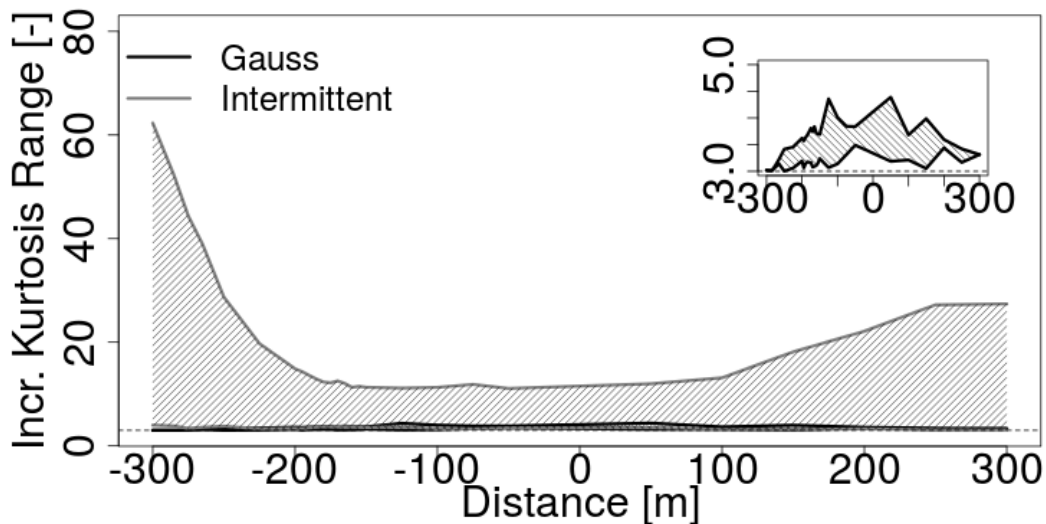


Figure 6.28: Evolution of the range of increment kurtosis of the Gaussian and intermittent windfields for τ between 0.01 s and 10 s at the centerline of the domain. The inlet shows the zoomed in Gaussian case.

Forces

After the wind field in the empty and the rotor containing domain has been studied, it will be focused on the forces and fatigue loads on the rotor. Again thrust and torque as well as axial and tangential forces are looked at.

In Figure 6.29a an excerpt of the time series of thrust and torque are compared under Gaussian inflow conditions, while in Figure 6.29b the thrust and corresponding wind speed in front of the turbine are plotted together. Because of the fact that the wind field is measured 50 m in front of the rotor, the time series for the wind has been shifted by the corresponding time (4.39 s) under assumption of Taylor's frozen turbulence hypothesis. For comparison reasons all time series have been normalized to zero mean and unity standard deviation.

The thrust and torque react nearly identically to the wind speed changes as can be seen in Figure 6.29a and are therefore very highly correlated with each other. One might think that also the wind speed shows similar patterns but as illustrated in Figure 6.29b the wind shows up much slower dynamics than the forces. However, on larger scales the forces follow pretty well the wind dynamics. The time series under intermittent conditions are not plotted here because the behavior is similar to the Gaussian cases.

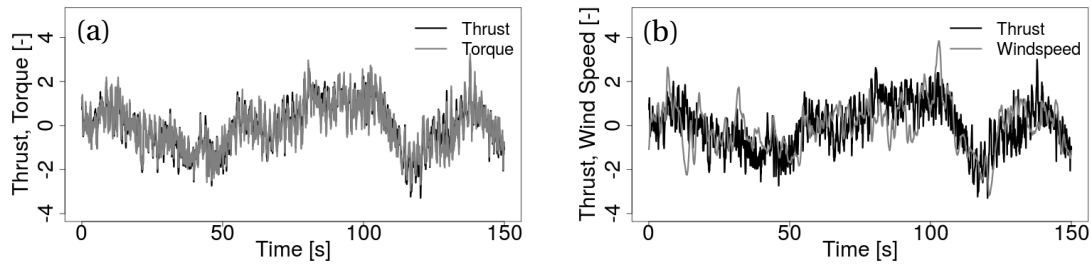


Figure 6.29: Time series of normalized (a) thrust and torque, and (b) thrust and wind speed (shifted by 4.39 s).

In Figure 6.30 the spectra of normalized torque, thrust and the Gaussian wind speed in front of the rotor are depicted. As already guessed from the time series, the spectra of thrust and torque are almost identical because of the high correlations. Both also show peaks at the 3P frequency of ≈ 0.6 Hz and its multiples for the rotational speed of 12.1 rpm. Those peaks also appear even though no tower is present due to the fact that the same wind structures are crossed by each blade in several rotations. Spatial as well as temporal autocorrelations of the wind are important here to achieve those frequencies. As supported by the time series in Figure 6.29b the wind speed itself shows a different spectrum which shows up more low frequent and less high frequent structures than the forces, except at the lowest frequency. This makes clear that the wind dynamics can not be transferred directly to the rotor dynamics, in fact the involved transformation is rather complex.

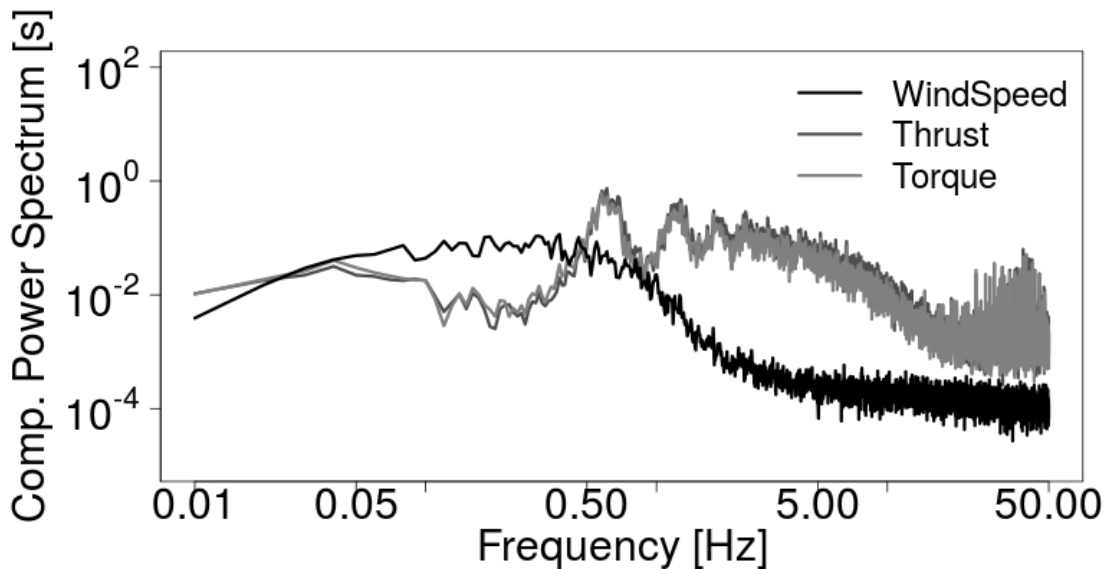


Figure 6.30: Spectra of torque, thrust and Gaussian wind.

In the next step the increment distributions of the integral forces are visualized in Figure 6.31 where the heavy-tails under intermittent but also Gaussian inflow conditions are visible. However the intermittent cases show much larger heavy-tails and a small peak in the middle. It is mentioned that these statistics are converted from the wind field to the forces but a Gaussianization effect takes place due to the spatial expansion of the blades which filters out extreme events. Furthermore the drastic change of power spectra in Figure 6.30 is an

indicator for a break up of the phase amplitude relation which was present in the wind and which is also very important for the change of its intermittent behavior.

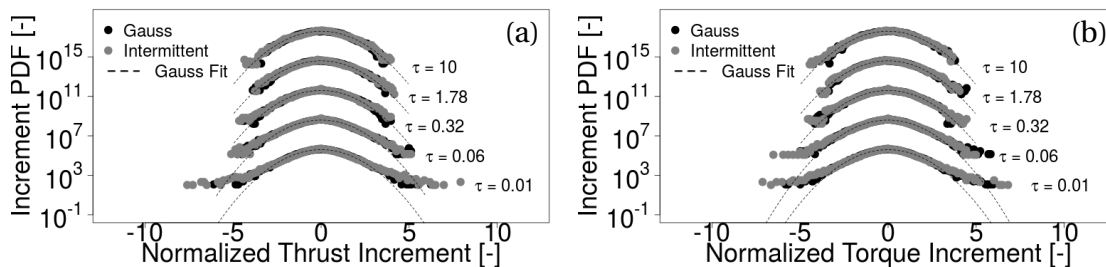


Figure 6.31: Increment distribution for Gaussian and intermittent wind fields of (a) thrust and (b) torque.

Figure 6.32 gives an overview over the increment kurtosis change with time delay τ . Gaussian as well as intermittent cases show an increment kurtosis larger than three for all time gaps according to the aforementioned reason. Although the Gaussianization effect changed the increment kurtosis of the intermittent case and the increment kurtosis of the Gaussian case increased, the intermittent simulation still shows higher increment kurtosis values for every studied time gap. Nevertheless, rather large fluctuations occur due to convergence issues, related to the short simulation time interval.

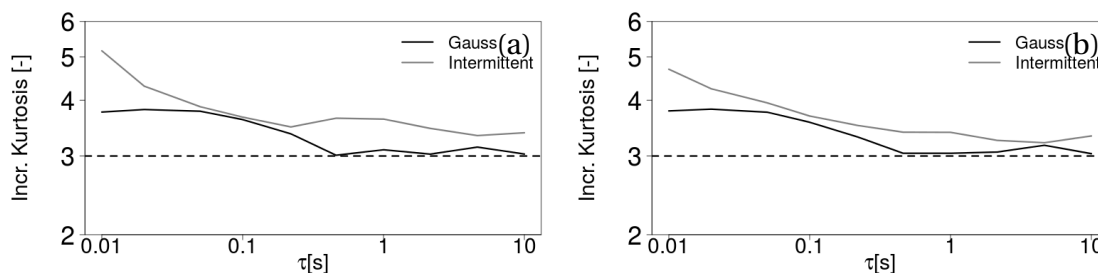


Figure 6.32: Increment kurtosis dependent on time delay for Gaussian and intermittent wind fields of (a) thrust and (b) torque.

Mean axial as well as tangential forces are compared between Gaussian and intermittent inflow conditions in Figure 6.33 where only slightly bigger contributions of intermittent wind to the forces can be perceived. Gaussian as well as intermittent fields also show similar standard deviations (shaded area) for both cases. Even though, small differences in the mean and standard deviation are present, it can be expected that intermittency has no direct impact on these quantities.

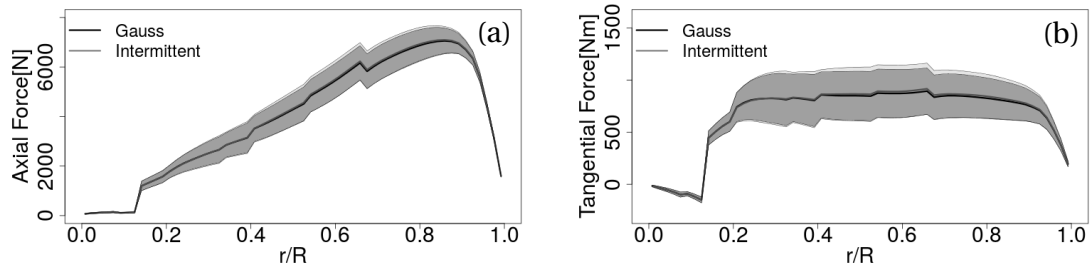


Figure 6.33: Force distribution across the blade in (a) axial and (b) tangential direction. The shaded areas mark the corresponding standard deviation.

Fatigue Loads

If now the equivalent fatigue loads are studied in the same way as in section 2.6, some differences become apparent as seen in Figure 6.34. The intermittent flow leads to a slight increase in EFL over a broad range of radial positions for tangential as well as axial forces.

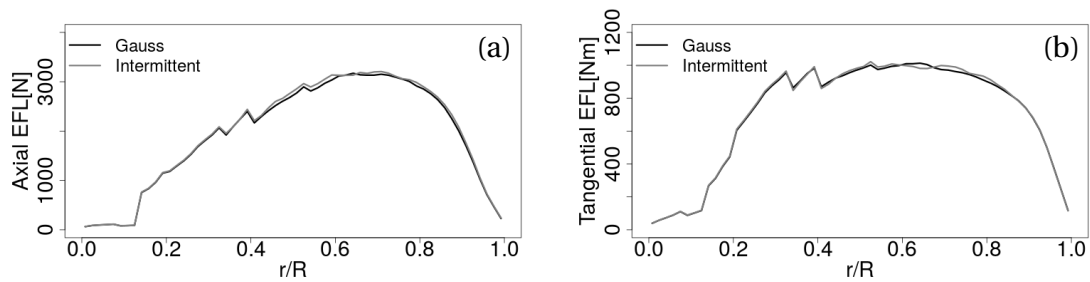


Figure 6.34: Equivalent fatigue loads of (a) axial and (b) tangential forces. The shaded areas mark the corresponding standard deviation.

Because the increase of loads for the intermittent case is of importance here, the differences of Gaussian and intermittent cases are plotted in form of the ratio of both in Figure 6.35. Axial as well as tangential loads show a difference of up to approximately 4% along the blade. Close to the blade root and the blade tip small differences between Gaussian and intermittent cases can be observed, but they are not relevant because the absolute loads are rather small.

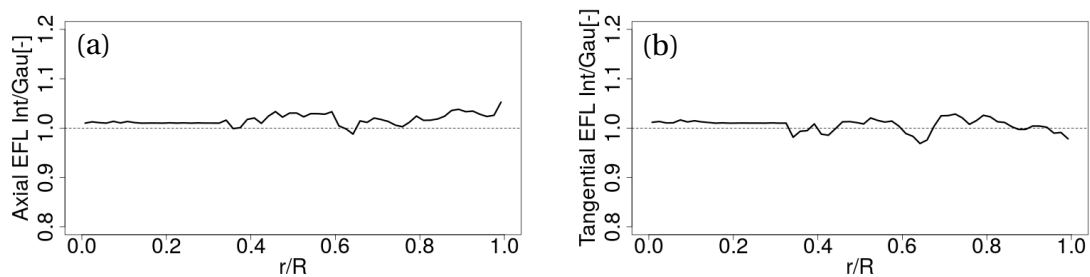


Figure 6.35: Ratio of Equivalent fatigue loads of (a) axial and (b) tangential forces.

To analyse the loads in more detail range histograms of thrust and torque have been created in Figure 6.36. Both histograms show no substantial difference between Gaussian and intermittent load cases in the small and mid-range region which might be surprising because the intermittent increment histograms reveal a slightly more pronounced peak around zero. However the difference between both simulation cases might be too small to result in visible differences in the range counts. It should also be kept in mind that range and increment histograms originate from fundamentally different data sets where especially the availability or unavailability of time information plays the biggest role.

More anticipated are the large range events which are slightly dominated by the intermittent inflow case for thrust as well as torque. Because the fatigue loads are directly affected by the heavy-tails due to the aforementioned involved Wöhler exponent m from Equation 2.31, it is expected that the EFL for the intermittent case are also slightly bigger.

The contribution of the ranges to the EFL, i.e. $n \cdot r^8$, is shown in Figures 6.37. Here the heavy weight of large range events becomes clear and it becomes more obvious, why the intermittent simulation case leads to higher loads. The intermittent and Gaussian loads are almost equally distributed but for high range events, the intermittent case has more counts, and with it higher EFL.

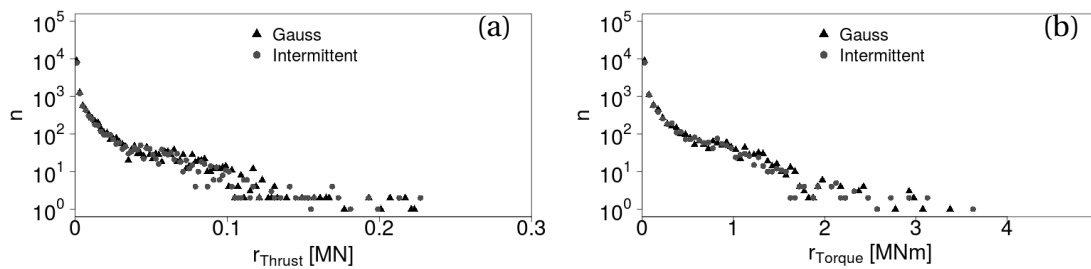


Figure 6.36: Range histograms with Gaussian and intermittent inflow for (a) thrust and (b) torque.

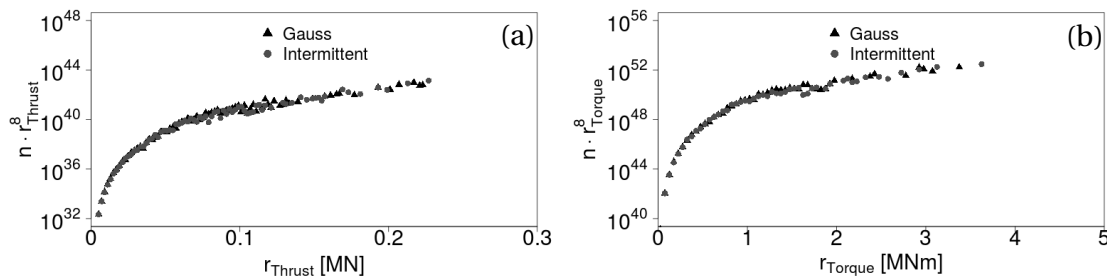


Figure 6.37: Contribution of ranges to EFL with Gaussian and intermittent inflow for (a) thrust and (b) torque.

Summary of Results

The results of the study under partially correlated inflow are summarized in Table 6.3 where the mean, standard deviation σ , maximal increment kurtosis K_{\max} and fatigue loads of the integral forces under Gaussian and intermittent inflow conditions are recorded. The given

errors are obtained by separating the corresponding time series into five distinct equally sized ensembles and calculating the ensemble standard deviation. For comparison reasons the ratios of the calculated quantities under Gaussian and intermittent inflow conditions are calculated in the last column.

Quite obvious are the almost equal mean and standard deviation for thrust as well as torque where the ratio for both inflow cases ranges from 100.6 % to 101.4 %. In contrast to that the increment kurtosis is quite different with an up to 37 % higher value for the intermittent case. However, even under Gaussian inflow conditions the increment kurtosis is larger than 3 which could also be seen in the increment PDF in Figures 6.27 and 6.31. For the fields studied here, parallels between increased EFL and heavy-tailed increment statistics, generated by the CTRW generator, might be drawn, because the EFL tends to be higher. Very strong fluctuation in the statistics, indicated by the errors, can be observed, but for the outcome of this section it can be argued that the actual time series is responsible for the EFL and not the five much smaller ensembles which are used for the error calculation. Nevertheless the increase of EFL by around 1 % is not very well-founded and might also be related to the increased standard deviation. An even bigger increment kurtosis for the intermittent case should be considered, which is not doable with the method used here because of the decaying process and convergence problems if the increment kurtosis becomes very big. The convergence problems are also visible in the errors of σ , K_{\max} and the EFL for the intermittent case, which are much higher than for Gaussian inflow conditions due to the short time series which are used as a basis for the error calculation.

Table 6.3: Thrust and torque comparison by mean, standard deviation σ , maximal increment kurtosis K_{\max} and EFL between Gaussian and intermittent partially correlated inflow fields.

		Gauss	Intermittent	Intermittent/Gauss [%]
Thrust [kN]	mean	700 ± 11	704 ± 10	100.6
	σ	37.4 ± 4.4	37.8 ± 9.3	101.1
	K_{\max}	3.76 ± 0.21	5.15 ± 0.37	137.0
	EFL	142 ± 17	145 ± 21	102.1
Torque [MNm]	mean	4352 ± 155	4415 ± 124	101.4
	σ	496.3 ± 58.1	501.4 ± 101.4	101.0
	K_{\max}	3.78 ± 0.18	4.69 ± 0.52	124.1
	EFL	1900 ± 222	1924 ± 296	101.3

6.2.3 Empty Domain Simulation with Fully Correlated Fields

To achieve an even better comparison of intermittent and non-intermittent inflows the same time series is injected at every grid point of the inflow patch such that the in-plane grid points are fully correlated with a correlation length of $r \rightarrow \infty$. This approach was already presented in section 5.0.2 for the airfoil simulations. Of course this simplification comes

with the cost of physicality because the correlation length is limited in reality. However the Gaussianization algorithm, which was explained in section 3.4.3, can be used here to achieve a much smoother Gaussian distribution for the one point histograms while the spectra are kept identical.

As done for the partially correlated cases, the wind field evolution in the empty domain is studied first where any effects coming from the rotor are not accounted for.

A snapshot for the two simulations with fully in-plane correlated velocity fields are shown in Figure 6.38. The full correlations are clearly visible in the middle, but in the upper and lower part deviations occur because of the mesh coarsening and the different mesh structure in general. The variance in streamwise direction is not changing on first glance and the structures are kept throughout the domain which gives rise to the expectation of a small energy loss. The decay mainly appears in the outer regions far away from the centerline. Some instabilities which look like vortices show up at some points in the Gaussian simulation which find their origin in numerical artifacts. Nevertheless because of the small number of occurrences they are not considered in the following studies.

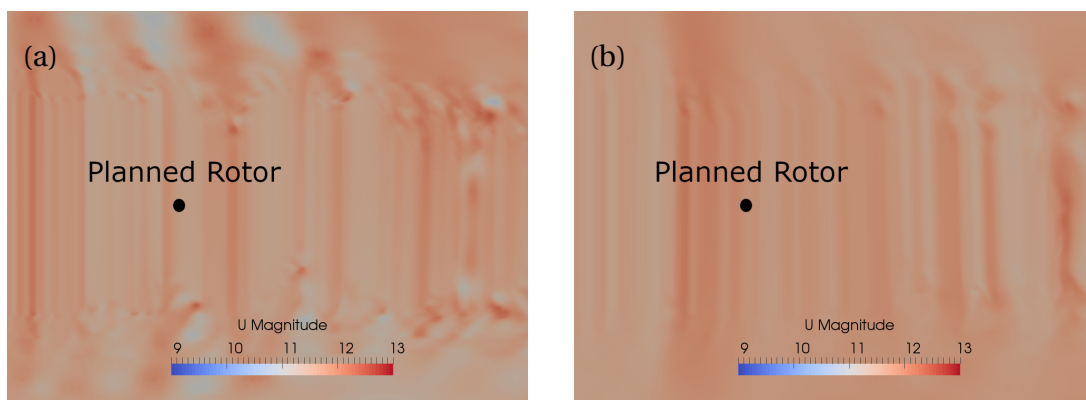


Figure 6.38: Snapshot of the flow field in an empty domain under fully correlated (a) Gaussian and (b) intermittent inflow conditions.

The mean velocity evolution is depicted in Figure 6.39a which is almost constant throughout the domain. Only a negligible increase of around 0.01 m/s occurs until the last measurement point close to the outlet. The standard deviation in Figure 6.39b is also very stable everywhere. In contrast to partial correlations no decay can be observed along the centerline. Instead, for the Gaussian flow field a very tiny increase can be noticed with its maximum 200 m behind the planned rotor position. The origin of this increase might be numerical issues which are also responsible for the small vertices in Figure 6.38a. But because this increase is less than 1% of the actual value it can also be neglected for the rotor simulations. So mean and standard deviation can be treated as almost identical for both fields.

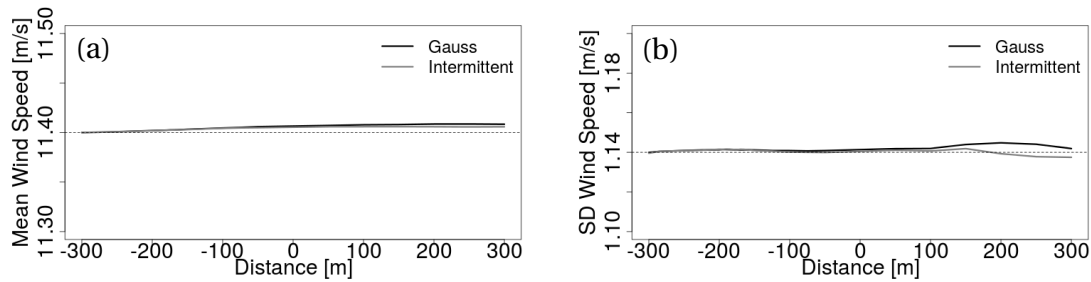


Figure 6.39: Evolution of (a) mean and (b) standard deviation of the fully in-plane correlated Gaussian and intermittent windfields at the centerline of the domain.

Close to the inlet and 50 m in front of the position where the rotor is planned the data is collected for the wind speed histograms in Figure 6.40. No clear bigger differences in the wind speed distributions can be observed between both locations which shows that a transport of the wind speed characteristics through the whole domain can be assumed by using such strongly correlated wind fields as it is done here. Both inflow cases do not completely fulfill the one point statistics of a Gaussian distribution, but the differences in the inner part are small thanks to the Gaussianization algorithm used here.

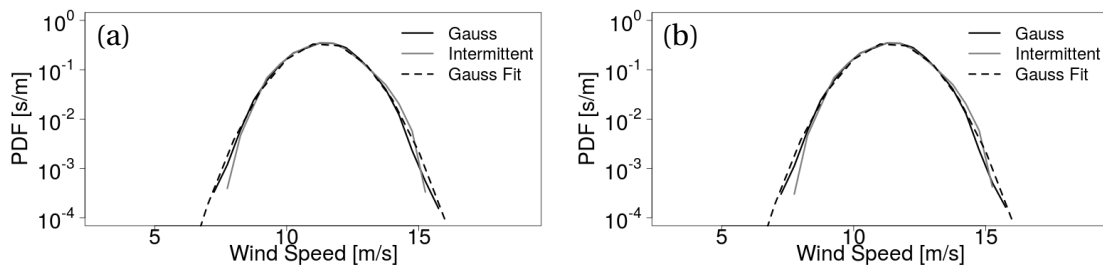


Figure 6.40: Distribution of wind speed in main stream direction for fully in-plane correlated Gaussian and intermittent wind fields (a) close to the inlet and (b) 50 m in front of the planned rotor in an empty domain.

The velocity increment histograms close to the inlet and the planned rotor are shown in Figure 6.41 where the difference between Gaussian and non-Gaussian fields is very pronounced even close to the rotor position. The heavy-tailed distribution does not change significantly which is a big contrast to the simulations where the fields are partially correlated in Figure 6.21b.

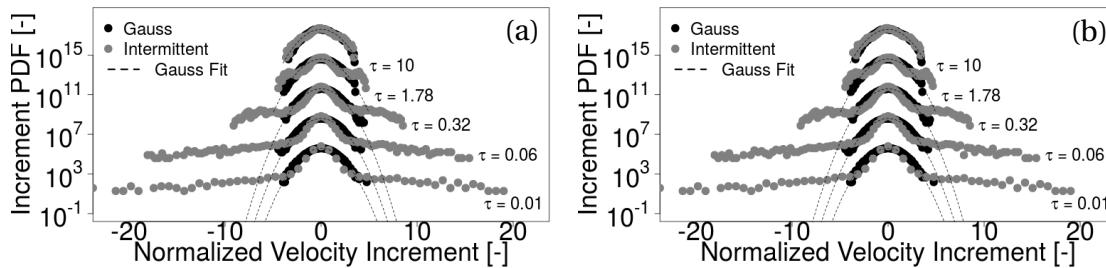


Figure 6.41: Increment distribution in main stream direction for fully in-plane correlated Gaussian and intermittent wind fields (a) close to the inlet and (b) 50 m in front of the planned turbine in an empty domain.

The almost unchanged increment statistics can be investigated in more detail by means of the maximal and minimal kurtosis, shown in Figure 6.42. From this plot no change at all can be seen throughout the whole domain which shows the power of full in-plane correlations if specific time series characteristics should be studied and no decay of turbulence is desired. Even though the increment kurtosis takes unrealistic high values, the fields can be used to investigate if the loads on the rotor are increased.

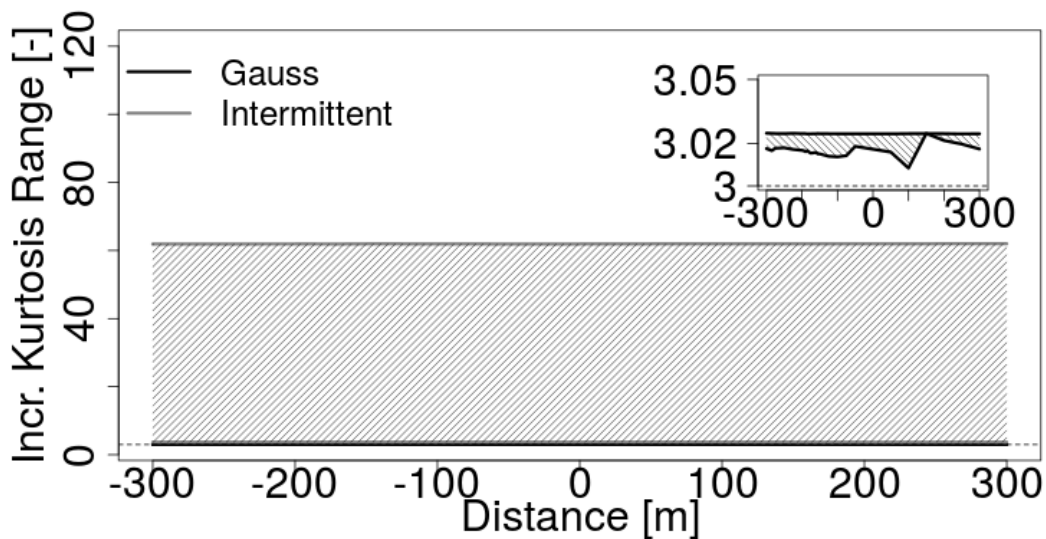


Figure 6.42: Evolution of minimal and maximal increment kurtosis of the fully in-plane correlated Gaussian and intermittent windfields at the centerline of the domain.

6.2.4 Rotor Simulation with Fully Correlated Fields

Finally the next step will be done by insertion of the rotor in the center of the domain at the planned position and redo the simulations with the same fully in-plane correlated wind fields as before.

Flow Fields

The velocity field at the same time point as in Figure 6.38 is shown in Figure 6.43. As for the partially correlated flow fields, the fields in front of the rotor are almost unchanged. The wake is meandering for the simulation shown here but not as strong as for the partially correlated wind fields. The intermittent case even shows less meandering effects but a good argumentation for this behavior can not be given.

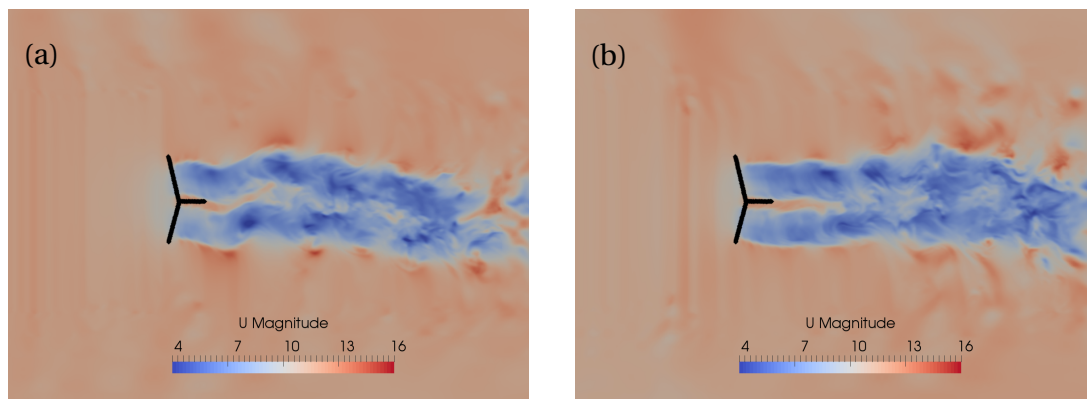


Figure 6.43: Snapshot of the flow field in the domain with a rotor under fully correlated (a) Gaussian and (b) intermittent inflow conditions. The inlet shows the zoomed in Gaussian case.

The mean wind speed and standard deviation are investigated in Figure 6.44. As already seen for the partially correlated fields in Figure 6.24a the mean value starts to drop because of the blockage effect of the rotor, then it experiences a speed up due to the jet in the middle of the rotor and finally it drops again. Interestingly the decay of the mean value differs from the analogue simulation with partially correlated fields. Those differences can be ascribed to uncertainties due to short wind time series. The standard deviation evolves in a totally different manner than for the cases mentioned earlier. In front of the rotor the constant value from the previous simulation without a rotor is kept, but surprisingly, now it does not drop while propagating downstream, but instead an increase can be noticed due to the turbulence generation by the moving rotor blades. Further downstream, at around 150 m behind the rotor, the standard deviation reaches a plateau and would be expected to drop to zero if the domain would be larger, because the strongly correlated structures are broken up and a decay in an analogue way to the partially correlated inflow case should appear.

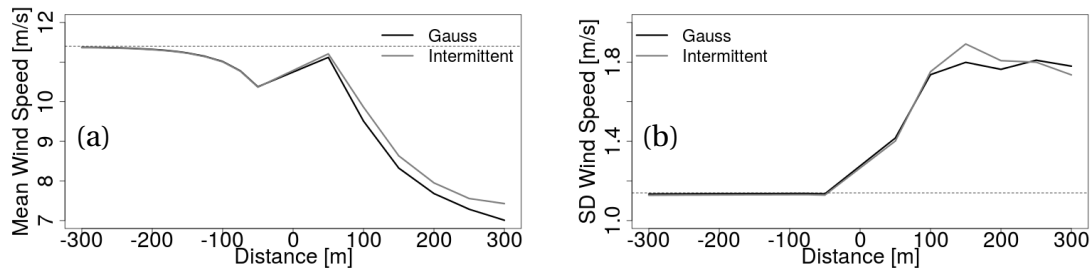


Figure 6.44: Evolution of (a) Mean and (b) standard deviation of the Gaussian and intermittent windfields at the centerline of the domain.

If the histograms for the wind speed at the centerline are compared near the inlet and in front of the rotor in Figure 6.45, no big difference can be observed. This let us conclude that the wind fields are approximately the same and the turbine is hit by the same wind field as injected.

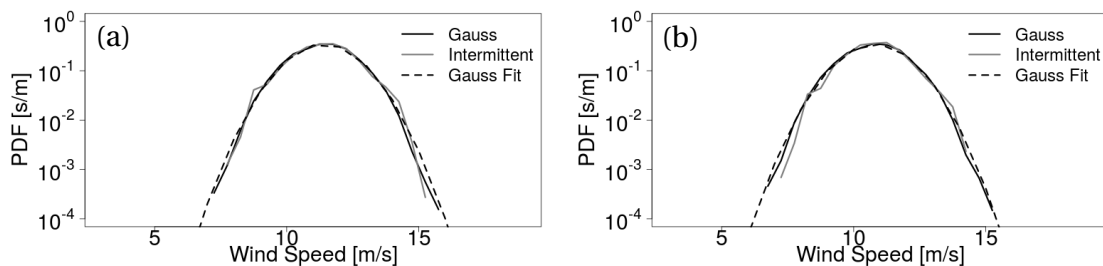


Figure 6.45: Distribution of wind speed in main stream direction for Gaussian and intermittent wind fields (a) close to the inlet and (b) 50 m in front of the rotor.

Figure 6.46 shows the compensated power spectra of both wind field types, which emphasizes the high similarity in front of the rotor. Except of small fluctuations in the small frequency range, both fields are almost indistinguishable and a load analysis can be performed without taking care of spectral differences.

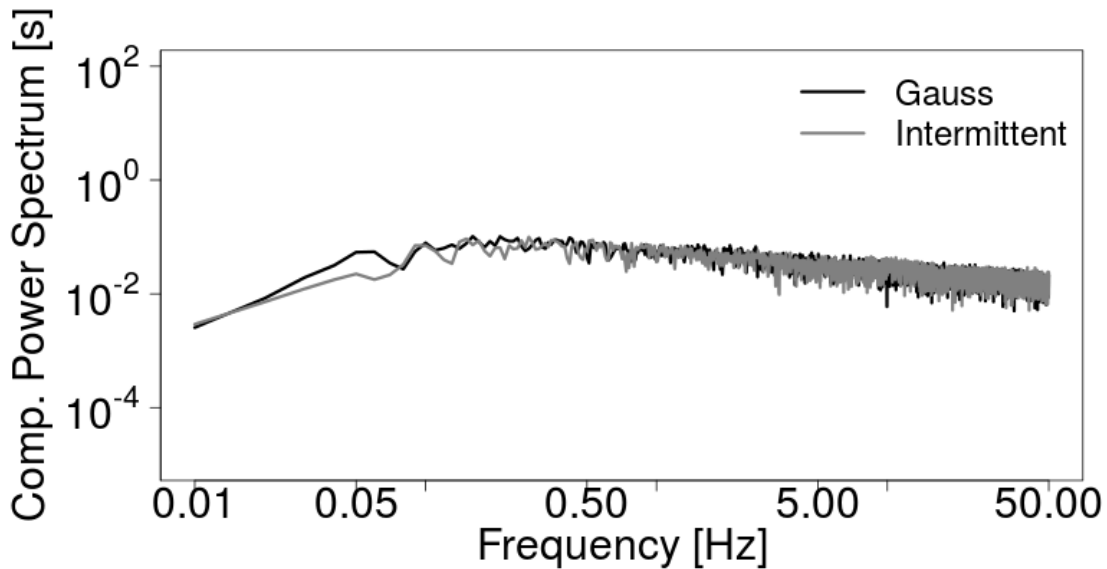


Figure 6.46: Spectra of both wind fields 50 m in front of the rotor.

The increments in Figure 6.47 are also almost the same and no big deviations are apparent. So in contrast to partial correlations the Gaussian inflow field preserves its Gaussianity in the increment statistics and the intermittent inflow field is still intermittent close to the rotor position. This allows a direct comparison of both types of fields with respect to induced forces and loads on the rotor.

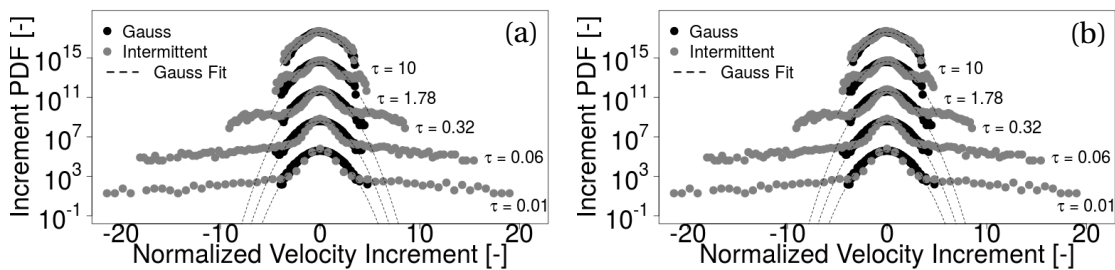


Figure 6.47: Increment distribution in main stream direction for Gaussian and intermittent wind fields (a) close to the inlet and (b) 50 m in front of the planned turbine in an empty domain.

The increment kurtosis can be measured at several points along the centerline and the outcome for the maximum and minimum is shown in Figure 6.48. For the intermittent case the increment kurtosis is very high everywhere and only a small drop is visible in the range where the jet occurs. In the wake of the turbine small fluctuations overlay the otherwise constant value. All in all no big change in the kurtosis happens for the intermittent case. The airfoil simulation in Figure 5.17c shows a very different behavior for fully correlated fields because the flow field is qualitatively very different to the current case. The rotating actuator lines in the present case act as forces on the flow field which do not immediately change the general direction of the flow like the airfoil boundary does, especially because the nacelle is not simulated. In addition the simulation setup is different in the sense that the airfoil is not rotating but static, and the spatial dimensions as well as the inflow fields are not comparable.

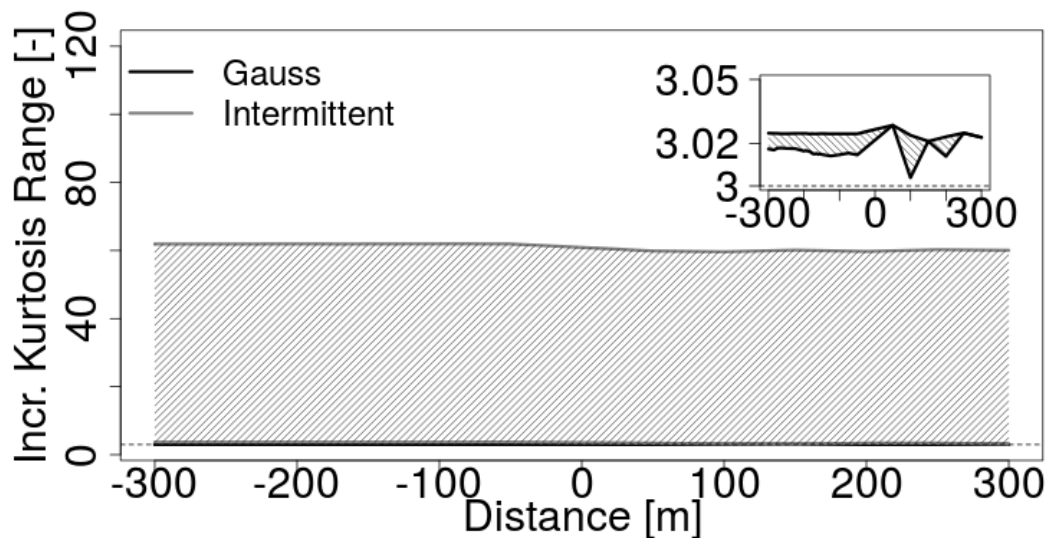


Figure 6.48: Evolution of the range of increment kurtosis of the fully in-plane correlated Gaussian and intermittent windfields for τ between 0.01 s and 10 s at the centerline of the domain. The inset shows the zoomed in Gaussian case.

Forces

The normalized thrust and torque time series for the Gaussian case in Figure 6.49a are as similar as for the partially correlated wind fields in Figure 6.29a but from Figure 6.49b it becomes clear that due to the full in-plane correlations of the wind the turbine directly reacts to the incoming wind time series. The averaging effect across the blade does not play any role in this case and the wind speed is directly transferred into forces. Again, the same effects could also be seen for the intermittent time series which makes it unnecessary to show them here additionally. It is also obvious that some frequency components, which were existing for partial correlations, are not present anymore.

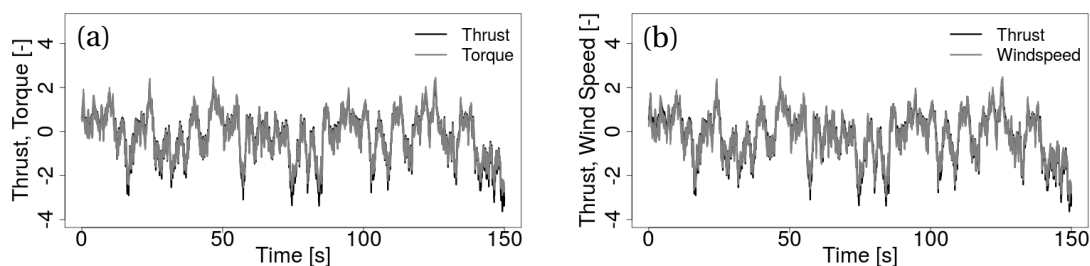


Figure 6.49: Time series of (a) thrust and torque, and (b) thrust and wind speed (shifted by 4.39 s).

The compensated power spectra in Figure 6.50 fits to the observations made for the time series from Figure 6.49 in the sense that all spectra are similar. The wind speed spectrum is slightly larger in the mid frequency range and smaller for high frequencies, but all in all the force spectra fit very well to the wind speed spectrum. In contrast to the force spectra

with partially correlated inflow fields in Figure 6.30 the 3P frequency is not visible for full in-plane correlation because all rotor blades are exposed to the same wind velocities at the same point in time. No spatial structures are available which can interact with the rotational frequencies.

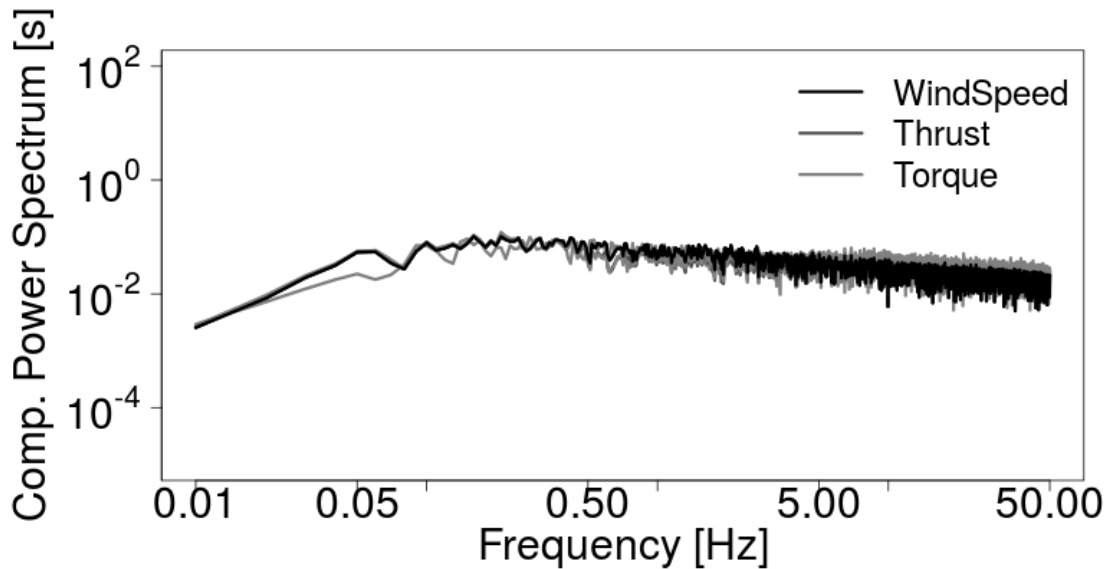


Figure 6.50: Spectra torque, thrust and Gaussian wind.

In the next step the increment distributions are visualized in Figure 6.51 where the expected heavy-tails under intermittent inflow conditions are obvious for thrust and torque. The same forces are almost Gaussian for the Gaussian inflow. Despite of this observation, it should be mentioned that the inflow is purely Gaussian but the forces shown here show up very small heavy-tails which were not existent in the wind. However the strong heavy-tails of the intermittent case are transferred from the wind to the forces without big losses because no filtering effect across the blade comes into play due to full in-plane correlations.

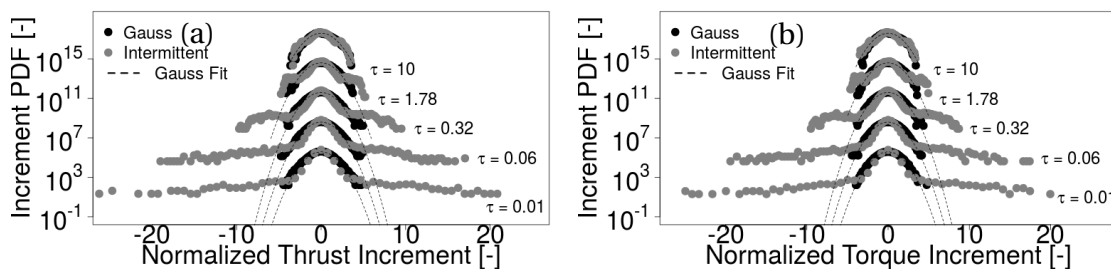


Figure 6.51: Increment distribution for Gaussian and intermittent wind fields of (a) thrust and (b) torque.

An overview over the increment kurtosis change with time delay τ is presented in Figure 6.52. While the Gaussian case has an increment kurtosis of almost three everywhere, the intermittent case starts above 200 and drops almost linearly, which is related to a power law. The short simulation time does not have a negative effect on the smoothness of the graph, in contrast to the results under partially correlated inflow conditions.

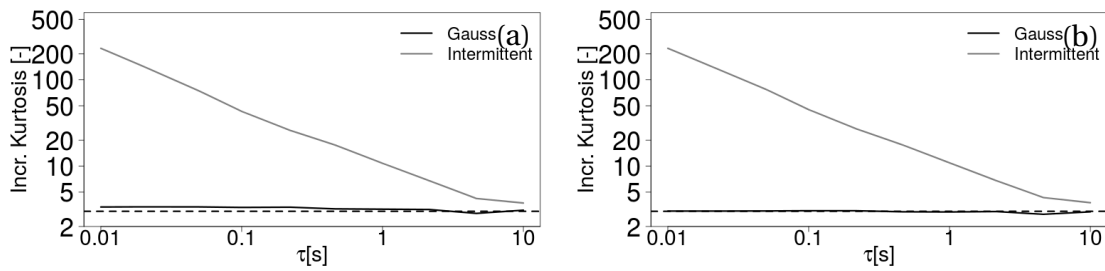


Figure 6.52: Increment kurtosis dependent on time delay for Gaussian and intermittent wind fields of (a) thrust and (b) torque.

The high comparability in the wind time series of intermittent and Gaussian inflows directly maps to the axial and tangential forces as seen in Figure 6.53. Both simulation cases lead to mean force distributions and standard deviations without any visible deviations.

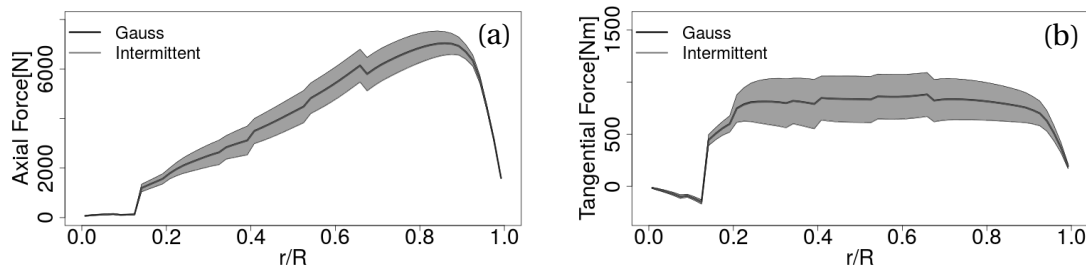


Figure 6.53: Force distribution across the blade in (a) axial and (b) tangential direction.

Fatigue Loads

Although the mean forces are not distinguishable, some differences occur for the fatigue loads in Figure 6.54. If compared to the results for partially correlated fields from Figure 6.34, a quite big gap in the loads between 20% and 95% span appears, where the loads resulting from intermittent wind fields are much higher than the loads with Gaussian origin.

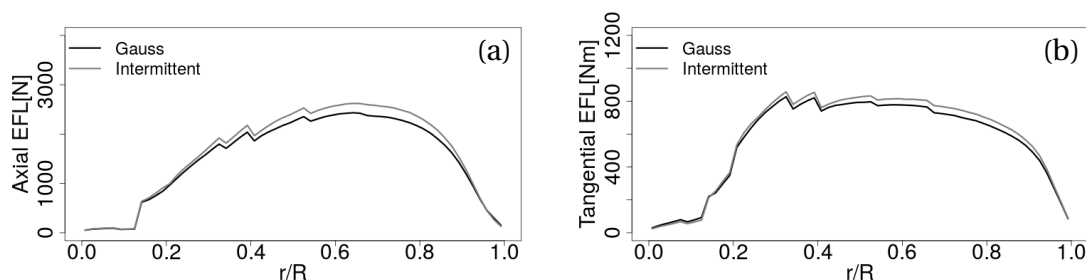


Figure 6.54: Equivalent fatigue loads of (a) axial and (b) tangential forces.

Relative values are investigated in Figure 6.55 where the ratio of the fatigue loads under intermittent and Gaussian inflow conditions is calculated for axial as well as tangential forces. In these pictures can be seen that the axial forces under intermittent inflow conditions are almost 10% higher than under Gaussian inflow conditions across the whole blade,

except for $r/R > 90\%$ where this ratio drops. Eventually, close to the tip the Gaussian case shows higher fatigue loads than the intermittent one. For the tangential forces it is different. The simulation with Gaussian inflow causes higher loads in the root region of the blade while everywhere else the intermittent case dominates. Because the wind fields are fully correlated in the whole rotor plane if no rotor is present, it could be concluded that the outer blade regions react differently to intermittency than the inner parts of the blade. But this could also be originating from other, maybe numerical, effects and is not studied in more detail.

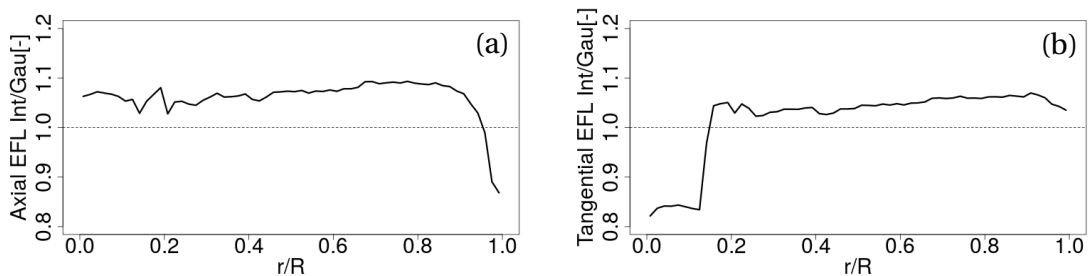


Figure 6.55: Ratio of Equivalent fatigue loads of (a) axial and (b) tangential forces.

In Figure 6.56 are the range histograms for thrust and torque under Gaussian and intermittent inflow conditions depicted. A clear difference between Gaussian and intermittent simulations can be found for both force types. Intermittent inflow leads to an increased amount of small and high ranges, while the Gaussian simulation case is close to the intermittent one for the medium ranges. It even dominates this part when the torque lies in the focus. In contrast to the simulation results with partially in-plane correlated fields from Figure 6.36 the increment statistics can more or less directly be related to the range histograms, i.e. increased probabilities of small and large increments can also be seen in more counts of the respective ranges. The weight in the EFL of large ranges is much heavier than of small ranges and therefore it is also expected that the intermittent case shows up increased fatigue loads.

Figure 6.57 gives an insight into the contribution to the EFL of the specific ranges. Here it becomes even more obvious that the intermittent inflow has a big impact on the EFL, because the high ranges are occupied by data points from the intermittent case.

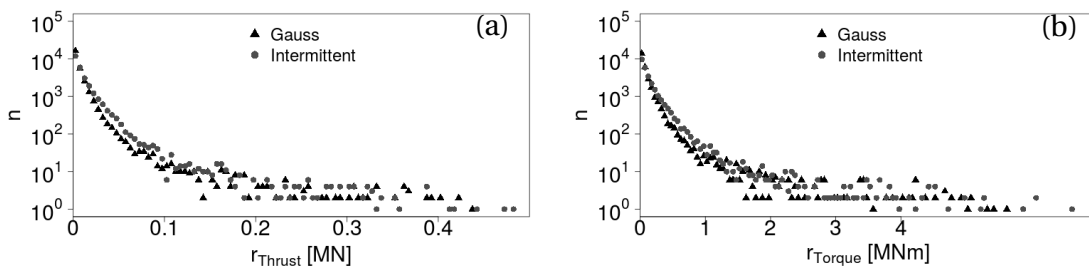


Figure 6.56: Range histograms with Gaussian and intermittent inflow for (a) thrust and (b) torque.

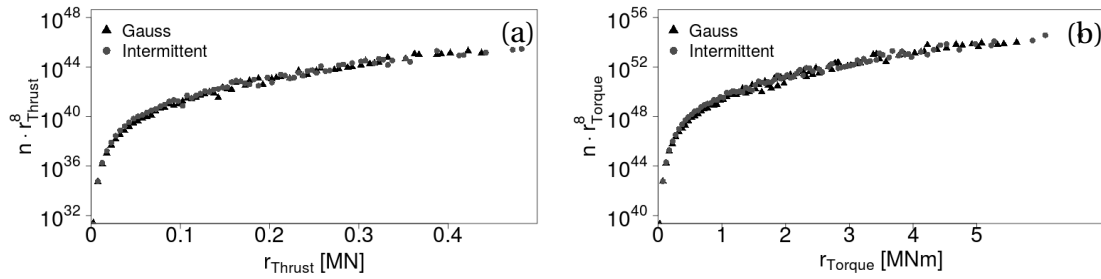


Figure 6.57: Contribution of ranges to EFL with Gaussian and intermittent inflow for (a) thrust and (b) torque.

Summary of Results

A summary of the results of the above simulations with fully in-plane correlated fields can be found in Table 6.4. The mean as well as the standard deviation show deviations below 1 % which is a prove of the good comparability quality of both fields. Because of the almost not existing decay in the simulation domain due to full correlations, rather strong deviations occur for the maximal increment kurtosis K_{\max} which is slightly larger than three for Gaussian fields but around 60 for the intermittent case. Therefore it is justifiable to attribute the increase in EFL of 4.8 to 6.6 % to the increased increment kurtosis in the CTRW fields. The errors, which are gained by separation of the time series into five distinct equally sized sub-samples and calculation of the ensemble standard deviation, are again much higher for the intermittent case. This shows how sensitive the recorded values are with respect to the length of the time series with a length of one fifth of the original one. The full time series still has a concrete mean, standard deviation, increment kurtosis and EFL and a clear and unambiguous relation between the increment kurtosis and the EFL can be found.

Table 6.4: Thrust and torque comparison by mean, standard deviation σ , maximal increment kurtosis K_{\max} and EFL between Gaussian and intermittent fully in-plane correlated inflow fields.

		Gauss	Intermittent	Intermittent/Gauss [%]
Thrust [kN]	mean	697 ± 9	696 ± 9	99.9
	σ	71.3 ± 4.9	70.9 ± 16.8	99.4
	K_{\max}	3.36 ± 0.16	61.59 ± 5.21	1833
	EFL	258 ± 24	275 ± 41	106.6
Torque [MNm]	mean	4290 ± 125	4281 ± 146	99.8
	σ	961.0 ± 76.6	960.0 ± 223.2	99.9
	K_{\max}	3.04 ± 0.16	56.3 ± 5.3	1852
	EFL	3472 ± 289	3638 ± 538	104.8

Convergence of EFL

In the following an observation from the simulations with fully correlated wind fields is picked up to be able to classify the quality of the previous results. The normalized time series of wind, torque and thrust in Figure 6.49 are nearly identical from which follows that the problem of finding EFL, gained from the thrust and torque time series, can be reduced to apply the rainflow count algorithm on the wind time series itself. Even if the EFL calculation of a wind time series does not result in loads in a physical sense, the qualitative results have to be equivalent to the thrust and torque related fatigue loads. Furthermore, the term EFL is also used in this context for the result of equation 2.31 with the wind time series as an input.

In order to study the convergence of the increment kurtosis and the EFL of the previous simulations with fully correlated wind fields, ten different realizations of Gaussian and intermittent time series with the parameters from above have been simulated over a range of 10000 s. For each simulation 20 subsets with different length, starting from 20 s up to 10000 s, have been created and the resulting increment kurtosis and EFL have been ensemble averaged. It can clearly be seen in Figure 6.58a that the increment kurtosis for all time series length is approximately 60 for the intermittent and 3 for the Gaussian time series as for the simulations above. However, the EFL in Figure 6.58b strongly depend on the time series length. They generally increase with increasing time series length for the Gaussian as well as intermittent inflow until a saturated level is reached. A minimal time series length of about 2000 s is needed for the EFL to be considered as converged. But even if the converged state is not reached for the 660 s intervals from the rotor simulations (vertical line), it is obvious that the intermittent simulation case shows higher fatigue loads than under Gaussian inflow conditions. Because an EFL difference of approximately 4-7 % can be observed between Gaussian and intermittent inflows in the converged region, the qualitative results from the rotor simulations in this chapter can be considered as correct with the specific simplified assumptions of the wind fields and the rotor.

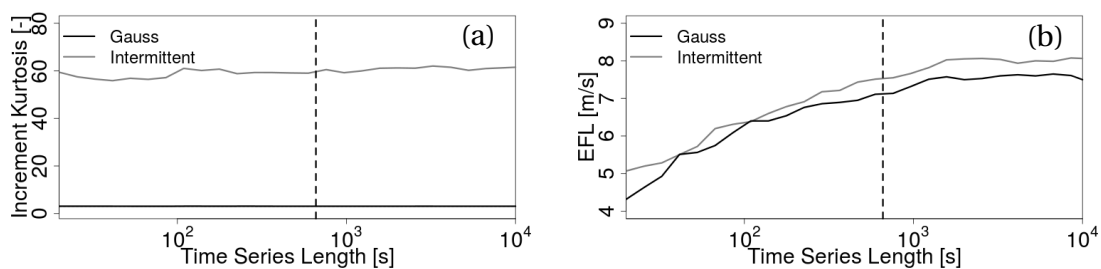


Figure 6.58: (a) Increment kurtosis and (b) EFL for wind time series of different length. The vertical dashed line marks the time series length of 660 s for the rotor simulations.

6.2.5 Discussion

Partially as well as fully in-plane correlated wind fields indicate that an increased increment kurtosis leads to increased fatigue loads. This result is much more significant for full correlations because of two major effects. The first one is the very high increment kurtosis which has a direct impact on the rotor loads. Second, deviations of the flow field in the plane in

front of the rotor are very small, i.e. the incoming inflow at each blade section is very similar and intermittency is not expected to be filtered across the blade or dominated by other effects.

Interestingly for the special case of full correlations it is possible to analyse the wind time series itself with the rainflow count algorithm, and not the forces, because the wind and force time series are almost identical, as seen in Figure 6.49b. For such simple studies the rotor effect can be neglected and general trends could be forecasted by a pure analysis of the wind fields. Nevertheless the fact should not be omitted that those fields are not physical at all and the representation of the rotor with rotating actuator lines is a strong simplification of reality. For studies, which are more industry specific, fully resolved blade simulations or other industry-like calculation tools [110] should lie in the focus for future studies with inflows which fulfill the IEC standards as well as consider the increment statistics of the flow field.

Chapter 7

Conclusions and Outlook

In this thesis the original CTRW model of Kleinhans [11], which incorporates higher order increment statistics in the generation of wind fields, has been improved in several ways and its turbulent main characteristics have been reported in the Gaussian limit. Those improvements are

- a corrected correlation matrix, which introduces exponentially decaying correlations to the wind field
- a new set of intuitive and physical parameters, which allows to write the energy spectrum and other derived turbulent properties in a compact way and which provides a subrange, where Kolmogorov's $-5/3$ law is nearly satisfied
- an alternative time distribution, the tempered Lévy distribution, where a much more consistent picture for the increment kurtosis with changing model parameters is achieved
- several correction algorithms to allow a good comparability of Gaussian and intermittent CTRW wind fields with respect to their increment statistics

With the improved CTRW model, the effect of an increased increment kurtosis could be studied in several CFD simulations:

For an open channel study, two different turbulence injection methods have been in the focus. It could be shown that a direct injection at the inlet of the channel leads to a conservation of the increment kurtosis along the whole channel, while the usage of an actuator leads to much smaller values, which made a comparison of Gaussian and intermittent wind fields difficult.

Next, the effect of an increased increment kurtosis on an airfoil and on a wind turbine rotor has been investigated. The main outcome of those simulations is that the increment kurtosis of the wind could be transferred to the airfoil and rotor forces. The fatigue loads for the airfoil as well as the rotor show a tendency to be higher, if the increment kurtosis is increased. Of special interest for industry applications might be the fact that compared to Gaussian inflow fields, the effect on the rotor loads is in the range of several percent, dependent on the inflow conditions. In this context, fully in-plane correlated wind fields

lead to higher fatigue than inflows with smaller correlation lengths.

Nevertheless some difficulties have to be taken into account if CFD should be used as the tool of choice for rotor simulations. First, the decay of turbulence is a very important point which should be considered. The original inflow field usually changes dramatically while it propagates through the domain. Not only the mean and the variance change their values but also the increment kurtosis which makes comparisons of two different wind fields difficult. Very intermittent inflow fields tend to have more Gaussian increment statistics while Gaussian inflow fields become more intermittent due to the development of a different type of turbulence within the domain. This behavior could be damped by usage of full in-plane correlations at the cost of physicality, but this step is only recommended if the focus lies on the increment statistics and not other maybe more important flow properties.

Second, the limitation of computational power also limits the spatial and temporal resolution as well as the overall dimensions of the inflow fields. But those are the requirements which are usually demanded for converged statistics of intermittent CTRW fields. A decision has to be made on how to satisfy the quality requirements on the statistics under affordable computational power.

As a future task, some restructurings on the CTRW model should be made in order to allow more realistic wind fields in terms of coherence, correlation and the scaling behavior of increment moments. Especially the third order moment, i.e. the skewness, is not modeled in a correct way and should be non-zero for realistic turbulence. For the correct spectral properties it should be studied if already existing spectral models like the Mann [2, 3] or the Kaimal model [4] could be extended by the intermittency concept via adding meaningful phase-amplitude relations to the generated wind fields in Fourier space. This would have the advantage that not only temporal but also spatial intermittency could be added, which is not considered at all in the CTRW model. A much more realistic load analysis would be possible and safety factors for the manufacturing of rotor blades could be reduced with the advantage that material usage as well as production costs could be lowered. However to the authors best knowledge no sophisticated approach for such an implementation has been developed at present.

As another possible improvement, cross correlations between the different velocity components could be implemented in an efficient way. The most simple but still inefficient approach would be to extend the correlation matrix by the cross correlations. But for a three component velocity field the total number of matrix entries would grow by a factor of nine. A drastic increase of the computational time for the involved Cholesky decomposition and an extremely inefficient field generation process would be the outcome.

In addition to the mentioned possible improvements, more studies on the characterization of intermittent CTRW fields have to be conducted. Up to now only ensemble averaged moments can be derived numerically, but the time averaged counterparts as well as spectra and other Fourier properties are not known at all and to the authors knowledge there is also no mathematical method available for this purpose.

Apart from this thesis, efforts were invested to study the effect of intermittent CTRW flow fields on fully resolved wind turbine rotors with flexible blades by usage of a fluid structure element code developed by Dose [111]. However statistical and numerical convergence

problems for such complex simulations made it impossible to achieve meaningful results. One of the future tasks could be to redo those simulations with an improved simulation setup and to analyse the loads on the rotor blades in a similar manner as done in this thesis. Intermittent inflow for yawed turbines could also be of interest in future studies as well as flows with shear, which is already part of the CTRW model, but not used in this thesis for the sake of simplicity.

Bibliography

- [1] I. IEC, “61400-1: Wind turbines part 1: Design requirements,” *International Electrotechnical Commission*, p. 177, 2005.
- [2] J. Mann, “The spatial structure of neutral atmospheric surface-layer turbulence,” *Journal of fluid mechanics*, vol. 273, pp. 141–168, 1994.
- [3] J. Mann, “Wind field simulation,” *Probabilistic engineering mechanics*, vol. 13, no. 4, pp. 269–282, 1998.
- [4] J. Kaimal, J. Wyngaard, Y. Izumi, and C. OR, “Spectral characteristics of surface-layer turbulence,” *Quarterly Journal of the Royal Meteorological Society*, vol. 98, no. 417, pp. 563–589, 1972.
- [5] F. Böttcher, C. Renner, H. Waldl, and J. Peinke, “Problematik der windböen,” *DEWI Magazin*, vol. 19, pp. 58–62, 2001.
- [6] F. Boettcher, C. Renner, H.-P. Waldl, and J. Peinke, “On the statistics of wind gusts,” *Boundary-Layer Meteorology*, vol. 108, no. 1, pp. 163–173, 2003.
- [7] F. Böttcher, *Statistische Analyse der atmosphärischen Turbulenz und allgemeiner stochastischer Prozesse*. PhD thesis, Universität Oldenburg, 2005.
- [8] B. Castaing, Y. Gagne, and E. Hopfinger, “Velocity probability density functions of high reynolds number turbulence,” *Physica D: Nonlinear Phenomena*, vol. 46, no. 2, pp. 177–200, 1990.
- [9] P. Milan, M. Wächter, and J. Peinke, “Turbulent character of wind energy,” *Physical review letters*, vol. 110, no. 13, p. 138701, 2013.
- [10] H. Haehne, J. Schottler, M. Waechter, J. Peinke, and O. Kamps, “The footprint of atmospheric turbulence in power grid frequency measurements,” *EPL (Europhysics Letters)*, vol. 121, no. 3, p. 30001, 2018.
- [11] D. Kleinhans, “Stochastische modellierung komplexer systeme,”
- [12] T. Mücke, D. Kleinhans, and J. Peinke, “Atmospheric turbulence and its influence on the alternating loads on wind turbines,” *Wind Energy*, vol. 14, no. 2, pp. 301–316, 2011.

- [13] H. Gontier, A. Schaffarczyk, D. Kleinhans, and R. Friedrich, "A comparison of fatigue loads of wind turbine resulting from a non-gaussian turbulence model vs. standard ones," vol. 75, no. 1, p. 012070, 2007.
- [14] C. M. Schwarz, S. Ehrich, and J. Peinke, "Wind turbine load dynamics in the context of turbulence intermittency," *Wind Energy Science*, vol. 4, no. 4, pp. 581–594, 2019.
- [15] C. Schwarz, S. Ehrich, R. Martín, and J. Peinke, "Fatigue load estimations of intermittent wind dynamics based on a blade element momentum method," in *Journal of Physics: Conference Series*, vol. 1037, p. 072040, IOP Publishing, 2018.
- [16] J. M. Jonkman, M. L. Buhl Jr, *et al.*, "Fast user's guide," *Golden, CO: National Renewable Energy Laboratory*, vol. 365, p. 366, 2005.
- [17] B. Jonkman and J. Jonkman, "Fast v8.16.00a-bjj," tech. rep., NREL, 2016.
- [18] J. Berg, A. Natarajan, J. Mann, and E. G. Patton, "Gaussian vs non-gaussian turbulence: impact on wind turbine loads," *Wind Energy*, vol. 19, no. 11, pp. 1975–1989, 2016.
- [19] J. A. Carlson, A. Jaffe, and A. Wiles, *The millennium prize problems*. Cambridge, MA, American Mathematical Society, Providence, RI: Clay Mathematics Institute, 2006.
- [20] S. B. Pope, *Turbulent flows*. Cambridge university press, 2001.
- [21] A. N. Kolmogorov, "Dissipation of energy in the locally isotropic turbulence," in *Dokl. Akad. Nauk SSSR A*, vol. 32, pp. 16–18, 1941.
- [22] A. S. Monin and A. Yaglom, "Statistical fluid mechanics ii," 1975.
- [23] F. Anselmet, Y. Gagne, E. Hopfinger, and R. Antonia, "High-order velocity structure functions in turbulent shear flows," *Journal of Fluid Mechanics*, vol. 140, pp. 63–89, 1984.
- [24] A. N. Kolmogorov, "A refinement of previous hypotheses concerning the local structure of turbulence in a viscous incompressible fluid at high reynolds number," *Journal of Fluid Mechanics*, vol. 13, no. 1, pp. 82–85, 1962.
- [25] K. Sreenivasan and P. Kailasnath, "An update on the intermittency exponent in turbulence," *Physics of Fluids A: Fluid Dynamics*, vol. 5, no. 2, pp. 512–514, 1993.
- [26] A. Morales, M. Wächter, and J. Peinke, "Characterization of wind turbulence by higher-order statistics," *Wind Energy*, vol. 15, no. 3, pp. 391–406, 2012.
- [27] C. Renner, *Markowanalysen stochastisch fluktuierender Zeitserien*. PhD thesis, Universität Oldenburg, 2002.
- [28] N. Jarrin, S. Benhamadouche, D. Laurence, and R. Prosser, "A synthetic-eddy-method for generating inflow conditions for large-eddy simulations," *International Journal of Heat and Fluid Flow*, vol. 27, no. 4, pp. 585 – 593, 2006. Special Issue of The Fourth International Symposium on Turbulence and Shear Flow Phenomena - 2005.

- [29] B. Stoevesandt, G. Schepers, P. Fuglsang, and S. Yuping, *Handbook of Wind Energy Aerodynamics*. Springer International Publishing, 2019.
- [30] T. S. Lund, X. Wu, and K. D. Squires, “Generation of turbulent inflow data for spatially-developing boundary layer simulations,” *Journal of Computational Physics*, vol. 140, no. 2, pp. 233 – 258, 1998.
- [31] P. R. Spalart, “Direct simulation of a turbulent boundary layer up to $r\theta = 1410$,” *Journal of Fluid Mechanics*, vol. 187, p. 61–98, 1988.
- [32] S. D. Mayor, P. R. Spalart, and G. J. Tripoli, “Application of a perturbation recycling method in the large-eddy simulation of a mesoscale convective internal boundary layer,” *Journal of the Atmospheric Sciences*, vol. 59, no. 15, pp. 2385–2395, 2002.
- [33] Y. Han, M. Stoellinger, and J. Naughton, “Large eddy simulation for atmospheric boundary layer flow over flat and complex terrains,” *Journal of Physics: Conference Series*, vol. 753, p. 032044, sep 2016.
- [34] M. Dörenkämper, B. Witha, G. Steinfeld, D. Heinemann, and M. Kühn, “The impact of stable atmospheric boundary layers on wind-turbine wakes within offshore wind farms,” *Journal of Wind Engineering and Industrial Aerodynamics*, vol. 144, pp. 146 – 153, 2015. Selected papers from the 6th International Symposium on Computational Wind Engineering CWE 2014.
- [35] M. Klein, A. Sadiki, and J. Janicka, “A digital filter based generation of inflow data for spatially developing direct numerical or large eddy simulations,” *Journal of computational Physics*, vol. 186, no. 2, pp. 652–665, 2003.
- [36] M. Breuer, “Effect of inflow turbulence on an airfoil flow with laminar separation bubble: An les study,” *Flow, Turbulence and Combustion*, vol. 101, pp. 433–456, Sep 2018.
- [37] R. Z. Szasz and L. Fuchs, “Computations of the flow around a wind turbine: Grid sensitivity study and the influence of inlet conditions,” pp. 345–352, 2010.
- [38] N. Kornev and E. Hassel, “Method of random spots for generation of synthetic inhomogeneous turbulent fields with prescribed autocorrelation functions,” *Communications in numerical methods in engineering*, vol. 23, no. 1, pp. 35–43, 2007.
- [39] R. Issa, “Solution of the implicitly discretised fluid flow equations by operator-splitting,” *Journal of Computational Physics*, vol. 62, no. 1, pp. 40 – 65, 1986.
- [40] H. Versteeg and W. Malalasekera, “An introduction to computational fluid dynamics: The finite volume method, 978-0131274983.”
- [41] D. Sale and A. Aliseda, “Sale, d. and aliseda, a. (2016) the flow field of a two-bladed horizontal axis turbine via comparison of rans and les simulations against experimental piv flume measurements,” 04 2016.

- [42] F. Bazdidi-Tehrani, D. Badaghi, M. Kiamansouri, and M. Jadidi, "Analysis of various in-flow turbulence generation methods in large eddy simulation approach for prediction of pollutant dispersion around model buildings," *Journal of Computational Methods In Engineering*, vol. 35, pp. 85–112, 02 2017.
- [43] A. Kubilay, D. Derome, and J. Carmeliet, "Analysis of time-resolved wind-driven rain on an array of low-rise cubic buildings using large eddy simulation and an eulerian multiphase model," *Building and Environment*, vol. 114, 12 2016.
- [44] P. Veers, "Modeling stochastic wind loads on vertical axis wind turbines," p. 910, 1984.
- [45] P. S. Veers, "Three-dimensional wind simulation," 1988.
- [46] T. Von Karman, "Progress in the statistical theory of turbulence," *Proceedings of the National Academy of Sciences of the United States of America*, vol. 34, no. 11, p. 530, 1948.
- [47] N. Troldborg, J. N. Sørensen, and R. Mikkelsen, "Actuator line simulation of wake of wind turbine operating in turbulent inflow," vol. 75, no. 1, p. 012063, 2007.
- [48] M. P. van der Laan and S. Andersen, "The turbulence scales of a wind turbine wake: A revisit of extended k-epsilon models," *Journal of Physics: Conference Series*, vol. 1037, p. 072001, 06 2018.
- [49] O. Eriksson, K. Nilsson, S.-P. Breton, and S. Ivanell, "Analysis of long distance wakes behind a row of turbines—a parameter study," vol. 524, no. 1, p. 012152, 2014.
- [50] Y. Kim, E. Jost, G. Bangga, P. Weihing, and T. Lutz, "Effects of ambient turbulence on the near wake of a wind turbine," *Journal of Physics: Conference Series*, vol. 753, p. 032047, sep 2016.
- [51] S. Paulsen and Uwe, "Simulation of shear and turbulence impact on wind turbine performance," 2018.
- [52] N. Dimitrov, M. C. Kelly, A. Vignaroli, and J. Berg, "From wind to loads: wind turbine site-specific load estimation with surrogate models trained on high-fidelity load databases," *Wind Energy Science*, vol. 3, no. 2, pp. 767–790, 2018.
- [53] T. J. Larsen and A. M. Hansen, "How 2 hawc2, the user's manual," 2007.
- [54] N. Mordant, P. Metz, O. Michel, and J.-F. Pinton, "Measurement of lagrangian velocity in fully developed turbulence," *Physical Review Letters*, vol. 87, no. 21, p. 214501, 2001.
- [55] R. Friedrich, "Statistics of lagrangian velocities in turbulent flows," *Physical review letters*, vol. 90, no. 8, p. 084501, 2003.
- [56] E. W. Montroll and G. H. Weiss, "Random walks on lattices. ii," *Journal of Mathematical Physics*, vol. 6, no. 2, pp. 167–181, 1965.

- [57] J. H. Schulz, E. Barkai, and R. Metzler, "Aging renewal theory and application to random walks," *Physical Review X*, vol. 4, no. 1, p. 011028, 2014.
- [58] B. B. Mandelbrot and J. W. Van Ness, "Fractional brownian motions, fractional noises and applications," *SIAM review*, vol. 10, no. 4, pp. 422–437, 1968.
- [59] R. Kupferman, "Fractional kinetics in kac–zwanzig heat bath models," *Journal of statistical physics*, vol. 114, no. 1, pp. 291–326, 2004.
- [60] D. Kleinhans, "Stochastische modellierung komplexer systeme,"
- [61] R. Metzler and J. Klafter, "The random walk's guide to anomalous diffusion: a fractional dynamics approach," *Physics reports*, vol. 339, no. 1, pp. 1–77, 2000.
- [62] B. Gnedenko, A. Kolmogorov, B. Gnedenko, and A. Kolmogorov, "Limit distributions for sums of independent," *Am. J. Math*, vol. 105, 1954.
- [63] P. H. Madsen, *Recommended practices for wind turbine testing and evaluation. 3. Fatigue loads*. 1990.
- [64] I. Rychlik, "A new definition of the rainflow cycle counting method," *International Journal of Fatigue*, vol. 9, no. 2, pp. 119 – 121, 1987.
- [65] T. A. Winter, *Modellierung dynamischer Lasten auf Windkraftanlagen unter dem Einfluss turbulenter Anströmung*. PhD thesis, Carl von Ossietzky Universität Oldenburg, 2016.
- [66] A. Cairoli and A. Baule, "Anomalous processes with general waiting times: Functionals and multipoint structure," *Physical review letters*, vol. 115, no. 11, p. 110601, 2015.
- [67] A. Cairoli and A. Baule, "Feynman–kac equation for anomalous processes with space- and time-dependent forces," *Journal of Physics A: Mathematical and Theoretical*, vol. 50, no. 16, p. 164002, 2017.
- [68] B. Baeumer and M. M. Meerschaert, "Tempered stable lévy motion and transient super-diffusion," *Journal of Computational and Applied Mathematics*, vol. 233, no. 10, pp. 2438 – 2448, 2010.
- [69] C. W. Gardiner *et al.*, *Handbook of stochastic methods*, vol. 3. springer Berlin, 1985.
- [70] G. I. Taylor, "The spectrum of turbulence," *Proceedings of the Royal Society of London. Series A-Mathematical and Physical Sciences*, vol. 164, no. 919, pp. 476–490, 1938.
- [71] D. Aronson and L. Löfdahl, "The plane wake of a cylinder: measurements and inferences on turbulence modeling," *Physics of Fluids A: Fluid Dynamics*, vol. 5, no. 6, pp. 1433–1437, 1993.
- [72] A. Baule and R. Friedrich, "Two-point correlation function of the fractional ornstein-uhlenbeck process," *EPL (Europhysics Letters)*, vol. 79, no. 6, p. 60004, 2007.

- [73] F. Puente León, U. Kiencke, and H. Jäkel, *Signale und Systeme*. Oldenbourg Verlag, 5. überarb. Aufl. ed., 2011.
- [74] G. M. Goerg, “Lambert w random variables—a new family of generalized skewed distributions with applications to risk estimation,” *Ann. Appl. Stat.*, vol. 5, pp. 2197–2230, 09 2011.
- [75] G. Goerg, “The lambert way to gaussianize heavy-tailed data with the inverse of tukey’s h transformation as a special case,” *The Scientific World Journal*, vol. 2015, 10 2010.
- [76] G. M. Goerg, “Lambertw: Probabilistic models to analyze and gaussianize heavy-tailed, skewed data,” 2020.
- [77] D. C. Hoaglin, “Summarizing shape numerically: The g-and-h distributions,” *Exploring data tables, trends, and shapes*, pp. 461–513, 2006.
- [78] M. K. Chung, P. Bubenik, and P. T. Kim, “Information processing in medical imaging: 21st international conference, ipmi 2009, williamsburg, va, usa, july 5-10, 2009,” *Proceedings, chapter Persistence Diagrams of Cortical Surface Data*, p. 681 f.
- [79] K. Kondo, S. Murakami, and A. Mochida, “Generation of velocity fluctuations for inflow boundary condition of les,” *Journal of Wind Engineering and Industrial Aerodynamics*, vol. 67, pp. 51–64, 1997.
- [80] M. S. Mohamed and J. C. LaRue, “The decay power law in grid-generated turbulence,” *Journal of Fluid Mechanics*, vol. 219, pp. 195–214, 1990.
- [81] L. Gilling and N. N. Sørensen, “Imposing resolved turbulence in cfd simulations,” *Wind Energy*, vol. 14, no. 5, pp. 661–676, 2011.
- [82] S. Sarkar and C. G. Speziale, “A simple nonlinear model for the return to isotropy in turbulence,” *Physics of Fluids A: Fluid Dynamics*, vol. 2, no. 1, pp. 84–93, 1990.
- [83] J. Kim, P. Moin, and R. Moser, “Turbulence statistics in fully developed channel flow at low reynolds number,” *Journal of fluid mechanics*, vol. 177, pp. 133–166, 1987.
- [84] W. Timmer, “The design and testing of airfoil du 91-w2-250,” in *Proc. IEA Joint Action. Aerodynamics of Wind Turbines. 6th Symposium*, 1992.
- [85] K. Rogowski and M. O. Hansen, “Rans simulations of flow past an du-91-w2-250 airfoil at high reynolds number,” in *E3S Web of Conferences*, vol. 44, p. 00150, EDP Sciences, 2018.
- [86] K. Rogowski, M. O. L. Hansen, R. Hansen, J. Piechna, and P. Lichota, “Detached eddy simulation model for the du-91-w2-250 airfoil,” in *Journal of Physics: Conference Series*, vol. 1037, p. 022019, IOP Publishing, 2018.

- [87] C. M. Velte, M. O. L. Hansen, K. E. Meyer, and P. Fuglsang, "Evaluation of the performance of vortex generators on the du 91-w2-250 profile using stereoscopic piv," in *International Symposium on Energy, Informatics and Cybernetics: Focus Symposium in the 12th World Multiconference on Systemics, Cybernetics and Informatics (WMSCI 2008)*, vol. 4, 2008.
- [88] M. Schramm, B. Stoevesandt, and J. Peinke, "Simulation and optimization of an airfoil with leading edge slat," in *Journal of Physics: Conference Series*, vol. 753, p. 022052, 2016.
- [89] S. Li, L. Zhang, K. Yang, J. Xu, and X. Li, "Aerodynamic performance of wind turbine airfoil du 91-w2-250 under dynamic stall," *Applied Sciences*, vol. 8, no. 7, p. 1111, 2018.
- [90] A. Morales, M. Wächter, and J. Peinke, "Characterization of wind turbulence by higher-order statistics," *Wind Energy*, vol. 15, no. 3, pp. 391–406, 2012.
- [91] P. R. Spalart, S. Deck, M. L. Shur, K. D. Squires, M. K. Strelets, and A. Travin, "A new version of detached-eddy simulation, resistant to ambiguous grid densities," *Theoretical and computational fluid dynamics*, vol. 20, no. 3, p. 181, 2006.
- [92] H. A. Madsen, N. N. Sørensen, C. Bak, N. Troldborg, and G. Pirrung, "Measured aerodynamic forces on a full scale 2MW turbine in comparison with EllipSys3D and HAWC2 simulations.," 2018.
- [93] Y. Kim, T. Lutz, E. Jost, S. Gomez-Irardi, A. Muñoz, B. Méndez, N. Lampropoulos, S. N., N. Sørensen, H. Madsen, P. van der Laan, H. Heißelmann, S. Voutsinas, and G. Papadakis, "Avatar deliverable d2.5: Effects of inflow turbulence on large wind turbines," *AVATAR Deliverable D2.5*.
- [94] J. Mann, "Wind field simulation," *Probabilistic Engineering Mechanics*, vol. 13, no. 4, pp. 269 – 282, 1998.
- [95] S. Ehrich, C. M. Schwarz, H. Rahimi, B. Stoevesandt, and J. Peinke, "Comparison of the blade element momentum theory with computational fluid dynamics for wind turbine simulations in turbulent inflow," *Applied Sciences*, vol. 8, no. 12, p. 2513, 2018.
- [96] J. N. Sørensen and W. Z. Shen, "Numerical Modeling of Wind Turbine Wakes," vol. 124, p. 393, 01 2002.
- [97] J. Jonkmann, S. Butterfield, W. Musial, and G. Scott, "Definition of a 5-MW Reference Wind Turbine for Offshore System Development," Tech. Rep. TP-500-38060, National Renewable Energy Laboratory, 15013 Denver W Pkwy, Golden, CO 80401, USA, February 2009.
- [98] OpenCFD, *OpenFOAM - The Open Source CFD Toolbox - User's Guide*. OpenCFD Ltd., United Kingdom, 1.4 ed., 11 Apr. 2007.
- [99] H. Rahimi, E. Daniele, B. Stoevesandt, and J. Peinke, "Development and application of a grid generation tool for aerodynamic simulations of wind turbines," *Wind Engineering*, vol. 40, no. 2, pp. 148–172, 2016.

- [100] H. Rahimi, *Improving Aerodynamic Engineering Models for Wind Turbines by means of Computational Fluid Dynamics*. Ph.D. Thesis , University of Oldenburg, 2018.
- [101] H. Rahimi, A. M. Garcia, B. Stoevesandt, J. Peinke, and J. G. Schepers, “An engineering model for wind turbines under yawed conditions derived from high fidelity models,” *Wind Energy*, 2018.
- [102] P. R. Spalart, S. Deck, M. L. Shur, K. D. Squires, M. K. Strelets, and A. Travin, “A new version of detached-eddy simulation, resistant to ambiguous grid densities,” *Theoretical and Computational Fluid Dynamics*, vol. 20, p. 181, May 2006.
- [103] S. Patankar and D. Spalding, “A calculation procedure for heat, mass and momentum transfer in three-dimensional parabolic flows,” *International Journal of Heat and Mass Transfer*, vol. 15, no. 10, pp. 1787 – 1806, 1972.
- [104] L. Prandtl, *Ludwig Prandtl Gesammelte Abhandlungen: zur angewandten Mechanik, Hydro- und Aerodynamik*. Springer-Verlag, 2013.
- [105] Z. Du and M. Selig, “A 3-d stall-delay model for horizontal axis wind turbine performance prediction,” in *1998 ASME Wind Energy Symposium*, p. 21, 1998.
- [106] J. Smagorinsky, “General Circulation Experiments with the Primitive Equations,” *Monthly Weather Review*, vol. 91, no. 3, pp. 99–164, 1963.
- [107] J. Jonkman, G. Hayman, B. Jonkman, and R. Damian, “AeroDyn v15 User’s Guide and Theory Manual (draft version),” tech. rep., NREL, July 2016.
- [108] J. G. Leishman and T. S. Beddoes, “A Semi-Empirical Model for Dynamic Stall,” *Journal of the American Helicopter Society*, vol. 34, pp. 3–17, 1989.
- [109] L. A. Martínez-Tossas, M. J. Churchfield, and S. Leonardi, “Large eddy simulations of the flow past wind turbines: actuator line and disk modeling,” *Wind Energy*, vol. 18, no. 6, pp. 1047–1060.
- [110] C. M. Schwarz, S. Ehrich, R. Martin, and J. Peinke, “Fatigue load estimations of intermittent wind dynamics based on a blade element momentum method,” *Journal of Physics: Conference Series*, vol. 1037, p. 072040, jun 2018.
- [111] B. Dose, *Fluid-structure Coupled Computations of Wind Turbine Rotors by Means of CFD*. PhD thesis, Carl von Ossietzky Universität, 2019.

List of publications

Peer-reviewed publications

- C. M. SCHWARZ, S. EHRICH, J. PEINKE: Wind turbine load dynamics in the context of turbulence intermittency, *Wind Energy Science*, 2019
- S. EHRICH: Turbulent Inflow Models, In: B. STOEVE SANDT, G. SCHEPERS, P. FUGLSANG, S. YUPING: Handbook of Wind Energy Aerodynamics, *Springer International Publishing*, 2019
- S. EHRICH, C. M. SCHWARZ, H. RAHIMI, B. STOEVE SANDT, J. PEINKE: Comparison of the Blade Element Momentum Theory with Computational Fluid Dynamics for Wind Turbine Simulations in Turbulent Inflow, *MDPI Applied Sciences*, 2018
- C. M. SCHWARZ, S. EHRICH, R. MARTÍN, J. PEINKE: Fatigue load estimations of intermittent wind dynamics based on a Blade Element Momentum method, *The Science of Making Torque from Wind*, Milano, Italy, 2018

Further Conferences Contributions

- S. EHRICH, C. M. SCHWARZ, H. RAHIMI, B. STOEVE SANDT, J. PEINKE: Investigation of the validity of the Blade Element Momentum Theory for wind turbine simulations in turbulent inflow by means of Computational Fluid Dynamics, *Journal of Physics: Conference Series*, 2018
- C. M. SCHWARZ, S. EHRICH, J. PEINKE: Super-Gaussian wind velocity increments and their impact on fatigue loads, *Wind Energy Science Conference*, Copenhagen, Denmark, 2017

Additional publications

- S. EHRICH, P. LIND, B. SHRESTHA, G. STEINFELD, J. TAMBKE, J. J. TRUJILLO, M. WÄCHTER, L. VERA TUDELA, H. WURPS, A. ZADOROZHNYI, M. KÜHN (Eds.): Probabilistische Lastbeschreibung, Monitoring und Reduktion der Lasten zukünftiger Offshore-Windenergieanlagen, *OWEA Loads Report*, 2017
- C. M. SCHWARZ, S. EHRICH, P. THOMAS: Turbulence Intermittency, *AVATAR Report D4.7*, 2016

Acknowledgements

This thesis would not be possible without the help and support of many people. First of all I would like to thank Prof. Dr. Joachim Peinke for giving me the opportunity to work in his TWiSt group on such an interesting topic and giving very constructive input for this work. Furthermore many thanks to Prof. Dr. Laura Lukassen for offering to evaluate this thesis.

Thanks to all my colleagues who spent the time at the university together with me, especially Bastian Dose and Hamid Rahimi, who always made the office life very enjoyable with several songs, and all the work related and non-work related talks, which made me smile day after day. However, without their support and simulation experience some of this work would not be possible.

I also want to thank a lot Carl Michael Schwarz for going the "intermittent" way together with me and for all the fruitful and interesting discussions where we solved simple and tried to solve seemingly unsolvable problems. Especially nerdy talks about prime numbers kept in my mind, but also very funny times with our office dog under the desk.

Also thanks a lot to all my CFD colleagues which are Lena (and our office dog Emma), Matthias, Cherif, Hassan, Ivàn, Jonas, Bernhard, Wided, Ghazaleh, Shumian, Leo and Samuel as well as my "stochastic" and "experimental" colleagues. I will always keep in mind the very enjoyable time at several conference locations and around the campfire at our group trips.

Special thanks go to my parents, and last but not least to my wife who followed me to Oldenburg, always supported me and gave me, together with my children, the time for this thesis when I needed it.

Curriculum vitae

Personal information:

Name Sebastian Ehrich
Birthday December 6th, 1984
Place of birth Potsdam, Germany
Citizenship German

Education:

01/2014 – Present PhD Student in Physics, C.v.O. University of Oldenburg
10/2005 – 09/2012 Diploma Studies in Physics, University of Potsdam

Professional experience:

01/2014 – Present Research fellow, ForWind, Institute of Physics, C.v.O. University of Oldenburg
08/2013 – 12/2013 Research assistant, Freie Universität Berlin, Germany
01/2013 – 04/2013 Research assistant, University of Potsdam, Germany
07/2011 – 09/2012 Student assistant, University of Potsdam, Germany

Erklärung

Ich erkläre hiermit, dass

- (a) eine Promotion zum Dr. rer. nat. angestrebt wird,
- (b) ich diese Arbeit selbständig verfasst und nur die angegebenen Hilfsmittel benutzt habe, und dass die Arbeit in Teilen bereits veröffentlicht bzw. zur Veröffentlichung eingereicht wurde,
- (c) diese Dissertation weder in ihrer Gesamtheit noch in Teilen einer anderen Hochschule zur Begutachtung in einem Promotionsverfahren vorgelegen hat.

Lehнин, den 13.03.2022

.....
(Name)

